

<https://doi.org/10.15388/vu.thesis.763>

<https://orcid.org/0000-0003-3782-7629>

VILNIUS UNIVERSITY

CENTER FOR PHYSICAL SCIENCES AND TECHNOLOGY

Vadzim Haronin

Pulsed Laser Deposition and Broadband Dielectric Spectroscopy of Complex Perovskite Materials

DOCTORAL DISSERTATION

Natural Sciences,
Physics (N 002)

VILNIUS 2025

The dissertation was prepared between 2020 and 2025 at Vilnius University (Vilnius, Lithuania).

Academic Supervisor – Prof. Habil. Dr. Jūras Banys (Vilnius University, Natural Sciences, physics – N 002).

This Doctoral Dissertation will be defended in a Public Meeting of the Dissertation Defence Panel:

Chairman — Prof. Dr. Gintaras Valušis (Vilnius University, Natural Sciences, Physics – N 002).

Members:

Assoc. Prof. Dr. Aleksandras Iljinas (Kaunas University of Technology, Technological Sciences, Materials Engineering – T 008).

Prof. Dr. Irmantas Kašalynas (Center for Physical Sciences and Technology, Natural Sciences, Physics – N 002).

Prof. Habil. Dr. Marco Kirm (University of Tartu, Technological Sciences, Materials Engineering – T 008).

Doc. Dr. Tomas Šalkus (Vilnius University, Technological Sciences, Materials Engineering – T 008).

The dissertation shall be defended at a public meeting of the Dissertation Defence Panel at 15:00 on 30th May 2025 in Room A101 of the National Center for Physical Sciences and Technology.

Address: Saulėtekio av., 3, Room A101., Vilnius, Lithuania.

The text of this dissertation can be accessed at the library of Vilnius University as well as on the website of Vilnius University:

www.vu.lt/lt/naujienos/ivykiu-kalendorius

<https://doi.org/10.15388/vu.thesis.763>

<https://orcid.org/0000-0003-3782-7629>

VILNIAUS UNIVERSITETAS
FIZINIŲ IR TECHNOLOGIJOS MOKSLŲ CENTRAS

Vadzim Haronin

Kompleksinių perovskito medžiagų nusodinimas impulsiniu lazeriu bei plačiajuostė dielektrinė Spektroskopija

DAKTARO DISERTACIJA

Gamtos mokslai,
Fizika (N 002)

VILNIUS 2025

Disertacija rengta 2020 – 2025 metais Vilniaus universitete.

Mokslinis vadovas – prof. habil. dr. Jūras Banys (Vilniaus universitetas, gamtos mokslai, fizika – N 002).

Gynimo taryba:

Pirmininkas — prof. dr. Gintaras Valušis (Vilniaus universitetas, gamtos mokslai, fizika – N 002).

Nariai:

doc. dr. Aleksandras Iljinas (Kauno technologijos universitetas, technologijos mokslai, medžiagų inžinerija – T 008).

prof. dr. Irmantas Kašalynas (Fizinių ir technologijos mokslų centras, gamtos mokslai, fizika – N 002),

prof. habil. dr. Marco Kirm (Tartu universitetas, technologijos mokslai, medžiagų inžinerija – T 008).

doc. dr. Tomas Šalkus (Vilniaus universitetas, technologijos mokslai, medžiagų inžinerija – T 008).

Disertacija ginama viešame Gynimo tarybos posėdyje 2025 m. gegužės mėn. 30 d. 15 val. Nacionalinio fizinių ir technologijos mokslų centro A101 posėdžių salėje. Adresas: (Saulėtekio al., 3, patalpos numeris A101, Vilnius, Lietuva),

Disertaciją galima peržiūrėti Vilniaus universiteto bibliotekoje ir VU interneto svetainėje adresu:

<https://www.vu.lt/naujienos/ivykiu-kalendorius>

ACKNOWLEDGMENTS

This dissertation represents the culmination of my doctoral research at Vilnius University. I am deeply grateful to all those who have contributed to my academic journey and supported me throughout this process.

First, I sincerely thank Dr. Juozas Šulskus, who noticed my email and topic and connected me with my current supervisor.

I extend my profound gratitude to Prof. Jūras Banys for his acceptance into the Doctor of Philosophy program under his supervision at the Institute of Applied Electrodynamics and Telecommunications. I am deeply grateful for his invaluable contributions, guidance, and unwavering support in procuring and analyzing the data, composing the papers, and completing this thesis.

Thank Dr. Robertas Grigalaitis for all your help from day one with the meeting and accommodation to a final discussion on research, organization matters, and other important aspects.

Thank all researchers that contributed to my work there and gave me valuable advice and support in my experiments and daily tasks: Sergejus Balčiūnas, Šarūnas Svirskas, Vidmantas Kalendra, Martynas Kinka, Artyom Plyushch, Darya Meisak, Mantas Šimėnas, Maksim Ivanov, Jan Macutkevič, Gediminas Usevičius, Dzmitry Tsyhanok, and all faculty staff members of Vilnius University who work behind unnoticed but are still necessary for the successful educational process.

I also would like to express my gratitude to the scientists at the Center for Physical Sciences and Technology and the Laser Research Center of Vilnius University: Algirdas Selskis, Rokas Kondrotas, Audrius Drabavičius, Evaldas Kažukauskas, Domas Paipulas, and Remigijus Juškėnas, who helped with the measurements and sample preparation.

I would also like to thank Prof. Marin Alexe for the opportunity to intern in his group at Warwick University and for his expertise in pulsed laser deposition and atomic force microscope techniques.

I am most grateful to my parents, Haronina Tatsiana and Haronin Pavel, for supporting and understanding me during my PhD studies and journeys.

CONTENTS

ACKNOWLEDGMENTS.....	5
1. INTRODUCTION.....	9
1.1. The aims of the work.....	12
1.2. The tasks of the dissertation.....	12
1.3. Scientific novelty.....	12
1.4. Author’s contribution.....	13
1.5. Statements presented for defense.....	14
1.6. Articles published on the topic of the dissertation.....	15
1.7. Conference contributions.....	15
2. LITERATURE REVIEW.....	17
2.1. Ferroelectric materials.....	17
2.2. Underlying principles of ferroelectricity.....	19
2.3. Phase transition in ferroelectric materials.....	24
2.3.1. Relaxor ferroelectric.....	28
2.3.2. Antiferroelectric materials.....	30
2.4. Ferroelectric domains.....	32
2.5. Dielectric relaxation models in ferroelectrics.....	34
2.5.1. Debye model.....	34
2.5.2. Cole-Cole model.....	36
2.5.3. Cole–Davidson model.....	38
2.5.4. Havriliak–Negami model.....	40
2.5.5. Resonance model.....	41
2.5.6. Empirical Cole-Cole model.....	42
2.6. Modeling variation of relaxation time in non-uniform materials.....	44
2.7. The importance of thin films and their applications.....	45
2.8. Motivation for using Pulsed Laser Deposition (PLD) in thin film fabrication.....	45
2.9. PLD fundamentals.....	46
2.9.1. Target.....	47
2.9.2. Vacuum chamber and ambient atmosphere.....	49

2.9.3. Ablation of the target	50
2.9.4. Thin film formation	51
2.9.5. Film growth control	57
2.9.6. Additional deposition parameters	61
3. EXPERIMENTAL METHODS AND MEASUREMENT TECHNIQUES.....	63
3.1. Pulsed Laser deposition systems	63
3.2 Dielectric spectroscopy measurement facilities	66
3.2.1. Low-frequency region	66
3.2.2. High-frequency region.....	67
3.2.3. Microwave region.....	69
4. RESULTS AND DISCUSSION	71
4.1. Investigation of dielectric and piezoelectric properties of PbZr _{0.2} Ti _{0.8} O ₃ film	71
4.1.1. Conclusion.....	82
4.2. Optimization of pulsed laser deposition parameters of 0.8(Na _{0.5} Bi _{0.5} TiO ₃)-0.2(BaTiO ₃) thin films	83
4.2.1. Conclusion and future work	114
4.3. Optimization of pulsed laser deposition parameters of ZrSnSe ₃ thin films	115
4.3.1. Conclusion and future work.	132
4.4. Dielectric investigation of Nb-doped and pure 0.7(BiFeO ₃)– 0.3(BaTiO ₃) ceramics.....	133
4.4.1. Conclusion.....	142
4.5. Dielectric investigation of PbHf _{1-x} Sn _x O ₃ material.....	143
4.5.1. Conclusion.....	148
5. SUMMARY	150
REFERENCES.....	151
6. SANTRAUKA LIETUVIŲ KALBA	173
6.1 Apžvalga.....	177
6.2. Eksperimentinė įranga ir metodai	181

6.3. $\text{PbZr}_{0,2}\text{Ti}_{0,8}\text{O}_3$ plėvelės dielektrinių ir pjezoelektrinių savybių tyrimas.....	183
6.4. $0,8(\text{Na}_0,5\text{Bi}_0,5\text{TiO}_3)-0,2(\text{BaTiO}_3)$ plonų plėvelių nusodinimo impulsiniu lazeriu parametrų optimizavimas.....	186
6.5. ZrSnSe_3 plonų plėvelių nusodinimo impulsiniu lazeriu parametrų optimizavimas.....	189
6.6. Nb legiruotos ir grynos $0,7(\text{BiFeO}_3)-0,3(\text{BaTiO}_3)$ keramikos dielektrinių savybių tyrimas.....	195
6.7. Dielektrinis $\text{PbHf}_{1-x}\text{Sn}_x\text{O}_3$ medžiagos tyrimas.....	201
6.8. Apibendrinimas.....	204
6.9. Nuorodos.....	205
6.10. Trumpa informacija apie disertacijos autorių.....	208
PUBLIKACIJŲ SĄRAŠAS.....	209

1. INTRODUCTION

Ferroelectric materials have attracted considerable attention because of their distinctive features [1], which render them essential in diverse technological applications, including sensors [2], actuators [3], memory devices [4], and energy storage systems [5]. Among these, the perovskite oxide family is one of the most intriguing ferroelectric material groups. The class of perovskites was first discovered in 1839 when Gustav Rose identified calcium titanate (CaTiO_3) and designated it "perovskite" in tribute to the Russian mineralogist L. A. Perovski [6]. This group comprises multiple compounds with a general formula of ABO_3 , where A and B denote distinct cation elements or a combination of two or more such ions. The physical properties of the entire family are highly variable; they can be metallic or dielectric and display many types of structural and ferroelectric order, depending on the composition and cationic arrangement [7].

One of the most important members of this perovskite family since their discoveries were lead-based perovskites, such as lead zirconate titanate ($\text{PbZr}_{0.2}\text{Ti}_{0.8}\text{O}_3$) and lead hafnate tin ($\text{PbHf}_{0.92}\text{Sn}_{0.08}\text{O}_3$). The lead ions in these materials induce substantial lattice distortions, augmenting spontaneous polarization — a fundamental attribute of ferroelectric materials. The substantial ionic radius of lead induces lattice strain that enhances the material's overall ferroelectric properties. Another aspect of these materials is that they are multi-component solid solution systems, and various properties can be achieved by altering the Zr: Ti or Hf: Sn ratio accordingly [8], [9].

One of the simple but effective methods to adjust stoichiometry for precise control of material properties is Pulsed Laser Deposition (PLD), which has become a versatile and successful technique for creating ferroelectric high-quality thin films [10]. The development of such materials into thin films has become a crucial research topic due to the demand for smaller sizes and improved performance in electronic devices [11] and the possibility of reaching properties that exceed the bulk properties of such materials [12], [13].

One of the main problems with lead-based ferroelectrics is the lead element itself, which gives them this unique property. Lead is a toxic heavy metal, and its use poses a substantial risk to the environment, health hazards, and problems with waste disposal and recycling issues [14]. To overcome this issue, the legislation from the European Union regarding the restriction of hazardous substances [15], along with an article published in Nature [16], served as significant catalysts for an initiative in the science and technology surrounding lead-free piezoceramics. Potential candidates to replace lead-based ferroelectrics include sodium bismuth titanate ($\text{Na}_{0.5}\text{Bi}_{0.5}\text{TiO}_3$), bismuth ferrite (BiFeO_3), and their modification with barium titanate (BaTiO_3) [17].

Sodium bismuth titanate ($\text{Na}_{0.5}\text{Bi}_{0.5}\text{TiO}_3$, NBT or BNT in literature) is seen as a possible substitute for lead zirconate titanate (PZT). It is a perovskite ferroelectric characterized by a rhombohedral crystallographic structure (space group: $R3c$) at room temperature. Due to its high Curie temperature of approximately $320\text{ }^\circ\text{C}$ and a substantial polarization of around $45\text{ }\mu\text{C}/\text{cm}^2$, NBT-based ceramics have garnered significant interest for energy storage applications. However, the high remanent polarization and the low breakdown strength harm energy storage applications [18]. Consequently, researchers primarily focus on reducing remanent polarization and enhancing the breakdown strength of NBT ceramic materials to enhance energy storage properties by creating a solid solution with barium titanate [19].

Another option is a bismuth ferrite (BiFeO_3 or BF), especially for high-temperature scenarios, owing to its elevated Curie temperature ($T_C \approx 825\text{ }^\circ\text{C}$) [20]. Still, pure BiFeO_3 ceramics are widely considered impractical as lead-free piezoceramics due to challenges such as high leakage current, difficulties in poling caused by a high coercive field, and poor piezoelectric coefficients, which restrict its practical use [20], [21]. In the BiFeO_3 - BaTiO_3 (BF-BT) solid solution system, it has been discovered that a small quantity of dopant is sufficient to decrease the significant leakage current [22]. A possible option for substitution could be Nb^{5+} donors on the B-site in BF-BT. It has been found that replacing Fe^{3+} with Nb^{5+} in BF-BT solid solutions can significantly reduce electronic conductivity and promote temperature stability [23].

One of the features of a pulsed laser deposition is an excellent base vacuum pressure and a flexible choice of the ambient atmosphere. This allowed us to work not only with oxygen-based perovskite materials, which require an oxygen atmosphere during deposition, but also with halide perovskites (ABX_3 , where A, B – metals, X – Se, S) that have applications in optoelectronic devices and must be deposited in an inert argon atmosphere to avoid oxygen impurities. One example of such material is a tin zirconium selenide ($ZrSnSe_3$), which can be used as the bottom electrode in solar cell devices. It's predicted to have a narrow bandgap of about 0.65 eV, be stable under ambient conditions, and is made up of earth-abundant, low-toxicity chemical components [24], [25].

This dissertation centers on the pulsed laser deposition of various perovskite films and broadband dielectric measurement of ferroelectric bulk materials and films. The objective is to investigate the pulsed laser deposition parameters of:

1. lead zirconate titanate ($PbZr_{0.2}Ti_{0.8}O_3$);
2. the composition of 80 % sodium bismuth titanate and 20 % of barium titanate ($0.8(Na_{0.5}Bi_{0.5}TiO_3)-0.2(BaTiO_3)$) and;
3. tin zirconium selenide ($ZrSnSe_3$).

Another significant aspect of the dissertation is the dielectric characterization of:

1. the lead zirconate titanate ($PbZr_{0.2}Ti_{0.8}O_3$);
2. lead hafnate doped with tin ($PbHf_{0.92}Sn_{0.08}O_3$) and;
3. undoped composition of 70% bismuth ferrite with 30 % barium titanate ($0.7(BiFeO_3)-0.3(BaTiO_3)$) and doped with 0.5% Nb;

and how these characteristics develop in a temperature range and a frequency domain. This research is a thorough investigation that examines the impact of doping, heating, and, in the case of thin film samples, different deposition conditions by PLD on the dielectric relaxation behavior and phase transitions.

1.1. The aims of the work

This thesis investigates the deposition of thin films of complex perovskite materials, namely $\text{PbZr}_{0.2}\text{Ti}_{0.8}\text{O}_3$, $0.8(\text{Na}_{0.5}\text{Bi}_{0.5}\text{TiO}_3)-0.2(\text{BaTiO}_3)$, ZrSnSe_3 , using Pulsed Laser Deposition (PLD). It also explores the temperature- and frequency-dependent dielectric properties of $\text{PbHf}_{1-x}\text{Sn}_x\text{O}_3$, Nb-doped and undoped $\text{BiFeO}_3-\text{BaTiO}_3$, and $\text{PbZr}_{0.2}\text{Ti}_{0.8}\text{O}_3$.

1.2. The tasks of the dissertation

1. Prepare thin films of $\text{PbZr}_{0.2}\text{Ti}_{0.8}\text{O}_3$ by Pulsed Laser Deposition and measure their dielectric and ferroelectric properties.

2. Prepare thin films of $0.8(\text{Na}_{0.5}\text{Bi}_{0.5}\text{TiO}_3)-0.2(\text{BaTiO}_3)$ by Pulsed Laser Deposition and analyze the effect of various deposition parameters on the quality and stoichiometry of the films.

3. Prepare thin films of ZrSnSe_3 by Pulsed Laser Deposition and optimize the deposition parameters to achieve the required properties for photovoltaic applications.

4. Measure the dielectric properties of pure and Nb-doped $\text{BiFeO}_3-\text{BaTiO}_3$ and investigate the effects of Nb doping on the dielectric relaxation dynamics in $\text{BiFeO}_3-\text{BaTiO}_3$ samples.

5. Investigate the dielectric properties and phase transition behavior of $\text{PbHf}_{0.92}\text{Sn}_{0.08}\text{O}_3$ crystals.

1.3. Scientific novelty

1. The new metal–ferroelectric–metal device structure was developed to investigate the dielectric properties of the $\text{PbZr}_{0.2}\text{Ti}_{0.8}\text{O}_3$, prepared by the Pulsed Laser Deposition method. This approach allowed us to reduce the adverse effects of the lattice defects in the film and achieve the remanent polarization value of $93 \mu\text{C}/\text{cm}^2$, which is higher than the theoretical value of $70 \mu\text{C}/\text{cm}^2$ in a bulk material.

2. The influence of the substrate buffer layer and deposition parameters on the quality and stoichiometry of the thin films of

0.8(Na_{0.5}Bi_{0.5}TiO₃)-0.2(BaTiO₃), prepared by the Pulsed Laser deposition, was investigated. The samples prepared with different buffer layers, target-to-substrate distance, substrate temperatures, ambient pressure, and laser fluence were analyzed by x-ray diffraction and scanning electron microscopy, allowing us to achieve optimal quality for dielectric applications.

3. For the first time, thin films of the ZrSnSe₃ were created with optimized deposition parameters by the Pulsed Laser Deposition from a single composition target, a modified composition target, and two partial composition targets (ZrSe₂ and SnSe) for a photovoltaic application.

4. Relaxor behavior of an Nb-doped BiFeO₃-BaTiO₃ solid solution was investigated for the first time using broadband dielectric spectroscopy, exploring a wide frequency range from 20 Hz to 30 GHz and a temperature range from 200 to 500 K. The results reveal the presence of thermally induced transitions between ordered and disordered states.

5. The permittivity of PbHf_{0.92}Sn_{0.08}O₃ crystals was investigated using broadband dielectric spectroscopy in a region from 20 Hz to 200 GHz, with a particular interest in the 10–100 GHz region where dispersion was expected to occur. A wide range of temperature measurements from 300 to 500 K allowed us to analyze the shifts of the dispersion peak from 20 Hz to 100 GHz between 470 and 500 K and the decrease in damping as the temperature approaches T_c, which is 494 K, as proven by measurement and the modified Cole-Cole model.

1.4. Author's contribution

The author prepared the sample using the Pulsed Laser Deposition of 0.8(Na_{0.5}Bi_{0.5}TiO₃)-0.2(BaTiO₃). ZrSnSe₃ was prepared in collaboration with Dr. Rokas Kondratas, and PbZr_{0.2}Ti_{0.8}O₃ was prepared by the author under the supervision of Dr. Marin Alexe at Warwick University. The author made most technological preparations using the Pulsed Laser Deposition facility (substrate preparation, facility maintenance). The author personally prepared all samples for

the dielectric investigations in the thesis (measurement of dimensions of the samples, contact preparation, cutting a sample into a thin rod for waveguide system measurement, etc.). The author also performed all dielectric measurements of the samples except for a terahertz range measurement in the investigation of $\text{PbHf}_{0.92}\text{Sn}_{0.08}\text{O}_3$ crystals. The author analyzed and fitted dielectric spectroscopy data and wrote the published articles with excellent support and discussion with S. Svirskas, O. Suvorova, R. Grigalaitis, J. Banyš, and other co-authors. AI technologies assisted with some of the aspects of the dissertation project.

1.5. Statements presented for defense

1. Lead Zirconate Titanate ($\text{PbZr}_{0.2}\text{Ti}_{0.8}\text{O}_3$) thin film deposited on SrTiO_3 substrate demonstrates significantly enhanced remanent polarization with a value of $93 \mu\text{C}/\text{cm}^2$, attributed to strain-induced effects caused by the substrate film lattice mismatch and highlights the unique impact of the film-substrate interactions on ferroelectric properties.

2. The structural quality, stoichiometry, and uniformity of $0.8(\text{Na}_{0.5}\text{Bi}_{0.5}\text{TiO}_3)\text{-}0.2(\text{BaTiO}_3)$ and ZrSnSe_3 thin films were strongly influenced by deposition parameters of the pulsed laser deposition method, such as buffer layer, laser fluence, substrate temperature, ambient pressure, and target-to-substrate distance. Optimized deposition parameters for NBT-BT film include a platinum buffer layer, laser fluence of $1.5 - 2.1 \text{ J}/\text{cm}^2$, substrate temperature of $600 \text{ }^\circ\text{C}$, 0.3 mbar O_2 ambient pressure, and 55 mm target to substrate distance. For ZrSnSe_3 , optimal parameters include a $0.3 \text{ J}/\text{cm}^2$ laser fluence, deposition pressure of 0.01 mbar of argon gas, substrate temperature of $150 \text{ }^\circ\text{C}$, target-to-substrate distance of 95 mm , and minimal spot size. Following this parameter, we are enabling the fabrication of high-quality crystalline films with precise stoichiometry and structural control, highlighting their potential for advanced technological applications.

3. The relaxor behavior in a solid solution of bismuth ferrite and barium titanate (70% BiFeO₃ and 30% BaTiO₃) shows complex thermally induced transitions between ordered and disordered states in the temperature range of 270 K to 400 K, revealed through broadband dielectric spectroscopy over a wide frequency range of 20 Hz to 30 GHz and temperature range of 200 K to 500 K.

4. Lead Hafnate Tin (PbHf_{0.92}Sn_{0.08}O₃) crystals exhibit notable shifts of the dielectric dispersion peak from 20 GHz to 100 GHz and changes in the damping coefficient between 470 and 500 K, near the Curie temperature, as identified through broadband dielectric spectroscopy and supported by the resonance dispersion model.

1.6. Articles published on the topic of the dissertation

1. V. Haronin, Z. Yang, R. Grigalaitis, I. Calisir, J. Banys, and D. A. Hall, "Broadband dielectric spectroscopy of Nb-doped 0.7BiFeO₃-0.3BaTiO₃ ceramics," *J. Phys. Commun.*, vol. 8, no. 6, pp. 0–8, 2024, doi: 10.1088/2399-6528/ad55a2.

2. Haronin, V., Jankowska-Sumara I., Kadlec C., Majchrowski A., Suvorova O., Grigalaitis R., & Banys J. (2024). Broadband dielectric spectroscopy of a PbHf_{1-x}Sn_xO₃ material. *Phase Transitions*, 1–6. doi: 10.1080/01411594.2024.2369838.

3. V. Haronin, M. Alexe, R. Grigalaitis, J. Banys. Semiconductive lead zirconate titanate thin films grown by pulsed laser deposition, *Lithuanian Journal of Physics*, Vol. 64, No. 2, pp. 101–106 (2024). doi: 10.3952/physics.2024.64.2.3.

1.7. Conference contributions

1. Growth of strontium titanate film by pulsed laser deposition, V. Haronin, S. Svirskas, A. Selskis, R. Grigalaitis, J. Banys, 44th Lithuanian National Physics Conference – 2021, October 6-8, Vilnius, Lithuania.

2. Pulsed laser deposition for the creation of strontium titanate coatings, V. Haronin, S. Svirskas, A. Selskis, R. Grigalaitis, J. Banys, IEEE ISAF-PFM-ECAPD – 2022, June 27 – July 1, Tours, France.
3. Broadband dielectric investigations of $0.7\text{BiFeO}_3\text{-}0.3\text{BaTiO}_3$ ceramics, V. Haronin, R. Grigalaitis, J. Banys, Z. Yang, Y. Li, D. A. Hall, Ceramics in Europe – 2022, July 10-14, Krakow, Poland.
4. Structural and electrical properties of epitaxial lead zirconate titanate grown by pulsed laser deposition, V. Haronin, M. Alexe, R. Grigalaitis, J. Banys, 15th International Meeting on Ferroelectricity – 2023, March 26-30, Tel-Aviv, Israel.
5. Broadband dielectric properties of re-entrant relaxor Nb-doped $\text{BiFeO}_3\text{-BaTiO}_3$ ceramics, V. Haronin, R. Grigalaitis, J. Banys, Z. Yang, Y. Li, D. A. Hall, ISAF-ISIF-PFM Joint Conference – 2023, July 23 - 27, Cleveland, USA.
6. Microwave measurement of $\text{PbHf}_{1-x}\text{Sn}_x\text{O}_3$ single crystal, V. Haronin, R. Grigalaitis, J. Banys, A. Majchrowski, I. Jankowska-Sumara, VI Polish-Lithuanian-Ukrainian Meeting on Physics of Ferroelectrics – 2023, September 11 – 15, Czestochowa, Poland.
7. Broadband dielectric measurements of $\text{PbHf}_{1-x}\text{Sn}_x\text{O}_3$ single crystal, V. Haronin, I. Jankowska-Sumara, A. Majchrowski, O. Suvorova, R. Grigalaitis, J. Banys, 45th Lithuanian National Physics Conference – 2023, October 25 – 27, Vilnius, Lithuania.
8. Electrical properties of epitaxial lead zirconate titanate grown by pulsed laser deposition, V. Haronin, M. Alexe, R. Grigalaitis, J. Banys, 45th Lithuanian National Physics Conference – 2023, October 25 – 27, Vilnius, Lithuania.
9. Broadband dielectric investigation of Nb-doped $\text{BiFeO}_3\text{-BaTiO}_3$ relaxor ceramics, V. Haronin, R. Grigalaitis, J. Banys, Z. Yang, Y. Li, D. A. Hall, 45th Lithuanian National Physics Conference – 2023, October 25 – 27, Vilnius, Lithuania.
10. Broadband dielectric measurements of $\text{PbHf}_{1-x}\text{Sn}_x\text{O}_3$ single crystal, V. Haronin, I. Jankowska-Sumara, C. Kadlec, A. Majchrowski, O. Suvorova, R. Grigalaitis, J. Banys, European Conference on Applications of Polar Dielectrics – 2024, June 16 – 19, Trondheim, Norway.

2. LITERATURE REVIEW

2.1. Ferroelectric materials

Ferroelectric materials constitute a significant category of electroceramic components and are commonly utilized as thermistors, transducers, and capacitors [26]. Even though it was discovered as a phenomenon in 1920 by Joseph Valasek, who was a graduate student working under the supervision of William Swann at the University of Minnesota, Minneapolis, US, it wasn't researched before 1946 after the future Nobel prize-winning physicist Vitaly Ginzburg wrote a classic paper called "Seignettelectric" At the time the name was given by effect that had been originally observed in Seignette salt [26]. The works of prominent crystal physicists Weiss, Pasteur, Pockels, Hooke, Groth, Voigt, and the Curie brothers from the previous century served as the historical foundation for the discovery of ferroelectricity. The discovery of barium titanate during World War II marked a significant acceleration in the research of ferroelectrics, which had started with the groundbreaking work on Rochelle salt and potassium dihydrogen phosphate [27].

Materials can be called ferroelectrics if the application of an external electric field reverses spontaneous electric polarization. Additionally, every ferroelectric material possesses reversible electrical polarization by nature, making it piezoelectric and pyroelectric. Since the internal electric dipoles of ferroelectric material are related to the lattice structure, modifications will alter the dipole's strength, specifically, the spontaneous polarization. The key concept for a ferroelectric material is a dipole moment, defined in equation (1):

$$P = \sum_i e_i r_i, \quad (1)$$

where e_i is the charge of the i th particle, and r_i is the radius vector of this charge.

Approximately one thousand ferroelectrics have been discovered. Table 1 lists a few of them, their year of discovery, and some key characteristics.

Table 1. A list of ferroelectric materials and their properties [28].

Compound	Chemical formula	Year discovered	Curie temperature, T_c (K)	Remanent polarization, P_s ($\mu\text{C}\cdot\text{cm}^{-2}$)	Crystal structure (at room temperature)
Rochelle salt	$\text{KNaC}_4\text{H}_4\text{O}_6\cdot 4\text{H}_2\text{O}$	1921	255 and 297	0.25	Monoclinic between the Curie points, Orthorhombic at other temperatures
Potassium dihydrogen phosphate	KH_2PO_4	1935	123	6.1	Orthorhombic
Barium titanate	BaTiO_3	1945	398	25	Tetragonal
Lithium niobate	LiNbO_3	1949	1415	10–30	Trigonal
Potassium niobate	KNbO_3	1949	400	20–40	Orthorhombic
Lead zirconate titanate	$\text{PbZr}_{1-x}\text{Ti}_x\text{O}_3$	1949	Depends on composition	20–97	Tetragonal for Ti-rich, Rhombohedral for Zr-rich
Lead titanate	PbTiO_3	1950	763	20–96.5	Tetragonal
Lead zirconate	PbZrO_3	1951	503	20–50	Orthorhombic

Key characteristics of ferroelectric materials include their values of the spontaneous polarization P_s and the Curie point, or transition temperature, T_c , at which the crystal transitions from the low-temperature polarized state to the high-temperature unpolarized state. Ferroelectric order tends to be destroyed by thermal motion at

temperatures above T_c and becomes paraelectric. Above the transition temperature, the permittivity of the material follows the law (2):

$$\varepsilon = \varepsilon_0 + \frac{C}{T - T_c}, \quad (2)$$

where C is the Curie constant, unique to the material correlated with the density and alignment of dipoles in the substance, T is an absolute temperature, and T_c is the Curie temperature. This law is called the Curie-Weiss law [29] and it's essential for predicting permittivity above T_c . The Curie-Weiss law does not hold for ferroelectric materials at temperatures significantly below T_c when spontaneous polarization dominates the material's activity [30].

2.2. Underlying principles of ferroelectricity

There are typically 230 space groups in crystals, of which 32 are crystalline classes, 11 classes of centrosymmetric structures possess a center of inversion and cannot exhibit macroscopic electric dipoles, as in these systems, the center of positive charges coincides with the center of negative charges. 20 of the 21 non-centrosymmetric classes are piezoelectric. Materials that belong to ten piezoelectric classes are also pyroelectric because they exhibit temperature-dependent spontaneous electric polarization. A unique polar axis of the crystals defines the direction of spontaneous polarization. The complete classification of the crystalline materials is presented in Figure 2.1.

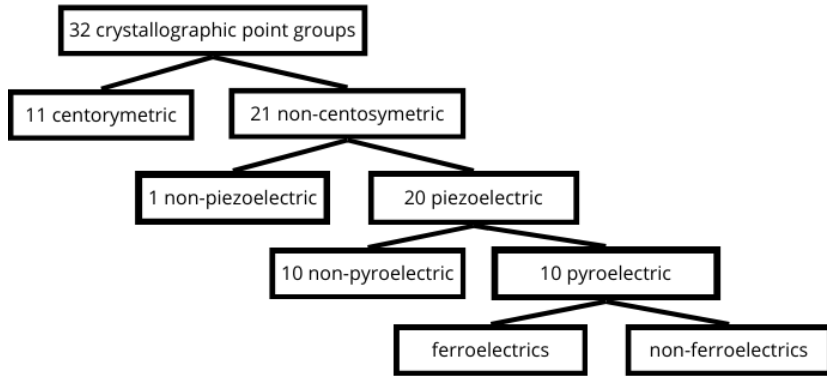


Figure 2.1. Hierarchical classification of crystalline material.

From another classification, ferroelectric material belongs to the ferroic material group (figure 2.2), which includes ferroelastic, ferroelectric, ferromagnetic, and ferrotoroidic, depending on time and space invariance and change. Any physical system can be defined by its behavior when subjected to space and time reversal. These parity operations exhibit just two eigenvalues, +1 and -1, which signify a sign change or no sign change, respectively, upon applying the parity operation. A ferroelectric crystal is defined, so other properties had to be defined. A crystal is said to be ferroelastic when it can be moved from one orientational state to another by applying mechanical stress and has several orientational states when both an electrical field and mechanical stress are absent [31].

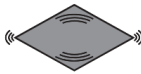
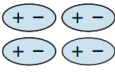
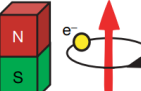
	Space	Invariant	Change
Time		Invariant	Change
Invariant		Ferroelastic 	Ferroelectric 
Change		Ferromagnetic 	Ferrotoroidic 

Figure 2.2. The four ferroic orders are categorized under the space and time parity operations. (Ferroelastic - deforms under stress with

spontaneous strain; ferroelectric - shows reversible electric polarization; ferromagnetic - has permanent magnetic moments due to aligned spins; ferrotoroidic - features a closed-loop toroidal magnetic structure.) [32].

Ferromagnetic crystals possess a spontaneous magnetic moment even in the absence of an applied magnetic field [33]. Ferrotoroidic crystals have an ordered arrangement of magnetic vortices, but it's currently debated whether to include them as a fourth form of ferroic order [32].

The phase transition refers to a change in the crystal structure of certain materials that causes spontaneous electric or magnetic polarization or depolarization, depending on the type of material and heating or cooling situation. The material changes symmetry during a ferroelectric phase transition, usually going from a high-temperature paraelectric phase to a low-temperature ferroelectric phase (or vice versa). The material's electric dipoles are randomly oriented and cancel each other out in the paraelectric phase, producing a net zero polarization [34].

The macroscopic polarization P for any finite-size system is defined as the dipole moment per unit volume averaged over the volume of a cell.

$$P = \frac{1}{V_{cell}} \sum_n q_n r_n, \quad (3)$$

where V_{cell} – cell volume, r_n - is the position vector of the charge q_n , P – polarization as in Maxwell equation ($\epsilon_0 \nabla \cdot E + \nabla \cdot P = \rho_{free}$, where ϵ_0 is the permittivity of the vacuum, E is the electric field, P is the polarization field, ρ_{free} is the free charge density, ∇ and is the divergence operator.

Summation of the overall charge in the elementary unit cell of the crystal. Polarization is parallel and proportional to the electric field E in a homogeneous, linear, non-dispersive, and isotropic dielectric medium:

$$P = \chi \varepsilon_0 E, \quad (4)$$

where ε_0 is the vacuum permittivity, χ is the electric susceptibility of the medium [33]. Consequently, the connection between displacement and electric field is:

$$D = \varepsilon_0(1 + \chi)E = \varepsilon E, \quad (5)$$

where D is a vector electric displacement that appears in Maxwell's equations and $\varepsilon = \varepsilon_0 \varepsilon_r$ is permittivity (ε_r is the relative permittivity of a material). Equation 5 can be substituted with the general linear relation.

$$\begin{cases} P_x = \varepsilon_0(\chi_{\varepsilon_{xx}} E_x + \chi_{\varepsilon_{xy}} E_y + \chi_{\varepsilon_{xz}} E_z) \\ P_y = \varepsilon_0(\chi_{\varepsilon_{yx}} E_x + \chi_{\varepsilon_{yy}} E_y + \chi_{\varepsilon_{yz}} E_z) \\ P_z = \varepsilon_0(\chi_{\varepsilon_{zx}} E_x + \chi_{\varepsilon_{zy}} E_y + \chi_{\varepsilon_{zz}} E_z) \end{cases} \quad (6)$$

The susceptibility tensor is made up of nine coefficients, $\chi_{\varepsilon_{xx}}, \chi_{\varepsilon_{xy}}, \dots$ [35]. In this case, P results from the convolution of the electric field E with the impulse response susceptibility χ . This convolution takes on a more straightforward form in the frequency domain. The connection for a linear time-invariant medium can be obtained by Fourier transforming it and using the convolution theorem.

$$D(\omega) = \varepsilon^*(\omega)E(\omega), \quad (7)$$

where ω is the applied field's frequency and ε^* is complex-valued permittivity. The Kramers-Kronig relations, which restrict the form of frequency dependence, result from the restriction of causality. One example of this phenomenon of frequency-dependent permittivity is material dispersion. The types of relaxation are presented in figure 2.3. This diagram illustrates a dielectric material exhibiting several optically active modes (N modes), as evidenced by the dielectric function's various peaks in the imaginary component (ε''). Each peak represents the contribution of a distinct optical mode to the dielectric response.

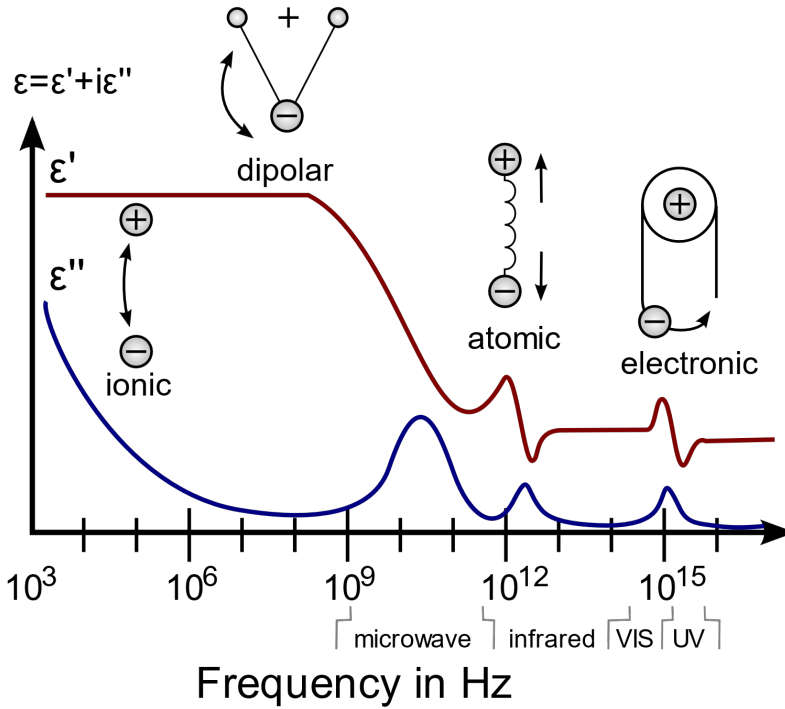


Figure 2.3. A spectrum of dielectric permittivity with N optically active modes, covering a broad frequency range. The real and imaginary parts of the permittivity are represented by ϵ' and ϵ'' , respectively. The picture labels several processes, including electronic and atomic resonances at higher energies, dipolar and ionic relaxation [36].

Consequently, the definition of permittivity turns into

$$D_0 e^{-i\omega t} = \epsilon^* E_0 e^{-i\omega t}. \quad (8)$$

The displacement and electric field amplitudes are denoted by D_0 and E_0 , respectively; i represents the imaginary unit. The low-frequency limit of permittivity, or static permittivity ϵ_0 , describes how a medium reacts to static electric fields. At the high-frequency limit (meaning optical frequencies), the real part of complex permittivity is commonly referred to as ϵ_∞ (or sometimes ϵ_{opt} [37]). Lyddane describes the ratio of

a static permittivity and the permittivity of optical frequencies in a Sachs–Teller relation, which connects the natural frequency of longitudinal optic lattice vibrations (phonons) (ω_{LO}) (1st peak on image 2.3) to the natural frequency of the transverse optical lattice vibration (ω_{TO}) (2nd and 3rd peak on figure 2.3):

$$\frac{\epsilon_0}{\epsilon_\infty} = \prod_{j=1}^n \frac{\omega_{LOj}^2}{\omega_{TOj}^2}. \quad (9)$$

The ϵ_0 and ϵ_∞ permittivity values are essential for a relaxation model to describe the dielectric response in ferroelectric materials. Examples of such relaxation models include the Debye model, Cole–Cole model, Cole–Davidson model, and Havriliak–Negami model [38].

2.3. Phase transition in ferroelectric materials

Based on an interpretation of permittivity data, it is possible to determine and categorize the kind of ferroelectric material being studied. At the Curie temperature T_c , conventional ferroelectrics dielectric permittivity (ϵ^*) exhibits a distinctive sharp peak (figure 2.4). The atomic locations in the crystal structure shift to align dipoles in a uniform direction during a well-defined phase transition from the paraelectric to the ferroelectric state, represented by this peak. The dielectric constant usually lowers and stabilizes as the temperature drops below T_c , which indicates the stable dipole alignment in the ferroelectric phase. One well-known example of a typical ferroelectric that displays this kind of activity is BaTiO_3 [39], in which the titanium atoms move out from the oxygen octahedra's core, resulting in the required dipolar moment for a larger average polarization than in a non-perovskite material.

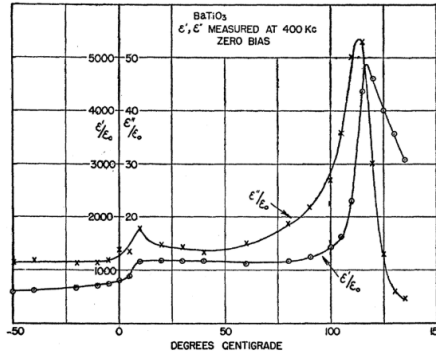


Figure 2.4. The ratio of real and imaginary parts of the dielectric function to the vacuum permittivity in BaTiO₃ material versus temperature [39].

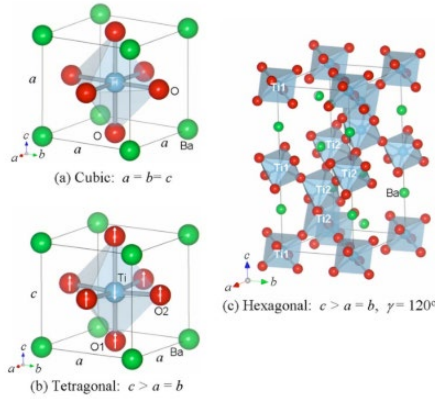


Figure 2.5. Crystal structures of (a) cubic, (b) tetragonal, and (c) hexagonal BaTiO₃ were drawn using refined crystal parameters. The green, light blue, and red spheres denote Ba, Ti, and O atoms. The arrows in (b) indicate the direction of displacements for Ti and O atoms with respect to the Ba atom. The solid line denotes the unit cell [40].

The displacement during this Ti substructure motion relates to the O and Ba substructures and can be categorized as a displacive phase transition (figure 2.5). A definition of the transition's nature could be found in the dynamics of the lowest frequency ("soft") optical phonon modes. The transition is displacive if a soft mode can move through the material at that point. There is almost no phonon if the soft mode is only

diffusive (non-propagating), but rather a large amplitude hopping motion between the order-disorder system's wells. Soft modes in many ferroelectrics lie between these two extremes [19].

The displacive group of ferroelectrics includes perovskite ABO_3 -type structures like $LiNbO_3$, $BaTiO_3$, and $KNbO_3$, among others. The ferroelectric phase transition in the order-disorder group of ferroelectrics is linked to a distinct ordering of ions. These are the H-bonds containing crystals with ferroelectric characteristics correlated with phonon mobility. Some instances include KH_2PO_4 , RS , TGS , CsH_2PO_4 , $PbHPO_4$, RbH_2PO_4 , and other [49].

Another classification of a phase transition process comes from Landau's phase transition theory. The central concept of this theory is an "order parameter," a quantity that is zero in the disordered phase and non-zero in the ordered phase. In the case of ferroelectrics, such an order parameter can be a polarization P . The free energy F of the system is expanded as a power series in the order parameter P :

$$F(P, T, E) = F_0 + \alpha P^2 + \beta P^4 + \gamma P^6 - EP, \quad (10)$$

where F_0 - the free energy in the absence of polarization, α , β , γ are coefficients dependent on temperature T , and T_c is the Curie temperature at which the phase transition occurs. We must assume that the coefficient α of the term in P^2 passes through zero at some temperature T_0 to produce a ferroelectric state:

$$\alpha = A(T - T_c), \quad (11)$$

where A is a linear coefficient, and T_c is a temperature lower or equal to a transition temperature. This equation connects the soft mode frequency with a Curie temperature, called the Cochran law [41]. When the α value is positive, the lattice is "soft" and on the verge of instability. In the event where α is negative, the unpolarized lattice is unstable.

If $\beta > 0$ and γ is negligible, the phase transition is second order (continuous). In this case, the energy minimum occurs at $P=0$ at $T > T_c$. When $T < T_c$, two symmetric minima develop at $P=\pm P_0$, which

describes a behavior of ferroelectric material with a spontaneous polarization.

Otherwise, when $\beta < 0$, we have to retain a γ term, and at the paraelectric and ferroelectric phases, the free energy will be equivalent at the transition temperature T_c . Figure 2.6 represents all possible configurations for a centrosymmetric prototype lattice of atoms and a phase transition process.

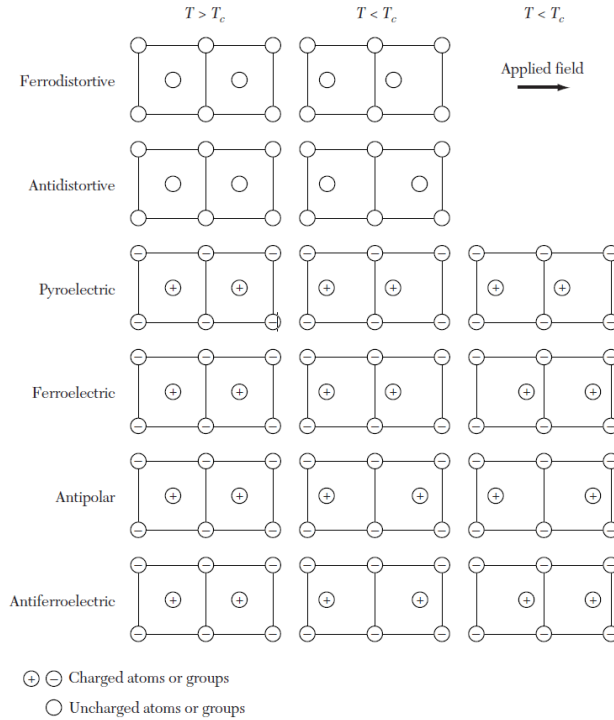


Figure 2.6. Schematic representation of fundamental types of structural phase transitions for a centrosymmetric prototype structure [42].

Based on this classification, let's look at some of the material types related to this thesis.

2.3.1. Relaxor ferroelectric

Relaxor ferroelectrics are ferroelectric materials with diffuse phase transitions and frequency-dependent dielectric properties. Unlike conventional ferroelectrics, relaxor ferroelectrics have a broad phase transition over a range of temperatures (thereof title “relaxors”), which exhibit a quick phase transition from a paraelectric to a ferroelectric phase at the Curie temperature. Polar nanoregions (PNRs), which are nanoscale areas where the local polarization is aligned in the order of nanometers, are thought to be responsible for this unusual behavior. This material is characterized by a few temperature values: T_f is a “freezing” temperature, where the material exhibits glass-like behavior, with less sensitivity to temperature changes and external fields, T_d which is depolarization temperature; T_c is a Curie temperature; T_m corresponds to maximum dielectric permittivity, T_B - Burn temperature, above which material properties follow the classic Curie-Weiss law. A graphical representation of the permittivity of such material is presented in figure 2.7.

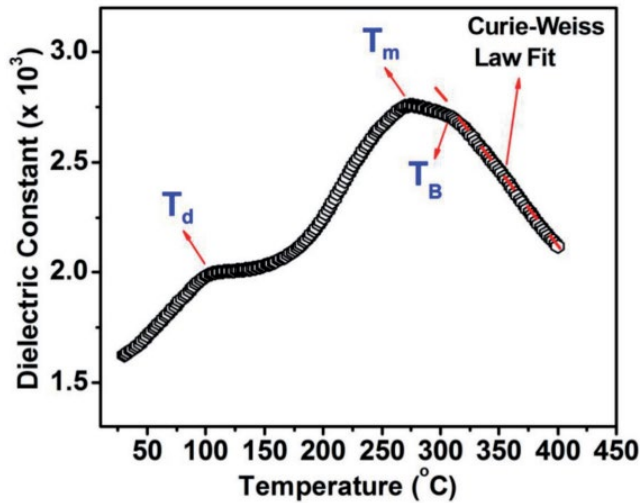


Figure 2.7. Various characteristic temperatures are associated with a temperature-dependent real part of the dielectric permittivity of relaxor ferroelectric [43].

The difference between ferroelectric and relaxor response also lies in the plane of movement of the atom inside the lattice structure. An example of such is presented in Figure 2.8.

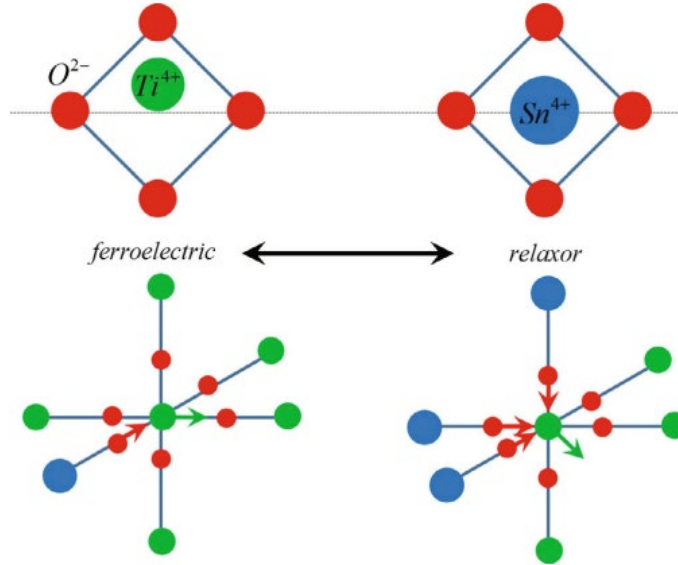


Figure 2.8. A schematic illustration showing how isovalent doping influences the atom movement in $\text{BaTi}_{1-x}\text{Sn}_x\text{O}_3$ (BTS) [44].

Such materials enter an ergodic relaxor state upon cooling from a T_c , forming these polar nanoregions. This transformation is not structural because there is no crystal structure change, but PNR still affects material properties. As the material cools further, from T_c down to T_f , it enters a nonergodic phase in which polar nanoregions (PNRs) become ‘frozen’, ceasing to influence the material’s properties. The nonergodic phase can change into the FE phase with a strong external electric field. This characteristic sets relaxor ferroelectric apart from dipolar glasses.

Another type of anomalous phase sequence is known to occur where the material returns to a disordered phase after passing through ordered and disordered phases after additional cooling. The re-entrant or reappearing phase is the term used to describe the low-temperature phase. While it loses the order parameter in the intermediate (ordered) phase, it is not precisely the same as in the high-temperature parent

phase. This indicates that the considered order parameter does not fully reflect the order-disorder processes in the system and can occur if the entropy of the reentrant disordered phase is smaller than that of the ordered phase. In addition to the actual reentrant behavior, there are circumstances in which the low-temperature phase preserves the order parameter of the intermediate phase. Still, the latter's macroscopic characteristics resemble those of a disordered phase. This may occur if the reentrant transition involves certain extra degrees of freedom that do not affect the principal order parameter [45].

An example of such materials is commonly a solid solution of doped PbTiO_3 : lead magnesium niobate (PMN) [46], lead lanthanum zirconate titanate (PLZT) [47], lead scandium niobate (PSN) [48] and other.

2.3.2. Antiferroelectric materials

Another class of dielectric materials with good energy storage properties is antiferroelectric materials. The primary cause of macroscopic spontaneous polarization in antiferroelectric materials is the antiparallel orientation of their dipoles. Moreover, antiferroelectric materials have low dielectric loss and exceptionally low remnant polarization — even lower than relaxor ferroelectrics. Because they may go from the antiferroelectric state to the ferroelectric phase with substantial saturation polarization when an electric field is applied to them and back again when the electric field is removed, antiferroelectric materials are prominent for various applications. The cause of this reversible change is thought to be a tiny variation in charge carrier-free energy between the field-induced ferroelectric phase and the initial antiferroelectric phase [49]. Since antiferroelectric materials typically have a double hysteresis loop (figure 2.9(d)), the discharge energy density area is square-shaped. As a result, it is generally higher than that in relaxor ferroelectrics.

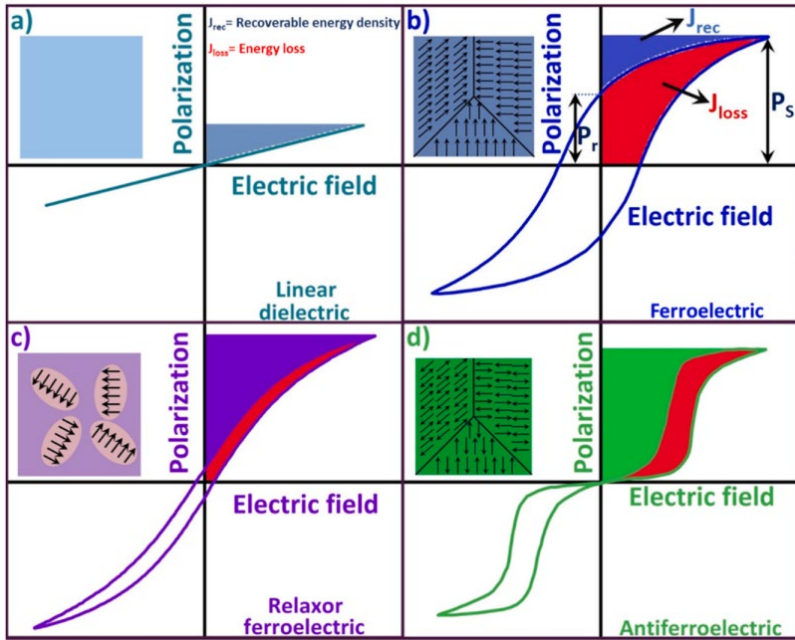


Figure 2.9. Schematics show the typical hysteresis loop for (a) linear dielectric, (b) ferroelectric, (c) relaxor ferroelectric, and (d) antiferroelectric materials. The insets show the type of domain orientation [50].

The phase diagrams of antiferroelectric material may also include phase transitions from antiferroelectric states into intermediate ferroelectric states before transition into the paraelectric state. This state of a material is not sharp, and in some materials, FE and AFE phases can exist at the same time if the external electric field and temperature have particular values specific to each material system, as shown in figure 2.10 [51].

Moreover, the phase transition in this case could produce a new incommensurate (IC) phase, which develops due to an IC transition triggered by the AFD (antiferrodistortive) soft mode. This implies that two distortions—one connected to octahedral tilts and the other to cation displacement ordering—co-occur at the phase transition in the case of $\text{PbHf}_{1-x}\text{Sn}_x\text{O}_3$ [52].

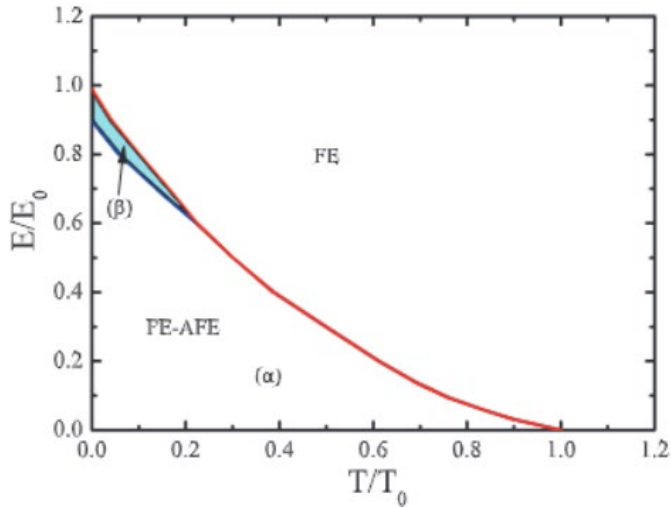


Figure 2.10. An antiferroelectric material's E-T phase diagram was obtained numerically by minimizing the free energy. Solid lines represent lines of first-order transitions. There are two mixed FE-AFE phases, (α) and (β) (shaded area) [51].

A well-known example of such material is lead zirconate [53], lead lanthanum zirconate titanate [54], sodium niobate [55] and others.

2.4. Ferroelectric domains

At the microstructural level, areas of homogeneous electrical polarization form domains in ferroelectric materials. When a crystal is cooled below T_c without any external electric field, each energetically degenerate path of spontaneous polarization occurs with equal likelihood throughout the crystal, resulting in the development of domain structures [56]. A domain, then, is a crystal section containing only one type of polarization. If ferroelectric crystals adhere to their boundary conditions - the overall average strain and polarization states brought about by forced displacements and charges at the crystal surfaces — they can adopt a stable, minimum-energy configuration of domains and domain walls.

The domain wall energy, the potential energy of the external loads, and the total energy stored in free space and crystal distortion are all

reduced when a ferroelectric crystal is in its equilibrium state [57]. To determine domain compatibility in a tetragonal crystal, we require that both strain and polarization match at the interface between domains according to these equations:

$$\varepsilon_i - \varepsilon_j = \frac{1}{2}(a \otimes n + n \otimes x) \quad (12)$$

$$(p_i - p_j) \cdot n = 0 \quad (13)$$

where i and j are two ferroelectric domains with a strain stress ε_i and ε_j , polarization vectors p_i and p_j , and the interface normal vector n to a compatible domain. According to this equation, there are two types of domain walls in the tetragonal crystal; orthorhombic crystals produce four domains, while rhombohedral crystals have three types of domains [58].

Ferroelectric domain walls, which exhibit localized variations in strain and symmetry, can be interpreted as topological defects within the material's parent crystal structure; moreover, their narrow width results in structural interfaces with intrinsic nanometer-scale dimensions. However, the formation and structure of domain walls in ferroelectric thin films cannot be fully explained solely by depolarizing fields and screening charges. The presence of structural defects in the crystal primarily dictates the actual conditions of the sample. To accommodate local symmetry variations, movable defects—often point-like—may accumulate at domain walls. Conversely, defects can pin domain walls, lowering their potential energy [59].

Several parameters, including the chemical composition, temperature, system size and shape, and crystal orientation, can influence the equilibrium domain structures of ferroelectric crystals. Going down from bulk material to a thin film can alter the domain composition of the material since it experiences continual strains within the plane of the film and low stress outside of the plane. This effect allows for a ferroelectric domain architecture by choosing a matching lattice constant between the film and the substrate [59]. This, of course,

is not without withdrawal of such methods as a significant amount of thread dislocations, which releases enormous stress inside the film [60].

Domain wall dynamics, reorientation of domains, complex domain structure, and elevated temperature contribute to the relaxation phenomena observed in these materials. Understanding and analyzing these relationships is essential for accurately predicting and customizing the electrical properties of materials. Different relaxation models, which are explained further, make this possible.

2.5. Dielectric relaxation models in ferroelectrics

2.5.1. Debye model

Relaxation, in a general sense, refers to the delayed response of a linear system to an external perturbation. The frequency dependence of permittivity, described by the Debye equation for ideal systems, characterizes this relaxation process. In contrast, resonance effects arise from distortions in electrical and ionic polarization, and these polarization distortions are influenced by the sample's environment, composition, and structural properties.

The physicist Peter Debye (1913) introduced and gave a name to this relaxation model [61]. According to the Debye theory, dipoles responded independently to the alternating field with a single relaxation time, and molecules had a spherical form. This model characterized dynamic polarization by a single relaxation time, so all the dipoles have the same time to respond to changes in an external electric field and return to their equilibrium state once the field is removed. The formula for this model is the following:

$$\varepsilon^* = \varepsilon_\infty + \frac{\varepsilon_s - \varepsilon_\infty}{1 + i\omega\tau}, \quad (14)$$

where ε_s is the static, low-frequency permittivity, τ is the medium's characteristic relaxation period, ε_∞ is the permittivity at the high-

frequency limit, and ω is an angular frequency. Graphically, this model is presented in figure 2.11.

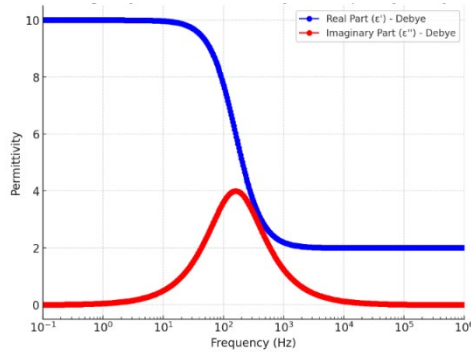


Figure 2.11. An example of the Debye model illustrating the real (ϵ') and imaginary (ϵ'') parts of the complex permittivity function ϵ^* for the following initial parameters: $\epsilon_s=10$, $\epsilon_\infty=2$, $\tau=1*10^{-3}$ s.

Since this model is characterized by a single relaxation time, the probability density function $f(\tau)$ for the Debye model is a Dirac delta function centered at the relaxation time τ_0 :

$$f(\tau) = \delta(\tau - \tau_0). \tag{15}$$

A graphic representation of this function is shown in figure 2.12.

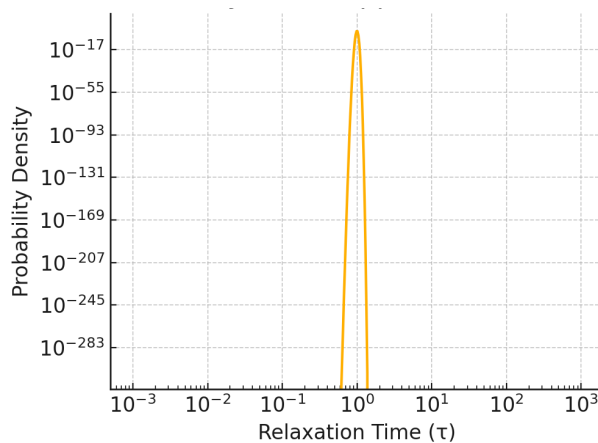


Figure 2.12. Probability Density Functions of the Debye model.

The Debye permittivity model is applied to various materials that show basic dipolar relaxation behavior. Most of these examples are simple materials, such as water and ethanol [62], biological tissues [62], concrete [63].

Though helpful, the Debye model has a few drawbacks, such as a single relaxation time, idealized conditions, a frequency range, and temperature dependency.

2.5.2. Cole-Cole model

Further development of this model was continued by K. S. Cole and R. H. Cole in their proposed work on a new model for nonhomogeneous dielectrics [64]. In this model, the distribution of relaxation times was introduced as a parameter, α ($0 < \alpha < 1$), to account for a spread in relaxation times. Using this model, it's possible to describe a more gradual relaxation process in complex systems with numerous relaxation processes and intricate interactions.

$$\varepsilon^* = \varepsilon_\infty + \frac{\varepsilon_s - \varepsilon_\infty}{1 + (i\omega\tau)^{1-\alpha}}, \quad (16)$$

where all parameters are the same as in the Debye equation.

Compared to the Debye model, the Cole-Cole model provides a more flexible and accurate description of materials with a broader distribution of relaxation times, accounting for deviations from ideal Debye behavior (figure 2.13).

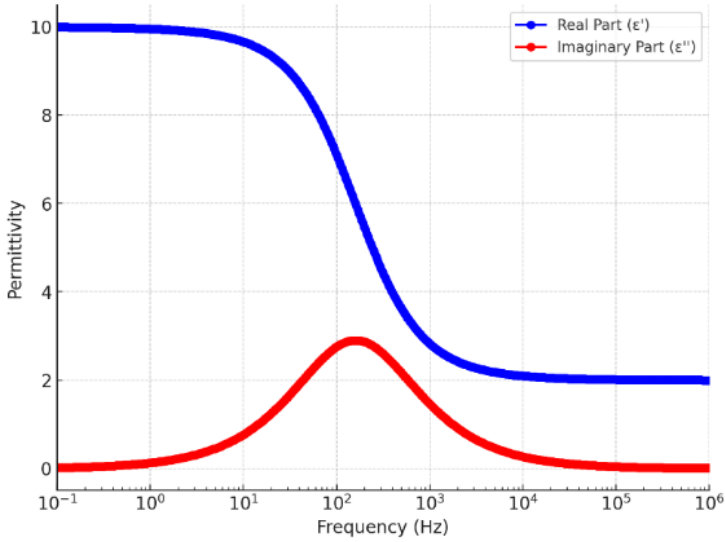


Figure 2.13. An example of the Cole-Cole model illustrating the real (ϵ') and imaginary (ϵ'') parts of the complex permittivity function ϵ^* for the following initial parameters: $\epsilon_s=10$, $\epsilon_\infty=2$, $\tau=1*10^{-3}$ s, $\alpha=0.2$.

The corresponding probability density functions for the relaxation times τ can be expressed as [65]:

$$G(\ln \tau) = \frac{1}{2\pi} \left(\frac{\sin(\pi\alpha)}{\cosh(\alpha \ln(\tau/\tau_0)) + \cos(\pi\alpha)} \right) \quad (17)$$

At $\alpha=1$, this distribution is reduced to a Debye distribution, as seen in figure 2.14. Reducing the α coefficient broadens the time distribution symmetrically.

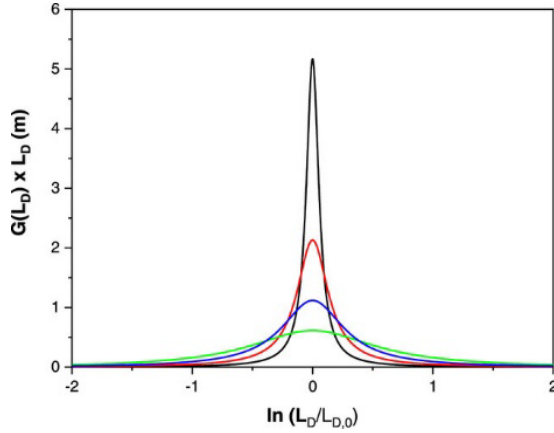


Figure 2.14. Probability Density Functions of the Cole-Cole model. (Black ($\alpha = 0.99$), red ($\alpha = 0.95$), blue ($\alpha = 0.90$) and green ($\alpha = 0.80$)) [66].

Examples of materials whose permittivity is explained by the Cole-Cole model include acrylic-based material [67], lead magnesium niobate (PMN) [68], alkylammonium halogenoantimonates (111), and bismuthates (111) [69].

The disadvantage of this model lies in the limitation of describing only the symmetrical broadening of a dispersion.

2.5.3. Cole–Davidson model

Some cases of permittivity data include asymmetrical broadening of dispersion. To have a better interpretation of the data observed on propylene glycol and glycerol, Davidson et al. proposed the following equation [70]:

$$\varepsilon^* = \varepsilon_\infty + \frac{\varepsilon_s - \varepsilon_\infty}{(1 + i\omega\tau)^\beta}, \quad (18)$$

where all parameters are the same as in the Debye equation, β ($0 < \beta < 1$) controls the distribution's width. An example of such a function is presented in figure 2.15.

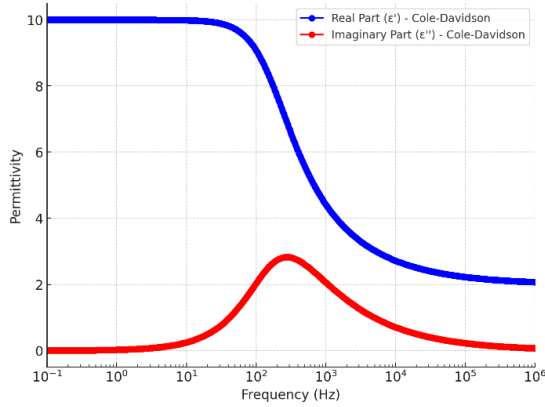


Figure 2.15. An example of the Cole-Davidson model illustrating the real (ϵ') and imaginary (ϵ'') parts of the complex permittivity function ϵ^* for the following initial parameters: $\epsilon_s=10$, $\epsilon_\infty=2$, $\tau=1*10^{-3}$ s, $\beta=0.8$.

The corresponding probability density function is [65]:

$$\begin{cases} \frac{\sin(\gamma\pi)}{\pi} \left(\frac{\tau}{\tau_0 - \tau}\right)^\gamma, & \tau < \tau_0 \\ 0, & \tau > \tau_0 \end{cases} \quad (19)$$

A graphic representation of this probability density function is presented in figure 2.16:

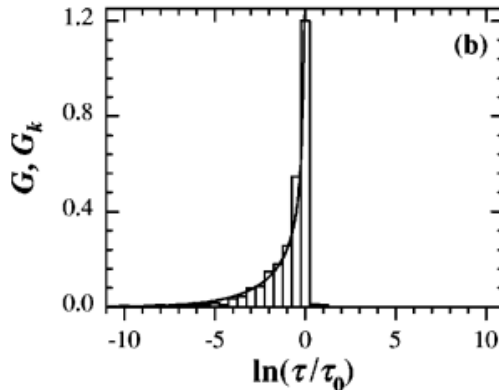


Figure 2.16. Simulated annealing direct signal analysis (SADSA) results for a computer-generated $\epsilon''(\omega)$ with a Davidson-Cole function ($\gamma=0.5$); G_k histogram, $G \ln(t)$ — from the analytical expression [65].

2.5.4. Havriliak–Negami model

To go even further with a description of dielectric data for some cases of complex dielectric data of polymers, S. Havriliak and S. Negami in 1967 reported the equation that integrated the Cole-Davidson and Cole-Cole formulas for 21 polymers [71], [72]. The equation for the Havriliak–Negami model is as follows:

$$\varepsilon^* = \varepsilon_\infty + \frac{\varepsilon_s - \varepsilon_\infty}{(1 + (i\omega\tau)^{1-\alpha})^\beta} \quad (20)$$

A graphical representation of such relaxation is presented in figure 2.17.

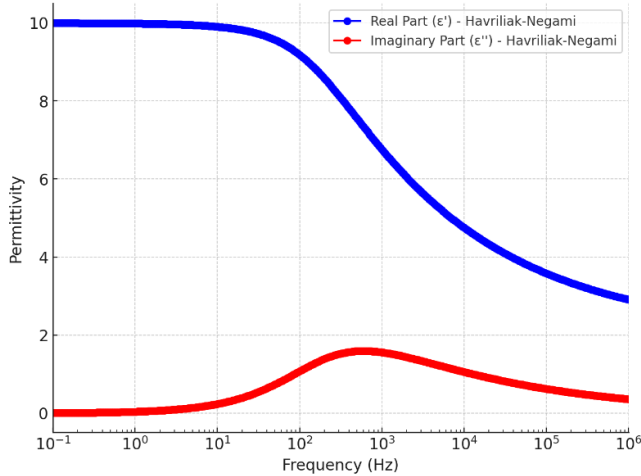


Figure 2.17. An example of the Havriliak–Negami model illustrating the real (ε') and imaginary (ε'') parts of the complex permittivity function ε^* for the following initial parameters: $\varepsilon_s=10$, $\varepsilon_\infty=2$, $\tau=1 \cdot 10^{-3}$ s, $\alpha=0.8$, $\beta=0.3$.

The formula for the probability density function of the Havriliak–Negami model is expressed as:

$$\frac{(\sin(\gamma\theta))/\pi}{\left(1 + 2\left(\frac{\tau}{\tau_0}\right)^\alpha \cos\left(\frac{\pi\alpha}{2}\right) + \left(\frac{\tau}{\tau_0}\right)^{2\alpha}\right)^{\gamma/2}} \quad (21)$$

with

$$\theta = \frac{\pi}{2} - \tan^{-1} \left(\frac{(\tau_0/\tau)^\alpha + \cos(\pi\alpha)}{\sin(\pi\alpha)} \right) \quad (22)$$

Graphically, this distribution is presented in figure 2.18.

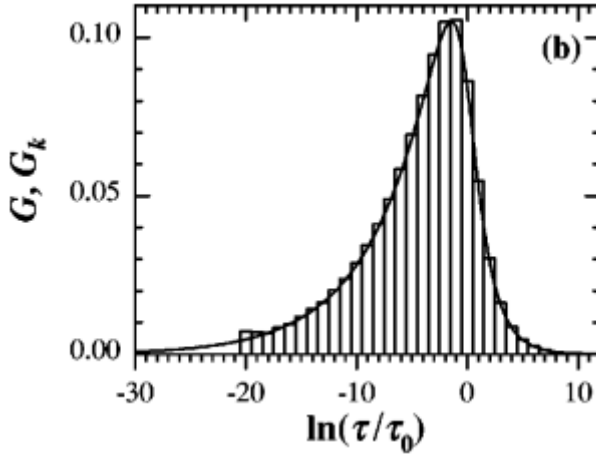


Figure 2.18. SADSAs results for a computer generated $\varepsilon''(\omega)$ with a the Havriliak-Negami function ($\alpha=0.6$, $\gamma=0.3$); G_k histogram, $G \ln(t)$ — from analytical expression [65].

2.5.5. Resonance model

According to figure 2.3, we also have different types of relaxation. The graph shows a sharper peak in the imaginary part near the THz range. Due to its sharpness, this peak could not be fitted by equations that describe relaxation processes at lower frequencies, so the resonance dispersion model must be used. The equation for this model is the following:

$$\varepsilon^* = \varepsilon_\infty + \frac{\Delta\varepsilon\omega^2}{\omega - \omega_0 + i\omega_0\gamma}, \quad (23)$$

where ε_∞ – permittivity at infinite frequency, $\Delta\varepsilon$ is a contribution to permittivity, ω is the measured frequency, ω_0 is the oscillation frequency, and γ is the damping coefficient [73].

From a perspective of lattice dynamics, the phonons begin to lag behind the external field as the frequency rises and gets closer to the resonant frequency ω_0 . A maximum energy exchange and a peak in ε'' indicate significant energy dissipation when the energy from the external field matches the natural frequency of phonons. The phase difference between the applied field and the polarization causes a sharp change in ε' . The graphic representation of this process is presented in figure 2.19.

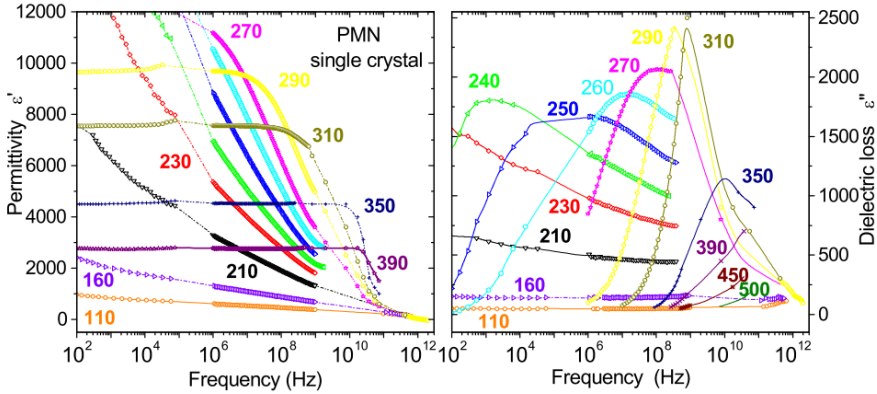


Figure 2.19. Frequency dependence of real and imaginary parts of the dielectric function in $\text{PbMg}_{1/3}\text{Nb}_{2/3}\text{O}_3$ taken at various temperatures [74].

2.5.6. Empirical Cole-Cole model

Some of the processes in materials may include more than one relaxation happening in a measurement range and mutually affect each other, as shown in figure 2.20. To resolve that and fit multiple processes simultaneously, an empirical Cole-Cole equation [64], modified to

include the conduction contribution to losses at low frequencies/high temperatures [75].

$$\varepsilon^* = \sum_{i=1}^n \left(\varepsilon_{\infty i} + \frac{\Delta\varepsilon_i}{1 + (i\omega\tau)^{1-\alpha_i}} \right) + \frac{\sigma}{2\pi i f k}, \quad (24)$$

where ω is the angle frequency, τ is the mean relaxation time, $\Delta\varepsilon$ is the strength of the relaxation process, ε_{∞} is the dielectric constant at infinite frequency, and α is a parameter that characterizes the dispersion's width.

The number of relaxation processes, denoted by the integer n , fluctuates between 1 and 2 based on the dispersion's complexity and is present in the dielectric spectra at a particular temperature. The third part of this expression represents the conduction contribution to the permittivity, which has been adjusted with an extra fitting parameter, k .

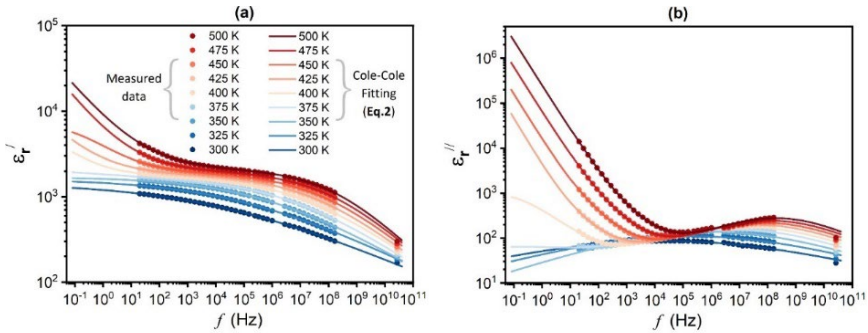


Figure 2.20. Frequency dependencies of the (a) real and (b) imaginary parts of dielectric permittivity of 0.5Nb-BiFeO₃-BaTiO₃ ceramics at different temperatures. Lines show the best fits of experimental data points according to equation (24) [75].

Other formulas that can also be used for a relaxation description, such as the Kohlrausch-Williams-Watts (KWW) relaxation functions [76], extended FZ model [77], fractional Zener (FZ) model [78] and modified FZ (MFZ) model [79], generalized gamma distribution model [80] are out of the scope of this dissertation.

2.6. Modeling variation of relaxation time in non-uniform materials

All these model equations, from Debye to extended Cole-Cole models, (14), (16), (18), (20), (23), (24), are required to estimate the relaxation time distribution on different molecular or atomic processes within a material while accounting for all possible flaws in a real sample. The Arrhenius equation can be used for samples with a single activation energy:

$$\tau(T) = \tau_0 \exp\left(\frac{E_a}{k_B T}\right), \quad (25)$$

where $\tau(T)$ - relaxation time at temperature, τ_0 - pre-exponential factor (characteristic time scale), E_a - activation energy, k_B - Boltzmann constant, T - absolute (measured) temperature.

In materials where the relaxation dynamics deviate from a basic Arrhenius behavior, the Vogel-Fulcher-Tammann equation describes the temperature dependence of relaxation times. This model is well-fitted for supercooled liquids and glasses, where the relaxation period grows considerably as the temperature approaches the glass transition temperature.

$$\tau(T) = \tau_0 \exp\left(\frac{E_a}{k_B(T - T_f)}\right), \quad (26)$$

where τ_0 , E_a , k_B , and T are the same as in the Arrhenius equation. T_f is the temperature at which the relaxation process "freezes."

For some other cases, it's worth mentioning the Williams-Landel-Ferry (WLF) model [81] that can specifically be used for the description of the temperature dependence of viscoelastic characteristics in polymers close to their glass transition temperature, and the Adam-Gibbs model that connects the configurational entropy of a supercooled liquid to the relaxation period, offering a thermodynamic viewpoint on the glass transition [82].

2.7. The importance of thin films and their applications

Concurrently, developments in synthesis, particularly those based on thin films, have made it possible to regulate the final materials with a level of control never before. These days, it is feasible to construct artificial heterostructures down to the unit cell, apply high strains through epitaxial lattice mismatch with a substrate, and precisely manipulate cation/anion chemistries and defect structures, all of which open new states of matter and phenomena.

Developing thin films of ferroelectric material can create complex structures of multiple materials. In Ho Nyung Lee et al. publication tricolor $\text{BaTiO}_3/\text{SrTiO}_3/\text{CaTiO}_3$ superlattices are one example; they cause a 50% boost in the ferroelectric polarization by hetero-interfacial coupling and coherent straining of the BaTiO_3 layer [83]. Another example of improvement of ferroelectric materials might be strain management, as comparable thin-film counterparts may tolerate biaxial strains of up to $\pm 3\%$ [84], [85]; the highest compressive strain yet recorded in $\text{BiFeO}_3/\text{YAlO}_3$ (110) is 6%, while the bulk material of it cracks or deforms at moderate tensile or compressive strains ($\sim 0.1\%$) [86].

These improved parameters of materials can be used in such applications as ferroelectric random-access memory (FeRAM) [87], energy storage capacitors [88], ferroelectric photovoltaic devices [89], tunable microwave devices [90] and other devices.

2.8. Motivation for using Pulsed Laser Deposition (PLD) in thin film fabrication

Because of its ability to produce thin films with stoichiometry similar to the target material, the pulsed laser deposition (PLD) technique has been successfully applied to a variety of chemically and structurally complex materials, including superconducting materials and chalcogenide glasses [91]. Several types of nanostructures have also been successfully created utilizing the PLD process without the

need for etching or a catalyst [92], [93]. Using the PLD process, nearly every material may be produced as high-quality thin films.

PLD-fabricated thin films are used in devices for various technologies, such as environmental medical implants, light and electron emitters, sensors, micromechanical devices, and different coatings. Furthermore, PLD has been applied to create a variety of nanostructures, including quantum dots, nanorods, and nanotubes of diverse materials [94], [95]. Compared to other deposition processes, PLD technology is more adaptable since it has virtually no constraints on the target material employed. Experimental research has also been done on PLD using liquid target materials and even frozen nitrogen and methane targets [96], [97]. Owing to the improvements made to the traditional PLD technology, it can now treat thin films of organic polymers, biomaterials, and inorganic solids that previously could not be deposited with such a deposition technique without irreversibly harming them [98].

2.9. PLD fundamentals

Pulsed Laser Deposition (PLD) is a physical vapor deposition (PVD) method for creating a thin film in materials science and engineering. A schematic image of this facility is presented in figure 2.21. It is a method for depositing thin films of various materials onto a substrate, and it involves the use of a pulsed laser to ablate (remove material from) a target, which then deposits onto a substrate to form a thin film [91]. Basic steps to create a sample with this method include several steps, such as target preparation, choosing and preparing a suitable substrate, ambient pressure, laser energy and fluence, deposition temperature and pressure, heating and cooling rate, and subsequent annealing. Also, parameters such as target scanning, substrate rotation, and gas flow speed might not be necessary for successful deposition, but they are still worth discussing.

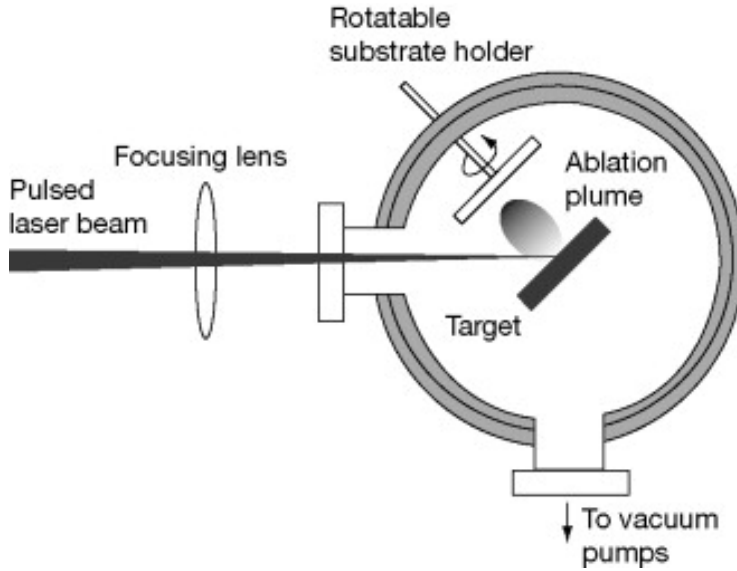


Figure 2.21. Scheme of pulsed laser deposition facility [99].

2.9.1. Target

The target (usually in a cylindrical tablet-like shape) of the desired material to be deposited is prepared and placed in a vacuum chamber. Usually, such targets are commercially available or could be prepared via the solid-state method by grinding and sintering powders, pressing them into a target, and finally sintering again. The compositional transfer between the target material and the substrate is a crucial factor for deposition. The composition of the thin film can deviate up to 30% from that of a target [100]. There are several variables here, including the density of the targets, how the grinding was performed, how many times the powders were ground, and the highest temperature used to sinter the target [101], volatility of elements of the target, and crystalline state of the target (monocrystal or polycrystal powder, as well as the crystalline size).

Density is one of the critical aspects of the target that affects the quality and properties of the film. The low density of the target could affect the sample's superconducting property and surface morphology [102]. The density of the target should be as high as possible because the formation of the microscopic particle [103] during the ablation of

the target could disturb the layer growth process and change that process to an island growth, which is usually not preferable for an epitaxial film. Also, a low density could lead to a faster usage of the target surface, which produces trenches on the surface of the target and deflects the plasma plume, which is also not preferable for the optimal deposition process [104].

Another aspect is the consideration of the atomic mass of the elements the target contains. The lighter elements tend to accelerate faster and scatter further away from the target-to-substrate direction compared to the heavier elements. For instance, the AuCu composition deposited by S. Canulescu et al. shows off-stoichiometric growth that varies significantly as a function of laser fluence [105]. Likewise, alterations in the volatility of the constituent species within the focal point can impact the composition of the film. High volatility of elements leads to the selective liquefaction and expulsion of the substance from the target during ablation, followed by re-vaporization from the substrate upon arrival. The resultant films may frequently lack sufficient light and volatile elements, potentially modifying the film's structural or functional attributes. The target can be configured with excess volatile atomic species to mitigate these effects. Such an example could be the targets of the lead zirconate titanate that, due to the volatility of lead from the target, can be prepared with a 10% excess of lead to compensate for that issue [106].

The target could also be in a monocrystal state, and this kind of material is usually a metal and a simple oxide that could be produced quickly in a monocrystal state. From a density point of view, such a target would have maximum theoretical density and reduce the amount of microparticles produced during ablation. However, V. Jakeš et al. report that the LiNbO_3 layers fabricated utilizing a polycrystalline target exhibited better surface smoothness and increased thickness in comparison to those deposited from a monocrystal under analogous experimental conditions [107]. The target question is complex and requires many parameters that should be counted to optimize the deposition parameters.

2.9.2. Vacuum chamber and ambient atmosphere

The entire process occurs in a vacuum chamber to prevent interference from the surrounding atmosphere. Usually, the pressure inside the chamber can vary from 10^{-6} up to 10^{-10} mbar [108]. To get to that level of vacuum, the tandem of 2 pumps is conventionally used: a rough scroll pump and a turbomolecular pump. The vacuum level is generally affected by the time this vacuum is supported, prior depositions inside the chamber, and the amount and quality of the targets and substrates loaded before the deposition. Factors that reduce the base pressure inside PLD chambers include the nanolayer of water vapor and elements of materials deposited and desorbed at the chamber's walls.

The size of the chambers is specified for a laser used for a specific facility, since highly energetic particles can induce sputter processes. Compact chambers are ideal for femtosecond laser-based systems requiring minimal working distance due to the short plasma plume [109].

Another aspect of pulsed laser deposition is ambient pressure. Typically, the chamber is filled with an inert gas to regulate the kinetic energy of the deposited adatoms [110] that can be stopped by collision with a gas molecule species while arriving on the substrate. Another functionality is the usage of reactive gas for the incorporation of other components into the film, such as O from O_2 , C from CH_4 , or N from NH_3 [111], as well as the adjusting thickness of the film itself. For example, Choopun et al. show that oxygen pressure strongly influences the nucleation and growth of the layers and determines the defect densities and the electrical and optical properties of the ZnO layers. The oxygen pressure should be optimized to grow high-quality layers with smooth surfaces for each growth stage. Low oxygen pressures are employed for nucleation, followed by higher oxygen pressures for the next stages of growth to obtain a smooth layer surface. The elevated oxygen pressure reduces surface desorption. Excessive increase of the oxygen pressure, however, leads to 3D growth of the film and high surface roughness [112].

2.9.3. Ablation of the target

A high-energy laser pulse is directed at the target, causing it to vaporize and ablate. This process creates a plume of material from ions, atoms, and molecules. For the PLD facility, the laser is one of the important aspects because the choice of laser matters for the deposition process and the material being deposited. The conventional wavelength range is 150–350 nm, corresponding to ultraviolet (UV) light. These wavelengths can be produced by an excimer laser, which relies on high-voltage discharges to excite noble gas mixtures, forming short-lived excimer molecules such as ArF and KrF that exist only in their excited state and rapidly decay, emitting ultraviolet (UV) photons as they return to their dissociated ground state. The following equation can estimate the electric field generated by the beams of this laser:

$$E = \sqrt{2\Phi/c\epsilon_0n}, \quad (27)$$

where Φ – power density (10^9 W/cm²), c – velocity of light, ϵ_0 – permittivity of vacuum, n – refractive index (1.5), E – electric field (10^6 V/cm). The electric field inside the material (10^6 V/cm) is sufficiently high to cause a dielectric breakdown. Thus, the material absorbs energy beyond its ablation threshold at high laser intensities, leading to ionization and plasma formation.

Each of the materials has its laser fluence, which is required for the stoichiometric deposition of a target material to a substrate [113]. The change of the laser fluence also changes the plasma plume size, which inherently changes the area of the distances where the deposition of the material will be stoichiometric. This also affects the film's uniformity, so all deposition parameters must be carefully adjusted to achieve optimal film uniformity (figure 2.22).

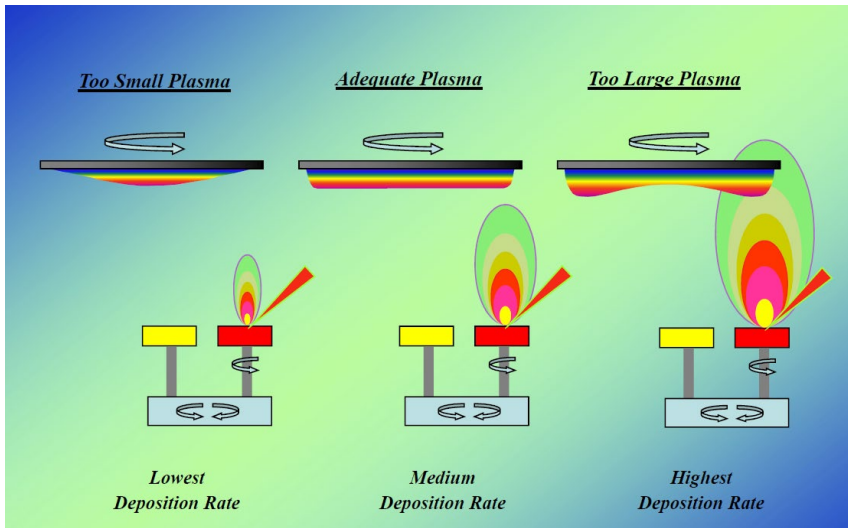


Figure 2.22. Plasma plume size versus uniformity of the films [114].

2.9.4. Thin film formation

The ablated material condenses on a substrate placed in the chamber, forming a thin film. The substrate can be of various materials, depending on the application. Chemical compatibility, comparable thermal expansion coefficients, and thermodynamically and chemically stable substrate surfaces are essential for epitaxial growth. For some applications, it is also crucial to choose selectively the chemical termination of the surface [115]. Examples of materials with a matching lattice constant are presented in figure 2.23.

If γ_o and γ_i are small compared to γ_s , the system gains energy when covered by the overlayer called Frank-Van der Merwe (FM) growth mode (2D morphology, layer-by-layer, or step-flow growth). This is a type of growth in which adsorbate-surface and adsorbate-adsorbate interactions are balanced in the development mode. Since lattice matching is necessary for this growth, it is regarded as the "ideal" growth process [117].

In the heteroepitaxial case, the structural mismatch of the overlayer and substrate leads to a monotonic increase in volume strain energy in a 2D pseudomorphic layer with increasing film thickness n . As a result, according to equation (28), the system transitions from 2D to 3D growth morphology at a specific thickness, creating an unstable condition. This kind of growth is called Stranski–Krastanov (SK) development mode (layer-plus-island growth at first, 3D morphology after critical thickness) [118], schematically presented in figure 2.24.

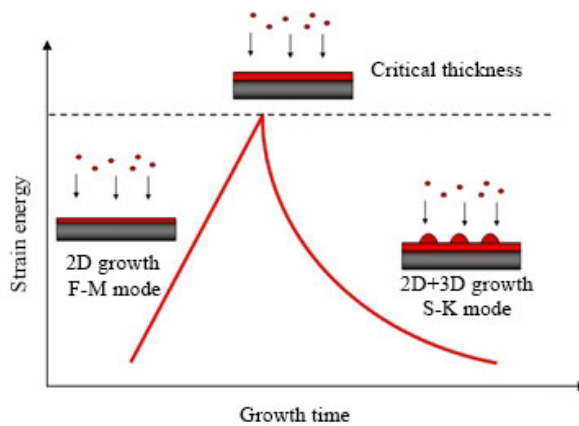


Figure 2.24. Evolution of Frank-van der Merwe (FM) to a Stranski–Krastanov (SK) growth mode [119].

If the layer-vacuum interface's free energy becomes more significant than the substrate-layer interface energy, then deposited material will form so-called mounds. This is called Volmer–Weber (VW) growth mode (3D morphology, island growth) [120]. All three modes are schematically presented in figure 2.25.

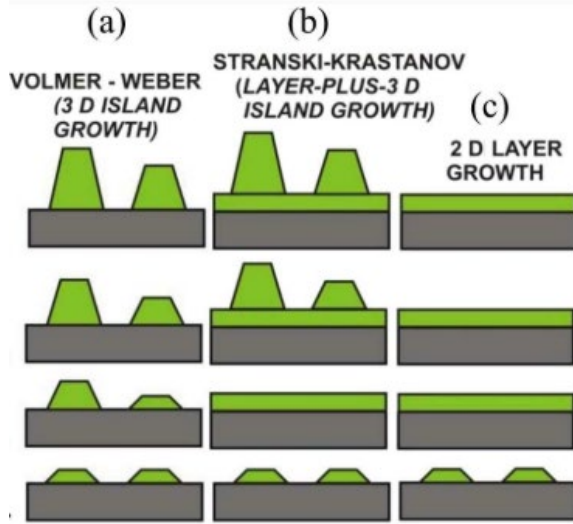


Figure 2.25. Schematic representations of (a) Volmer-Weber, (b) Stranski-Krastanov, (c) Frank-van der Merwe growth modes [121].

The interplay between the interaction of the film with the substrate and the interaction among adatoms within the film shapes the structure and morphology of a heteroepitaxial thin film at equilibrium. This interplay highlights the differences in chemical bond strength parallel and perpendicular to the interface. Critical measures of these interactions are the isosteric heat of adsorption (V_0) and the lateral adatom attraction (ϵ_1). The molecular dynamics simulation results, presented in figure 2.26 as a "phase diagram," show how different growth modes arise based on the relationship between V_a , ϵ_a , and the lattice misfit (m) [122] The lattice constant can be directly measured using diffraction techniques such as X-ray diffraction (XRD) or electron diffraction. In contrast, surface tensions require indirect estimation methods that depend on complex thermodynamic models and interface conditions.

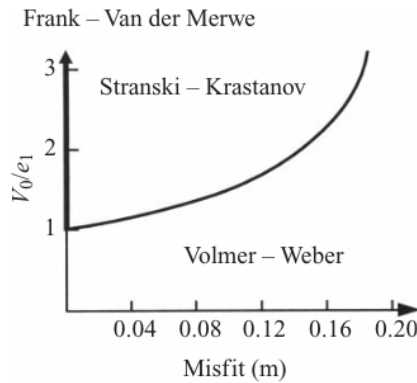


Figure 2.26. Phase diagram of growth mode on an f.c.c. (100) surface in the substrate strength V_0/e_1 versus misfit m plane [123].

The strain relief factors mentioned above and the categorization of growth modes into FM, VW, and SK are only relevant for growth circumstances near thermodynamic equilibrium, that is, at high substrate temperatures and low deposition fluxes. This is one of the reasons for the elevated temperature of the substrate during deposition. This temperature rise may facilitate the creation of crystalline structures. It has been shown that surface mobility and the temperature of the surface substrate aid the distribution of energetic particles around the substrate, as shown in figure 2.27 [124]–[126]. A different instance is bringing a sample in a match with a thin film, which will be deposited and nucleated in a high-temperature phase. This can induce stress during cooling inside deposited films and enhance the piezoelectric properties of the film due to differences in lateral thermal expansion coefficients [127]–[129].

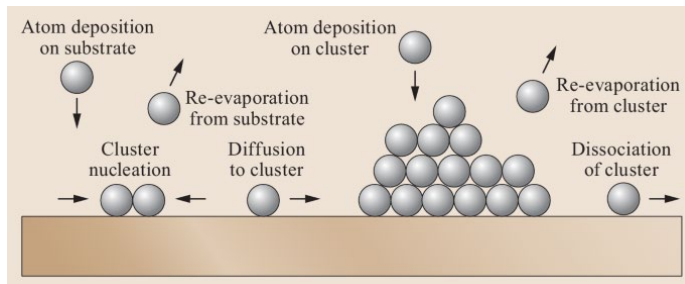


Figure 2.27. Nucleation and growth processes involved in film fabrication [130].

Figure 2.28 illustrates the processes taken into consideration during epitaxial deposition. Following deposition (a), surface atoms are free to move (b–e) or desorb (g), at which point structural flaws may develop (f). A crystal surface is defined as the outermost atomic layer, where atoms experience reduced coordination, resulting in dangling bonds. When a vacancy (missing atom) is present, neighboring atoms exhibit one or more dangling bonds, making them energetically unstable. As a result, bulk diffusion can occur when nearby atoms migrate to fill the vacancy, restoring local coordination and minimizing surface energy.

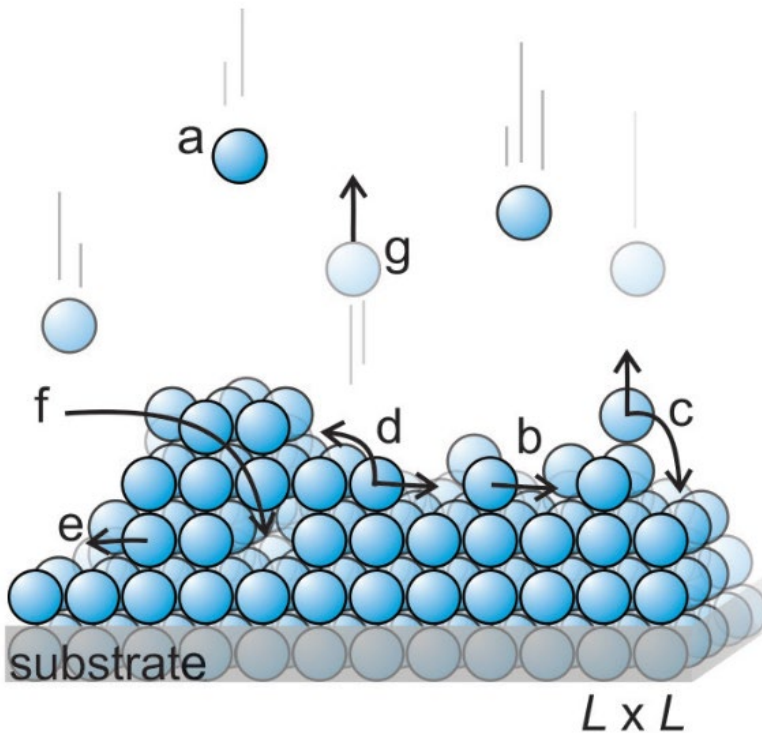


Figure 2.28. Processes during epitaxial thin film growth: (a) deposition of atoms, arriving from the solid sources on the surface of a growing film; (b) surface diffusion to a more stable position; (c) atom in an unstable position, without lateral bonds, which can either desorb to the vacuum volume or diffuse to a more stable position; (d) surface diffusion or migration to a higher kink lattice; (e) possible surface diffusion forming overhang; (f) hole formed in the structure volume; and (g) desorption [131].

2.9.5. Film growth control

Adjusting parameters such as laser energy, the pulse length, the target-substrate distance, and the deposition time can control the thickness and composition of the thin film.

Fluence and laser energy are commonly used terms to describe laser light. Laser energy is one part of a controllable parameter of the laser fluence – the quantity of energy a laser beam projects onto a surface per unit area. The standard unit of measurement is joules per square centimeter (J/cm^2). Fluence, which is frequently used to characterize the intensity of laser irradiation on a target material, is a crucial characteristic in laser-material interactions [132].

Laser interaction with a solid target could be described as energy transfer by exciting free electrons or by exciting electronic or vibrational transitions in atoms, ions, molecules, or optically active defects. In the case of laser-irradiated dielectric, where $h\nu$ is smaller than E_{bg} , the laser may cause multiphoton or multiple-photon transitions between valence and conduction bands or one-photon transitions between surface or defect states to the conduction band.

Multiphoton band-to-band transitions also result in the production of excitons and electron-hole pairs; however, given that the volume, the number of electron-hole pairs, and the desorption yields produced by multiphoton transitions are comparable to those made by one-photon band-to-band transitions driven by much weaker light sources, such as electron storage rings. The density of electronic excitation generated by multiphoton transitions is extremely low. Defect states can resonantly boost multiphoton band-to-band transitions, which significantly increases the number of electron-hole pairs and the density of electronic excitation [133].

$I(z)$, the laser light's intensity as a function of depth, is described by the equation:

$$I(z) = I_0 \cdot \exp \left\{ - \left(\sum_i \alpha_i(\omega) + \sum_j \beta_j(\omega)I + \sum_k \gamma_k(\omega)I + \dots \right) z \right\} \quad (29)$$

where I is the incoming intensity and α , β , and γ , respectively, the one-, two-, and three-photon absorption coefficients corresponding to the absorbing species (i , j , k). The ellipses in equation (29) denote higher-order absorption processes. While specific laser systems may produce transitions for excitation when one photon is in a material, in the case of dielectrics, multiphoton or multiple-photon transitions are required to create a plasma deposition plume.

The plasma kinetic energy and density rise in response to increased laser incident energy. Higher laser incident energy can improve the mobility of deposited atoms on the substrate surface; hence, additional laser incident energy can improve the crystallinity of as-deposited films. On the other hand, excessive laser incident energy might result in excessive plasma density. Furthermore, bulky granules may result from excessive laser incident energy [134]. So, the laser fluence has a short window of fluences during which the facility will produce smooth and stoichiometric films.

Another aspect of the laser pulses is their duration. Pulse duration affects the energy absorbed by the bulk material target, determining how much material is eliminated during laser ablation. Usually, the laser pulse interaction with the target is followed by the dissipation of the absorbed laser energy. The removal of material by laser ablation can be explained by two main mechanisms: thermal vaporization, which occurs when electron-phonon collisions raise the local temperature above the vaporization point, and the Coulomb explosion, which occurs when the bulk materials release excited electrons and create a relatively strong electric field that expels the ions inside the impact area [135]. Depending on the type of laser, pulse duration can last from a few tens of femtoseconds up to tens of nanoseconds. While femtosecond and

picosecond lasers are considered ultrafast pulses, a nanosecond pulse is a long pulse, causing different interactions with solid matter, as shown in figure 2.29.

This laser interaction duration affects the number of particles produced during the ablation, photochemical reaction, and phase transition, which can start after one nanosecond of pulse duration on a target. The duration of the laser pulse, as well as the target material's characteristics and the usage of nano-, pico-, and femtosecond laser regimes, determine the size and shape of the nanoparticles [136]. According to Hamad et al. [137] the picosecond laser (10 ps and 1064 nm wavelength) created more significant quantities of spherical silver nanoparticles than the nanosecond (5 ns and 532 nm wavelength) and femtosecond (100 fs and 800 nm wavelength) lasers.

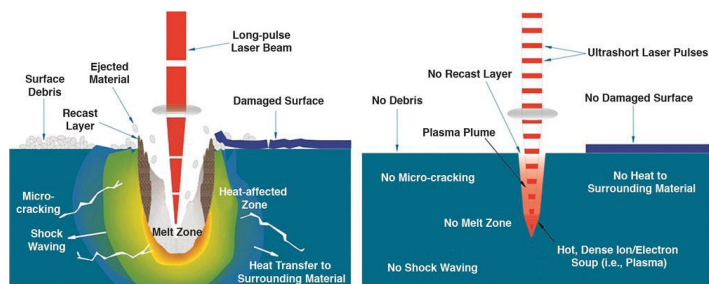


Figure 2.29. Long-pulse and ultrafast-pulse laser interaction with target material [138].

On the other hand, while using a short pulse can reduce the particle size, less interaction with the target leads to a smaller amount of ejected matter and longer deposition time while striving to achieve the required film thickness. C. Ristoscu and I. Mihailescu show that the speed of deposition is reduced from a $0.7 \text{ \AA}/\text{pulse}$ for a nanosecond pulse to a $0.0033 \text{ \AA}/\text{pulse}$ for a femtosecond pulse (but need to notice that a laser fluence was 10 times smaller, but for a same laser fluence and picosecond pulse rate of deposition was $0.05 \text{ \AA}/\text{pulse}$ which is consistent with this statement) [139].

Another issue might arise from the absorption of one or multiple photons, which could be relevant for large bandgap materials. It is

necessary to note if the material removal occurs at or below the ablation threshold, which denotes the lowest laser intensity required for material removal. Below the ablation threshold, most of the laser energy is converted into heat, and only a tiny amount of material is ejected from the target [137]. The ablation threshold vs pulse length dependency is depicted in figure 2.30.

Target-substrate distance is one of the minor but still helpful parameters that could assist in depositing high-quality films. As discussed before, laser fluence can drastically change the stoichiometry of the material. Still, at the same time, a long laser pulse tends to create multiple particles during laser-to-target interaction. Y. Ma et al. show that at shorter target-to-substrate distances (30-35 mm), high kinetic energy particles caused surface defects and larger grains. At 40 mm, a balance of kinetic energy and particle concentration resulted in the best film quality. Increasing the distance beyond 40 mm reduced particle energy and poor film quality due to lower surface migration rates [140]. Also, this parameter is indirectly connected to ambient pressure by the interaction of a plasma plume with an ambient atmosphere. R. Castro-Rodriguez et al. describe that the target-substrate distance is critical for determining the final energy and angular distribution of atoms in the plasma plume. The ratio between the oxygen atom density and the system's characteristic density determines the optimal target-to-substrate distance for film growth [141].

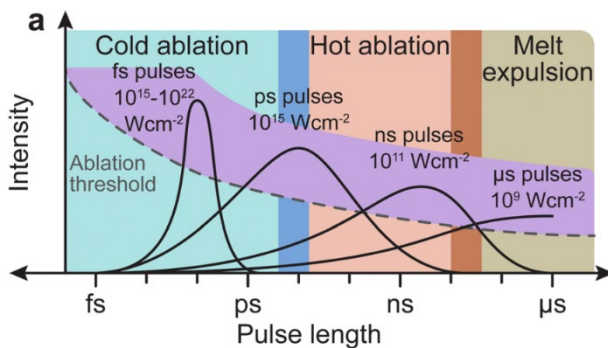


Figure 2.30. The three physical domains, which correspond to the respective time scales for the laser pulse length, are melt expulsion, hot ablation, and cold ablation [100].

Precise laser rastering is essential to ensure even target ablation and prevent surface morphology from causing plume deviation. The plume should always be perpendicular to the substrate surface. If the target is eroded unevenly, the plume will be displaced from its original position and can form off-stoichiometric films. To achieve uniform laser ablation, a top-hat beam profile (shaped by a beam mask) must be scanned across the target to ensure consistent material removal [109].

Other parameters, such as laser frequency, affect deposition in a way that alters the deposition rate while possibly increasing the porosity of the films [142]. At some critical pressure, most of the ablated species will condense in the gas phase due to the ablation plume's extremely efficient confinement, which is also visible through the luminescence part of the excited plasma species. Also, differences in deposition pressure can increase the surface roughness of the film and promote a growth mode change [143]. Another aspect is preventing micrometer-sized particulates (“boulders”) that could be ripped off from the target surface from reaching the substrate and disturbing the growing [10].

Based on all aspects above, deposition time for desirable thickness can be achieved by optimizing the combination of all these parameters, plus pulse frequency, which is in a range of 1 to 30 Hz and sometimes even up to 4 kHz in the case of excimer laser [144] and 40 kHz in the case of Ti:sapphire laser [145]. However, in most cases, the optimal repetition rate is usually less than 10 Hz [146], [147].

2.9.6. Additional deposition parameters

Before deposition, the target should be treated with sandpaper to remove the upper layer, which has already been irradiated by the laser and represents a non-stoichiometric composition of the target [148]. Then, the target is mounted on a carousel, rotated, and rastered during deposition. This ensures uniform deposition and prevents pits from forming on the target, which could hinder plasma distribution. Additionally, for more uniform deposition, the substrate should also be rotated. This effect is negligible in the case of small substrate sizes, but

it becomes more noticeable with larger-diameter substrates. Examples of these parameters and their effects are shown in figure 2.31.

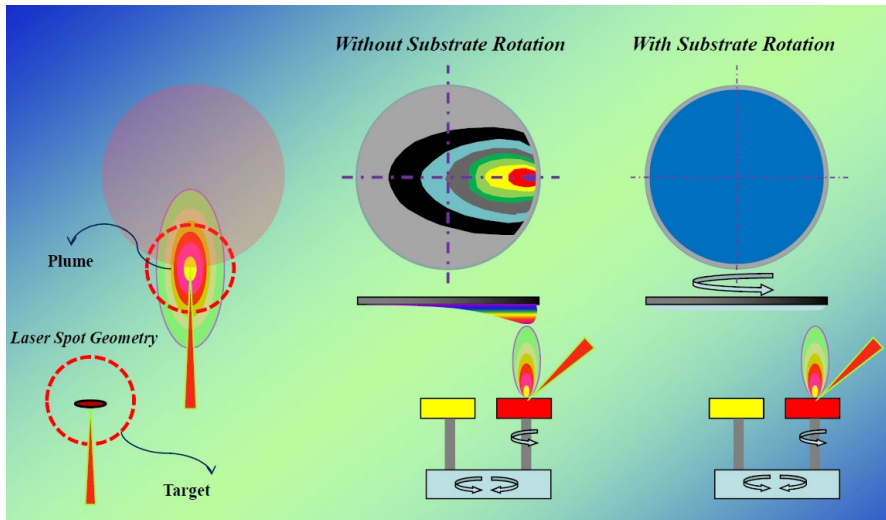


Figure 2.31. Effect of the other parameters, such as laser spot geometry and substrate rotation on the uniformity of the film [114].

3. EXPERIMENTAL METHODS AND MEASUREMENT TECHNIQUES

3.1. Pulsed Laser deposition systems

Commercial pulsed laser deposition systems provided by the TSST company (The Netherlands), equipped with a Coherent COMPex Pro 205F KrF laser ($\lambda = 248$ nm, pulse length 20 nm (FWHM), maximum repetition rate 50 Hz, maximum pulse energy 700 mJ, and average power of 5 W), were used for film growth. Schematically, this system is presented in figure 2.21, and the actual facility with signed main components is viewed in figure 3.1.

Main and load-lock chambers were equipped with a tandem of rough and turbomolecular pumps: Agilent Technologies SH-110 and Pfeiffer Vacuum HiPace 300 water-cooled for the main chamber and Pfeiffer Vacuum MVP 015-2 and HiPace 80 water-cooled for the load-lock chamber.

This pumping system allowed a vacuum level of around 10^{-7} mbar for load-lock and 10^{-9} mbar for the main chamber. Substrates and targets are loaded and unloaded through the load lock, which reduces pumping time while allowing for keeping an ultra-high vacuum and avoiding contamination.

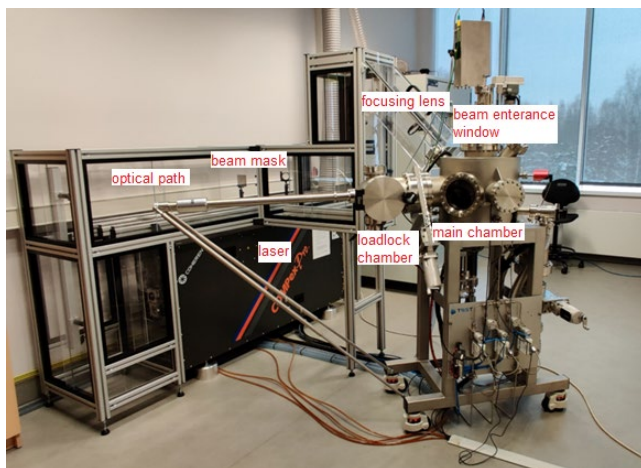


Figure 3.1. Photo of the pulsed laser deposition system.

The laser beam, guided through a variable beam mask to cut inhomogeneous parts of a beam, as an output energy distribution, is described as nearly “top hat” along the horizontal axis and near-Gaussian along the vertical axis. Guidance of this beam from the laser to a target is aided by UV-grade fused silica mirrors, with a laser beam incident on the coating side and a planoconvex lens with a 75 mm diameter so that the beam is passed through the lens and focused on a target. Each mirror and lens reduces the beam energy by $\sim 10\%$, so the final energy on the target may vary. To control it, on the opposite side of the chamber, related to the beam window, a laser energy meter is installed (Coherent EnergyMax). The scheme of a beam path is presented in figure 3.2. This scheme for the current facility can differ depending on the employed laser and desired laser fluence (usually, the laser path is around 5 meters).

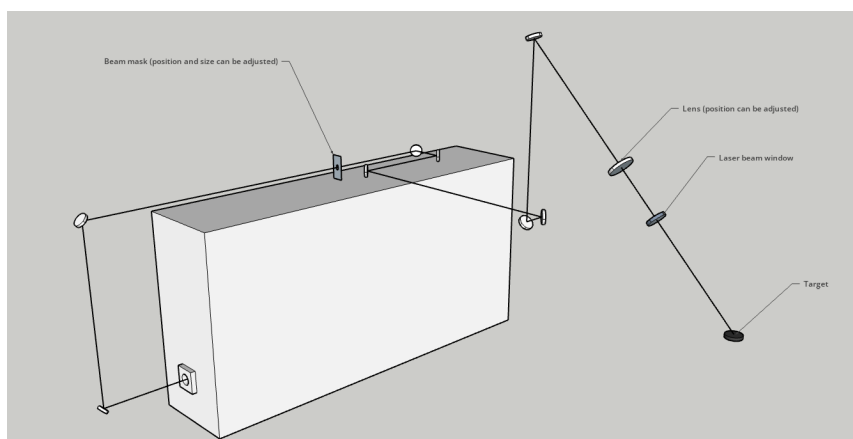


Figure 3.2. Scheme of a laser beam path from the laser to the target.

For the newly filled gas, the beam energy measured by the internal laser detector is around 740 mJ at the highest discharge voltage of 27 kV and approximately half that at the lowest discharge voltage of 19 kV. In contrast, behind a target carousel (and outside the chamber), our detector shows us energy of around 50 mJ (in the case of 27 kV). This energy, combined with an adjustable beam mask, which allowed spot sizes to be varied from 4.42 mm^2 to 0.34 mm^2 , and the focus distance (figures 3.3 (a) and (b)), resulted in a laser fluence range from 3 J/cm^2

to 1 J/cm². The fluence is calculated using the equation: $F = \frac{E}{S_{ss}}$, where F is the fluence, E is the detected energy (corrected by +10% due to the chamber window transmission loss), and S_{ss} represents the beam spot area.

The current configuration does not allow for higher energy levels, while lower energy levels can be achieved through gas degradation. As gas degradation progresses, beam energy decreases, and the production of the beam by the laser ceases at approximately 70 mJ, as measured by the laser detector.

The beam path from a laser exit to the main chamber entrance window is enclosed with plexiglass panes to ensure that any reflection and diffraction of the beams will not interfere with operation. Thus, the facility can be operated without personal protection equipment.

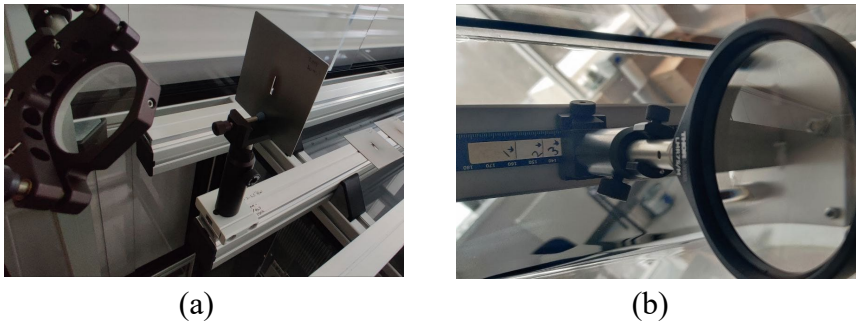


Figure 3.3. Image of (a) the adjustable position of a beam mask with a different mask and (b) the adjustable position of a lens near the entrance window.

Substrates were heated by a resistive heater integrated into the sample holder, reaching temperatures up to 950°C. The substrate temperature was monitored using a thermocouple. Three process gases were available: pure O₂, N₂, and Ar.

Lead Zirconate Titanate (PbZr_{0.2}Ti_{0.8}O₃) thin films were deposited using a custom-built NELE PLD facility at Warwick University under the supervision of Prof. Marin Alexe. This facility has specifications similar to standard PLD systems; minor variations do not significantly affect the results.

3.2 Dielectric spectroscopy measurement facilities

The connecting link of all scientific publications included in this thesis is the measurement method of dielectric spectroscopy over a wide frequency and temperature range. The principles and techniques of operation of these measuring systems are given below.

3.2.1. Low-frequency region

The bridge method is an excellent approach to determining the dielectric characteristics of materials in the low frequency range from 20 Hz to 1 MHz. Samples were measured using the precision LCR meter HP4284A (Hewlett-Packard, USA). This technique compares the dielectric material containing unknown capacitance with reference capacitors in a bridge circuit.

The following formulas can be used to recalculate the dielectric permittivity based on the capacitance (C) and loss tangent ($tg \delta = \varepsilon''/\varepsilon'$) of the sample, which is measured by an LCR meter:

$$\varepsilon' = \frac{(C_s - C_0)d}{\varepsilon_0 S} + 1 \quad (30)$$

$$\varepsilon'' = \varepsilon' tg \delta = \frac{C_s tg \delta_s - C_0 tg \delta_0}{C_s - C_0} \quad (31)$$

where index s indicates parameters of this system with the sample and zero means without it; C are the capacitances, $tg \delta$ are the tangent losses, d is the distance between the capacitor plates (sample thickness), S is the area of the sample, ε_0 is the dielectric permittivity of vacuum.

Contacts were made of painted silver and magnetron-sputtered copper/gold. The measurement was carried out during the cooling cycle using the standard cooling rate of 1 K/min. To break frozen PNRs (where applicable) and maintain the same starting conditions, bulk ceramics samples were typically annealed up to 500 K during measurement. Samples with silver paste contacts were annealed at 500°C for 2 hours to eliminate ethanol residues, preventing potential

interference with electrical characterization. In all studies, a handmade furnace was utilized for the heating mode (300 – 500 K). The vapor from liquid nitrogen (which cools to 120 K) and the closed-cycle helium cryostat (which cools down to 40 K) were employed for cooling below room temperature. Temperature was measured with different platinum RTDs and thermocouples, depending on temperature ranges.

3.2.2. High-frequency region

High-frequency dielectric measurements in a range from 1 MHz up to 1 GHz were performed by a coaxial line spectrometer. Due to cable inductance, the traditional flat capacitor approach measurements with LCR meters are unreliable above 1 MHz. This technique uses vector network analyzers (VNAs) to measure the scattering parameters. The specimen is positioned at the end of the coaxial transmission line, between the inner conductor and the short piston, forming a capacitor [149]. The typical setup for measurements is displayed in figure 3.4.

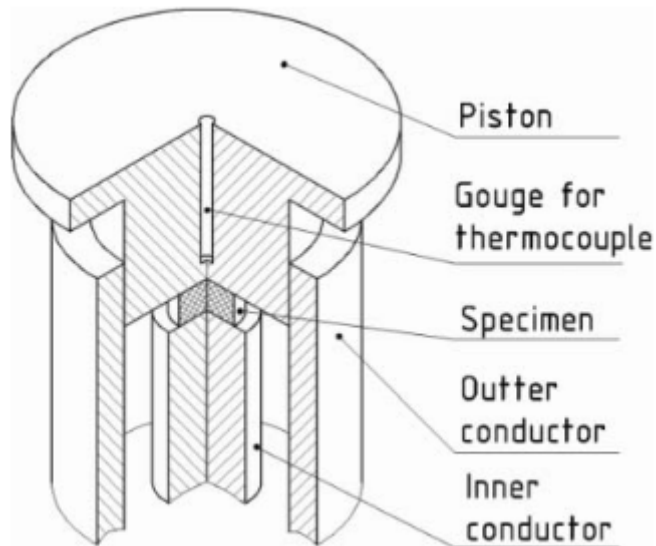


Figure 3.4. Coaxial measurement line.

The complex reflectivity coefficient was measured with an Agilent 8714 ET (Agilent Technologies, USA) vector network analyzer. It is

expected that only the primary (TEM) mode can propagate at the measuring frequencies due to the size of the coaxial lines R_1 and R_2 . A quasi-static method performs well at low frequencies of this range (wavelength is $\lambda = \frac{c}{f} \gg R_2, d$ and wavelength in the sample $\lambda^* = \frac{\lambda}{\sqrt{\epsilon^*}} \gg r, d$). In this instance, a quasi-static approach can be used to explain the complex impedance and complex reflection coefficient of the measured capacitor:

$$R^* = \frac{Z_s^* - Z_0}{Z_s^* + Z_0}, \quad (32)$$

where Z_s^* and Z_0 are measured and the system impedance, respectively, R^* is the complex reflection coefficient. This condition also implies that the sample size and coaxial line dimensions should be small enough for higher frequencies in this range.

For this frequency range, the plane capacitor model is applicable with $Z_s^* = \frac{1}{\omega C_s^*}$. Following the real and imaginary part of permittivity:

$$\epsilon' = \frac{d}{\epsilon_0 S} \left(\frac{-2R \sin \varphi}{\omega Z_0 (1 + 2R \cos \varphi + R^2)} - C_0 \right) \quad (33)$$

$$\epsilon'' = \frac{d}{\epsilon_0 S} \left(\frac{1 - R^2}{\omega Z_0 (1 + 2R \cos \varphi + R^2)} \right), \quad (34)$$

where R and φ are the modulus and phase of complex reflection coefficients, which are directly measured.

At high frequencies, related to a sample permittivity, the field in a sample will become inhomogeneously distributed: $E = A J_0 \frac{kr}{\sqrt{\epsilon}}$, where A is a model constant, depending on the geometry of the shape, r is the distance from the disc-shaped sample center, J_0 – is the order Bessel function, and k is a wavenumber. The field in the sample can be considered quasihomogeneous when the following conditions are fulfilled:

$$r \leq \frac{0.24\lambda}{2\pi\sqrt{\epsilon}} \quad (35)$$

Inhomogeneities in the coaxial line introduce systematic errors, which increase with increasing frequency. To tackle this issue, calibration procedures using short, open, and 50-ohm load calibration procedures were utilized before the measurement of samples [150].

3.2.3. Microwave region

Since the relaxation frequency in many materials with order-disorder phase transitions only softens in the microwave region, the minimum in $\epsilon^*(T)$ is not seen in dielectric data acquired in the frequency range most examined, below 1 MHz. Because the soft mode is infrared active in both the paraelectric and ferroelectric phases, this technique is more suitable than alternative techniques [74].

Based on a limitation that imposes measurement of the dominant TE_{10} mode and its cutoff frequency in our measurement, we use three different waveguides in the X band (8-12.5 GHz), K α -band (26 – 40 GHz), and Q band (36 – 55 GHz). The material sample, shaped like a rectangular rod, is positioned in the middle of the rectangular waveguide (figure 3.5). The sample was glued by silver paste into a sample holder, a metallic plate with a hole the same size as a waveguide cross-section. Additionally, two metallic plates, solid and with a hole, were used to calibrate the measurement facility and reduce systematic error.

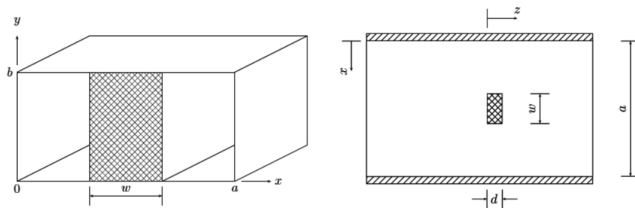


Figure 3.5. Diagram of a partially filled waveguide with a rectangular rod positioned in the middle [151].

Generators (ГКЧ-60 for X band, P2-65 for Ka-band, and P2-68 for Q band, USSR) together with a scalar network analyzer (Elmika R2400, Lithuania) were used to measure frequency-dependent reflection R^* and transmission coefficient T^* . If the sample satisfies the conditions $\alpha_0 = kr \ll 1$, the R^* is expressed as follows:

$$R^* = -\frac{4(\varepsilon^* - 1)J_1(\beta_0)}{\pi\Delta_1\sqrt{\left(\frac{2a}{\lambda}\right)^2 - 1}} \quad (36)$$

And

$$\Delta_1 = \varepsilon^*J_1(\beta_0) \left[H_0^{(2)}(\alpha_0) + 2 \sum_{m=1}^{\infty} (-1)^m H_0^{(2)}(mka) \right] - \sqrt{\varepsilon^*}J_0(\beta_0)H_1(\alpha_0), \quad (37)$$

where J_0, J_1 are the Bessel functions, $H_0^{(2)}, H_1$ are the Hankel functions, $\beta_0 = k_0\sqrt{\varepsilon}r$, a is the width of the waveguide wall and λ – wavelength in a vacuum.

When dielectric losses in permittivity are near zero. The frequency at which it reflects: $\nu_0 = \frac{c}{2\pi r\sqrt{\varepsilon}}$. When the losses increase, the measurement method error also increases. For a frequency higher than ν_0 , one of the possible solutions is to decrease the radius of the sample further. The optimal range for determining ε^* lies in $0.2 < R^* < 0.85$.

Then, the Newton method was chosen to calculate dielectric permittivity. Values were calculated by iteration, and the limits and initial values of ε' and ε'' were selected based on a measurement in bridge and coaxial systems. Final conditions were

$$R - f_1(\varepsilon', \varepsilon'') < \delta \text{ and } T - f_2(\varepsilon', \varepsilon''), \quad (38)$$

where δ is the accuracy of calculations, and it was usually selected at 0.001, which is comparable to the accuracy of the measurement.

4. RESULTS AND DISCUSSION

4.1. Investigation of dielectric and piezoelectric properties of $\text{PbZr}_{0.2}\text{Ti}_{0.8}\text{O}_3$ film

Lead Zirconate Titanate (PZT) is one of the most widely used commercial piezoelectric ceramics, valued for its high piezoelectric response, thermal stability, and cost-effectiveness. Several deposition techniques have been developed to meet the diverse requirements of PZT film fabrication, including chemical and physical vapor-phase deposition methods (CVD and PVD), Chemical Solution Deposition (CSD), and the sol-gel method [152].

CVD techniques, such as metal-organic CVD (MOCVD) and atomic layer deposition (ALD), provide precise film composition, thickness, and conformality control. CVD allows for the deposition of PZT films at lower temperatures than PVD, reducing the thermal budget for device integration. Nonetheless, CVD methods can be complex, requiring expensive precursors and specialized equipment [153]. Achieving the precise stoichiometry of the mixed oxide phase presents challenges, particularly in the quantity of lead. This is due to the high volatility and diffusivity of both lead precursors and their ions [154].

Chemical Solution Deposition (CSD) is an alternative deposition technique for PZT films that has gained significant attention due to its unique advantages. CSD involves the transformation of precursor solutions into a solid film through controlled chemical reactions. This method offers several benefits, including low processing temperatures, compatibility with various substrates, and the capability to fabricate complex multilayer structures. Despite its advantages, CSD does have limitations, including the potential for residual impurities and the need for post-annealing to achieve optimal film properties [155], [156].

Sol-gel deposition offers several advantages, including low-temperature processing, compatibility with a wide range of substrates, and achieving dense, crack-free films [157]. Sol-gel methods provide reasonable control over film composition and thickness and the potential for multilayer structures. However, sol-gel films may exhibit

lower piezoelectric coefficients [158] and increased porosity than those deposited using other methods. The requirement for multiple deposition and annealing steps can also extend the overall fabrication time [159].

PVD techniques, such as sputtering and evaporation, offer excellent film thickness and composition control. One of them is Pulsed Laser Deposition. PLD is a highly effective method for PZT film deposition, providing a high growth rate (>100 nm/h), superior crystalline quality, and stoichiometric accuracy [91], as well as exceptional surface morphology, facilitating the fabrication of high-performance test structures such as plan-parallel capacitors [160].

Pulsed laser deposition was employed to produce epitaxial oxide heterostructures consisting of $\text{La}_{0.67}\text{Sr}_{0.33}\text{MnO}_3$ (LSMO) and $\text{PbZr}_{0.2}\text{Ti}_{0.8}\text{O}_3$ (PZT) on a SrTiO_3 (STO) single-crystal substrate oriented along the (100) direction, covering an area of 25 mm^2 . The structure of this sample is presented in figure 4.1.

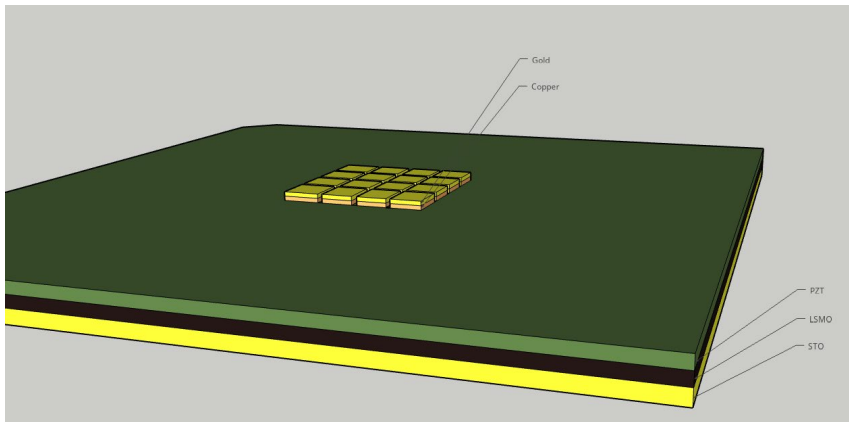


Figure 4.1. Scheme of the structure (not on scale).

Selecting a comparable substrate and buffer layer with minimal difference in lattice constant is essential for facilitating layer-by-layer film formation and achieving high-quality epitaxy, as lattice constant compatibility is vital for epitaxial deposition (figure 2.23). The lattice constant of our PZT composition at the deposition temperature is 3.953 \AA [181]. For bottom contact, we chose the lanthanum strontium manganite (LSMO) with lattice constant $a = 3.876\text{ \AA}$ [182], and for

substrate, we chose a strontium titanate (STO) substrate with lattice constant $a = 3.905 \text{ \AA}$ [183]. Both these materials have minimal lattice mismatch with our film and will benefit epitaxial growth and the excellent quality of the PZT film.

Copper and gold contacts, each with a thickness of 25 nm, were deposited by sputtering using a TEM support grid with a square pattern. Copper was directly applied to the PZT layers to enhance the robustness of the top contact pad during needle connection to the device. To minimize the effect of defects inside a single device, the mesh of the TEM grid was chosen to be 300, and the square size of each top contact was $3346 \mu\text{m}^2$.

SrTiO_3 (001) substrates with a miscut angle of less than 0.5° were acquired for this work. For the epitaxial growth of high-quality LSMO and PZT thin films, SrTiO_3 (001) substrates with either a TiO_2 - or SrO -terminated surface are often required. To achieve this, the STO substrate underwent ultrasonic cleaning using acetone to remove all oils, greases, and organic residues that may have accumulated on the substrate during handling or storage. Then, it was cleaned with isopropanol to remove any residual organic contaminants and acetone traces, leaving a clean and residue-free surface. After that, the substrate was chemically etched using a 10:1 buffered hydrofluoric solution for 20 seconds [161]. A picture of the untreated surface of the STO substrate by the atomic force microscope is presented in figure 4.2.

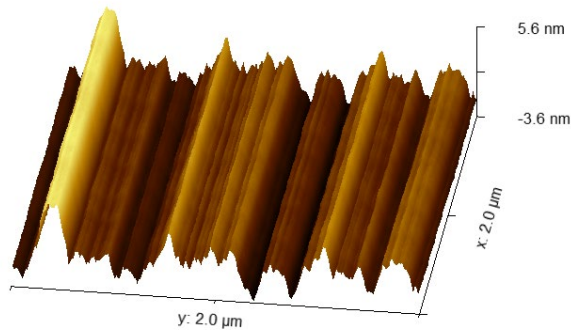


Figure 4.2. Atomic force microscope image of strontium titanate substrate before BHF treatment.

This figure illustrates the surface features of a strontium titanate (STO) substrate before any treatment. The surface exhibits irregularities characterized by distinct ridges and valleys. The height variation spans roughly from -3.6 nm to +5.6 nm across a $4 \mu\text{m}^2$ area. The observed characteristics show a surface exhibiting considerable roughness and irregularities, which are characteristic of untreated STO substrates.

While chemical etching can help expose crystallographic planes, it does not provide the same energy-driven atomic reorganization as annealing. So, the next step was annealing at 1100°C for 2 hours. This process formed a vicinal surface with atomically flat terraces, as shown in figure 4.3.

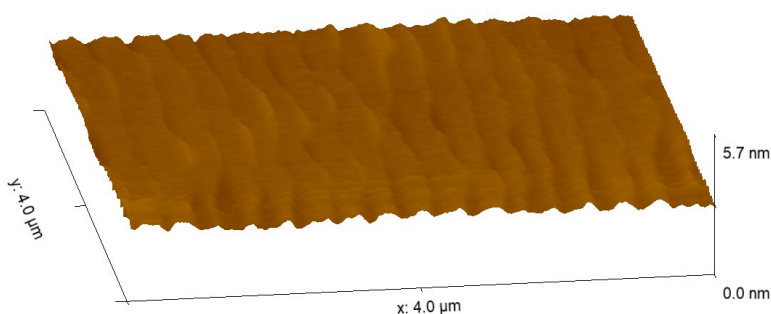


Figure 4.3. Atomic force microscope picture of strontium titanate sample after etching and annealing.

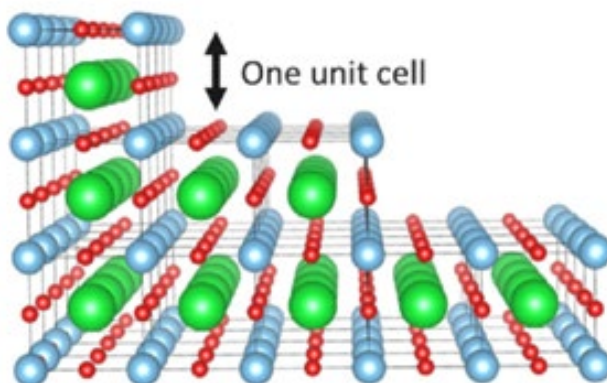


Figure 4.4. Schematic representation of a SrTiO₃(001) surface with TiO₂ terminations only. Sr atoms are represented in green, Ti in blue and O in red. (adapted from a [161]).

Figure 4.3 shows an STO substrate's atomic force microscopy (AFM) scan following BHF treatment and annealing. A schematic depiction of the resulting surface is provided in figure 4.4. The treatment has led to a significantly smoother surface, clearly demonstrated by the uniformity of the features. The distance between each terrace is around 260 nm. The step height is around 220 pm, around half of a strontium titanate lattice length (390.5 pm) across a surface area of $16 \mu\text{m}^2$, which confirms that we successfully produced a TiO_2 -terminated layer. The enhanced surface reflects the effective preparation of the substrate, increasing its efficiency for future deposition procedures. The treatment effectively diminishes roughness and ensures a more consistent termination layer, which is advantageous for epitaxial growth.

The PZT film was deposited under precise parameters to optimize its growth and characteristics. Deposition parameters include a substrate temperature of $555 \text{ }^\circ\text{C}$, an ambient pressure of 0.2 mbar, and 10,000 laser pulses. The laser maintained a consistent energy fluence of 1 J/cm^2 . Following the deposition, the samples were subjected to an in-situ annealing procedure in an environment of O_2 at a pressure of 200 mbar. The annealing process began once the temperature cooled to $250 \text{ }^\circ\text{C}$ and continued for 30 minutes. Annealing is performed to reduce the number of oxygen vacancies and minimize film leakage. The cooling rate of the sample was $20 \text{ }^\circ\text{C}$ per minute. The film's thickness was around 90 nm. The dielectric properties of the film were measured using an HP4284A LCR meter equipped with a needle probe station. The measurements were conducted across a frequency range of 20 Hz to 1 MHz, and the temperature range was set between 300 and 500 K.

During the initial stages of growth, the PZT layer progresses by filling the terraces of the underlying LSMO template layer (which reflects initial STO substrate characteristics), with a layer-by-layer growth mode prevailing even for thicker PZT films ($t \approx 90 \text{ nm}$) [159]. Once the layer-by-layer growth regime is established, epitaxial growth is typically observed, provided the substrate surface. In this regime, the substrate exerts a significant influence on the morphology of the

growing film, compelling the film to adopt an epitaxial orientation and achieve optimal growth [159]. In our study, the quality of the STO crystals used as substrates has proven to be a critical factor, as shown in figure 4.5.

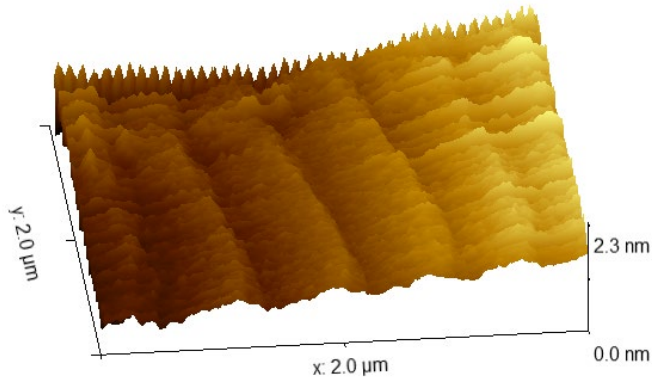


Figure 4.5. Atomic force microscope image of PZT film.

A close match of the lattice constant is also required to promote the growth of a_1/a_2 -domains for the out-of-plane phase polarization. As we can see from figure 4.6, our sample has a partly relaxed film showing mixed a/c -domains [162].

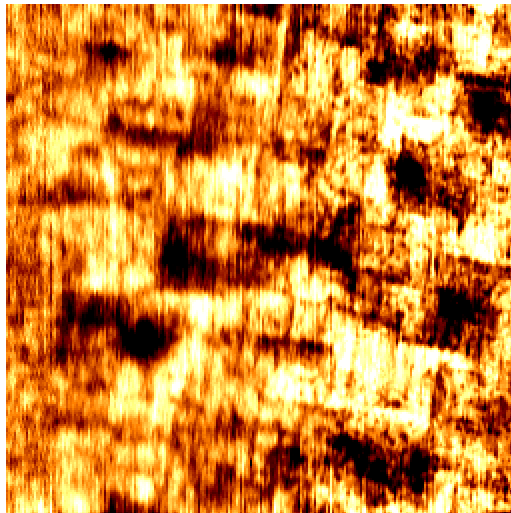


Figure 4.6. Characterization of the epitaxial PZT thin films by Piezoelectric Force Microscopy (PFM). The scan dimensions were $4 \mu\text{m}^2$.

During PZT deposition, part of the material is also deposited on the side of the sample. To contact the bottom contact, our LSMO layer, the sample angle was crushed to expose it, and painted with silver paste. As part of a probe station, the needles were attached to a top electrode and a brass plate with silver paste on top to establish a connection with a bottom contact. The schematic of this measurement setup is presented in figure 4.7.

The temperature was recorded using a Keithley Integra 2700 multimeter linked to the probe station. The ferroelectric characteristics were examined at room temperature using the aixACCT measurement equipment (Aachen, Germany).

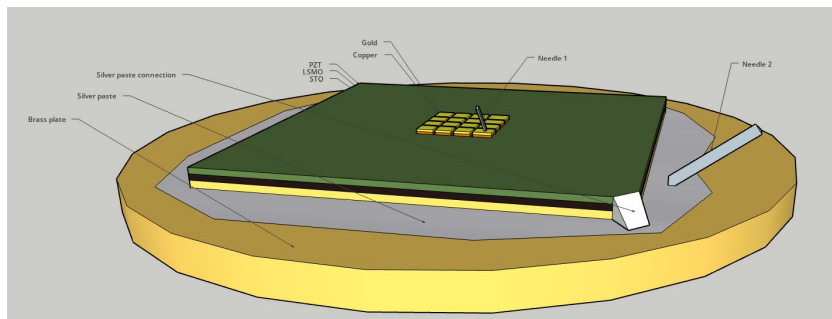


Figure 4.7. Scheme of the measurement setup.

Figure 4.8 displays the standard hysteresis loops for the sample's polarization and switching current. The polarization loop demonstrates characteristic ferroelectric behavior, characterized by a clear remnant polarization and coercive voltage. Moreover, the present loop exhibits hysteresis, which signifies the existence of ferroelectric characteristics in the device. The distinct peaks of positive and negative current measurements in the sample are evidence of a polarization reversal.

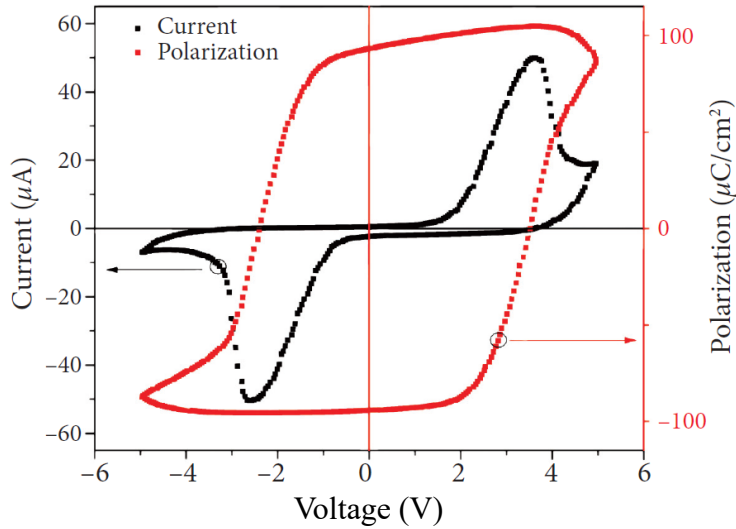


Figure 4.8. The polarization and current hysteresis loops were measured for a ferroelectric capacitor of LSMO/PZT/Cu/Au layers. The measurements were achieved by applying a triangle voltage pulse with a frequency of 1 kHz.

The remanent polarization of our strained tetragonal 20/80 PZT is $93 \pm 5 \mu\text{C}/\text{cm}^2$, which is the typical value [128]. The value of the remnant polarization and the coercive field ($E_c \approx 301 \pm 10 \text{ kV}/\text{cm}$) is almost identical to that of the a/c-domain samples. The remnant polarization value is considerably lower than in the c-domain samples because polydomain samples can be easily polarized. In addition, it is essential to mention that the polarization value P_r achieved through experimentation exceeds the theoretical value of $70 \mu\text{C}/\text{cm}^2$, which is commonly estimated for bulk single crystals, as stated in the reference [163]. This can be explained by residual strain inside the film that promotes out-of-plane polarization.

The piezoelectric loop exhibits a slight loop displacement towards the positive side, indicating the presence of a minor internal field (E_{in}) oriented towards the top electrode, likely due to the utilization of distinct electrode types. The internal field is often associated with defect pairs of negatively charged acceptor ions and positively charged oxygen vacancies, forming electric dipoles [12]. The IV curve exhibits

substantial leakage at high fields, restricting the range of applicable fields.

The dielectric permittivity was estimated from capacitance measurements (see figure 4.9). The dielectric loss, which usually occurs due to the relaxation of space charge and domain walls, has been observed to decrease as the frequency of the external field increases. Two significant factors can explain the decrease in the imaginary part of the dielectric permittivity with frequency. The first one is related to extrinsic sources and can be attributed to the leakage current in interfaces between an Au/Cu contact and PZT layers. The second cause is related to the ferromagnetic-metal to paramagnetic-insulator transition of our LSMO layer.

The high-frequency tail dispersions can be precisely modeled using classical Cole-Cole functions. Nevertheless, these functions are deficient in describing the low-frequency plateaus of ϵ and σ . Instead, the constant phase-angle (CPA) function offers a more precise description of the data in the low-frequency section of the graphs. This phenomenon can be attributed to numerous charge carriers, which alter the characteristics of the material, transforming it from a dielectric to a semiconductor [164].

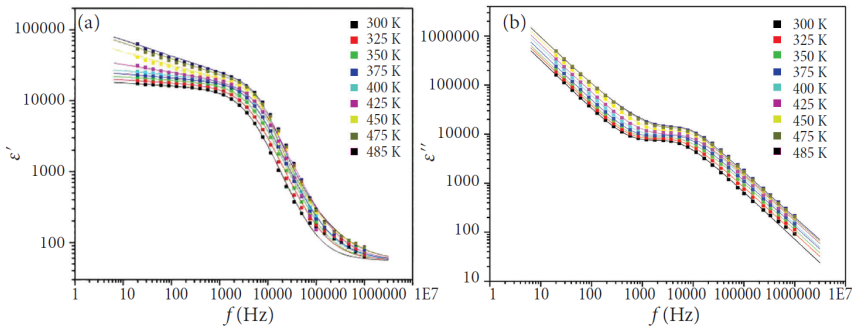


Figure 4.9. The frequency dependence of the real (a) and imaginary (b) parts of the permittivity data of the PZT film. The solid lines accurately correspond to the data points using the Raicu relation.

The fit was calculated using formula (39), which combines Debye-type and “universal” responses and considers the contribution of

conduction, which may be observed experimentally at the low-frequency side, was proposed by Raicu [165].

$$\varepsilon(i\omega) = \varepsilon_{\infty} + \frac{\sigma}{i\omega} + \frac{\varepsilon_0 - \varepsilon_{\infty}}{[(i\omega\tau)^{\alpha} + (i\omega\tau)^{1-\beta}]^{\gamma}} \quad (39)$$

This function, initially proposed by Dr. Raicu for biological tissues, can also be used in nonbiological systems, where the existence of particles and particle aggregates is a factor that strongly affects the notion of interparticle interactions. This is probably the case for our film since, during deposition, particles are produced and can affect the result of the dielectric measurement.

Figure 4.10 depicts the correlation between the average relaxation time and the reciprocal value of the temperature. The data points reflect the mean relaxation times at specific temperatures, and the line is a result of fitting by the Arrhenius equations (25) [12].

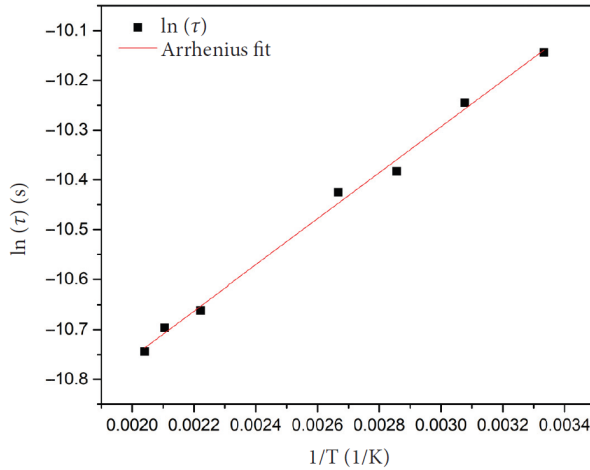


Figure 4.10. The mean relaxation time in PZT ceramics vs inverse temperature. The data points are fitted using the Arrhenius equation (25).

According to this fit, the activation energy is determined to be 436 K (37.6 meV). When applying heat to a ferroelectric sample, a low-intensity measurement field with a strength of less than $10 \text{ V}\cdot\text{mm}^{-1}$ is

used. This phenomenon induces oscillations in domain walls. The investigated PZT samples exhibit a process with an energy magnitude of approximately $U = 40$ meV. This energy represents the early oscillations of the domain walls within the local potential well [166].

The impedance data, comprising the real component (Z') and the imaginary part (Z''), can be visualized as a Nyquist plot to illustrate the impedance spectrum of the system, as depicted in figure 4.11. The distinct time constants of each RC element result in a clear differentiation between the semicircles of the PZT film and the LMSO film within the temperature range. The real part of the characteristic impedance between the different minima in the imaginary part represents the macroscopic resistivity of LSMO (the left semicircle) and PZT (the right semicircle).

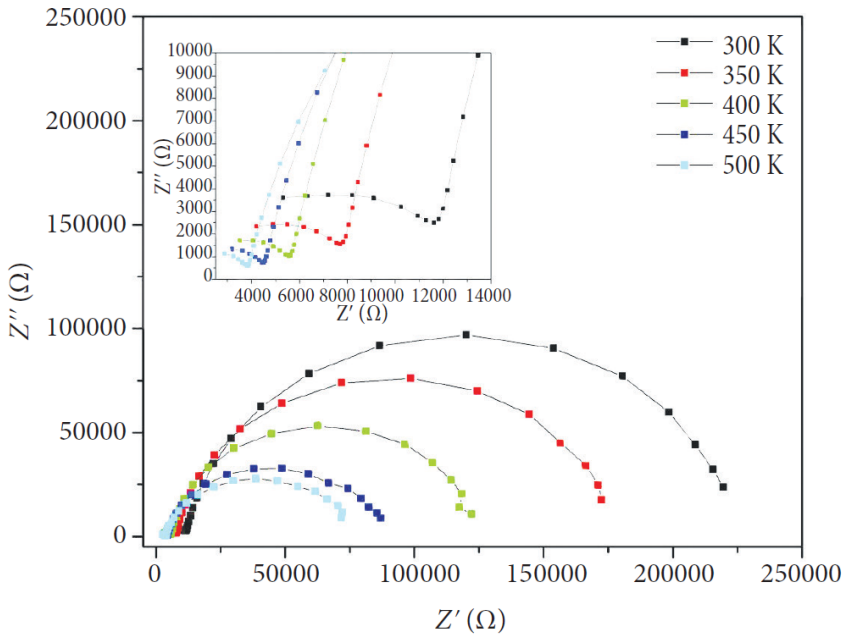


Figure 4.11. The Nyquist plot displays the relationship between Z' and Z'' (including the characteristic resistivity of the high-frequency region in the inset).

As the temperature rises, the diameter of the conduction-related arc in the bulk material decreases, and the center of the semicircular arc shifts toward the origin of the complex plane plot. The displacement of the starting point of the semicircular curve towards the center of the complex plane graph indicates a decrease in the sample's resistive properties.

This change is linked to the temperature rise and attributed to grain boundary conduction. As the Nyquist plots indicate, the dielectric response in the sample studied is primarily intrinsic.

4.1.1. Conclusion

High-quality epitaxial $\text{PbZr}_{0.2}\text{Ti}_{0.8}\text{O}_3$ (PZT) thin films were successfully deposited using pulsed laser deposition (PLD), demonstrating the versatility and precision of this method. The films showed exceptional ferroelectric characteristics with a remanent polarization of $93 \mu\text{C}/\text{cm}^2$. This figure is significantly greater than the $70 \mu\text{C}/\text{cm}^2$ theoretical value in bulk PZT. This enhancement was attributed to internal stresses resulting from lattice constant and thermal expansion coefficient mismatches between the PZT layer and the underlying $\text{La}_{0.7}\text{Sr}_{0.3}\text{MnO}_3$ (LSMO) buffer layer. Atomic force microscopy (AFM) was used to determine the homogeneity of the PZT films, which came out to be about 2.3 nm. The film's thickness was estimated at 100 nm.

The frequency-dependent dielectric behavior of the films, modeled using the Raicu relation, revealed a transition from dielectric-like to semiconductor-like behavior at lower frequencies. This finding emphasizes how interface effects and inherent material characteristics affect the dielectric relaxation processes. Additionally, Nyquist plot analysis identified two distinct relaxation regions: one linked to the resistivity of the PZT film itself and the other associated with the LSMO buffer layer. These observations highlight how important substrate and film characteristics are in influencing the device's overall performance.

Further stoichiometry and interface engineering advancements may allow additional ferroelectric and dielectric property improvements.

Future work should also focus on the effects of film thickness and substrate material on polarization and relaxation behavior.

4.2. Optimization of pulsed laser deposition parameters of $0.8(\text{Na}_{0.5}\text{Bi}_{0.5}\text{TiO}_3)\text{-}0.2(\text{BaTiO}_3)$ thin films

A Pulsed Laser deposition facility was used to prepare the samples from a custom-made $0.8(\text{Na}_{0.5}\text{Bi}_{0.5}\text{TiO}_3)\text{-}0.2(\text{BaTiO}_3)$ target. The substrates used were silicon with silver deposited via thermal evaporation and silicon with platinum deposited by sputtering.

The target was tested with an X-ray diffraction (XRD) measurement to ensure that our film's chemical composition was identical to the target and could achieve stoichiometric growth.

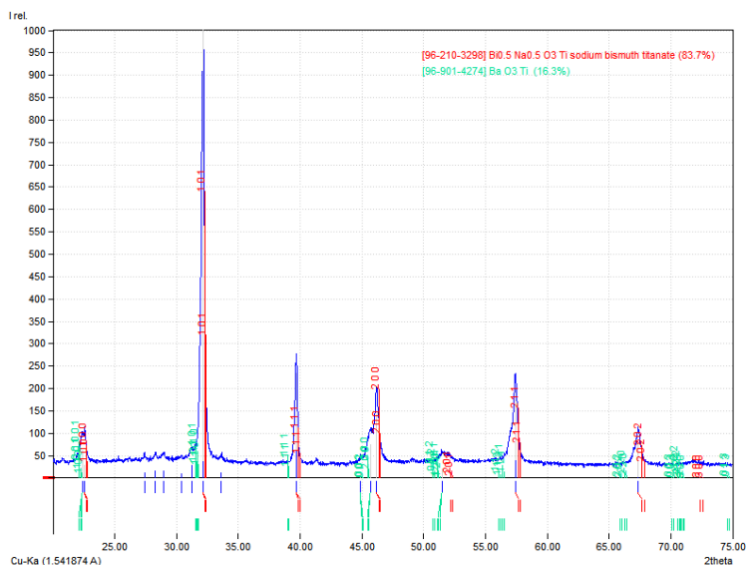


Figure 4.12. XRD pattern of $0.8(\text{Na}_{0.5}\text{Bi}_{0.5}\text{TiO}_3)\text{-}0.2(\text{BaTiO}_3)$ target.

As we can see from the X-ray diffraction pattern, plotted in figure 4.12, the signal mostly matches a [96-210-3298] Crystallography Open Database entry for a sodium bismuth titanate, with some alteration due to the presence of Barium Titanate (entry [96-901-4274]).

Phases and Elements (Weight %) calc. by RIR method

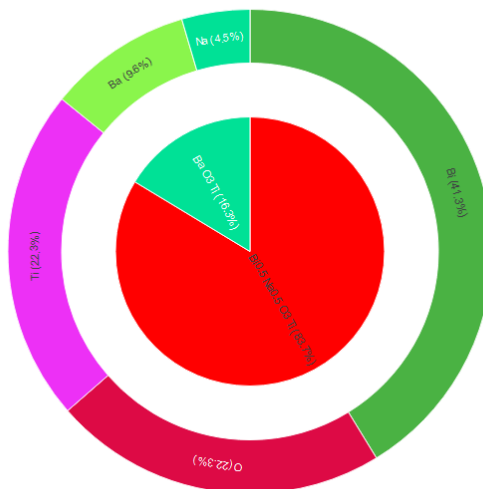


Figure 4.13. Reference Intensity Ratio (RIR) method diagram of our target.

The percentage value of elements, analyzed by the Reference Intensity Ratio (RIR) method (figure 4.13), shows an almost identical composition of intended NBT-BT, close to 20% of BT.

X-ray Fluorescence (XRF) also estimated the target's chemical composition and confirmed this estimation.

Table 2. Comparison of data from the RIR and XRF methods

Method/Element	Bi	Ba	Ti	Na	O
RIR	41.3	9.6	22.3	4.5	22.3
XRF	46.289	16.87	23.71	5.5	5.695

This analysis is only partly correct since organic elements (e.g., H, C, N, O) do not give a strong signal in XRF analysis. Our sample should contain around 22.26 weight % of O, which this method incorrectly detects. Fluorescence photons from these elements are too low in energy to be transmitted through air and are not efficiently detected using conventional Si-based detectors.

Effect of laser fluence (substrate with silver buffer layer)

One of the significant parameters that can be optimized and investigated is fluence, which is essential for a complex material. We prepared a set of samples with varying fluence to evaluate its impact on film stoichiometry. Table 3 contains all the sample deposition parameters that have been used to investigate the effect of laser fluence on the quality of the film for the first type of substrate with silver as a buffer layer. The silver layer was prepared by thermal evaporation and had a thickness of around 250 nm.

Table 3. Pulsed laser deposition (PLD) parameters for all samples were used to investigate the effect of fluence.

Deposition parameter	Sample 34	Sample 35	Sample 36	Sample 41	Sample 42
Fluence, J/cm ²	0.9	0.6	0.3	1.2	1.5
Common parameters: T: 600 °C, P: 0.3 mbar O ₂ , f: 5 Hz, T-S distance: 55 mm, N: 72000					

The scanning electron microscope (SEM) images of sample 34 in figure 4.14 illustrate a surface scan of the sample. Our thin layer is characterized by a porous, granular structure exhibiting diverse morphologies at various magnifications. At a magnification of 50,000x (figure 4.14(a)), the material exhibits interconnecting holes and irregular crystalline grains, suggesting a rough surface morphology potentially affected by the quality of the buffer layer. At a lower magnification of 500x (figure 4.14(b)), with a scale of 200 μm, the surface has a more uniform appearance with a repetitive texture, indicating consistent porosity throughout a broader region.

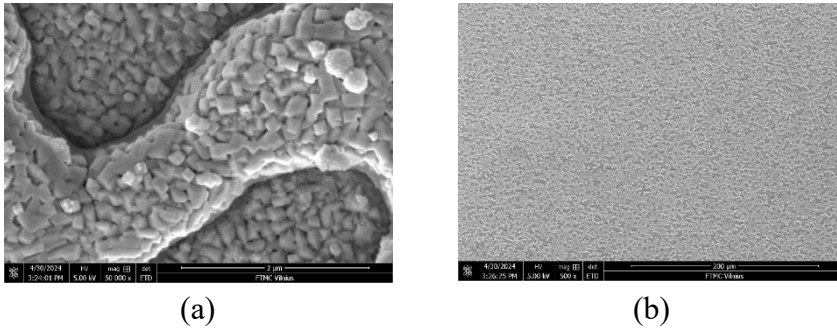


Figure 4.14. Scanning electron microscope images at (a) 50000x magnification and (b) 500x magnification of sample 34 grown at 0.9 J/cm^2 fluence.

Since the deposition temperature was chosen to be $600 \text{ }^\circ\text{C}$, some of the silver evaporated from the surface of the samples, together with our film. This is probably due to the thermal evaporation method's poor adhesion between the silicon substrate and the silver deposited. In this case, silver is evaporated from the surface of our substrate before deposition and during heating to the deposition temperature. This idea is supported and presented further by the fact that on an energy-dispersive x-ray (EDX) measurement, we see the difference in composition between the hill area and the pits.

Another option might be that silver deposited this way is inherently unevenly distributed on the top of our sample. This idea is supported by the fact that different areas of that sample look similar under magnification and contain the same patterns of polycrystalline layers. Also, some residual silver is still included in the pit area. Hence, the idea is that silver can move under high temperatures and low pressure and, instead of maintaining a uniform layer, create a porous structure.

An energy-dispersive X-ray analysis was performed to investigate the element distribution in our film. Figure 4.15 depicts a scanning electron microscope picture of areas where the spectrum of elements was measured.

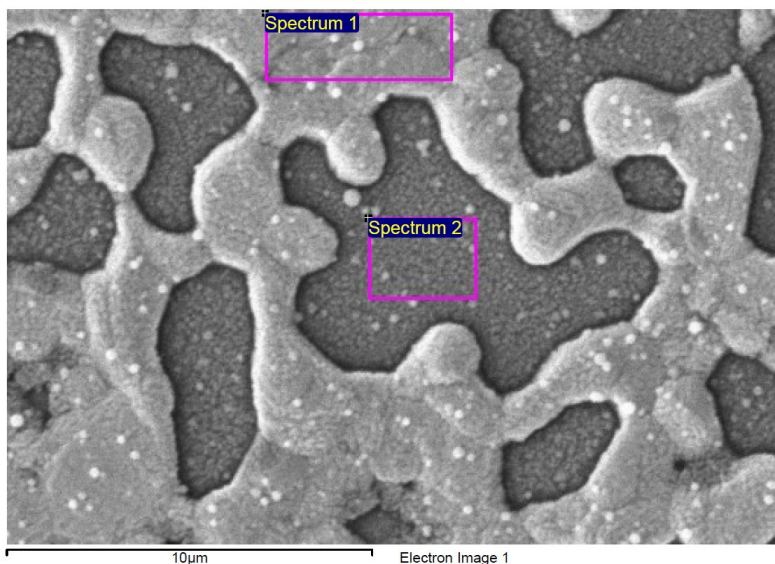


Figure 4.15. SEM image of EDX analysis areas for sample 34.

The SEM-EDX image shows a porous morphology with interconnected channels and moderately defined features. Particles can be observed on a whole surface, and the shapes of channels can be attributed to island growth. Table 4 contains data on the energy-dispersive X-ray of sample 34.

Table 4. EDX analysis of the areas in sample 34.

Area/Element	O	Na	Si	Ti	Ag	Ba	Bi
Spectrum 1	58.61	1.19	2.19	8.79	20.17	2.01	7.05
Spectrum 2	35.72	0.76	49.21	6.56	0.18	1.88	5.69

The EDX data for this sample highlights significant oxygen content (58.61%) in Spectrum 1, alongside silver (20.17%), titanium (8.79%), and bismuth (7.05%), indicating a forming film with off-stoichiometric elemental distribution. In contrast, Spectrum 2 shows higher silicon content (49.21%) with oxygen (35.72%), suggesting significant silver removal from this area.

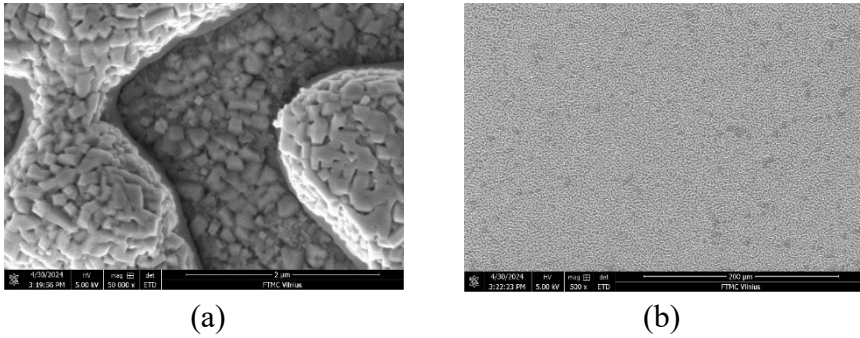


Figure 4.16. SEM images at (a) 50000x magnification and (b) 500x magnification of sample 35 grown at 0.6 J/cm² fluence.

SEM pictures of sample 35 (figure 4.16) deposited with a 0.6 J/cm² exhibit analogous characteristics, suggesting no significant changes in the film's morphology. Both high-magnification image sets (50,000x) exhibit a granular, crystalline structure with interconnecting pores, indicating a rough surface morphology. Nonetheless, there may be minor discrepancies in grain size and crystalline density, which show the effect of fluence. Both samples' low-magnification photos (500x) show a homogeneous surface texture with recurring patterns, suggesting consistent porosity or surface morphology across large areas.

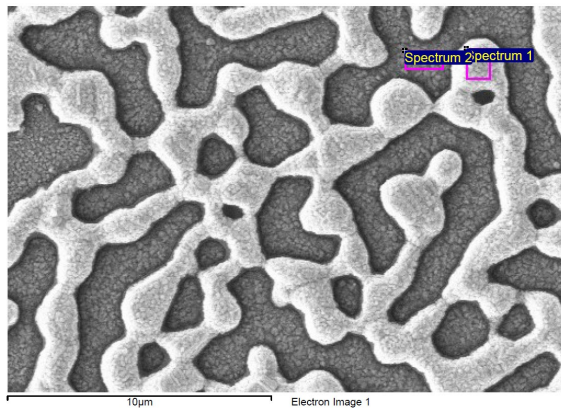


Figure 4.17. SEM image of EDX analysis areas for sample 35.

The energy-dispersive X-ray of sample 35 (figure 4.17) reveals a porous structure like sample 34, characterized by sharper edges and more distinct voids, presumably resulting from decreased energy deposition at 0.6 J/cm^2 .

Table 5. EDX analysis of the areas in sample 35.

Area/Element	O	Na	Si	Ti	Ag	Ba	Bi
Spectrum 1	57.84	0.61	0.67	8.37	23.29	2.15	7.07
Spectrum 2	36.19	0.92	50.02	5.84	0.41	1.67	4.95

EDX examination of spectrum 1 indicates a significant silver content (23.29%) alongside oxygen (57.84%), titanium (8.37%), and bismuth (7.07%), demonstrating a clear trend with a slightly elevated silver concentration compared to sample 34. This might be an effect, and Spectrum 2 reveals elevated silicon concentration (50.02%) and oxygen (36.19%), implying regions of diminished material coverage where the substrate may be more exposed. These characteristics correspond to a reduced fluence, resulting in a less dense deposition.

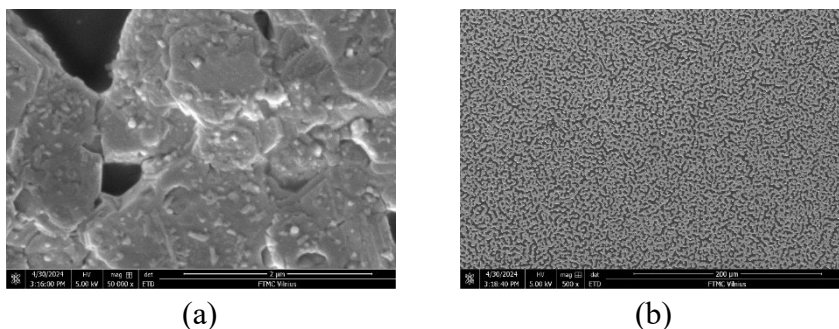


Figure 4.18. SEM images at (a) 50000x magnification and (b) 500x magnification of sample 36 grown at 0.3 J/cm^2 fluence.

The SEM images of sample 36 (figure 4.18), grown at the smallest fluence of 0.3 J/cm^2 , contrast with samples 34 and 35 on surface shape and structure. At a magnification of 50,000x, the present sample exhibits bigger, plate-like patterns mixed with bigger grains, in contrast to the finer, more uniformly distributed granular structures shown in

previous photos. At low magnification (500x), both samples display a consistent, repeated surface texture; nevertheless, the current image seems somewhat rougher, potentially suggesting an even smaller film thickness, which is consistent with the effect of reducing fluence for deposition.

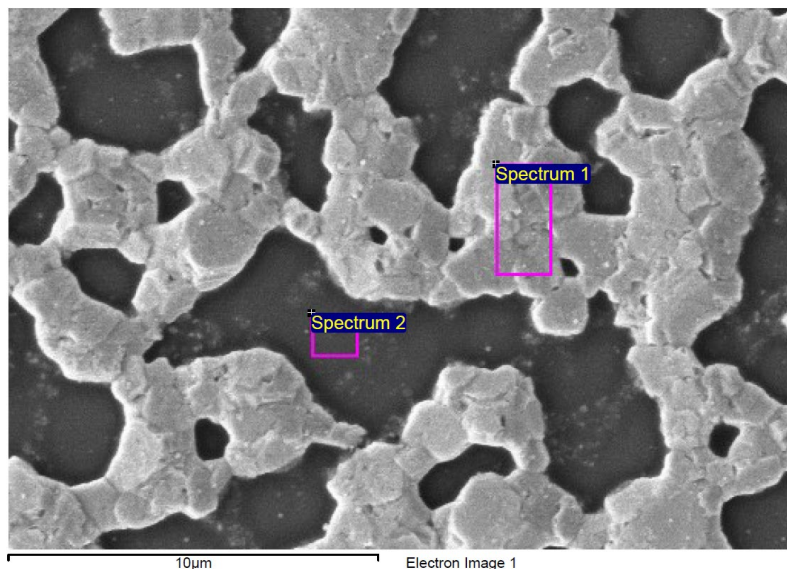


Figure 4.19. SEM image of EDX analysis areas for sample 36.

Figure 4.19 displays a clear skeletal architecture featuring bigger, well-defined voids, suggesting limited material deposition resulting from the lowest fluence of 0.3 J/cm^2 .

Table 6. EDX analysis of the areas in sample 36.

Area/Elements	O	Na	Ti	Ag	Bi
Spectrum 1	24.57	0.32	1.56	72.01	1.55
Spectrum 2	84.67	4.00	5.09	1.79	4.46

The Energy-dispersive X-ray data from spectrum 1 reveals a predominant silver content of 72.01%, accompanied by somewhat lower levels of oxygen at 24.57% and titanium at 1.56%, suggesting the presence of discrete silver-rich areas. Spectrum 2, conversely, exhibits

a significantly elevated oxygen content (84.67%), accompanied by little contributions from sodium (4.00%) and titanium (5.09%), presumably indicative of a predominant concentration of NBT material since energy-dispersive X-ray didn't detect any traces of Ba. These observations indicate a significant decrease in material coverage and a quality change of deposited film from a higher to lower barium titanate content in our sodium bismuth titanate–barium titanate composition at the lowest deposition energy.

As observed, further decreases in deposition fluence negatively affect the stoichiometry of the film to the point where not all elements of the material are present or detectable by EDX. We can also see that the sample's chemical composition deviates from the target, so to fix that, we must increase the fluence above 1 J/cm^2 .

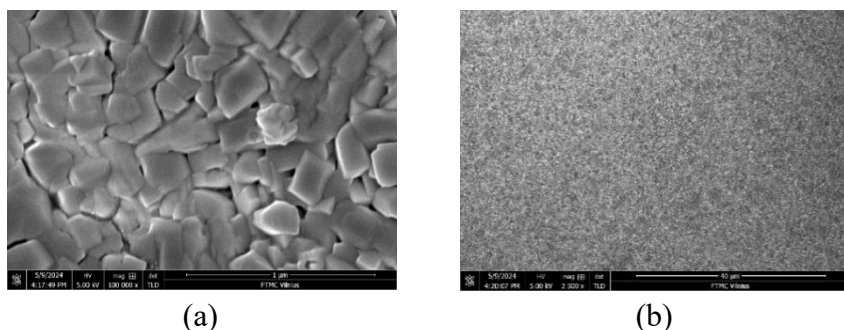


Figure 4.20. SEM images at (a) 100000x magnification and (b) 2500x magnification of sample 41 grown at 1.2 J/cm^2 fluence.

The scanning electron microscope pictures in figure 4.20 of a sample grown at 1.2 J/cm^2 exhibit a compact, crystalline architecture characterized by distinct, angular grains at high magnification 100,000x, starkly contrasting the more granular and porous morphologies noted in earlier samples. The prominent, well-defined grains in the present sample indicate improved crystal formation, perhaps resulting from increased deposition energy. "At a low magnification of 2,500x, the sample shows a homogeneous texture without visible flaws, indicating consistent material coverage and better surface quality than the coarser, more heterogeneous textures in

previous images. These observations indicate that the sample is coming toward optimum fluence to facilitate dense, crystalline growth and homogeneity.

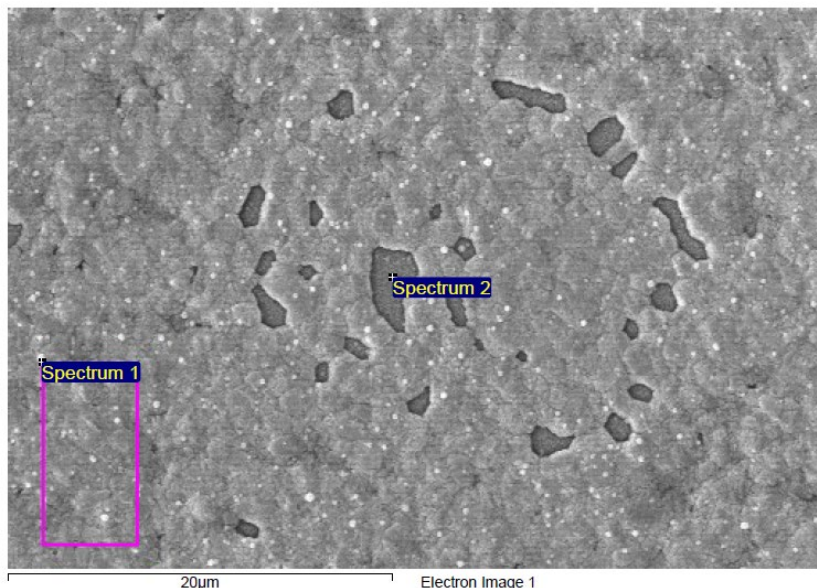


Figure 4.21. SEM image of EDX analysis areas for sample 41.

Table 7. EDX analysis of the areas in sample 41.

Area/Element	O	Na	Ti	Ag	Ba	Bi
Spectrum 1	62.39	2.71	13.06	9.20	3.31	9.33
Spectrum 2	70.31	2.49	13.85	0.18	3.00	10.17

This energy-dispersive X-ray picture (figure 4.21) depicts a surface characterized by a generally homogeneous distribution of grains and dispersed voids. The designated areas, Spectrum 1 and Spectrum 2, emphasize regions of significance for elemental analysis. The EDX readings for Spectrum 1 indicate elevated oxygen content (62.39%), substantial titanium (13.06%), and bismuth (9.33%), suggesting an approaching balanced elemental ratio. Spectrum 2 exhibits a higher oxygen concentration (70.31%) alongside comparable titanium levels (13.85%) and a somewhat increased bismuth content (10.17%). In comparison, silver is present in minor amounts (0.18%), indicating an

area with a diminished silver presence and potentially higher film thickness.

Compared to the prior EDX results, this sample demonstrates a more uniform and oxygen-enriched composition on the surface, presumably indicating variations in deposition conditions. This sample has a more homogeneous distribution of elements than prior samples with pronounced silver-dominated zones (e.g. Sample 36), particularly with titanium and bismuth uniformly present in both spectra. The findings indicate that the existing deposition parameters facilitate a more uniform film development with less material separation and silver aggregation.

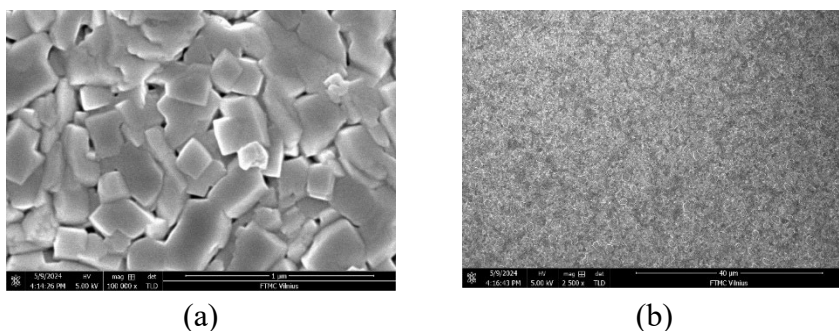


Figure 4.22. SEM images at (a) 100000x magnification and (b) 2500x magnification of sample 42 grown at 1.5 J/cm^2 fluence.

The scanning electron microscope images (figure 4.22) of sample 42 reveal a crystalline structure characterized by distinct, angular grains and sharp edges at high magnification 100,000x, suggesting regulated growth conditions and an enhanced degree of faceting relative to earlier samples with smaller or more porous configurations. The granules are closely packed and homogeneous, indicating optimum deposition conditions such as elevated temperature or fluence. At a low magnification of 2,500x, the surface exhibits a uniform texture with consistent feature distribution and no discernible defects or significant voids, indicating enhanced material coverage and deposition uniformity. These data indicate improved crystal growth and surface quality relative to previously studied samples.

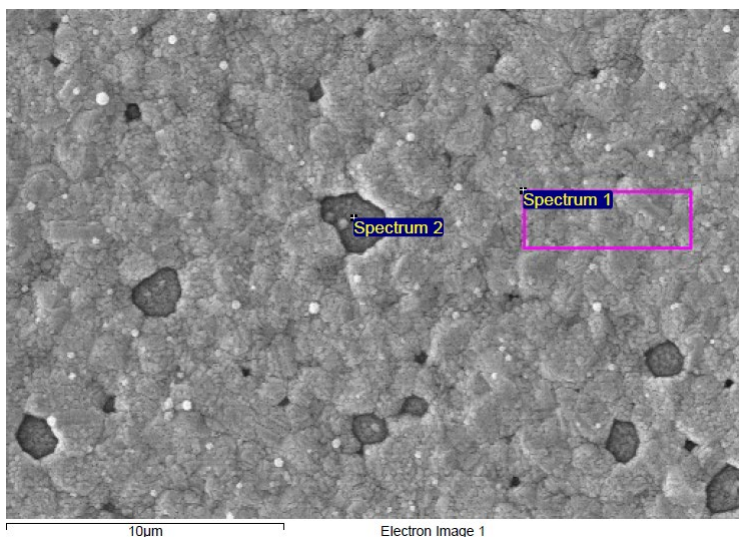


Figure 4.23. SEM image of EDX analysis areas for sample 42.

Table 8. EDX analysis of the areas in sample 42.

Area/Element	O	Na	Ti	Ag	Ba	Bi
Spectrum 1	62.17	2.74	11.81	11.57	3.16	8.56
Spectrum 2	60.92	4.46	18.44	0.16	5.26	10.76

This scanning electron microscope picture in figure 4.23, depicting a sample deposited at 1.5 J/cm^2 , reveals a moderately smooth surface with dispersed voids and consistent grain distribution. The EDX data indicates apparent compositional differences between spectrum 1 and spectrum 2. In Spectrum 1, oxygen (62.17%) predominates, supplemented by modest titanium (11.81%) and silver (11.57%), indicating a future increase in our film elemental distribution with well-integrated silver areas. In Spectrum 2, oxygen levels are elevated (60.92%), while titanium (18.44%) and bismuth (10.76%) are markedly enhanced, accompanied by little silver (0.16%), indicating a silver-deficient area. This sample demonstrates a more uniform elemental distribution than prior samples, yet the compositional heterogeneity among spectra reveals localized differences, possibly affected by the increased fluence of 1.5 J/cm^2 . The increased fluence promotes

reducing isolated silver-rich areas seen in lower-fluence samples, leading to a more uniform and well-integrated film.

Data from Spectrum 1 of EDX analysis of all samples (Table 9) were plotted against a deposition fluence to analyze the fluence's effect on our film's stoichiometry. We can see a clear trend in the case of each component that a linear fit can describe. The results of this analysis are presented in figure 4.24.

Table 9. EDX analysis of all samples to include only elements of our material composition.

Fluence (J/cm ²)	Oxygen	Sodium	Titanium	Barium	Bismuth
0.3	87.78	1.14	5.57	--	5.54
0.6	76.06	0.8	11	2.83	9.3
0.9	75.49	1.53	11.32	2.59	9.08
1.2	68.71	2.98	14.38	3.65	10.28
1.5	70.3	3.1	13.36	3.57	9.68
Ideal	60	8	20	4	8

As we can see, the increase in fluence allows us to approach stoichiometric growth and better cover the substrate's surface.

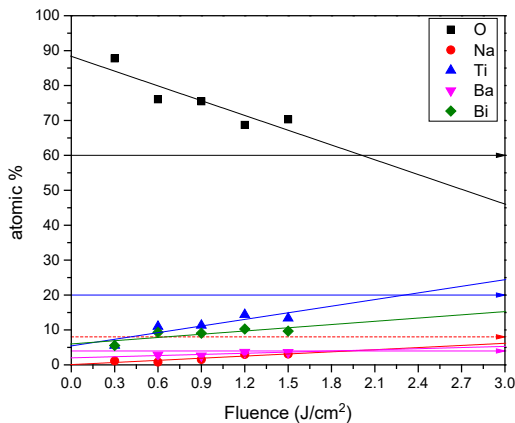


Figure 4.24. Atomic percentage of the element in a film against fluence during deposition.

In figure 4.24, arrows represent an atomic percent in an ideal $0.8(\text{Na}_{0.5}\text{Bi}_{0.5}\text{TiO}_3)\text{-}0.2(\text{BaTiO}_3)$ material (O 60%, Ti 20%, Ba 4%, Bi and Na 8%), and solid lines are projections of the fluence's effect on the film's chemical composition (the red line of Na also represents the concentration of Bi, the green line). Zooming at a lower atomic percent is demonstrated in figure 4.25.

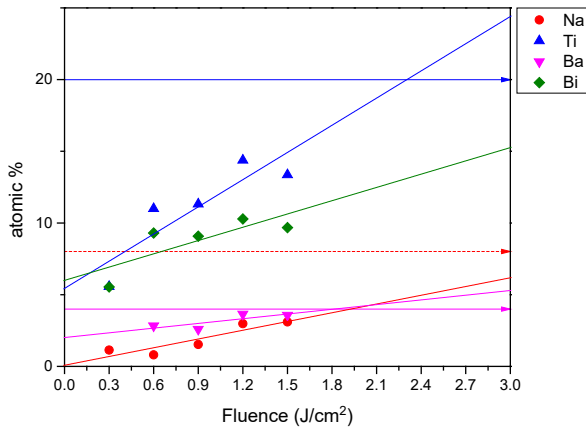


Figure 4.25. The atomic percentage of the element in a film against fluence during deposition (zoom to a lower atomic percentage of elements).

Based on these projections, we can assume each element's optimal fluence for a match with perfect target stoichiometry. In our case, it is 2 J/cm^2 for O, 2.3 J/cm^2 for Ti, 0.66 J/cm^2 for Bi, 3.9 J/cm^2 for Na, and 1.8 J/cm^2 for Ba. Assuming this is a correct estimation and adjusting for an abundance of the element inside our sample, we can safely say that the optimal fluence for stoichiometric growth will be around 2.1 J/cm^2 .

This data also tells us that achieving stoichiometric growth is hard for such complex material, and one of the future works might be creating a new target with element composition adjusted to the deposition rate of each element.

This might include adding the Na element with a reduction of the Bi element since both elements require very different fluence for the ideal composition of the $0.8(\text{Na}_{0.5}\text{Bi}_{0.5}\text{TiO}_3)\text{-}0.2(\text{BaTiO}_3)$ films.

Effect of substrate temperature (substrate with silver buffer layer)

We also investigated the increase in substrate temperature up to 650 °C and the decrease to 550 °C with scanning electron microscope images and energy-dispersive X-ray analysis measurements.

Table 10 presents key deposition parameters for all samples used to investigate the effect of temperature. Sample 34 was chosen as a reference point since this sample was made before fluence analysis, and based on the literature review, 0.9 J/cm² was used as an arbitrary reference fluence.

Table 10. Pulsed laser deposition (PLD) parameters for all samples were used to investigate the effect of substrate temperature.

Deposition parameters	Sample 38	Sample 34	Sample 37
Temperature	550 °C	600 °C	650 °C
Common parameters: F: 0.9 J/cm ² , P: 0.3 mbar O ₂ , f: 5Hz, T-S distance: 55 mm, N: 72000			

Sample 34 was presented before in a chapter about fluence optimization, so we shall continue to sample 38, whose SEM images are in figure 4.26.

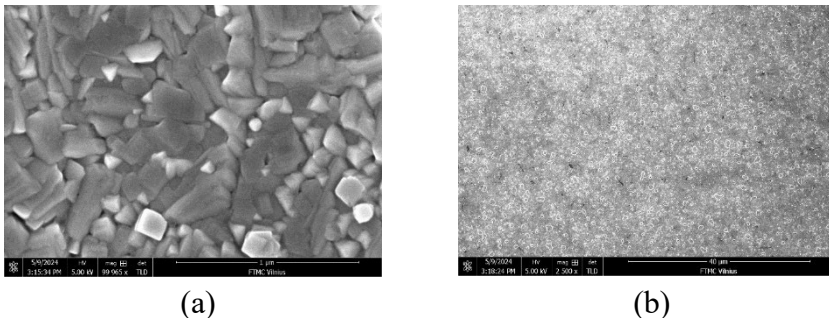


Figure 4.26. Scanning electron microscope images at (a) 99965x magnification and (b) 2500x magnification of sample 38 grown at 550 °C substrate temperature.

The scanning electron microscope pictures of a sample grown at 550°C exhibit notable variations when contrasted with the initial sample grown at 600°C under identical fluence conditions. Under high magnification, the present sample displays angular, slightly elongated grains with a densely packed yet less crystalline structure, in contrast to the initial sample's smaller, more uniform grains and distinct crystalline characteristics. At low magnification, the latest sample has a consistent texture with minor changes, akin to the first sample, although devoid of the pronounced surface definition noted. The reduced deposition temperature hindered proper distribution, resulting in a smaller, more porous, and less organized surface than the sample deposited at 600°C.

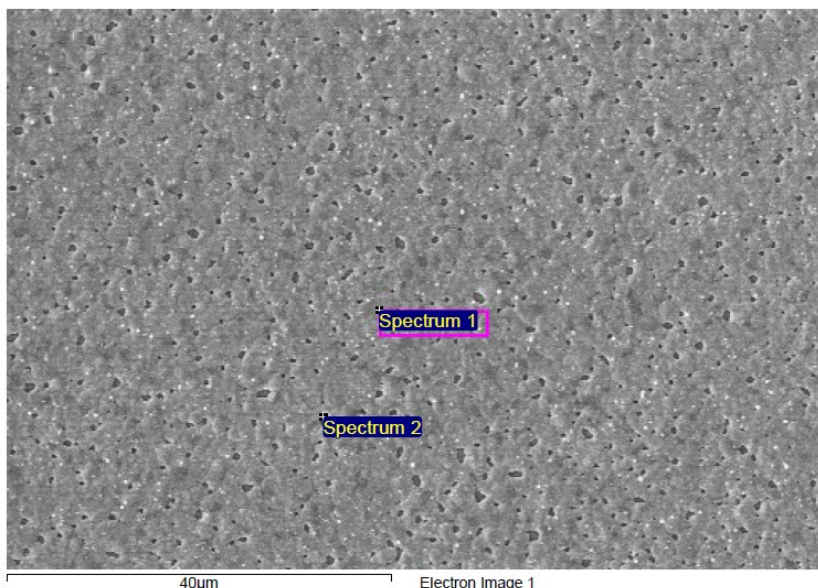


Figure 4.27. SEM image of energy-dispersive X-ray analysis areas for sample 38.

Table 11. EDX analysis of the areas in sample 38.

Area/Elements	O, %	Na, %	Ti, %	Ag, %	Ba, %	Bi, %
Spectrum 1	61.18	3.12	11.22	14.13	2.81	7.54
Spectrum 2	68.43	3.56	13.81	0.90	3.44	9.87

The scanning electron microscope picture and energy-dispersive X-ray data (table 11) for the sample grown at 550°C exhibit a similar concentration of elements compared to the initial sample grown at 600°C. The porosity changes underscore the impact of reduced deposition temperature, leading to better coverage of the sample's surface with angular, slightly elongated grains.

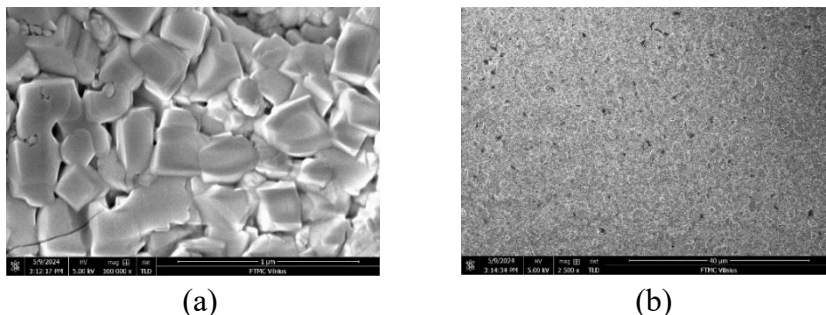


Figure 4.28. SEM images at (a) 100000x magnification and (b) 2500x magnification of sample 37 grown at 650 °C substrate temperature.

The scanning electron microscope pictures of the sample grown at 650°C exhibit notable disparities compared to those grown at 550°C and 600°C. At higher magnification, the 650°C sample displays larger, well-defined grains with sharp edges, signifying improved crystal growth and surface energy-induced faceting resulting from the increased deposition temperature. Conversely, the sample at 550°C has smaller, less distinct grains with a denser structure, while the 600°C sample displays moderately sized, homogeneous grains with a more polished crystalline look. At low magnification, the 650°C sample exhibits a reasonably uniform surface with enhanced texture consistency compared to the slightly porous texture noted at 550°C and the smoother, more continuous look at 600°C. The elevated deposition temperature of 650°C significantly enhances grain development and refines crystalline characteristics, indicating a better substrate temperature for producing well-faceted, high-quality thin films.

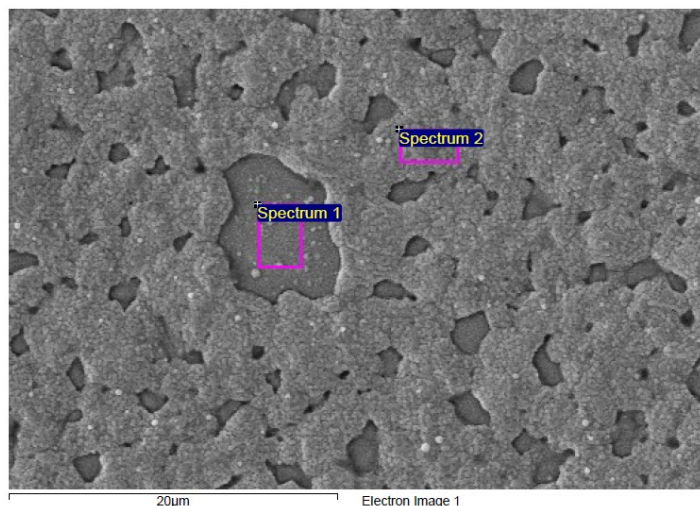


Figure 4.29. SEM image of EDX analysis areas for sample 37.

Table 12. Energy-dispersive X-ray analysis of the areas in sample 37.

Area/Elements	O	Na	Ti	Ag	Ba	Bi
Spectrum 1	67.45	2.96	14.78	0.31	3.85	10.65
Spectrum 2	64.39	2.84	14.24	4.95	3.19	10.39

The SEM picture and EDX data from figure 4.29 and Table 12 for the sample grown at 650°C exhibit distinct differences from those developed at 550°C and 600°C. The 650°C sample has a surface with more pronounced voids and stronger grain boundaries. The energy-dispersive X-ray examination of Spectrum 1 indicates a high oxygen content of 67.45% and notable titanium presence at 14.78%, with negligible silver at 0.31%. In contrast, Spectrum 2 exhibits a marginally reduced oxygen level of 64.39% and an increased silver content of 4.95%. This data advises us that most of our buffer layer of silver has already been evaporated from the surface of our substrate at this temperature. The increased growth temperature of 650°C seems to have the same chemical composition as samples prepared at other temperatures.

Table 13 contains all the data needed to estimate the effect of deposition temperature on the stoichiometry of our films.

Table 13. Energy-dispersive X-ray analysis of all samples to include only NBT-BT material elements.

Substrate temperature	O	Na	Ti	Ba	Bi
550	71.25	3.63	13.06	3.27	8.78
600	75.49	1.53	11.32	2.59	9.08
650	67.66	2.97	14.83	3.86	10.68

A graphical representation of the data in Table 13 is presented in figure 4.30.

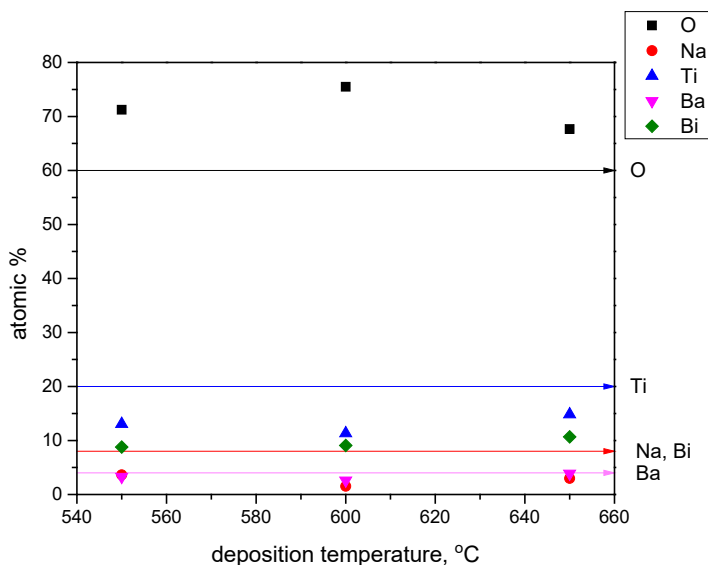


Figure 4.30. The atomic percentage of the element in a film against deposition temperature during deposition.

Changing the deposition temperature shows no traceable changes to film composition, as shown in figure 4.30. One outstanding feature in this analysis is that the bismuth content steadily increased with the substrate temperature. We may assume that higher deposition temperatures may shift the sodium bismuth titanate and barium titanate material balance in our composition toward the 1st one.

In all previous samples, one of the main problems that prevented our sample from our further dielectric measurement was the fact that a silver layer that we deposited on top of the silicon substrate had a small adhesion to our silicon and could easily be removed by annealing, which unintentionally happens during our deposition at such temperatures. To combat this issue, other samples with sputtered platinum layers were used, and the results of this sample work as a base for future optimization of deposition parameters.

Effect of target to substrate (T-S) distance (substrate with platinum buffer layer)

Based on a previous analysis, samples 58, 59, and 60 were made with the following deposition parameters. 1.5 J/cm^2 fluence was chosen as a reference fluence to investigate the effect of variation of other deposition parameters on the morphology and composition of the sample.

Table 14. Pulsed laser deposition (PLD) parameters for all samples were used to investigate the effect of target-to-substrate distance.

Deposition parameter	Sample 58	Sample 59	Sample 60
Target to substrate (T-S) distance, mm	55	75	95
Common parameters: T: 600 oC, P: 0.3 mbar, F: 1.5 J/cm^2 , f: 5 Hz, N: 100000 pulses			

Based on previous optimizations of fluence, the best-estimated fluence value was around 2.1 J/cm^2 . Unfortunately, due to the limitation of the facility at the time, the maximum fluence was around 1.5 J/cm^2 , which we are used. This is also based on a fluence investigation, so we would not have any unprecedented effect from elevated fluence. The slightly elevated number of counts was introduced to make the film even thicker and ease the dielectric measurements of these samples, which goes parallel to this research.

The effect of a target-to-distance ratio was investigated by creating three samples at various distances: 55 mm, 75 mm, and 95 mm. The samples were analyzed using SEM and XRD methods.

Sample 58 was deposited at a 55 mm target-to-substrate distance. The SEM scan of its surface is shown in figure 4.31.

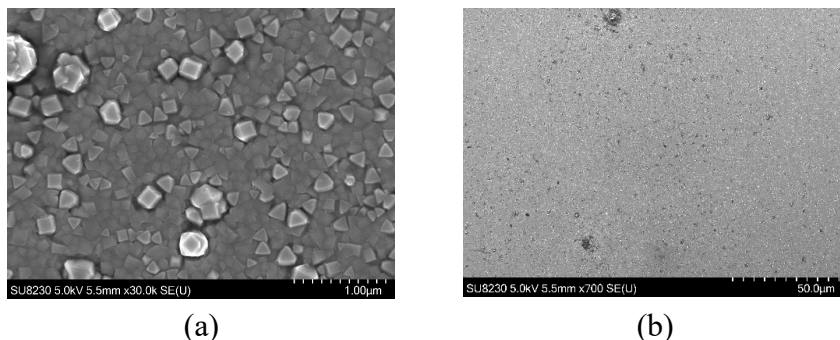


Figure 4.31. SEM images at (a) 30000x magnification and (b) 700x magnification of sample 58 grown at a 55 mm target to the substrate distance.

We can see the effect of a better substrate by the absence of visible voids on our surface in both higher and lower magnification. The surface exhibited distinct grains characterized by sharp, cubic forms. The composition includes clearly defined granular structures, probably in the form of crystallites. The particles exhibit a relatively uniform size and shape, characterized by cube-like forms and irregular triangular configurations. At increased magnification, the particles exhibit sharp edges, suggesting a high level of crystalline quality. Clustering is observed in specific areas, likely resulting from aggregation during the deposition process.

Sample 59 was deposited at a considerable distance of 75 mm. The scanning electron microscope images of the surface of this sample are presented in figure 4.32.

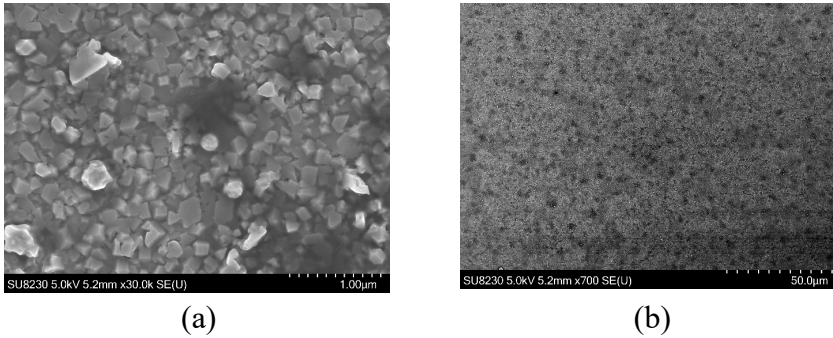


Figure 4.32. SEM images at (a) 30000x magnification and (b) 700x magnification of sample 59 grown at a 75 mm target to the substrate distance.

The grain size was slightly reduced compared to the sample deposited at 55 mm. The crystallites in this sample exhibit a more irregular shape than those in Sample 58. Observations suggest an increased presence of voids or spaces among the crystallites, which indicates a reduction in coverage density. Observations of larger particles or agglomerates indicate potential differences in the deposition rate. Sample 59 exhibits a coarser texture, characterized by more significant and irregularly shaped particles mixed with smaller ones.

Sample 60 was deposited at the biggest target-to-substrate distance of 95 mm. Such a significant distance reduces the deposition rate and creates an uneven surface. If the deposition temperature is not high enough to promote material exchange between platelets by surface migration, succeeding layers will form on top of the first islands, resulting in a discontinuous layer [167]. This elucidates the platelet-like characteristics of the film presented in figure 4.33.

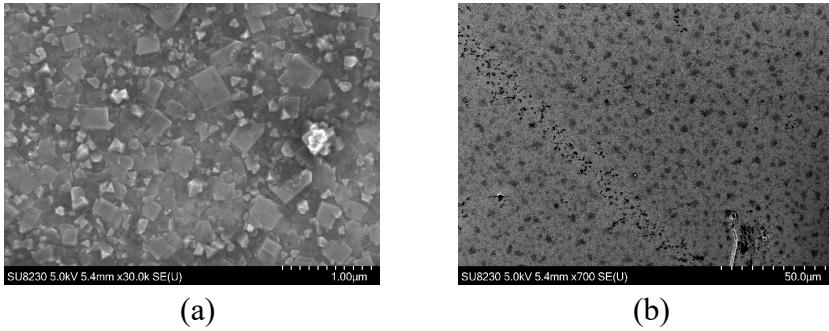


Figure 4.33. Scanning electron microscope images at (a) 30000x magnification and (b) 700x magnification of sample 60 were deposited at a 95 mm target to the substrate distance.

The grain structure exhibits irregularity, characterized by smaller grains in contrast to samples subjected to higher temperatures. The surface shows a greater variety of irregularly shaped and distributed crystallites. Certain regions exhibit dark characteristics indicative of insufficient film coverage or clustering. Crystallites exhibit a flatter morphology characterized by less defined edges, suggesting possible variations in their growth dynamics. It exhibits flattened or distorted crystallites, which may mean reduced mobility during deposition.

This result shows that each of the samples has polycrystal film features, and the X-ray diffraction method was employed to distinguish between the quality of this film.

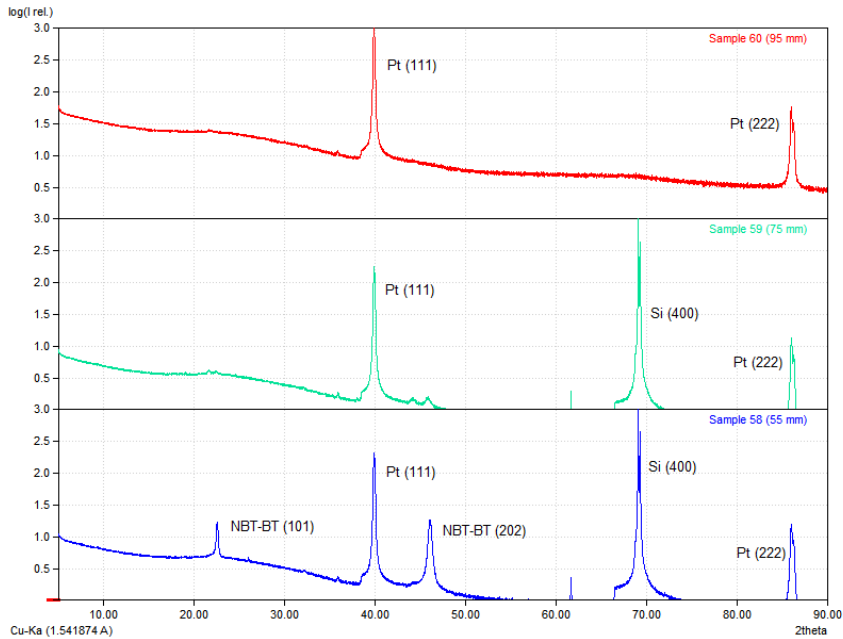


Figure 4.34. X-ray diffraction spectrum of x-ray intensity vs 2θ angle for sample 58 (55 mm), sample 59 (75 mm), and sample 60 (95 mm).

Since platinum, in (111) crystallographic order, matches our film, some of the preset peaks on this figure belong to our platinum buffer layer or our silicon substrate layer, described in figure 4.34. To compare the quality of the film, we can discuss the peaks around 22.5° and 46° cannot be attributed to our contact layer or substrate.

Pure $\text{Na}_{0.5}\text{Bi}_{0.5}\text{TiO}_3$ at room temperature possesses rhombohedral symmetry, while BaTiO_3 has a tetragonal structure. The rhombohedral phase of pure NBT at room temperature is characterized by a single (2 0 2) peak. The ceramic has a rhombohedral perovskite structure for all (1-x)NBT-xBT systems with $x < 0.065$. As x (i.e., the mole concentration of BT) increases, a tetragonal phase rises continuously. At $x = 0.08$, the ceramic becomes a pure tetragonal phase. This is evident by the splitting of the (2 0 2) diffraction peak to (0 0 2) and (2 0 0) peaks, as observed in the (1-x)NBT-xBT ceramic [168], [169].

From our data, we can assume that our sample deposited at the lowest distance is an NBT-BT film with a BT concentration of less than

6.5%. The sample deposited at 75 mm has a splitting of the (202) diffraction peak figure, so the concentration of BT is more than 6.5%.

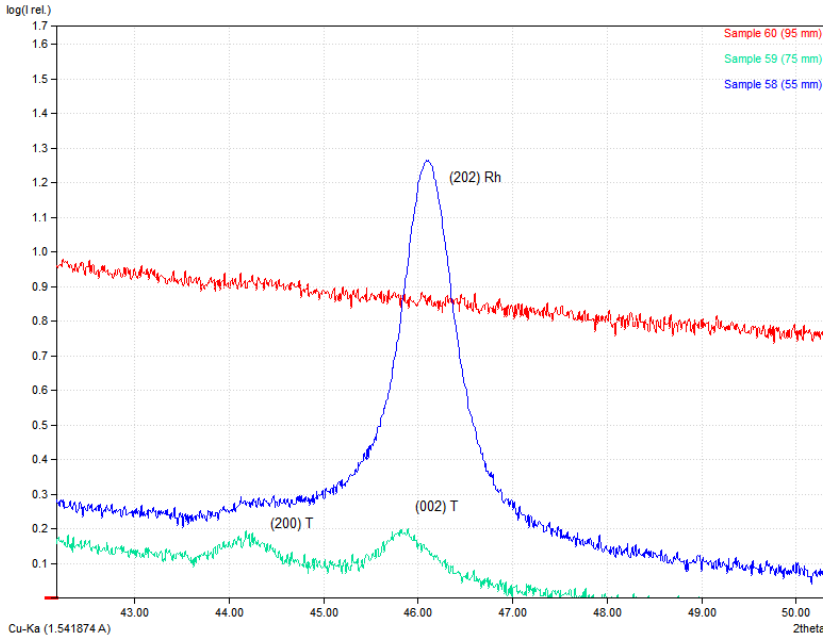


Figure 4.35. Zoom to a region of 46° 2θ angle of X-ray diffraction data graph of the samples deposited at various distances.

Another explanation for this data is that this prominent peak in the x-ray diffraction measurement of sample 58 indeed belongs to our composition. Scan peaks in our target x-ray diffraction (figure 4.35) are slightly offset from the Crystallography Open Database entry. Further confirmation from a dielectric spectroscopy method is required to resolve this question, and it is one of this project's future and current topics.

This effect is also visible from a 22.5° 2θ angle, with the possibility of distinguishing a very weak tetragonal peak in sample 60.

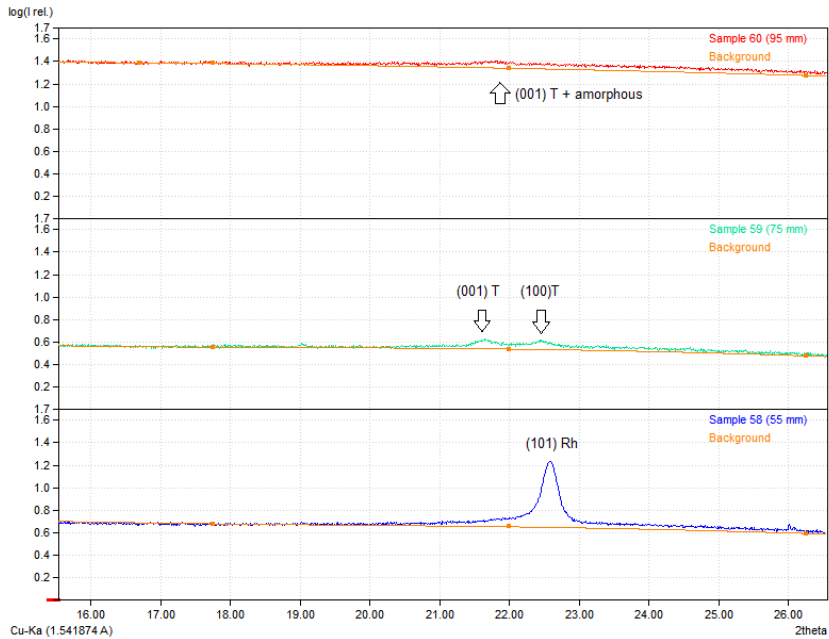


Figure 4.36. Zoom to a region of 22.5° 2θ angle of the X-ray diffraction data graph.

Based on X-ray diffraction analysis, sample 60 is mostly amorphous, with possible traces of a distorted tetragonal phase as indicated by the minor feature at 21.6° . The NBT-BT film here is poorly crystallized. Sample 59 has 2 tetragonal orientations. The film may also contain amorphous regions, indicating incomplete crystallization or strain. Sample 58 has a well-crystallized rhombohedral phase, with sharp peaks indicating good crystallinity and a well-oriented film. The absence of a second peak or broadening suggests fewer defects and no significant amorphous content.

Effect of substrate temperature (substrate with platinum buffer layer)

Two more samples with 550 and 650 °C deposition temperatures were made to investigate the effect of deposition temperature on a new substrate, since the porosity of the films skewed the last one. Table 15 contains all samples that were created to explore this parameter.

Table 15. Pulsed laser deposition (PLD) parameters for all samples were used to investigate the effect of substrate temperature.

Deposition parameter	Sample 61	Sample 58	Sample 62
Substrate temperature	550 °C	600 °C	650 °C
Common parameters: P: 0.3 mbar, F: 1.5 J/cm ² , f: 5 Hz, N: 100000 pulses, T-S distance: 55 mm.			

SEM images of sample 58, deposited at 600 °C, presented earlier, and SEM images of sample 61, deposited at 550 °C substrate temperature are shown in figure 4.37.

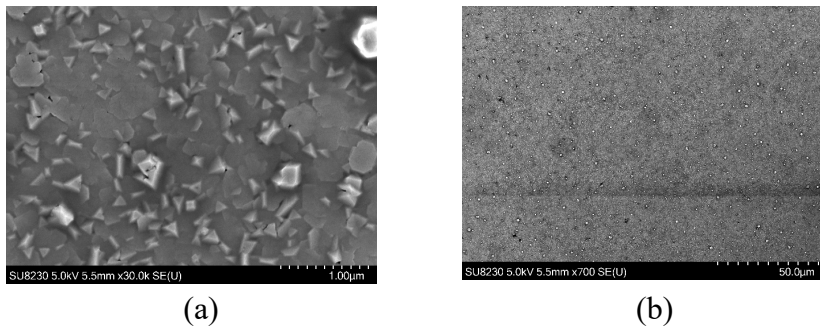


Figure 4.37. SEM images at (a) 30000x magnification and (b) 700x magnification of sample 61 deposited at a 550 °C substrate temperature.

The SEM images (figure 4.37) of Sample 61 display consistent and compact thin film characteristics by distinct crystallites, primarily triangular and irregular in form. The surface exhibits uniform coverage at low magnification with few defects or voids. The crystallites display distinct facets and surfaces at elevated magnifications, suggesting average crystalline quality. The distribution of grain sizes seems somewhat broader, featuring occasionally larger grains mixed in with the smaller ones. The film exhibits adequate packing and minimal gaps, indicating semi-optimized deposition conditions at 550°C. Sample 61 demonstrates good morphology, showcasing only slight surface imperfections.

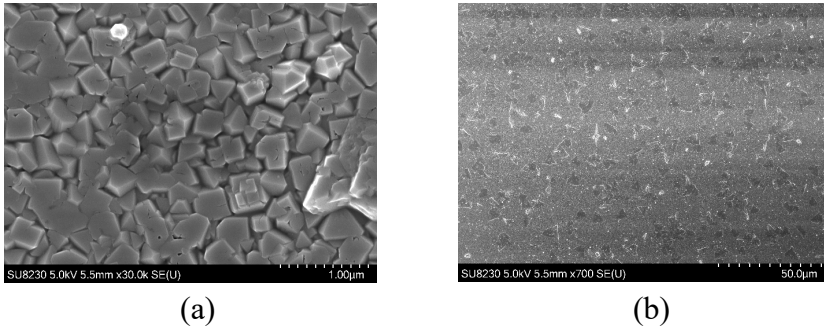


Figure 4.38. SEM images at (a) 30000x magnification and (b) 700x magnification of sample 62, deposited at a 650 °C substrate temperature.

The SEM image analysis of sample 62 reveals a non-uniform surface with prominent triangular and plate-like crystallites scattered across the film. These more extensive features are distinct and irregularly distributed at lower magnifications, suggesting nucleation or growth dynamics variations. Higher magnification shows a densely packed matrix of minor, angular crystallites beneath the larger structures, indicating a multi-scale morphology. The crystallites exhibit sharp edges and well-defined facets, reflecting good crystalline quality. The observed structure suggests a deposition process influenced by elevated substrate temperature (650 °C), leading to anisotropic growth and a mixed granular and columnar morphology.

XRD analysis of the effect of the substrate temperature is presented in figure 4.39.

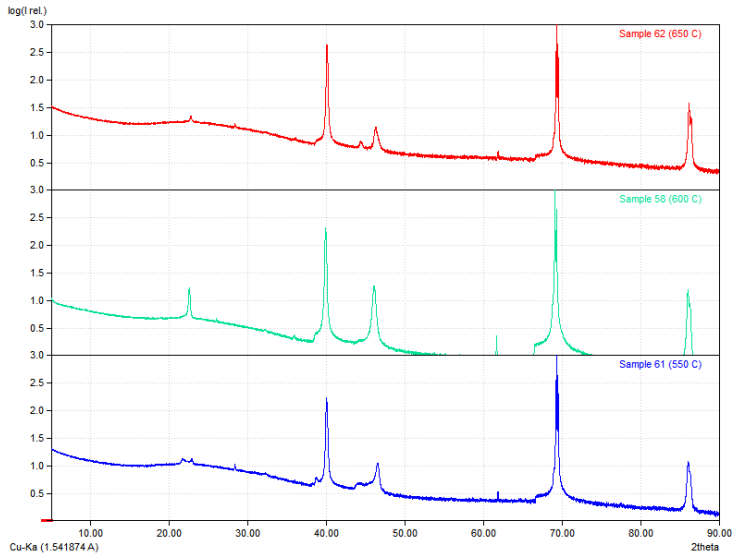


Figure 4.39. X-ray diffraction spectrum of x-ray intensity vs 2θ angle for samples deposited at various substrate temperatures: sample 61 (550 °C), sample 58 (600 °C), and sample 62 (650 °C).

We can see the changes in the peaks of our film depending on deposition temperature, similar to the effect of deposition distance.

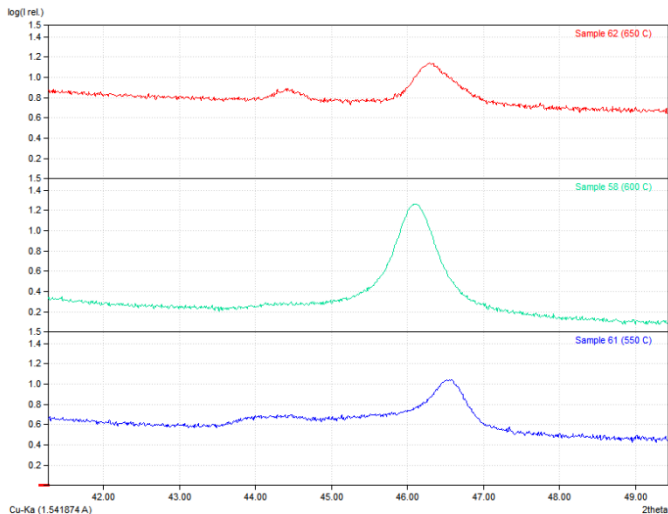


Figure 4.40. Zoom to a region of 46° 2θ angle of X-ray diffraction data graph of the samples deposited at various temperatures.

The XRD patterns for Samples 62, 58, and 61 demonstrate significant differences affected by deposition temperature. Sample 58, deposited at 600°C, exhibits a pronounced and sharp peak of about 46.5°, indicative of high crystallinity and a dominant rhombohedral orientation corresponding to the NBT-preferred crystal structure. Sample 61, deposited at a lower temperature of 550°C, shows a broader and less intense peak at the same place, combined with higher background noise, signifying a more amorphous structure or increased disorder in the film. Sample 62, deposited at the maximum temperature of 650°C, has two pronounced peaks attributed to a tetragonal structure of NBT-BT material with a BT concentration of more than 6.5%. These results indicate that elevated deposition temperatures (as shown in Sample 62) may change the BT composition inside an NBT-BT film.

Effect of deposition pressure (substrate with platinum buffer layer)

The pressure effect was also investigated with scanning electron microscopy and the x-ray diffraction method and presented further.

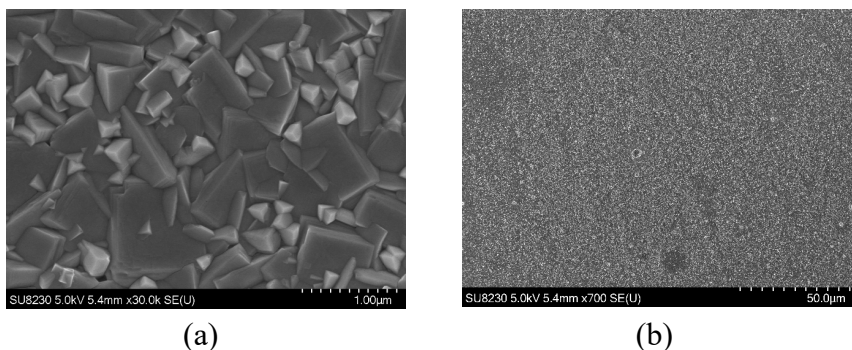


Figure 4.41. SEM images at (a) 30000x magnification and (b) 700x magnification of sample 63, deposited at a 0.06 mbar.

The SEM images of NBT-BT deposited at an oxygen pressure of 0.06 mbar display a dense and notably granular morphology. At lower magnifications, the surface exhibits a consistent layer of small crystallites interspersed with occasional larger, rounded agglomerates. At the highest magnifications, the crystallites display distinct edges and

a stratified structure, suggesting anisotropic growth. The lower oxygen pressure probably enhanced the mobility of adatoms, leading to the compact growth seen in the film. Another aspect of low pressure is less resistance to high-energy particles and ions, which causes prevention orientation to grow, as shown further on an XRD scan.

Figure 4.41 compares the x-ray diffraction pattern of sample 58, growing at 0.3 mbar, and sample 63, growing at 0.06 mbar oxygen pressure during deposition.

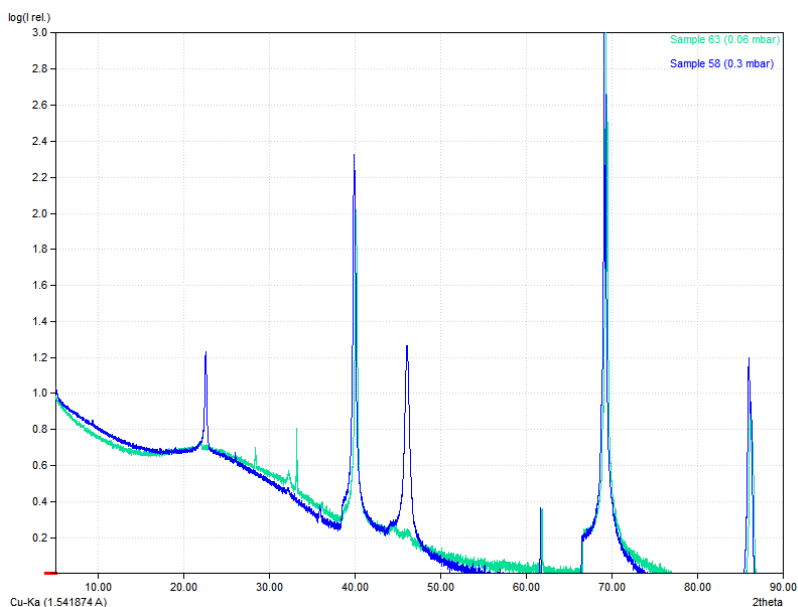


Figure 4.41. XRD data of x-ray intensity vs 2θ angle for samples 58 (0.3 mbar) and 63 (0.06 mbar).

X-ray diffraction (XRD) results for samples 63 and 58 are shown in the image. Both samples appear to have crystalline structures based on the strong peaks, particularly in the higher 2θ range. Sample 63, prepared at lower oxygen pressure, displays almost no peak at 22.5° and 46.5° 2θ angle, indicating disordered growth. XRD data show us that reducing the oxygen pressure dramatically reduces the oriental growth of the film. This is visible in a zoom of 46.5° 2θ angle in figure 4.42.

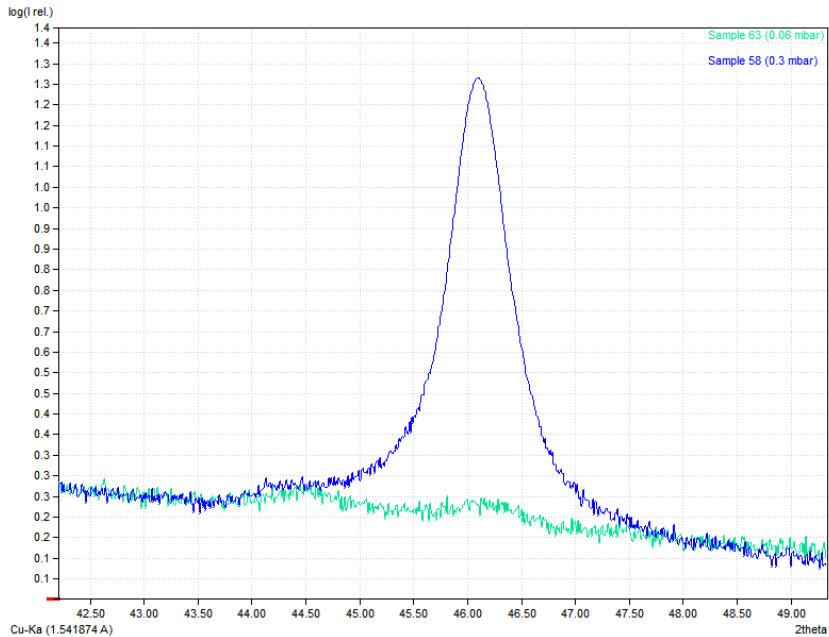


Figure 4.42. Zoom to a 46 2θ angle of the X-ray diffraction spectrum of x-ray intensity vs. 2θ angle for sample 58 (0.3 mbar), sample 63 (0.06 mbar).

4.2.1. Conclusion and future work

The optimization of deposition parameters for $0.8(\text{Na}_{0.5}\text{Bi}_{0.5}\text{TiO}_3)$ - $0.2(\text{BaTiO}_3)$ (NBT-BT) thin films resulted in significant improvements in crystalline quality and surface morphology.

Films deposited at 600°C showed strong crystallinity with a dominating rhombohedral phase, with a lattice parameter of 4.04 \AA , according to X-ray diffraction (XRD) research. In contrast, higher deposition temperatures promoted a transition to a tetragonal phase, which may influence the dielectric and ferroelectric properties. These results highlight the importance of precisely regulating the deposition temperature to preserve the intended phase composition.

SEM analysis revealed that lower oxygen pressures during deposition led to disordered growth and increased surface roughness. Nevertheless, films with the best stoichiometry and smoothness were created at an intermediate oxygen pressure of 0.3 mbar, reaching the

smallest roughness compared to other samples. This intermediate pressure also helped maintain a uniform distribution of bismuth and sodium ions, as confirmed by energy-dispersive X-ray spectroscopy (EDX), ensuring phase stability and improved dielectric performance.

Despite these advances, the study identified areas requiring further investigation. Future research should concentrate on intermediate oxygen pressures and substrate material variations to improve film quality. Incorporating dielectric spectroscopy and detailed phase transition studies would also provide deeper insights into the impact of deposition conditions on material properties.

The future direction of the investigation of deposition parameters might include these changes:

- Temperature: 600°C or marginally elevated (up to 700°C with careful consideration).

- Pressure: Evaluate intermediate pressures such as 0.15 mbar.

- Distance: A 55-75 mm range appears to be a favorable compromise for balancing crystallinity and surface quality.

- Fluence: A minor increase (approximately 1.8-2.1 J/cm²) is recommended to manage the chemical composition.

Evaluating these adjusted conditions and integrating the resulting XRD, SEM, and electrical measurements will help optimize the process for optimal dielectric properties.

4.3. Optimization of pulsed laser deposition parameters of ZrSnSe₃ thin films

Thin-film fabrication of SnZrSe₃ is crucial for enhancing the optoelectronic performance of photovoltaic applications. Thin films provide high absorption efficiency with minimal material usage, making them ideal for large-scale applications where material cost and sustainability are key concerns. Additionally, thin films enhance device performance by enabling precise control over thickness, uniformity, and interface quality, directly impacting the efficiency and stability of devices such as solar cells and infrared photodetectors.

The application of Pulsed Laser Deposition (PLD) for the fabrication of SnZrSe₃ thin films presents numerous significant benefits. Initially, PLD demonstrates strong compatibility with intricate materials such as chalcogenides, as it effectively preserves the stoichiometry of the target material in the deposited film. This preservation is essential for maintaining the distinct optoelectronic properties of SnZrSe₃. PLD enables meticulous regulation of film thickness at the nanometer level, a critical factor for adjusting the optical and electrical properties required for peak device performance. Furthermore, PLD functions within a regulated setting (typically a vacuum or a designated gas atmosphere), minimizing contamination risks and improving the film's purity and quality.

Moreover, PLD's adaptability to modifying deposition parameters (including fluency, frequency, and substrate temperature) enables the customization of the film's properties to satisfy application requirements, such as attaining the optimal bandgap alignment in multi-junction solar cells. The fabrication of high-quality, uniform, and stoichiometrically accurate thin films through PLD significantly improves the efficiency, stability, and scalability of SnZrSe₃-based devices, positioning it as a highly beneficial technique for advancing sustainable photovoltaic technology.

Initial condition

Initially, four targets of ZrSe₂, SnSe, SnZrSe₃ (and later, this target was modified with the addition of 40% ZrSe₂, so the overall composition was 40% ZrSe₂ + 60% SnZrSe₃) were used for deposition. ZrSe₂ and SnSe were purchased from Testbourne Ltd., and SnZrSe₃ was made using a solid-state reaction (starting elements Sn, Zr, Se) mixed in the ampoule and annealed at 700 °C for 48h. Then, crystals were ground into powder and cold-pressed under 100 MPa pressure into a pellet.

We used two approaches to create desired thin films:

1. Optimize deposition parameters of ZrSe_2 and SnSe targets to create a multilayer of these materials and anneal them into a single thin film.

2. Use a custom-made SnZrSe_3 target to create a thin film of such material in a single deposition.

The criteria for a good film would be:

1. Clean surface morphology without any droplets or structures.
2. Accurate Sn/Zr/Se ratio (Se concentration could be adjusted later by annealing in a Se-rich atmosphere)

3. Absent or minimal traces of oxygen and any other contamination. Contamination of oxygen is critical to any Ti, Zr-containing compounds. Since our target is not a single material, oxygen may be bound to Ti or Zr elements, and preventing oxide creation is critical. Selenides are not exactly very stable, so breaking them and forming Zr-oxides in the presence of oxygen is much easier.

Both approaches have pros and cons, so let's discuss them.

Optimization of ZrSe_2 deposition

Laser fluence

Since this material had never been made before by a Pulsed Laser Deposition system, we had to optimize the deposition parameters, including substrate temperature, ambient pressure, laser fluence, target-to-substrate distance, laser repetition rate, and spot size.

One of the first tests was made to find optimal fluence, a critical parameter in this system, due to the requirement for a precise ZrSn ratio. Another aspect is oxygen contamination. The $\text{SnZr}(\text{Se}, \text{O})_3$ alloy forms if oxygen is added to the lattice. Oxygen can't be easily removed afterward, and the bandgap would be greater than anticipated and required for further purposes. An argon atmosphere with ambient pressure was chosen for deposition to combat this issue.

Initial deposition parameters were chosen arbitrarily based on Dr. Rokas Kondratas' previous experience with the material.

Table 16. Deposition parameters for investigation of the effect of laser fluence for ZrSe₂.

Parameters/Samples	ZR01	ZR02	ZR03
Fluence, J/cm ²	1	0.63	0.3
Common parameters: T: ≈ 23 °C (here and further room temperature (RT)), P: 0.01 mbar Ar, T-S distance: 55 mm, f: 5 Hz			

Scanning electron microscopy images of these samples are presented in figure 4.43.

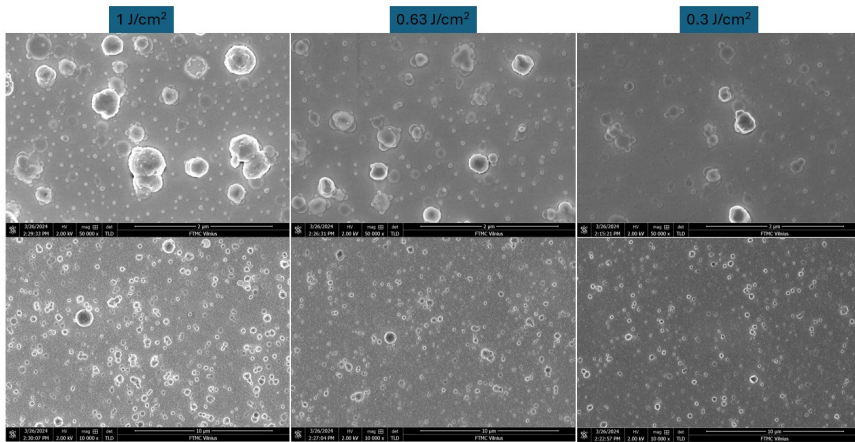


Figure 4.43. SEM images of ZrSe₂ samples that were made using different fluences.

One of the main problems — “boulders” — affects these films and prevents the growth of a uniform films. This is caused by high energy and prolonged beam interaction with the material, which produces shockwaves and creates particles simultaneously with our plasma (figure 2.29). We can also see that the number of particles on the surface is reduced together with the reduction of the fluence, so later, the fluence for the sample was chosen between 0.3 and 0.6 J/cm².

The Se/Zr ratio was not optimal (according to the chemical formula, the ideal ratio would be 2:1). Oxygen concentration was estimated

based on energy-dispersive X-ray analysis. It showed no traces of it, which is required for good film quality (table 17).

Table 17. Se/Zr ratio and oxygen percentage dependence on fluence.

Sample	Se/Zr ratio	Oxygen
ZR01, F: 1 J/cm ²	3.6	If present, minimal
ZR02, F: 0.63 J/cm ²	4.0	If present, minimal
ZR03, E: 0.3 J/cm ²	4.1	If present, minimal

Ambient pressure

To investigate the effect of the pressure on surface morphology, three samples were prepared at 0.3 J/cm² fluence with the following pressure: vacuum, 0.01 mbar, and 0.1 mbar, and presented in figure 4.44.

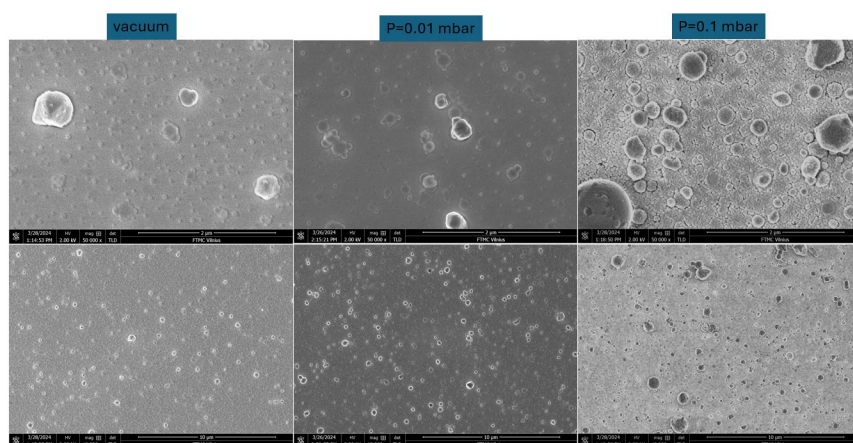


Figure 4.44. SEM images of the ZrSe₂ sample that were deposited under various pressures.

As we can see, in a vacuum, the film looks smooth, but a large abundance of small particles (~50 nm in diameter) appeared in the film. The film deposited at 0.1 mbar of argon pressure shows some big particles and increased porosity of the film, which is also an undesirable feature for our samples. The most optimal deposition pressure is around 0.01 mbar, with fewer small particles and almost no big particles. Also,

some particles have irregular, nonspherical shapes, which could indicate the Stranski–Krastanov (SK) film growth mode.

Substrate temperature

Figure 4.45 presents the effect of temperature on the morphology of the ZrSe_2 film. As we can see, increasing temperature helps to reduce the number of irregular particles, suppressing SK film growth mode by increasing surface energy (28). Also, further increasing the substrate temperature to 250 °C helps reduce the number and size of the particles.

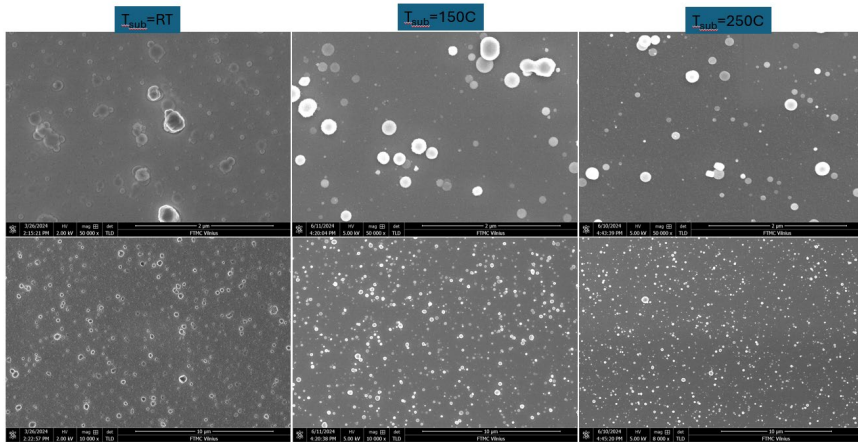


Figure 4.45. SEM images of the ZrSe_2 sample that were deposited under various substrate temperatures.

The temperature increase also positively affects the amount of oxygen contamination while driving the Se/Zr ratio off from its ideal point of 2.0.

Table 18. Se/Zr ratio and oxygen percentage dependence on temperature.

Sample	Se/Zr ratio	Oxygen
ZR06, $T_{\text{sub}} = \text{RT}$	2.0	~ 6%
ZR08, $T_{\text{sub}} = 150\text{ }^{\circ}\text{C}$	1.8	~ 1% / 0.7 %
ZR07, $T_{\text{sub}} = 250\text{ }^{\circ}\text{C}$	0.9	If present, minimal

Based on this analysis, we assume that a temperature of 150°C helps suppress particle issues without significantly affecting our Se/Zr ratio. Also, as we should have mentioned, the composition of the droplets deviates from a film composition, and these droplets are Zr-rich with an increased amount of oxygen. So, reducing the number of droplets would benefit both directions, reducing the amount of oxygen and bringing the Se/Zr ratio to optimal.

Target to substrate distance

To explore this deposition parameter, three samples were made from 55 mm (a default T-S distance) to 115 mm, which is near the maximum of our facility. The SEM images of the analysis of the morphology of these samples are presented in Figure 4.46.

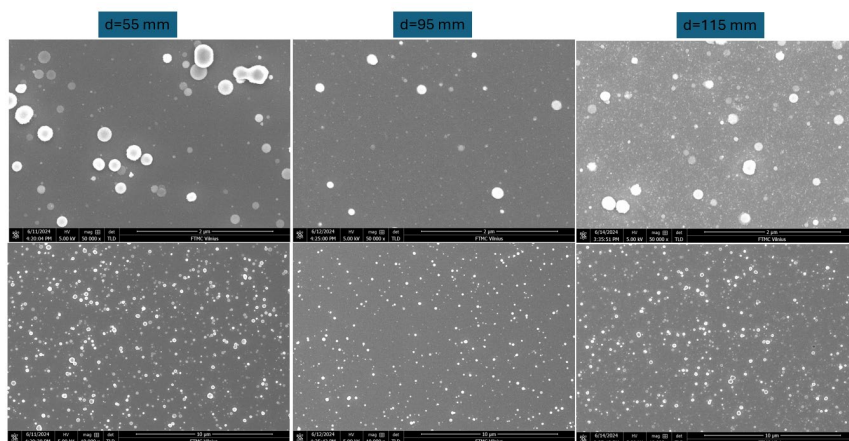


Figure 4.46. SEM images of ZrSe_2 samples that were deposited at various T-S distances.

As we can see from the figure, closer distances have the most significant number of particles and the largest particles from all the samples, which is logical since our nanosecond impulse laser may create many particles during the target's ablation. Distance 95 mm shows better performance with fewer particles. Still, surface roughness starts to increase, probably due to the lower energy of the incoming

material and less mobility of adatoms on top of the substrate. Distance 115 mm shows more unclear particles and increased roughness, as expected. Another aspect of particles is that they gather more oxygen than our film, so removing them would benefit the surface roughness and decrease oxygen contamination.

Table 19. Se/Zr ratio and oxygen percentage dependence on the target-to-substrate distance.

Sample	Se/Zr ratio	Oxygen
ZR08, d=55 mm	1.8/2.2/0.72	~1% / 0.7% [without droplets from the selected area] / 5% [on the droplet]
ZR09, d=95 mm	1.55/1.8	~0.65 / 0.56 [without droplets]
ZR10, d=115 mm	1.8/2.0	~1.1 / 0.9 [without droplets]

Sr/Zr ratio remains stable, and oxygen contamination was kept at a low level.

The thickness of the film was estimated based on a cross-section measurement of sample ZR10 and was around 65 nm, as shown in figure 4.47. The average deposition speed per pulse was estimated to be around 2.7 pm per pulse (24000 pulses and 65 nm thickness), so each pulse made less than a layer of material. Of course, all the parameters above significantly affect the deposition speed so that each sample would have a slightly different thickness based on a change in deposition parameters.

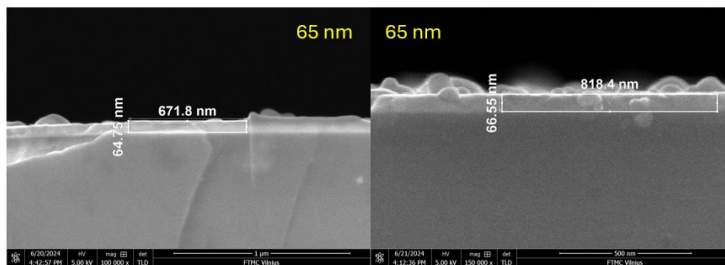


Figure 4.47. SEM image of the thickness measurement of ZrSe₂ film.

Pulse frequency

One possible parameter that could affect the deposition of the materials is the laser's repetition rate, which could be changed between 1 and 20 Hz (in our facility).

Two samples at 5 and 2 Hz were prepared and analyzed.

In short, no apparent effect of reducing the repetition rate was observed, except for slightly reducing the number of particles on the sample's surface (figure 4.48). This could be because laser interaction creates a shockwave that dissipates inside a target, so the next shockwave created by the beam could interact with the echoes of the previous one and make more particles.

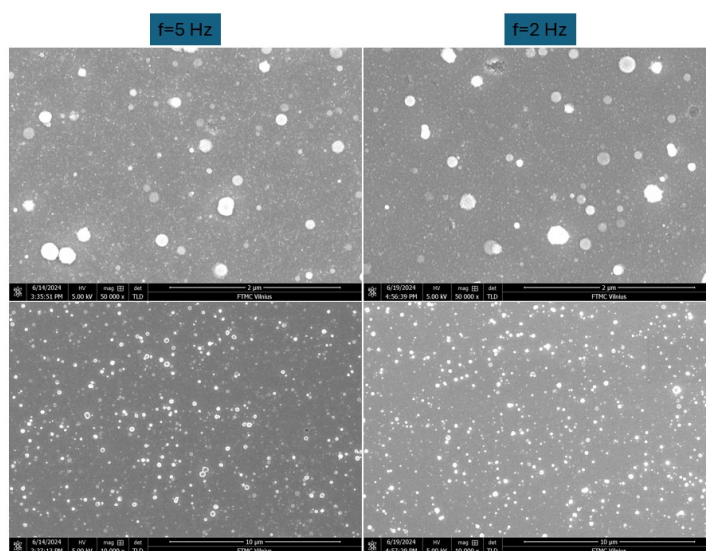


Figure 4.48. SEM images of $ZrSe_2$ samples that were deposited at various repetition rates.

Spot size

One of the important and rarely observed effects of the pulsed laser deposition is the spot size of the laser since the laser energy is usually described in the form of laser energy reading from the internal laser (which gives us no information about actual laser energy after all-

optical system and laser mask), laser energy measured before laser window or after a target (which is close to an exact value) or as a laser fluence, which is a correct way, but from this value it's hard to estimate a spot size without information about an energy that is delivered to the target.

SEM image of 2 samples, prepared at different spot sizes while maintaining the same fluence, is presented in figure 4.49.

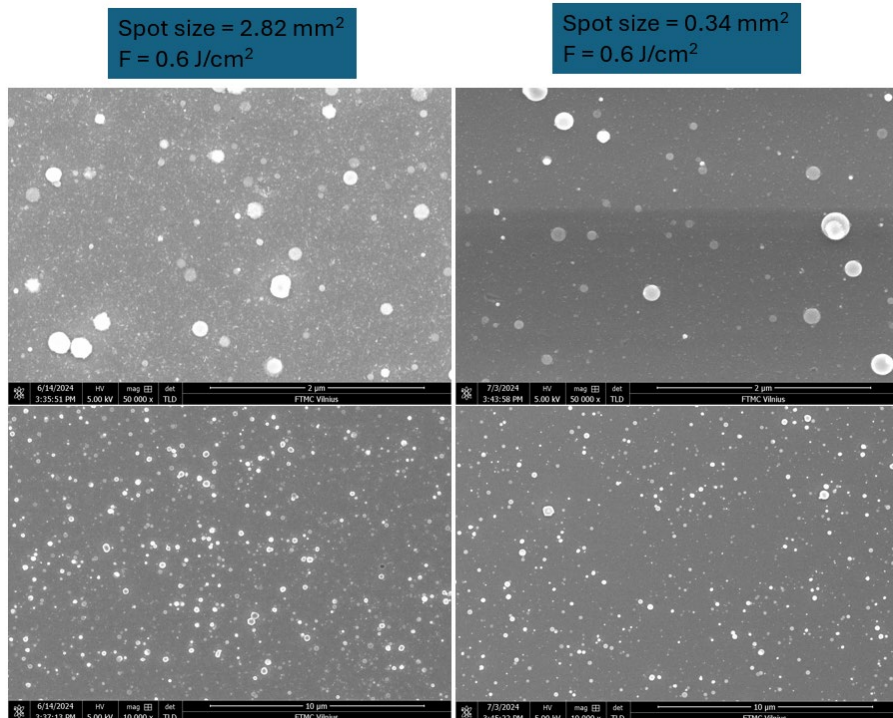


Figure 4.49. SEM images of $ZrSe_2$ samples that were deposited at various beam spot sizes.

As we can see, smaller spot sizes, while maintaining the same fluence, may promote a cleaner surface with fewer particles. This is probably connected to the size of the shockwave produced and the thickness of the film (which is smaller because smaller spot sizes generally produce less deposition material per pulse).

Table 20. Se/Zr ratio and oxygen percentage dependence on the spot size.

Sample	Se/Zr ratio	Oxygen
ZR12, SS=0.344	1.3/1.5	0.75 / 0.82 [without droplets]
ZR13, SS=2.82	1.75	~1.1

Optimization of deposition parameters of SnSe material

Laser fluence

Unlike a ZrSe₂ material, SnSe can be quickly produced without changing any parameters from a ZrSe deposition and shows an excellent morphology without particles. SEM images of the SnSe sample are shown in figure 4.50.

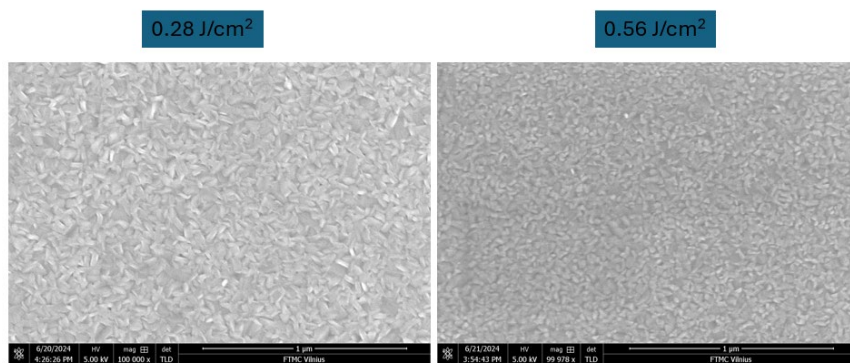


Figure 4.50. SEM images of SnSe samples deposited at various fluences.

Increase of fluence of the laser producing a more compact surface with fewer visible grains.

Optimization of deposition parameters for ZrSnSe₃ single target

In creating a ZrSnSe₃ film from ZrSe₂ and SnSe targets, we encountered a problem with a ZrSe₂ target. We cannot have a clear surface and correct stoichiometry simultaneously. To tackle this issue,

we tried using a single target of $ZrSnSe_3$ material made by a solid-state method. The result of parameter optimization is presented next.

Deposition pressure

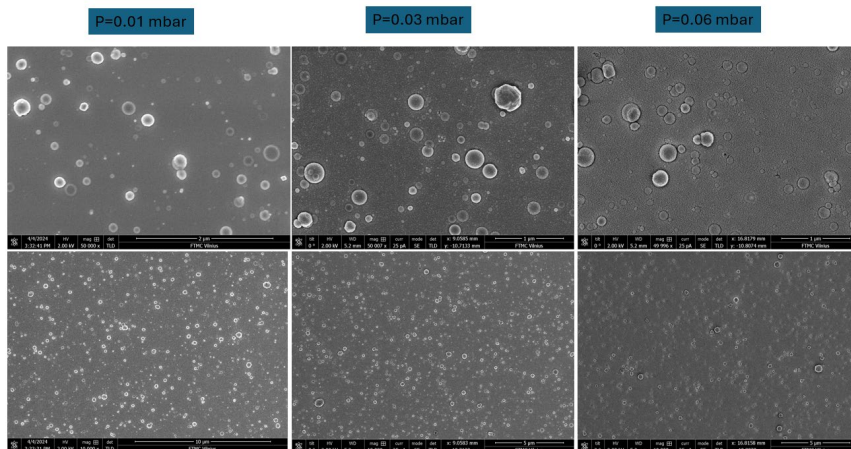


Figure 4.51. SEM images of $ZrSnSe_3$ thin film deposition from a single target.

As pressure has decreased from 0.06 mbar to 0.01 mbar, the surface roughness has reduced, as seen in figure 4.51. However, the overall number of particles has increased, so there is a tradeoff in decreasing pressure even in such a small range of values.

Table 21. Se/Zr ratio and oxygen percentage dependence on the argon pressure

Sample	Sn/Zr ratio	Oxygen, at%
TZS03, 1×10^{-2} mbar	2.5 / 1.5	If present, minimal
TZS01, 3×10^{-2} mbar	1.0	~14%
TZS02, 6×10^{-2} mbar	1.61	~36-48%

However, we chose to continue with the least pressure since increasing the argon pressure during deposition significantly increases the oxygen concentration in a film, which is a critical parameter for the film.

Laser fluence

During the optimization process of ZrSe_2 , we determined that the fluence should be in the range of $0.3 - 0.6 \text{ J/cm}^2$ since increasing to a higher value leads to even more significant amounts of particles and oxygen contamination.

Another path to investigate was to reduce further the laser fluence, which wasn't available during the previous deposition due to a facility limitation.

Figure 4.52 shows the effect of reducing fluence from 0.3 J/cm^2 to 0.1 J/cm^2 .

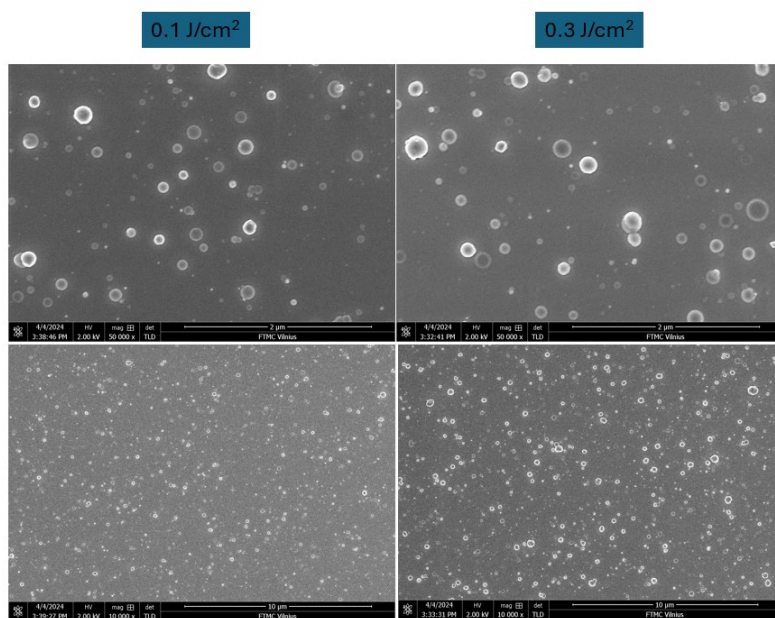


Figure 4.52. SEM images of ZrSnSe_3 samples deposited with a 0.1 J/cm^2 and 0.3 J/cm^2 fluence.

As we can see from the figure, no visible changes are observed; the surface roughness and number of particles are the same. But another problem is that such low fluence produces almost no plasma, and this film is extremely thin. So, no benefits of using even lower fluence were

observed, and our range of chosen fluence was confirmed from both sides.

Table 22. Se/Zr ratio and oxygen percentage dependence on the fluence.

Sample	Sn, at%	Zr, at%	Se, at%	Sn/Zr ratio	Oxygen, at%
TZS03, E=0.3 J/cm ²	8.5 / 1.7	3.4 / 1.1	15.5 / 3.34	2.5 / 1.5	If present, minimal
TZS04, E=0.1 J/cm ²	1.7	0.6	2.6	2.8	If present, minimal

This was also confirmed by EDX measurement. All element concentrations are deficient compared to a signal from a Si substrate. This issue also affects the precision of confirmation of the Sn/Zr ratio, so there are no benefits in any direction.

Target to substrate distance

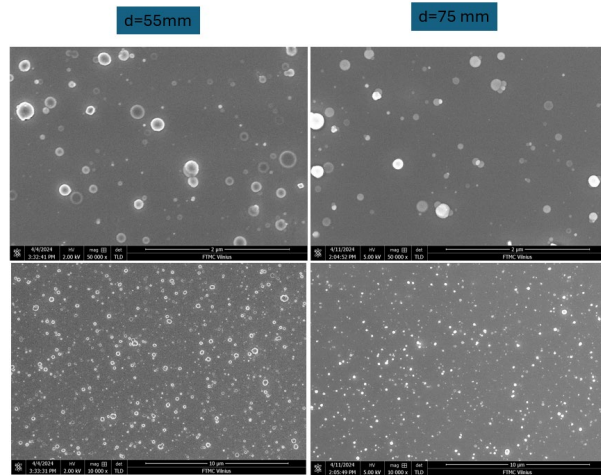


Figure 4.53. SEM image of ZrSnSe₃ films with different T-S distances.

As in the case of ZrSe₂, for ZrSnSe₃, we also see a beneficial effect of increasing the target-to-substrate distance with an observable

reduction of particles. The Sn/Zr ratio is the same, and oxygen contamination is minimal in both cases.

Substrate temperature

Figure 4.54 shows the SEM images of $ZrSnSe_3$ films deposited at different substrate temperatures. At 200 °C, surface roughness has increased, and SnSe composition starts to form, which is undesirable for our film. This is also confirmed at 300 °C, where we can see Zr-rich droplets and needle/pallet shapes on the surface, which is how a SnSe looks.

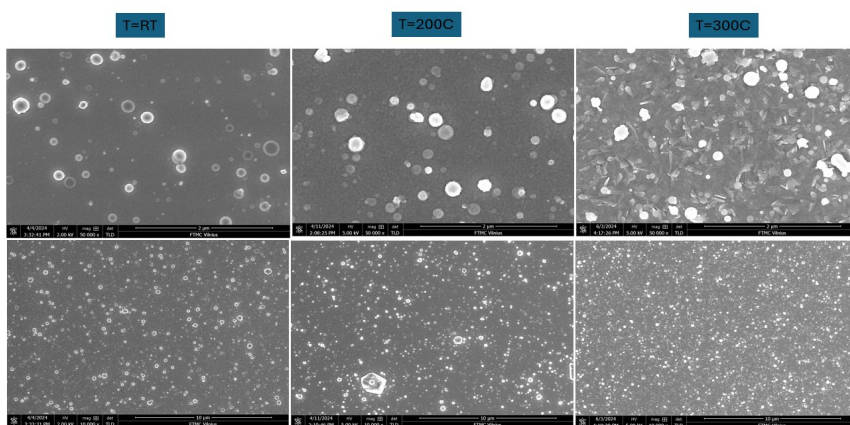


Figure 4.54. SEM images of $ZrSnSe_3$ deposited at various substrate temperatures.

Table 23. Se/Zr ratio and oxygen percentage dependence on the temperature.

Sample	Sn, at%	Zr, at%	Se, at%	Sn/Zr ratio	Oxygen, at%
TZS03, T=RT	8.5 / 1.7	3.4 / 1.1	15.5 / 3.34	2.5 / 1.5	If present, minimal
TZS06, T=200 °C	8.3 / 1.6	2.7 / 1.1	15.3 / 3.4	3.0 / 1.5	If present, minimal
TZS07, T=300 °C	1.3 / 0.3	0.8 / 0.3	1.7 / 0.4	1.6 / 1.0	~1%

Also, at such high temperatures as 300 °C, we see a significant reduction in thickness, which is observable by reduced atomic percentage in EDX measurements.

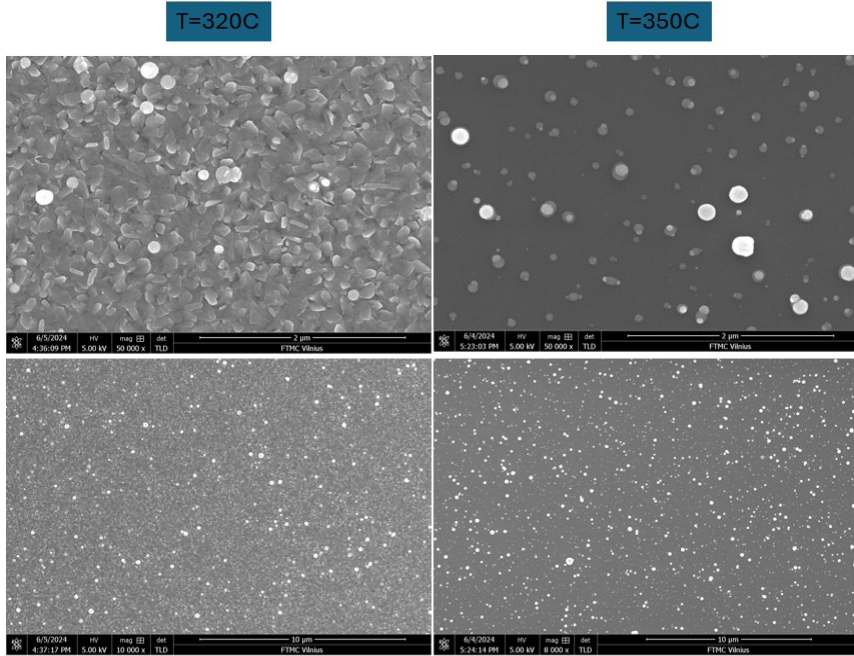


Figure 4.55. SEM images of $ZrSnSe_3$ deposited at various substrate temperatures.

Further temperature increases significantly reduce the thickness of the film as the surface's energy becomes so great that material coming to the surface is easily thermally removed from it.

Table 24. Se/Zr ratio and oxygen percentage dependence on the higher temperature.

Sample	Sn, at%	Zr, at%	Se, at%	Sn/Zr ratio	Oxygen, at%
TZS09, T=320 °C	1.10	0	1.16	N/A	If present, minimal
TZS08, T=350 °C	0	0.26	0.16	N/A	If present, minimal

This is also confirmed by EDX measurement, where film at 320 °C is extremely thin and looks like a SnSe (needle/plate shapes), while film at 350 °C loses all tin element and is probably just a ZrSe₂.

Based on this measurement, we can draw a projection showing how deposition parameters change our film and in which direction we should proceed.

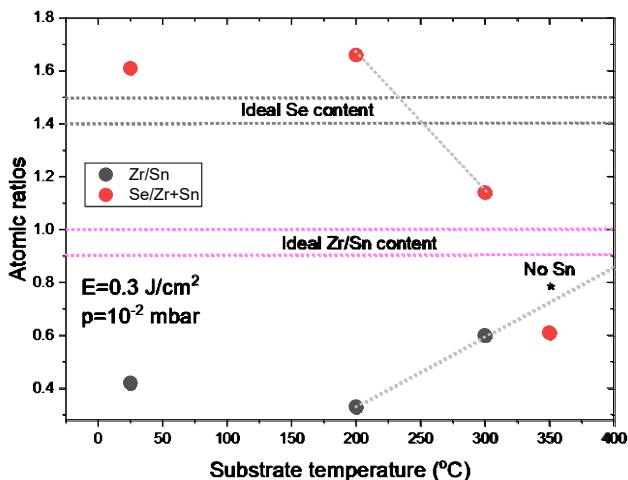


Figure 4.56. Dependence of atomic ration in ZrSnSe₃ samples from a deposition temperature.

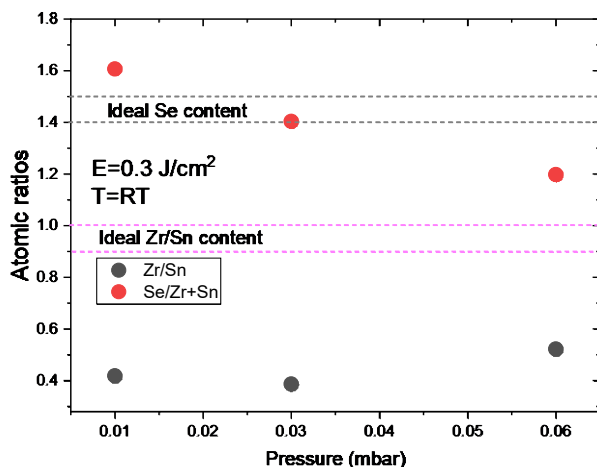


Figure 4.57. Dependence of atomic ration in ZrSnSe₃ samples from deposition pressure.

From this projection, we can see that the ideal ratio between Zr and Sn is unreachable for the current target, so another target with an additional excess of Zr must be prepared and used to achieve the ideal Zr/Sn ratio. This has also been done but hasn't brought any improvement.

Optimization of new ZrSnSe₃ target

To tackle the issue of nonstoichiometric growth from a single ZrSnSe₃ target, it was modified with the addition of 40% of ZrSe₂, so the overall composition was 40% ZrSe₂ + 60% SnZrSe₃. The deposition results from this target with the following deposition parameters are presented in Table 25.

Table 25. Se/Zr ratio and oxygen percentage dependency on temperature and fluence for new SnZrSe₃ target.

Sample composition	O, at %	Sn/Zr	Se/(Sn+Zr)	Si, at. %
TZS11, F=0.3 J/cm ² T _{sub} =200°C	none	7.5	1.20	94
TZS12, F=0.3 J/cm ² T _{sub} =250°C	none	6.5	1.07	94
TZS13, F=0.3 J/cm ² T _{sub} =300°C	~1.0	4.1	0.7	97
TZS14, F=0.5 J/cm ² T _{sub} =200°C	not clear, but some	2.7	1.60	30

As we can see, increasing the Zr content in a target still does not bring us to the desired element ratio, so this approach isn't beneficial.

4.3.1. Conclusion and future work.

ZrSnSe₃ thin films were successfully fabricated using pulsed laser deposition (PLD) with a custom-made solid-state target. Optimization

of the deposition parameters revealed several critical findings. The approach to making this film from a single target was unsuccessful. Zr and Sn components have different ionization values and can be deposited simultaneously with the proper stoichiometry (unless a tailored target is created). With particle sizes ranging from 50 to 100 nm, films produced at lower pressures showed higher particle density but decreased surface roughness. Higher substrate temperatures (above 300 °C) caused significant material loss and the formation of undesirable SnSe phases, as observed in SEM analysis. These findings demonstrate how carefully the deposition pressure and substrate temperature must be balanced to maintain the films' stoichiometry and structural integrity.

Future studies should focus on minimizing oxygen contamination and optimizing the Sn/Zr ratio to enhance film quality and performance for a future device. Investigating a stacked layer of ZrSe₂ and SnSe films and annealing it in an argon atmosphere to create a single ZrSnSe₃ film with the desired surface quality and stoichiometry may be a viable option for future research on the stoichiometry and homogeneity of the film.

4.4. Dielectric investigation of Nb-doped and pure 0.7(BiFeO₃)–0.3(BaTiO₃) ceramics.

The pure (0.7BiFeO₃–0.3BaTiO₃) and Nb-doped (0.7BiFe_{0.995}Nb_{0.005}O₃–0.3BaTiO₃) ceramics were created using the solid-state reaction method. This method is the earliest, most straightforward, and still predominant process for producing inorganic solids. It involves combining powdered reactants, potentially shaping them into pellets or other forms, and heating them in a furnace for extended durations. Solid-state reactions are inherently slow because they exhibit significant atomic inhomogeneity despite the reactants being thoroughly mixed at the particle level (e.g., on a size of 1 μm). To attain atomic-level mixing of reactants, it is essential to facilitate solid-state counter diffusion of ions among distinct particles to combine

atoms of various elements in the appropriate ratio to synthesize the desired product [170].

The powders used in the synthesis were Bi_2O_3 (99%), Fe_2O_3 (99%), BaCO_3 (99%), TiO_2 (99%), and Nb_2O_5 (99.99%) obtained from Sigma-Aldrich in Gillingham, UK. The powders were subjected to calcination at 800 °C for 4 hours. The choice of calcination temperature is essential, as changes in this temperature may alter the dielectric properties of the material. T. Zheng et al., in their work, show that a calcination temperature of 800 °C helps to reduce dielectric losses by 2 times [171].

Subsequently, the samples were sintered at 1010 °C for 3 hours. This process produced ceramic samples with a relative density of 95% [172]. Sintering temperature also similarly reduces dielectric losses, as a temperature higher than 950 °C helps to increase grain size [171].

The X-ray diffraction measurements revealed that these samples possess a perovskite structure with a single phase and rhombohedral R3c crystal symmetry [172]. Planar capacitor structures were created by applying silver contacts on both sides of the disk-shaped sample.

The dielectric spectra of the BF-BT ceramics were studied across a wide frequency range spanning from 20 Hz to 30 GHz, at temperatures ranging from 200 to 500 K. Three distinct dielectric measurement equipment were utilized to cover a broad spectrum of frequencies, and they are described in a previous section of this work (3. Measurement techniques).

Figure 4.58 displays the temperature variations of the complex dielectric permittivity's real and imaginary components for pure (undoped BF-BT) and Nb-doped (0.5Nb-BF-BT) BF-BT ceramics. Both cases show that the actual component of the material's properties changes with frequency and increases dramatically when heated from 200 K. There is a noticeable increase at 350 K, followed by a more steady rise before reaching the maximum dielectric value at the Curie point of 740 K [172]. This is also consistent with Curie temperature, which was measured in another sample with the same calcination temperature. A calcination temperature of 800 °C allowed us to reach the maximum Curie temperature compared to other possible calcination temperatures. The increase of the T_C may be associated with

compositional variations during calcination, particularly for the loss of Bi [171].

The imaginary part of permittivity for the Nb-doped ceramic exhibits a frequency-dependent maximum between 270 and 400 K. This maximum shifts towards higher temperatures as the frequency increases. It also correlates with the abnormal rise in rhombohedral distortion within this temperature range, as reported in the reference [172]. The undoped BF-BT also exhibited relaxing effects but to a lesser extent.

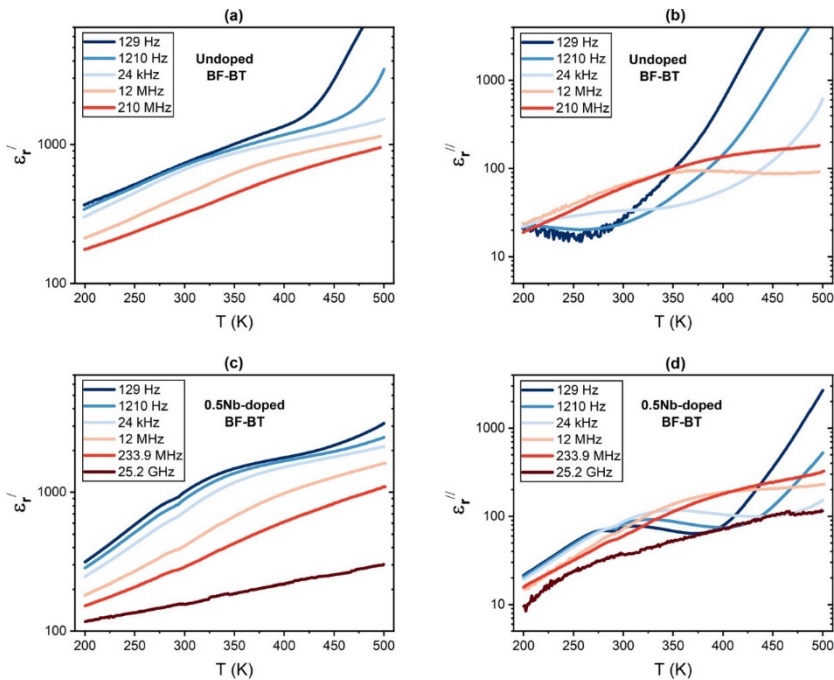


Figure 4.58. The temperature dependence of the real (ϵ_r') and imaginary (ϵ_r'') components of the complex dielectric permittivity of undoped (a)-(b) and 0.5Nb-doped $\text{BiFeO}_3\text{-BaTiO}_3$ (BF-BT) ceramics (c)-(d) was measured across a wide range of frequencies [75].

Thermally activated dielectric behavior is typically associated with disordered solids such as dipolar glasses or relaxor ferroelectric materials. These materials exhibit a wide range of relaxation periods due to polar nano regions (PNRs) or frustrated dipoles. The rapid

increase in the imaginary part of the dielectric constant (ϵ_r'') when the temperature is above 400 K, as illustrated in figures 4.58 (b) and (d), is caused by the growing conductivity (σ) due to the clear inverse relationship with frequency in this temperature range [173].

Unlike most relaxor ferroelectrics (RF), where the relaxor-type dielectric dispersion happens at greater temperatures compared to the phase transition to the ferroelectric state (if it happens), in this case, the ferroelectric phase occurs at a higher temperature than the RF state. As previously mentioned, the above sequence of transitions is typical of reentrant phenomena. It typically involves disrupting an organized state, resulting in a disorganized state, or the simultaneous presence of organized and disorganized states at varying scales [174]–[176]. Interpreting such behavior can be tricky since comparable types of dielectric dispersion may arise from several mechanisms, such as domain wall relaxation or charge accumulation at grain interfaces. However, the previous findings indicate that these impacts are linked to the disturbance of ferroelectric arrangement at lower temperatures, potentially caused by the migration of Bi^{3+} ions away from the polar axis [172], [177]–[179]. This investigation explicitly examines the dielectric relaxation in Nb-doped BF-BT ceramics, with a particularly noticeable relaxation intensity.

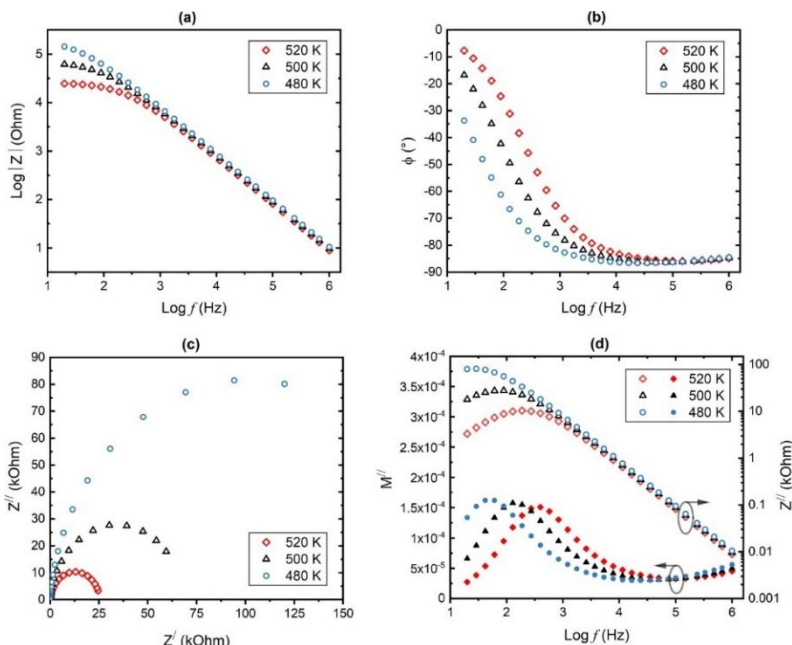


Figure 4.59. The impedance spectroscopy data for Nb-doped BF-BT ceramics is displayed in various forms to demonstrate the shift from a primarily capacitive ($f < -45^\circ$) to resistive ($f > -45^\circ$) electrical response at lower frequencies and elevated temperatures. The requested charts include (a) impedance magnitude and (b) phase angle bode plots, (c) complex impedance plots, and (d) bode plots for the imaginary parts of complex modulus and impedance [75].

When the temperature is high enough, and the frequency is low, the resistive component of the complex impedance, Z' , becomes more significant than the capacitive component, Z'' , and the phase angle, f , changes from -90° to closer to zero. These changes can be seen in figures 4.59 (a) and (b) of the Bode plots. The extrapolated interception of the semi-circular arc in figure 4.59 (c) corresponds to the resistance of the analogous circuit, represented by a parallel C-R network when it intersects with the real Z' axis. This resistance is inversely proportional to conductivity and dielectric loss. The relationship between temperature and electrical properties is clear: as temperature rises, resistance falls while conductivity and dielectric loss increase. The analogous circuit also includes bulk permittivity and conductivity,

which contribute to reduced resistance at higher temperatures due to the thermal activation of charge carriers [180]. The Bode plots for the imaginary parts of complex impedance and modulus, Z'' and M'' correspondingly (figure 4.59(d)), show peaks that align closely at the peak frequency, suggesting a high level of electrical uniformity [181].

Figure 4.60 displays the frequency-dependent complex permittivity data acquired at different temperatures, providing further insights into the dielectric relaxation characteristics. To analyze the dielectric spectra, we utilized an empirical Cole-Cole equation (24) [64] that was modified to incorporate the conduction contribution to losses at low frequencies/high temperatures [182]. This equation was used to model experimental complicated permittivity data and provide estimates of the dielectric parameter values. The fitting approach utilized the Levenberg–Marquardt algorithm, a nonlinear least square method. The OriginLab software was utilized to create these algorithms to fit the experimental data using the formula (24).

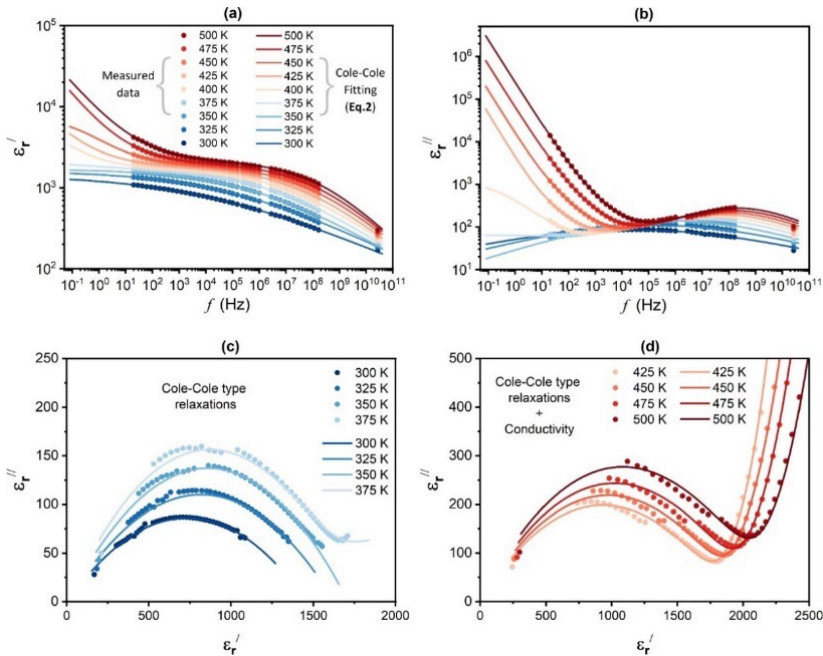


Figure 4.60. The frequency dependence of the real and imaginary components of the dielectric permittivity of 0.5Nb-BiFeO₃-BaTiO₃ ceramics at various temperatures are shown. The lines represent the

optimal matches of the experimental data points based on equation (24). The complex permittivity (Cole-Cole) graphs depict the thermally-activated conduction losses at both low (c) and high (d) temperature ranges [75].

The dielectric measurements measured between 300 and 350 K exhibit a single dispersion across the tested frequency range, as depicted in figures 4.60 (a) and (b). The dispersion becomes more pronounced at lower frequencies as the temperature decreases. However, it remains symmetrical and was modeled using equation (24) with a single relaxation process ($n = 1$). A single dielectric relaxation mechanism is also evident from the semi-circular shape observed in the Cole-Cole plot for the complicated permittivity, as depicted in figure 4.60(c). Between 350 K and 400 K, the dielectric dispersion curves show the emergence of an extra low-frequency lossy process, as depicted in figures 4.60 (b) and (d). This phenomenon is attributable to rising electrical conductivity, as mentioned before. At temperatures beyond 450 K, there is a slight rise in the fundamental part of the dielectric permittivity that occurs alongside the increasing dielectric losses. The observed phenomenon can be explained by the accumulation of localized electrical charges at the interfaces between grains and their movement at high temperatures, commonly referred to as Maxwell-Wagner relaxation [183].

At temperatures above 400 K, low and high-frequency dispersions remain present. The way they change with temperature follows a consistent pattern, and the same method may be used to analyze their frequency variations. However, a more meticulous examination revealed slight flaws in the alignment at the frequency range of 10^4 - 10^6 Hz (around the point of minimal dielectric losses). The most accurate alignments were achieved by incorporating a secondary Cole-Cole method. Due to the mild nature of this relaxation and its significant overlap with the high-frequency relaxation, it is not feasible to conduct a detailed analysis of the process. The calculated k values (1.001 at 500 K, 1.006 at 475 K, 1.012 at 450 K, and 1.069 at 425 K) were

consistently near 1, indicating that the conduction contribution to ϵ_r'' is the main factor at higher temperatures.

As previously mentioned, the high-frequency dispersion exhibits significant changes due to temperature, and we successfully determined the temperature dependence of the parameters associated with the Cole-Cole process (figure 4.61). The parameter α , which denotes the extent of the dielectric dispersion, exhibits a linear increase from around 0.68 at 500 K to 0.85 at 300 K. This indicates that the system shows a wide range of polar entities with varying relaxation durations, even at the highest temperature of 500 K. This figure exhibits a distinct deviation from Debye-type dispersion ($\alpha=0$), which is characterized by the presence of only one type of dipole and one relaxation time. Another parameter, $\Delta\epsilon$, exhibits an inverse relationship with temperature, in contrast to the parameter α . This indicates that the relaxation process diminishes overall dielectric permittivity as the temperature decreases.

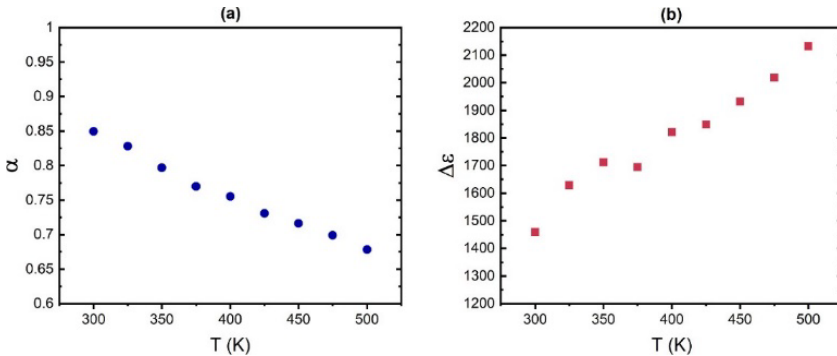


Figure 4.61. The temperature dependence of the dielectric dispersion parameter, α , and the strength of the relaxation, $\Delta\epsilon$, in 0.5Nb-BiFeO₃-BaTiO₃ ceramics.

The relationship between the mean relaxation time and the inverse temperature is demonstrated in figure 4.62. The presented data corresponds to fitting results obtained by approximating the frequency dependencies of the dielectric permittivity using the Cole-Cole formula, along with the Vogel-Fulcher-Tamman law (26). These laws are commonly used to describe the relaxation dynamics in inhomogeneous systems, such as relaxor ferroelectrics [184]. The Vogel-Fulcher-

Tamman relationship can be understood as a standard Debye relaxation characterized by a temperature-dependent activation energy. The activation energy grows as the temperature diminishes, reaching indeterminate near freezing. In the context of relaxors, a more practical interpretation of this relationship is that E_a stands for the activation energy for polarization fluctuations of an isolated cluster, with T_f serving as a measure of the interaction energy and the temperature dependence resulting from the formation of short-range order between nearby clusters. It is possible that dipole and dipole-induced dipole exchanges could be used to interact between the ferroelectric clusters. Additionally, the clusters might interact elastically through local rhombohedral distortions, which would suggest that they are superparaelastic above the freezing temperature and may freeze into an orientational glassy form [185].

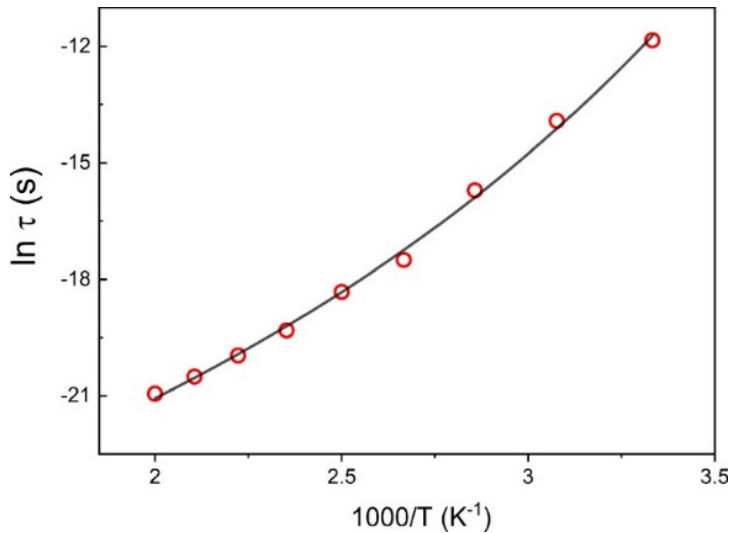


Figure 4.62. The mean relaxation time in $0.5\text{Nb-BiFeO}_3\text{-BaTiO}_3$ ceramics exhibits an inverse relationship with temperature.

The curve fitted to the experimental data strongly correlates with the following parameters: $\tau_0=1.73\times 10^{-12}$ s, $T_f=158\pm 16\text{K}$, and $E_a=0.194$ eV. Based on the acquired data, it is apparent that the average relaxation time grows as the temperature decreases and significantly diverges from the Arrhenius rule at a temperature of zero ($T_f=0$). Therefore, this

relaxation process has similarities to the relaxation processes observed in dipolar glasses or relaxor ferroelectrics, which are characterized by a wide range of relaxation periods [186]–[188]. The activation energy is within the normal range observed for these systems [187]. Compared to a pure BF-BT composition, Nb doping of BF-BT material greatly increases the activation energy of the material, showing that the long-range ordered dipole configuration is complex to develop under an electric field because of the weak contact between PNRs [189], [190].

4.4.1. Conclusion

The dielectric and ferroelectric properties of Nb-doped 0.7(BiFeO₃)-0.3(BaTiO₃) (BF-BT) ceramics were comprehensively analyzed, indicating the presence of a relaxation mechanism at low temperatures. A wide distribution of relaxation times was found using broadband dielectric spectroscopy, characterized by a noticeable deviation in the average relaxation time. The utilization of the empirical Cole-Cole relaxation model demonstrates a wide range of relaxation times, characterized by a noticeable deviation in the average relaxation time.

This mechanism is like the relaxor ferroelectric or dipolar glass relaxations and occurs in the temperature range of 250 to 500 K. The adherence to the Vogel-Fulcher-Tamman law is critical, as it exhibits a freezing temperature of 158 K and a corresponding activation energy of 0.194 eV. These values are in line with those observed in other relaxor ferroelectric materials.

It is important to note that this temperature range is significantly lower than the ferroelectric phase transition temperature of 740 K. The material's activation energy was changed by Nb doping, suggesting a higher energy barrier for dipole reorientation. This improvement indicates that Nb doping effectively suppresses leakage currents and stabilizes the ferroelectric phase. Furthermore, the dielectric response exhibited nonergodic relaxor behavior, characterized by a low-frequency dependence at low temperatures. The measured dielectric constant reached a maximum of 2500 at 1 kHz and 500 K, with a loss

tangent of 0.21, highlighting the material's potential for low-loss applications.

Future work should explore the effects of varying Nb doping levels on phase transition dynamics and dielectric performance. Combining dielectric spectroscopy with structural characterization techniques such as transmission electron microscopy (TEM) could provide further insights into the microstructural origins of the observed relaxor behavior.

4.5. Dielectric investigation of $\text{PbHf}_{1-x}\text{Sn}_x\text{O}_3$ material

$\text{PbHf}_{0.92}\text{Sn}_{0.08}\text{O}_3$ crystals were grown by a spontaneous crystallization technique at the Institute of Applied Physics MUT in Warsaw, Poland, as detailed in the reference [191]. The crystals were transparent and shaped like little cubes and rods. Using silver paste, electrodes were applied to the opposing faces of the crystals for dielectric measurements in bridge and coaxial systems.

The dielectric spectra of $\text{PbHf}_{0.92}\text{Sn}_{0.08}\text{O}_3$ (PHS) crystals were analyzed across a wide frequency range spanning from 20 Hz to 3 THz. The measurements were conducted at temperatures ranging from 300 K to 500 K. Four measuring facilities were used to cover this extensive frequency range:

The 20 Hz up to 12.5 GHz range was covered by method, explained in a (3. Measuring method section).

Time-domain THz spectroscopy was used to collect data within the frequency range of 200 GHz to 3 THz. Terahertz (THz) pulses were generated using a Ti: sapphire femtosecond laser and a commercially available large-area semiconductor interdigital emitter TeraSED (GigaOptics). The sample was affixed to a c-cut sapphire substrate to prevent breakage and then thinned to 16 micrometers. The object was inserted into a furnace equipped with optical ports, utilizing a transparent opening of 2 mm in diameter, and subjected to temperatures reaching up to 500 K. As the experiment was performed in transmission mode, a sapphire substrate without any additional layers was also tested up to a temperature of 500 K. This allowed for the assessment of the

permittivity of the sample. Further information regarding the experimental configuration and data computation can be found in References [192], [193].

Figure 4.63 illustrates the relationship between temperature and the complex permittivity of the PHS crystal. The temperature T_1 , which is 433 K during the cooling process, represents the point at which the transition between phases A2 and A1 occurs [194]. During the measurement, we notice the occurrence of temperature hysteresis, a characteristic trait of first-order phase transitions. Adding tin (Sn) ions to PbHfO_3 does not cause the intermediate (IM) phase formation. This could be because the tin concentration in our PHS ($\text{PbHf}_{1-x}\text{Sn}_x\text{O}_3$) compounds was below 6%, the minimum level required for the intermediate phase to form [194]. The transition from phase A2 to phase PE occurs at the critical temperature T_c , around 490 K. The fluctuations in the imaginary permittivity component at the critical temperature (T_c) can be ascribed to imperfections in the crystal structure, leading to increased losses at lower frequencies.

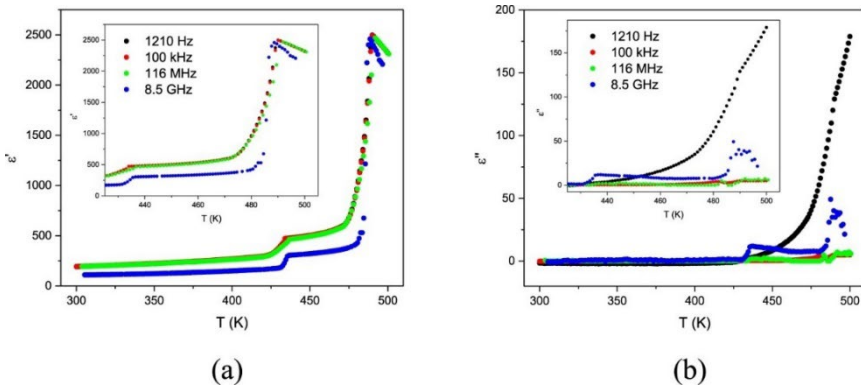


Figure 4.63. The temperature dependencies of the real (a) and imaginary (b) part of the complex permittivity of PHS crystals at various frequencies.

The frequency dependence of the complex permittivity (figures 4.64 and 4.65) exhibits three separate phenomena: low-frequency dispersion below 10^2 Hz, substantial loss of permittivity starting from 1 GHz, and small dispersion in the terahertz (THz) range. The latter process takes

place at temperatures over 450 K. As the Curie temperature approaches, the graph exhibits a maximum value in the imaginary component at a frequency of 8.5 GHz. The sharpness of this peak prevented it from being accurately described by classical equations that explain relaxation processes. By measuring the complex reflection coefficient R and the complex transmission coefficient of the dominant TE_{10} electromagnetic wave from the sample, we can calculate the possible values of ϵ' and ϵ'' that satisfy the relation between ϵ^* and R and T . This leads to multiple possible solutions for the inverse problem ϵ^* , μ^* (R , T) [151]. Consequently, the data obtained from the X-band waveguide measurement may only be correlated with the experiment's fitting.

To examine that peak, we can employ the resonance dispersion formula (23) by combining two fitted peaks: one in the gigahertz (GHz) range and another in the terahertz (THz) range. The peak frequency shifts from 20 to 100 GHz as the temperature increases from 470 to 500 K, but the damping reduces as the temperature approaches T_c .

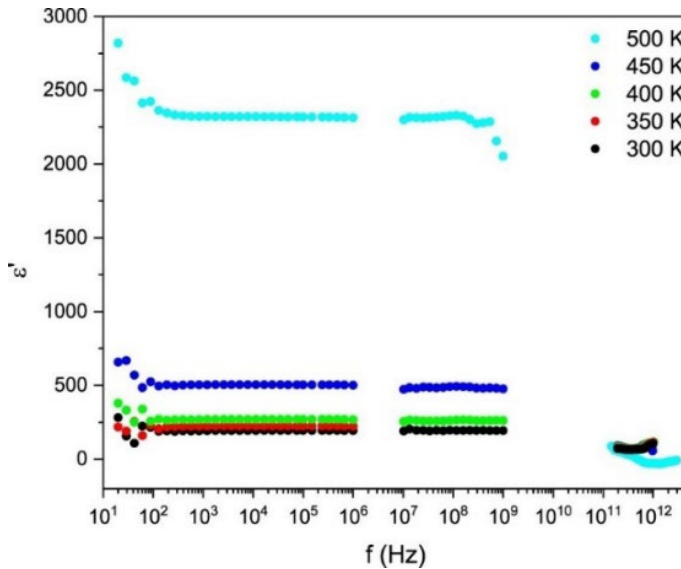


Figure 4.64. Frequency-dependent changes in the real component of the permittivity data of PHS ceramics at various temperatures.

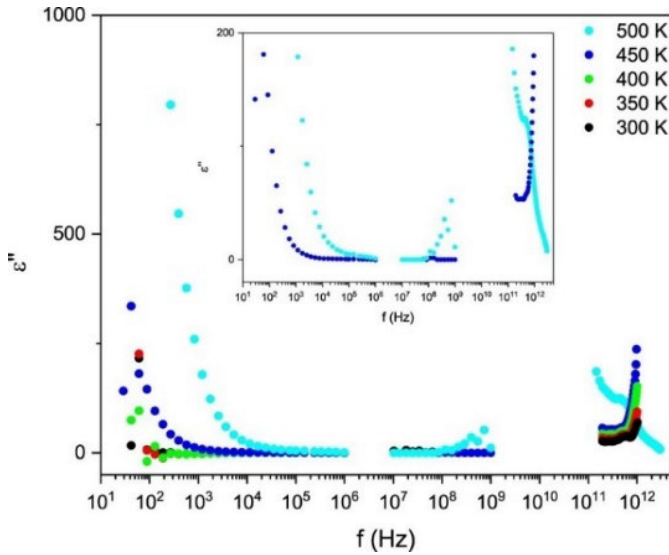


Figure 4.65. Frequency-dependent changes in the imaginary component of the permittivity data of PHS ceramics at various temperatures.

The first term in the equation's summation accounts for the increase in the imaginary component of the permittivity observed in the higher frequency range of our coaxial measurements (about 1 GHz) and the lower frequency range of our waveguide measurements (starting from 8.5 GHz). The second component of the equation represents a significantly smaller peak in the measurements' terahertz (THz) range [195].

Figure 4.66 displays the experimental findings, indicating that the PHS sample's primary variation in dielectric properties occurs within the 10-100 GHz range. This variation is characterized by a substantial increase in permittivity and a notable rise in losses at frequencies exceeding 1.2 THz. Moreover, the temperature dependence of permittivity at frequencies below the dispersion region matches the static permittivity behavior, indicating the absence of dispersion at lower frequencies. The results are comparable to the findings reported in another study involving $\text{AgTaO}_3\text{-AgNbO}_3$ solution [196].

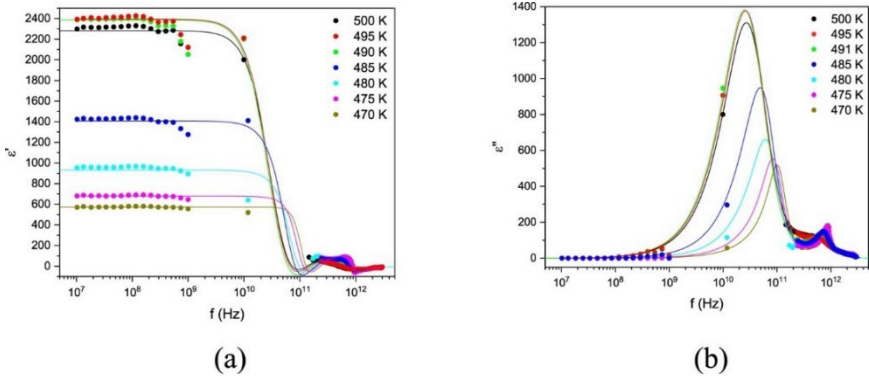


Figure 4.66. The frequency dependence of the real (a) and imaginary (b) parts of the permittivity data of PHS ceramics at high temperatures are shown. The lines represent the optimal alignment of the experimental data points according to formula (23).

Figure 4.67 displays the plotted relationship between temperature and the oscillator's frequency, representing the resonance dispersion peak around the phase transition temperature.

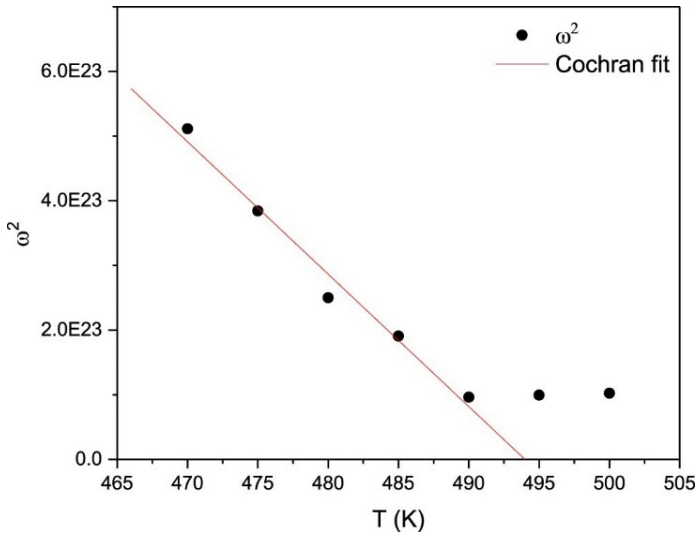


Figure 4.67. The soft mode's frequency dependence.

The soft mode in antiferroelectric materials exhibits a temperature-dependent softening behavior, as described by the Cochran law (11) [197].

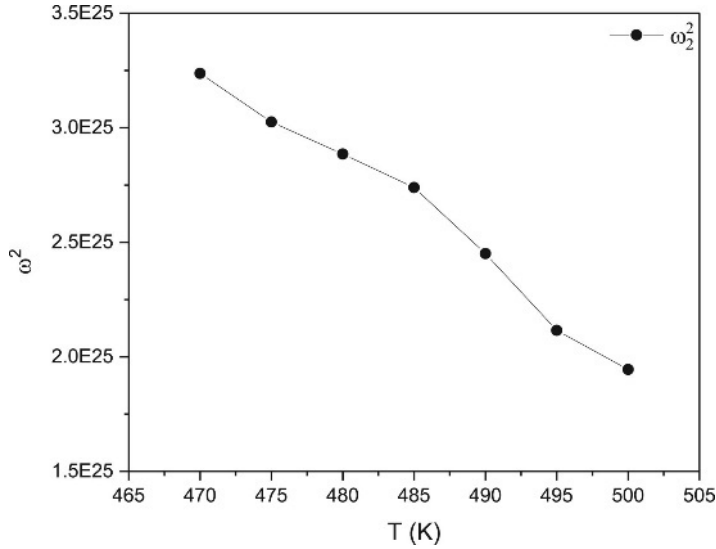


Figure 4.68. THz mode frequency dependence.

Figure 4.68 displays the relationship between temperature and the second mode's frequency, representing the resonance dispersion peak in the THz zone. This mode exhibits minimal deviations in temperature dependence at T_c within the reported temperature range.

4.5.1. Conclusion

$\text{PbHf}_{0.92}\text{Sn}_{0.08}\text{O}_3$ (PHS) crystals exhibited unique dielectric and structural properties, providing valuable insights into their phase transition dynamics. Broadband dielectric spectroscopy revealed a first-order phase transition near the Curie temperature of 494 K, accompanied by significant hysteresis effects. Resonance-type dispersion was observed, which can be attributed to the presence of a soft mode. The material maintains its structural integrity while displaying improved dielectric performance, as seen by the lack of intermediate phases at low Sn concentrations (<6%).

Previous studies using Raman scattering [194] And diffuse X-ray scattering [191]. We hypothesized the presence of at least two soft modes in PHS compounds with different levels of Sn. The low-

frequency soft mode has been associated with a disturbance in the Pb ion substructure. This condition causes changes in polar areas above the critical temperature, even at elevated temperatures. The current dielectric dispersion of the resonance type is likely associated with the low-frequency mode stated. Therefore, this behavior indicates that the transition from the paraelectric phase is primarily characterized by an order-disorder mechanism and influenced by dynamic polar regions. These regions transform ferroelectric fluctuations below the critical temperature, forming an intermediate phase. This phase is particularly evident in samples with higher concentrations of Sn [194].

5. SUMMARY

This thesis describes the experimental application of pulsed laser deposition to enhance the properties of these materials and a broadband dielectric investigation of various materials (films and bulk). The following conclusions are obtained:

1. Lead Zirconate Titanate ($\text{PbZr}_{0.2}\text{Ti}_{0.8}\text{O}_3$) thin films on strontium titanate (SrTiO_3) substrates demonstrate enhanced piezoelectric effect by 32% from bulk samples, highlighting the unique impact of nanoscale dimensions and strain effect.

2. The effect of deposition parameters of $0.8(\text{Na}_{0.5}\text{Bi}_{0.5}\text{TiO}_3)$ - $0.2(\text{BaTiO}_3)$ was investigated, and various methods confirmed the optimal quality of the films and showed good smoothness of the film with a stoichiometry close to our target material.

3. Thin films of ZrSnSe_3 were investigated with multitarget and single-target approaches. The effect of deposition parameters of thin films of ZrSe_2 was obtained and can be used to prepare multilayer structures to achieve the required quality of ZrSnSe_3 films.

4. The re-entrant relaxor behavior in a solid solution of bismuth ferrite and barium titanate (70% BiFeO_3 and 30% BaTiO_3) solid solutions show complex thermally induced transitions between ordered and disordered states, revealed through broadband dielectric spectroscopy over a wide frequency from 20 Hz to 20 GHz and temperature range 270 K to 400 K.

5. Lead Hafnate Tin ($\text{PbHf}_{0.92}\text{Sn}_{0.08}\text{O}_3$) crystals exhibit notable shifts in the dispersion peak and changes in the damping coefficient near the Curie temperature, which is 494 K, as identified through broadband dielectric spectroscopy and supported by the resonance dispersion model.

REFERENCES

- [1] Y. Sekine, R. Akiyoshi, and S. Hayami, "Recent advances in ferroelectric metal complexes," *Coord. Chem. Rev.*, vol. 469, p. 214663, 2022, doi: 10.1016/j.ccr.2022.214663.
- [2] D. Damjanovic, "Ferroelectric sensors," *IEEE Sens. J.*, vol. 1, no. 3, pp. 191–206, 2001, doi: 10.1109/JSEN.2001.954832.
- [3] A. R. Balakrishna, J. E. Huber, and C. M. Landis, "Nano-actuator concepts based on ferroelectric switching," *Smart Mater. Struct.*, vol. 23, no. 8, 2014, doi: 10.1088/0964-1726/23/8/085016.
- [4] R. S. Lous, "Ferroelectric Memory Devices, How to store the information of the future?," no. July, p. 23 pp, 2011, [Online]. Available:
<https://www.rug.nl/research/zernike/education/topmasternanoscience/ns190lous.pdf>
- [5] K. Yao, S. Chen, S. C. Lai, and Y. M. Yousry, "Enabling Distributed Intelligence with Ferroelectric Multifunctionalities," *Adv. Sci.*, vol. 9, no. 1, pp. 1–30, 2022, doi: 10.1002/advs.202103842.
- [6] M. De Graef and M. E. McHenry, *Structure of Materials: An Introduction to Crystallography, Diffraction and Symmetry*. Cambridge University Press, 2007. [Online]. Available: <https://books.google.lt/books?id=nJHSqEseuIUC>
- [7] S. Li, Y. Pan, W. Wang, and Y. Li, "CsPbX₃ (X = Cl, Br, I) perovskite quantum dots embedded in glasses: Recent advances and perspectives," *Chem. Eng. J.*, vol. 434, no. October 2021, p. 134593, 2022, doi: 10.1016/j.cej.2022.134593.
- [8] S. Yang *et al.*, "Large magnetostriction from morphotropic phase boundary in ferromagnets," *Phys. Rev. Lett.*, vol. 104, no. 19, 2010, doi: 10.1103/PhysRevLett.104.197201.
- [9] I. Jankowska-Sumara, A. Majchrowski, and J. Žmija, "Electrical, thermal, and dielectric properties of PbZr_{1-x}Sn_xO₃ (0 ≤ x ≤ 0.3) single crystals," *J. Mater. Sci.*, vol. 44, no. 12, pp. 3229–3234, 2009, doi: 10.1007/s10853-009-3432-9.
- [10] A. J. Haider, T. Alawsi, M. J. Haider, B. A. Taha, and H. A.

- Marhoon, “A comprehensive review on pulsed laser deposition technique to effective nanostructure production: trends and challenges,” *Opt. Quantum Electron.*, vol. 54, no. 8, pp. 1–25, 2022, doi: 10.1007/s11082-022-03786-6.
- [11] L. W. Martin and A. M. Rappe, “Thin-film ferroelectric materials and their applications,” *Nat. Rev. Mater.*, vol. 2, no. 2, 2016, doi: 10.1038/natrevmats.2016.87.
- [12] J. D. S. Guerra, R. J. Portugal, A. C. Silva, R. Guo, and A. S. Bhalla, “Investigation of the conduction processes in PZT-based multiferroics: Analysis from Jonscher’s formalism,” *Phys. Status Solidi Basic Res.*, vol. 251, no. 5, pp. 1020–1027, 2014, doi: 10.1002/pssb.201350336.
- [13] S. S. Das, Z. Fox, M. D. Mia, B. C. Samuels, R. Saha, and R. Droopad, “Demonstration of ferroelectricity in PLD grown HfO₂-ZrO₂ nanolaminates,” *AIMS Mater. Sci.*, vol. 10, no. 2, pp. 342–355, 2023, doi: 10.3934/matensci.2023018.
- [14] P. Kumari, R. Rai, S. Sharma, M. Shandilya, and A. Tiwari, “State-of-the-art of lead free ferroelectrics: A critical review,” *Adv. Mater. Lett.*, vol. 6, no. 6, pp. 453–484, 2015, doi: 10.5185/amlett.2015.4086.
- [15] S. Bogaert, M. van Acoleyen, I. van Tomme, L. De Smet, D. Fleet, and R. Salado, “Study on RoHS and WEEE Directives European Commission DG Enterprise and Industry,” p. 320, 2008, [Online]. Available: http://ec.europa.eu/environment/waste/weee/pdf/rpa_study.pdf
- [16] Y. Saito *et al.*, “Lead-free piezoceramics,” *Nature*, vol. 432, no. 7013, pp. 84–87, 2004, doi: 10.1038/nature03028.
- [17] J. Wu, “Perovskite lead-free piezoelectric ceramics,” *J. Appl. Phys.*, vol. 127, no. 19, 2020, doi: 10.1063/5.0006261.
- [18] Z. Li *et al.*, “A Brief Review of Sodium Bismuth Titanate-Based Lead-Free Materials for Energy Storage: Solid Solution Modification, Metal/metallic Oxide Doping, Defect Engineering and Process Optimizing,” *Crystals*, vol. 13, no. 2, 2023, doi: 10.3390/cryst13020295.
- [19] H. W. Cheng *et al.*, “Combinatorial studies of (1-

- x)Na_{0.5}Bi_{0.5}TiO₃-xBaTiO₃ thin-film chips,” *Appl. Phys. Lett.*, vol. 85, no. 12, pp. 2319–2321, 2004, doi: 10.1063/1.1794352.
- [20] G. Catalan and J. F. Scott, “Physics and applications of bismuth ferrite,” *Advanced Materials*, vol. 21, no. 24, pp. 2463–2485, 2009. doi: 10.1002/adma.200802849.
- [21] T. Rojac *et al.*, “BiFeO₃ Ceramics: Processing, Electrical, and Electromechanical Properties,” *J. Am. Ceram. Soc.*, vol. 97, no. 7, pp. 1993–2011, Jul. 2014, doi: 10.1111/jace.12982.
- [22] I. Calisir and D. A. Hall, “Chemical heterogeneity and approaches to its control in BiFeO₃-BaTiO₃ lead-free ferroelectrics,” *J. Mater. Chem. C*, vol. 6, no. 1, pp. 134–146, 2017, doi: 10.1039/c7tc04122e.
- [23] P. Chaudhary, R. Shukla, S. Dabas, and O. P. Thakur, “Enhancement of structural, magnetic, dielectric, and transport properties of Nb substituted 0.7BiFeO₃-0.3BaTiO₃ solid solution,” *J. Alloys Compd.*, vol. 869, p. 159228, 2021, doi: <https://doi.org/10.1016/j.jallcom.2021.159228>.
- [24] R. Kondrotas *et al.*, “Band gap engineering by cationic substitution in Sn(Zr_{1-x}Ti_x)Se₃ alloy for bottom sub-cell application in solar cells,” *J. Mater. Chem. A*, vol. 11, no. 48, pp. 26488–26498, 2023, doi: 10.1039/d3ta05550g.
- [25] R. Kondrotas *et al.*, “Synthesis and physical characteristics of narrow bandgap chalcogenide SnZrSe₃,” *Open Res. Eur.*, vol. 2, pp. 1–26, 2023, doi: 10.12688/openreseurope.15168.2.
- [26] L. E. Cross and R. E. Newnham, “History of Ferroelectrics,” *Ceram. Civiliz.*, vol. III, pp. 289–305, 1987.
- [27] A. S. Amar S Bhalla, “Ferroelectricity: 100 years on – Physics World.” <https://physicsworld.com/a/ferroelectricity-100-years-on/> (accessed Jul. 12, 2024).
- [28] N. Izyumskaya, Y. Alivov, and H. Morkoç, “Oxides, oxides, and more oxides: High-oxides, ferroelectrics, ferromagnetics, and multiferroics,” *Crit. Rev. Solid State Mater. Sci.*, vol. 34, no. 3–4, pp. 89–179, 2009, doi: 10.1080/10408430903368401.
- [29] N. W. Ashcroft and N. D. Mermin, *Solid State Physics*. Cengage Learning, 2011. [Online]. Available:

- https://books.google.lt/books?id=x_s_YAAACAAJ
- [30] Z. Liu, H. Wu, W. Ren, and Z. G. Ye, *Piezoelectric and ferroelectric materials: Fundamentals, recent progress, and applications*, vol. 1–10. Elsevier, 2023. doi: 10.1016/B978-0-12-823144-9.00069-8.
- [31] K. Aizu, “Possible Species of ‘Ferroelastic’ Crystals and of Simultaneously Ferroelectric and Ferroelastic Crystals,” *Journal of the Physical Society of Japan*, vol. 27, no. 2. pp. 387–396, 1969. doi: 10.1143/JPSJ.27.387.
- [32] B. B. Van Aken, J. P. Rivera, H. Schmid, and M. Fiebig, “Observation of ferrotoroidic domains,” *Nature*, vol. 449, no. 7163, pp. 702–705, 2007, doi: 10.1038/nature06139.
- [33] J. C. Charles Kittel, *Introduction to solid state physics*, vol. 6, no. 1. 1957. doi: 10.1016/0022-5096(57)90051-0.
- [34] R. W. Whatmore, “Piezoelectric and Pyroelectric Materials and Their Applications BT - Electronic Materials: From Silicon to Organics,” L. S. Miller and J. B. Mullin, Eds. Boston, MA: Springer US, 1991, pp. 283–290. doi: 10.1007/978-1-4615-3818-9_19.
- [35] D. J. Griffiths, *Introduction To Electrodynamics 4Th Edition*. 1981.
- [36] S. W. Ellingson, *Electromagnetics*, vol. 2. Blacksburg: VA: Virginia Tech Publishing, 2020. doi: 10.21061/electromagnetics-vol-2.
- [37] P. Hofmann, *Solid State Physics: An Introduction*. Wiley, 2015. [Online]. Available: <https://books.google.lt/books?id=SUcxBwAAQBAJ>
- [38] Y. P. Kalmykov, W. T. Coffey, D. S. F. Crothers, and S. V. Titov, “Microscopic models for dielectric relaxation in disordered systems,” *Phys. Rev. E - Stat. Physics, Plasmas, Fluids, Relat. Interdiscip. Top.*, vol. 70, no. 4, p. 11, 2004, doi: 10.1103/PhysRevE.70.041103.
- [39] S. Roberts, “Dielectric and piezoelectric properties of barium titanate,” *Phys. Rev.*, vol. 71, no. 12, pp. 890–895, 1947, doi: 10.1103/PhysRev.71.890.

- [40] M. Yashima *et al.*, “Size effect on the crystal structure of barium titanate nanoparticles,” *J. Appl. Phys.*, vol. 98, no. 1, 2005, doi: 10.1063/1.1935132.
- [41] W. Cochran, “Crystal stability and the theory of ferroelectricity,” *Adv. Phys.*, vol. 9, no. 36, pp. 387–423, 1960, doi: 10.1080/00018736000101229.
- [42] M. E. Lines and A. M. Glass, *Principles and Applications of Ferroelectrics and Related Materials*. OUP Oxford, 2001. [Online]. Available: <https://books.google.lt/books?id=p6ruJH8C84kC>
- [43] L. K. Pradhan and M. Kar, “Relaxor Ferroelectric Oxides: Concept to Applications,” in *Multifunctional Ferroelectric Materials*, D. R. Sahu, Ed. Rijeka: IntechOpen, 2021. doi: 10.5772/intechopen.96185.
- [44] C. W. Ahn *et al.*, “A brief review on relaxor ferroelectrics and selected issues in lead-free relaxors,” *J. Korean Phys. Soc.*, vol. 68, no. 12, pp. 1481–1494, 2016, doi: 10.3938/jkps.68.1481.
- [45] A. A. Bokov and Z. G. Ye, *Reentrant phenomena in relaxors*, no. March 2016. 2016. doi: 10.1002/9781118935743.ch23.
- [46] G. A. Smolenskii and A. I. Agranovskaya, “DIELECTRIC POLARIZATION AND LOSSES OF SOME COMPLEX COMPOUNDS,” *Zhur. Tekh. Fiz.*, vol. 28, 1958.
- [47] P. Wawrzęta and J. Korzekwa, “PLZT type ceramics as a material for applications in power pulse capacitors,” *Proc. 2012 21st IEEE Int. Symp. Appl. Ferroelectr. held jointly with 11th IEEE Eur. Conf. Appl. Polar Dielectr. IEEE PFM, ISAF/ECAPD/PFM 2012*, pp. 1–4, 2012, doi: 10.1109/ISAF.2012.6297840.
- [48] V. Bobnar, H. Uršič, G. Casar, and S. Drnovšek, “Distinctive contributions to dielectric response of relaxor ferroelectric lead scandium niobate ceramic system,” *Phys. Status Solidi Basic Res.*, vol. 250, no. 10, pp. 2232–2236, 2013, doi: 10.1002/pssb.201349259.
- [49] M. H. Zhang *et al.*, “Electric-field-induced antiferroelectric to ferroelectric phase transition in polycrystalline NaNbO₃,” *Acta Mater.*, vol. 200, pp. 127–135, 2020, doi:

- 10.1016/j.actamat.2020.09.002.
- [50] A. Jain, Y. G. Wang, and L. N. Shi, “Recent developments in BaTiO₃ based lead-free materials for energy storage applications,” *J. Alloys Compd.*, vol. 928, p. 167066, 2022, doi: 10.1016/j.jallcom.2022.167066.
- [51] R. Pirc, B. Rožič, J. Koruza, G. Cordoyiannis, B. Malič, and Z. Kutnjak, “Anomalous dielectric and thermal properties of Ba-doped PbZrO₃ ceramics,” *J. Phys. Condens. Matter*, vol. 27, no. 45, 2015, doi: 10.1088/0953-8984/27/45/455902.
- [52] I. Jankowska-Sumara, M. Paściak, M. Kądziołka-Gaweł, M. Podgórna, A. Majchrowski, and K. Roleder, “Local properties and phase transitions in Sn doped antiferroelectric PbHfO₃ single crystal,” *J. Phys. Condens. Matter*, vol. 32, no. 43, 2020, doi: 10.1088/1361-648X/ab9bca.
- [53] A. K. Tagantsev *et al.*, “The origin of antiferroelectricity in PbZrO₃,” *Nat. Commun.*, vol. 4, 2013, doi: 10.1038/ncomms3229.
- [54] B. Xu, N. G. Pai, and L. E. Cross, “Lanthanum doped lead zirconate titanate stannate antiferroelectric thin films from acetic acid-based sol-gel method,” *Mater. Lett.*, vol. 34, no. 3–6, pp. 157–160, 1998, doi: 10.1016/S0167-577X(97)00165-1.
- [55] M. H. Zhang, L. Fulanović, C. Zhao, and J. Koruza, “Review on field-induced phase transitions in lead-free NaNbO₃-based antiferroelectric perovskite oxides for energy storage,” *J. Mater.*, vol. 9, no. 1, pp. 1–18, 2023, doi: 10.1016/j.jmat.2022.09.008.
- [56] J. J. Wang, B. Wang, and L. Q. Chen, “Understanding, Predicting, and Designing Ferroelectric Domain Structures and Switching Guided by the Phase-Field Method,” *Annu. Rev. Mater. Res.*, vol. 49, pp. 127–152, 2019, doi: 10.1146/annurev-matsci-070218-121843.
- [57] Y. C. Shu and K. Bhattacharya, *Domain patterns and macroscopic behaviour of ferroelectric materials*, vol. 81, no. 12. 2001. doi: 10.1080/13642810108208556.
- [58] P. R. Potnis, N. T. Tsou, and J. E. Huber, “A review of domain modelling and domain imaging techniques in ferroelectric

- crystals,” *Materials (Basel)*, vol. 4, no. 2, pp. 417–447, 2010, doi: 10.3390/ma4020417.
- [59] J. Nordlander *et al.*, “Ferroelectric domain architecture and poling of BaTiO₃ on Si,” *Phys. Rev. Mater.*, vol. 4, no. 3, 2020, doi: 10.1103/PhysRevMaterials.4.034406.
- [60] Y. L. Li, S. Y. Hu, and L. Q. Chen, “Ferroelectric domain morphologies of (001) PbZr_{1-x}Ti_xO₃ epitaxial thin films,” *J. Appl. Phys.*, vol. 97, no. 3, 2005, doi: 10.1063/1.1849820.
- [61] P. Debye, “Über die intensitätsverteilung in den mit röntgenstrahlen erzeugten interferenzbildern,” *Verhandlungen Der Dtsch. Phys. Gesellschaft*, vol. 15, pp. 738–752, 1913.
- [62] J. A. Huisman, W. Bouten, J. A. Vrugt, and P. A. Ferré, “Accuracy of frequency domain analysis scenarios for the determination of complex dielectric permittivity,” *Water Resour. Res.*, vol. 40, no. 2, 2004, doi: 10.1029/2002WR001601.
- [63] W. L. Lai, T. Kind, and H. Wiggenhauser, “A study of concrete hydration and dielectric relaxation mechanism using ground penetrating radar and short-time Fourier transform,” *EURASIP J. Adv. Signal Process.*, vol. 2010, no. December 2010, 2010, doi: 10.1155/2010/317216.
- [64] K. S. Cole and R. H. Cole, “Dispersion and Absorption in Dielectrics I. Alternating Current Characteristics,” *J. Chem. Phys.*, vol. 9, no. 4, pp. 341–351, Apr. 1941, doi: 10.1063/1.1750906.
- [65] M. Grimau and E. Laredo, “Distribution of relaxation times from dielectric spectroscopy using monte carlo simulated annealing: application to (formula presented),” *Phys. Rev. B - Condens. Matter Mater. Phys.*, vol. 60, no. 18, pp. 12764–12774, 1999, doi: 10.1103/PhysRevB.60.12764.
- [66] V. Compañ, R. Díaz-Calleja, J. Díaz Boils, and J. Escorihuela, “Distribution of Relaxation Times: Debye Length Distribution versus Electrode Polarization by a Cole–Cole Relaxation Model,” *J. Electrochem. Soc.*, vol. 169, Jan. 2022, doi: 10.1149/1945-7111/ac4bf9.
- [67] H. Wang, L. Yang, X. Zhang, and M. H. Ang, “Permittivity, loss

- factor and Cole-Cole model of acrylic materials for dielectric elastomers,” *Results Phys.*, vol. 29, no. August, p. 104781, 2021, doi: 10.1016/j.rinp.2021.104781.
- [68] D. Viehland, S. Jang, L. Eric Cross, and M. Wuttig, “The dielectric relaxation of lead magnesium niobate relaxor ferroelectrics,” *Philos. Mag. B Phys. Condens. Matter; Stat. Mech. Electron. Opt. Magn. Prop.*, vol. 64, no. 3, pp. 335–344, 1991, doi: 10.1080/13642819108207624.
- [69] G. Bator and R. Jakubas, “Dielectric Dispersion in Ferroelectrics $[\text{NH}_2(\text{CH}_3)_2]_3\text{Sb}_2\text{Cl}_9$ and $[\text{NH}_2(\text{CH}_3)_2]_3\text{Sb}_2\text{Br}_9$,” *Phys. Status Solidi*, vol. 147, no. 2, pp. 591–600, 1995, doi: 10.1002/pssa.2211470230.
- [70] D. W. Davidson and R. H. Cole, “Dielectric Relaxation in Glycerine,” *J. Chem. Phys.*, vol. 18, no. 10, p. 1417, Oct. 1950, doi: 10.1063/1.1747496.
- [71] S. Havriliak and S. Negami, “A complex plane representation of dielectric and mechanical relaxation processes in some polymers,” *Polymer (Guildf.)*, vol. 8, pp. 161–210, 1967, doi: [https://doi.org/10.1016/0032-3861\(67\)90021-3](https://doi.org/10.1016/0032-3861(67)90021-3).
- [72] S. Havriliak and S. Negami, “A complex plane analysis of α -dispersions in some polymer systems,” *J. Polym. Sci. Part C Polym. Symp.*, vol. 14, pp. 99–117, Mar. 2007, doi: 10.1002/polc.5070140111.
- [73] B. A. Strukov and A. P. Levanyuk, *Ferroelectric Phenomena in Crystals: Physical Foundations*. Springer Berlin Heidelberg, 1998. [Online]. Available: <https://books.google.lt/books?id=P7PvAAAAMAAJ>
- [74] S. Kamba, “Soft-mode spectroscopy of ferroelectrics and multiferroics: A review,” *APL Mater.*, vol. 9, no. 2, 2021, doi: 10.1063/5.0036066.
- [75] V. Haronin, Z. Yang, R. Grigalaitis, I. Calisir, J. Banys, and D. A. Hall, “Broadband dielectric spectroscopy of Nb-doped $0.7\text{BiFeO}_3\text{-}0.3\text{BaTiO}_3$ ceramics,” *J. Phys. Commun.*, vol. 8, no. 6, pp. 0–8, 2024, doi: 10.1088/2399-6528/ad55a2.
- [76] F. Alvarez, A. Alegria, and J. Colmenero, “Relationship between

- the time-domain Kohlrausch-Williams-Watts and frequency-domain Havriliak-Negami relaxation functions,” *Phys. Rev. B*, vol. 44, no. 14, pp. 7306–7312, 1991, doi: 10.1103/PhysRevB.44.7306.
- [77] M. F. P. Costa and C. Ribeiro, “A modified fractional Zener model to describe the behaviour of a carbon fibre reinforced polymer,” *AIP Conf. Proc.*, vol. 1558, no. 1, pp. 606–609, Oct. 2013, doi: 10.1063/1.4825564.
- [78] A. Arikoglu, “A new fractional derivative model for linearly viscoelastic materials and parameter identification via genetic algorithms,” *Rheol. Acta*, vol. 53, no. 3, pp. 219–233, 2014, doi: 10.1007/s00397-014-0758-2.
- [79] D. Hao, D. Li, and Y. Liao, “Parameter identification of modified fractional Zener model for thermorheological materials,” *J. Non. Cryst. Solids*, vol. 409, pp. 106–119, 2015, doi: 10.1016/j.jnoncrysol.2014.11.015.
- [80] M. Mead, M. Nassar, and S. Dey, “A generalization of generalized gamma distributions,” *Pakistan J. Stat. Oper. Res.*, vol. 14, no. 1, pp. 121–138, 2018, doi: 10.18187/pjsor.v14i1.1692.
- [81] P. Bartolomeo, J. F. Chailan, and J. L. Vernet, “On the use of WLF equation to study resin curing by dielectric spectroscopy,” *Polymer (Guildf.)*, vol. 42, no. 9, pp. 4385–4392, 2001, doi: 10.1016/S0032-3861(00)00733-3.
- [82] E. Masiewicz, A. Grzybowski, K. Grzybowska, S. Pawlus, J. Pionteck, and M. Paluch, “Adam-Gibbs model in the density scaling regime and its implications for the configurational entropy scaling,” *Sci. Rep.*, vol. 5, no. July, pp. 1–13, 2015, doi: 10.1038/srep13998.
- [83] H. N. Lee, H. M. Christen, M. F. Chisholm, C. M. Rouleau, and D. H. Lowndes, “Strong polarization enhancement in asymmetric three-component ferroelectric superlattices,” *Nature*, vol. 433, no. 7024, pp. 395–399, 2005, doi: 10.1038/nature03261.
- [84] R. J. Zeches *et al.*, “Supporting Online Material for A Strain-Driven Morphotropic Phase Boundary in BiFeO₃,” *Science (80-*

- .), vol. 324, no. November, pp. 63–67, 2009, [Online]. Available:
www.sciencemag.org/cgi/content/full/326/5955/977/DC1
- [85] H. M. Christen, J. H. Nam, H. S. Kim, A. J. Hatt, and N. A. Spaldin, “Stress-induced R-MA-MC-T symmetry changes in BiFeO₃ films,” *Phys. Rev. B - Condens. Matter Mater. Phys.*, vol. 83, no. 14, pp. 1–7, 2011, doi: 10.1103/PhysRevB.83.144107.
- [86] P. Gumbsch, S. Taeri-Baghdadrani, D. Brunner, W. Sigle, and M. Rühle, “Plasticity and an inverse brittle-to-ductile transition in strontium titanate,” *Phys. Rev. Lett.*, vol. 87, no. 8, pp. 85505-1-85505-2, 2001, doi: 10.1103/PhysRevLett.87.085505.
- [87] Y. Wang, W. Chen, B. Wang, and Y. Zheng, “Ultrathin ferroelectric films: Growth, characterization, physics and applications,” *Materials (Basel)*, vol. 6, no. 9, pp. 6377–6485, 2014, doi: 10.3390/ma7096377.
- [88] H. Palneedi, M. Peddigari, G. T. Hwang, D. Y. Jeong, and J. Ryu, “High-Performance Dielectric Ceramic Films for Energy Storage Capacitors: Progress and Outlook,” *Adv. Funct. Mater.*, vol. 28, no. 42, pp. 1–33, 2018, doi: 10.1002/adfm.201803665.
- [89] X. Han, Y. Ji, and Y. Yang, “Ferroelectric Photovoltaic Materials and Devices,” *Adv. Funct. Mater.*, vol. 32, no. 14, pp. 1–17, 2022, doi: 10.1002/adfm.202109625.
- [90] A. K. Tagantsev, V. O. Sherman, K. F. Astafiev, J. Venkatesh, and N. Setter, “Ferroelectric materials for microwave tunable applications,” *J. Electroceramics*, vol. 11, no. 1–2, pp. 5–66, 2003, doi: 10.1023/b:jecr.0000015661.81386.e6.
- [91] R. Eason, S. Barrington, C. Grivas, T. May-Smith, and D. Shepherd, “Pulsed Laser Deposition of Thin Films: Applications-Led Growth of Functional Materials,” in *Pulsed Laser Deposition of Thin Films: Applications-Led Growth of Functional Materials*, 2006, pp. 383–420. doi: 10.1002/0470052120.
- [92] Z. W. Liu and C. K. Ong, “Synthesis and size control of ZnO nanorods by conventional pulsed-laser deposition without catalyst,” *Mater. Lett.*, vol. 61, no. 16, pp. 3329–3333, 2007, doi: 10.1016/j.matlet.2006.11.066.

- [93] D. Yu *et al.*, “Catalyst-free synthesis of ZnO nanorod arrays on InP (001) substrate by pulsed laser deposition,” *Mater. Lett.*, vol. 62, no. 25, pp. 4063–4065, 2008, doi: 10.1016/j.matlet.2008.04.079.
- [94] R. Triboulet and J. Perrière, “Epitaxial growth of ZnO films,” *Prog. Cryst. Growth Charact. Mater.*, vol. 47, no. 2–3, pp. 65–138, 2003, doi: 10.1016/j.pcrysgrow.2005.01.003.
- [95] S. Singh *et al.*, “Structure, microstructure and physical properties of ZnO based materials in various forms: Bulk, thin film and nano,” *J. Phys. D. Appl. Phys.*, vol. 40, no. 20, pp. 6312–6327, 2007, doi: 10.1088/0022-3727/40/20/S15.
- [96] G. W. Yang, “Laser ablation in liquids: Applications in the synthesis of nanocrystals,” *Prog. Mater. Sci.*, vol. 52, no. 4, pp. 648–698, 2007, doi: 10.1016/j.pmatsci.2006.10.016.
- [97] T. Ishiguro, T. Shoji, and H. Inada, “Synthesis of C-N and Si-C films by pulsed laser ablation with frozen N₂ and CH₄ targets,” *Appl. Phys. A Mater. Sci. Process.*, vol. 69, no. 7, pp. 149–152, 1999, doi: 10.1007/s003399900213.
- [98] K. Rodrigo, B. Toftmann, J. Schou, and R. Pedrys, “Laser-induced ion emission during polymer deposition from a flash-frozen water ice matrix,” *Chem. Phys. Lett.*, vol. 399, no. 4–6, pp. 368–372, 2004, doi: 10.1016/j.cplett.2004.10.052.
- [99] Z. Liu, “4.09 - Laser Applied Coatings,” B. Cottis, M. Graham, R. Lindsay, S. Lyon, T. Richardson, D. Scantlebury, and H. B. T.-S. C. Stott, Eds. Oxford: Elsevier, 2010, pp. 2622–2635. doi: <https://doi.org/10.1016/B978-044452787-5.00141-4>.
- [100] N. A. Shepelin, Z. P. Tehrani, N. Ohannessian, C. W. Schneider, D. Pergolesi, and T. Lippert, “A practical guide to pulsed laser deposition,” *Chem. Soc. Rev.*, vol. 52, no. 7, pp. 2294–2321, 2023, doi: 10.1039/d2cs00938b.
- [101] H. B. Albargi *et al.*, “Relevance of the preparation of the target for PLD on the magnetic properties of films of iron-doped indium oxide,” *Coatings*, vol. 9, no. 6, pp. 1–15, 2019, doi: 10.3390/COATINGS9060381.
- [102] L. Liu, Y. Li, X. Wu, Y. Yao, M. Wang, and B. Wang, “Effect of

- target density on the growth and properties of YGBCO thin films deposited by pulsed laser deposition,” *Appl. Surf. Sci.*, vol. 388, pp. 77–81, 2016, doi: 10.1016/j.apsusc.2016.03.151.
- [103] J. H. Kim, S. Lee, and H. S. Im, “Effect of target density and its morphology on TiO₂ thin films grown on Si(100) by PLD,” *Appl. Surf. Sci.*, vol. 151, no. 1, pp. 6–16, 1999, doi: 10.1016/S0169-4332(99)00269-X.
- [104] M. Dinescu and R. Physics, “Thin films development by pulsed laser-assisted deposition,” *Ann. Univ. Craiova, Phys.*, vol. 20, no. October 2014, pp. 43–56, 2020.
- [105] S. Canulescu, M. Döbeli, X. Yao, T. Lippert, S. Amoroso, and J. Schou, “Nonstoichiometric transfer during laser ablation of metal alloys,” *Phys. Rev. Mater.*, vol. 1, no. 7, 2017, doi: 10.1103/PhysRevMaterials.1.073402.
- [106] Y. Ma, J. Song, X. Wang, Y. Liu, and J. Zhou, “Synthesis, Microstructure and Properties of Magnetron Sputtered Lead Zirconate Titanate (PZT) Thin Film Coatings,” *Coatings*, vol. 11, no. 8, 2021, doi: 10.3390/coatings11080944.
- [107] V. Jakeš, K. Rubešová, J. Erben, P. Nekvindová, and M. Jelínek, “Modified sol-gel preparation of LiNbO₃ target for PLD,” *Opt. Mater. (Amst.)*, vol. 35, no. 12, pp. 2540–2543, 2013, doi: 10.1016/j.optmat.2013.07.019.
- [108] P. K. Bhattacharya, R. Fornari, and H. Kamimura, “Comprehensive semiconductor science and technology,” 2011. [Online]. Available: <https://api.semanticscholar.org/CorpusID:107999794>
- [109] T. Venkatesan, “Pulsed laser deposition - Invention or discovery?,” *J. Phys. D. Appl. Phys.*, vol. 47, no. 3, 2014, doi: 10.1088/0022-3727/47/3/034001.
- [110] S. Zhu, Y. Ryu, H. W. White, and Y. Yang, “Effects of ambient pressure in pulsed laser deposition - Morphology and composition study of epitaxial ZnSe film,” *Appl. Surf. Sci.*, vol. 127–129, pp. 584–588, 1998, doi: 10.1016/S0169-4332(97)00710-1.
- [111] J. P. Borrajo *et al.*, “Pulsed laser deposition of bioactive glass

- films in ammonia and disilane atmospheres,” *Appl. Surf. Sci.*, vol. 248, no. 1–4, pp. 369–375, 2005, doi: 10.1016/j.apsusc.2005.03.084.
- [112] S. Choopun *et al.*, “Oxygen pressure-tuned epitaxy and optoelectronic properties of laser-deposited ZnO films on sapphire,” *Appl. Phys. Lett.*, vol. 75, no. 25, pp. 3947–3949, 1999, doi: 10.1063/1.125503.
- [113] J. Schou, “Physical aspects of the pulsed laser deposition technique: The stoichiometric transfer of material from target to film,” *Appl. Surf. Sci.*, vol. 255, no. 10, pp. 5191–5198, 2009, doi: 10.1016/j.apsusc.2008.10.101.
- [114] “private conversation with Dr. Jeonggoo Kim, Neocera LLC.”
- [115] T. K. M. Lippert, “Thin Film Deposition of Functional Materials by Pulsed Laser Deposition,” pp. 1–11, 2012, [Online]. Available: <http://www.azom.com/article.aspx?ArticleID=5986>
- [116] A. R. Damodaran *et al.*, “New modalities of strain-control of ferroelectric thin films,” *J. Phys. Condens. Matter*, vol. 28, no. 26, 2016, doi: 10.1088/0953-8984/28/26/263001.
- [117] C. F. Frank and J. H. van der Merwe, “One-dimensional dislocations. I. Static theory,” *Proc. R. Soc. Lond.*, vol. 198, pp. 205–216, 1949.
- [118] I. N. Stranski and L. Krastanow, “Zur Theorie der orientierten Ausscheidung von Ionenkristallen aufeinander,” *Monatshefte für Chemie und verwandte Teile anderer Wissenschaften*, vol. 71, pp. 351–364, 1937, [Online]. Available: <https://api.semanticscholar.org/CorpusID:93219029>
- [119] “SK growth.” https://pweb.cc.sophia.ac.jp/shimolab/html-e/sk_growth-e.html (accessed Jul. 26, 2024).
- [120] M. Volmer and A. Weber, “Nucleus Formation in Supersaturated Systems,” *Zeitschrift für Phys. Chemie*, vol. 119, no. 1, pp. 277–301, 1926, doi: doi:10.1515/zpch-1926-11927.
- [121] K. Krupski, T. Kobiela, and A. Krupski, “Growth morphology of ultrathin Pb layers on Ni(001),” *Acta Phys. Pol. A*, vol. 125, no. 5, pp. 1159–1162, 2014, doi: 10.12693/APhysPolA.125.1159.
- [122] G. Parker, “Growth Modes,” *Encycl. Mater. Sci. Technol.*, no. M1,

- pp. 3683–3693, 2001.
- [123] M. H. Grabow and G. H. Gilmer, “Thin film growth modes, wetting and cluster nucleation,” *Surf. Sci.*, vol. 194, no. 3, pp. 333–346, 1988, doi: 10.1016/0039-6028(88)90858-8.
- [124] P. R. Willmott and J. R. Huber, “Pulsed laser vaporization and deposition,” *Rev. Mod. Phys.*, vol. 72, no. 1, pp. 315–328, 2000, doi: 10.1103/revmodphys.72.315.
- [125] T. García *et al.*, “Pulsed laser deposition process of PLZT thin films using an infrared Nd:YAG laser,” *Appl. Surf. Sci.*, vol. 252, no. 10, pp. 3783–3788, 2006, doi: 10.1016/j.apsusc.2005.05.062.
- [126] T. García, P. Bartolo-Pérez, E. de Posada, J. L. Peña, and M. Villagrán-Muniz, “Studies of pulsed laser deposition processes of BaTiO₃ thin films,” *Surf. Coatings Technol.*, vol. 201, no. 6, pp. 3621–3624, 2006, doi: 10.1016/j.surfcoat.2006.08.117.
- [127] S. Trolier-Mckinstry and P. Muralt, “Thin film piezoelectrics for MEMS,” *J. Electroceramics*, vol. 12, no. 1–2, pp. 7–17, 2004, doi: 10.1023/B:JECR.0000033998.72845.51.
- [128] I. Vrejoiu, G. Le Rhun, L. Pintilie, D. Hesse, M. Alexe, and U. Gösele, “Intrinsic ferroelectric properties of strained tetragonal PbZr 0.2Ti0.8O₃ obtained on layer-by-layer grown, defect-free single-crystalline films,” *Adv. Mater.*, vol. 18, no. 13, pp. 1657–1661, 2006, doi: 10.1002/adma.200502711.
- [129] J. M. Dekkers *et al.*, “Monocrystalline YBa₂Cu₃O_{7-x} thin films on vicinal SrTiO₃ (001) substrates,” *Appl. Phys. Lett.*, vol. 83, no. 25, pp. 5199–5201, 2003, doi: 10.1063/1.1633010.
- [130] V. Nazabal and P. Němec, “Amorphous Thin Film Deposition BT - Springer Handbook of Glass,” J. D. Musgraves, J. Hu, and L. Calvez, Eds. Cham: Springer International Publishing, 2019, pp. 1293–1332. doi: 10.1007/978-3-319-93728-1_37.
- [131] C. I. Fornari, G. Fornari, P. H. de O. Rappl, E. Abramof, and J. dos S. Travelho, “Monte Carlo Simulation of Epitaxial Growth,” *Epitaxy*, 2018, doi: 10.5772/intechopen.70220.
- [132] R. F. Haglund, “2. Mechanisms of Laser-Induced Desorption and Ablation,” *Exp. Methods Phys. Sci.*, vol. 30, no. C, pp. 15–138, 1997, doi: 10.1016/S0076-695X(08)60394-4.

- [133] H. B. Nielsen, J. Reif, E. Matthias, E. Westin, and A. Rosén, “Multiphoton-Induced Desorption from BaF₂(111) BT - Desorption Induced by Electronic Transitions DIET III,” 1988, pp. 266–273.
- [134] S. M. Pawar *et al.*, “Effect of laser incident energy on the structural, morphological and optical properties of Cu₂ZnSnS₄ (CZTS) thin films,” *Curr. Appl. Phys.*, vol. 10, no. 2, pp. 565–569, 2010, doi: 10.1016/j.cap.2009.07.023.
- [135] N. L. Lahaye, S. S. Harilal, P. K. Diwakar, and A. Hassanein, “The effect of laser pulse duration on ICP-MS signal intensity, elemental fractionation, and detection limits in fs-LA-ICP-MS,” *J. Anal. At. Spectrom.*, vol. 28, no. 11, pp. 1781–1787, 2013, doi: 10.1039/c3ja50200g.
- [136] P. G. Kuzmin *et al.*, “Porous nanoparticles of Al and Ti generated by laser ablation in liquids,” *Appl. Surf. Sci.*, vol. 258, no. 23, pp. 9283–9287, 2012, doi: 10.1016/j.apsusc.2011.08.108.
- [137] A. Hamad, L. Li, and Z. Liu, “A comparison of the characteristics of nanosecond, picosecond and femtosecond lasers generated Ag, TiO₂ and Au nanoparticles in deionised water,” *Appl. Phys. A Mater. Sci. Process.*, vol. 120, no. 4, pp. 1247–1260, 2015, doi: 10.1007/s00339-015-9326-6.
- [138] E. Lundin, “Small-scale laser cutting for stent, tube fabrication.” <https://www.thefabricator.com/tubepipejournal/article/lasercutting/small-scale-laser-cutting-for-stent-tube-fabrication> (accessed Aug. 01, 2024).
- [139] C. Ristoscu and I. Mihailescu, “Effect of Pulse Laser Duration and Shape on PLD Thin Films Morphology and Structure,” *Lasers - Appl. Sci. Ind.*, no. February, 2011, doi: 10.5772/24950.
- [140] Y. Ma, L. Liu, X. Ren, and A. Liu, “The effect of target-substrate distance on surface morphology and properties of β -FeSi₂ films prepared by pulsed laser deposition,” *IOP Conf. Ser. Mater. Sci. Eng.*, vol. 452, no. 2, 2018, doi: 10.1088/1757-899X/452/2/022153.
- [141] R. Castro-Rodríguez, S. Palomares-Sánchez, F. Leccabue, E. Arisi, and B. E. Watts, “Optimal target-substrate distance in the

- growth of oxides thin films by pulsed laser deposition,” *Mater. Lett.*, vol. 57, no. 22–23, pp. 3320–3324, 2003, doi: 10.1016/S0167-577X(03)00066-1.
- [142] A. Rebhi *et al.*, “Effect of the helium background gas pressure on the structural and optoelectronic properties of pulsed-laser-deposited pbs thin films,” *Nanomaterials*, vol. 11, no. 5, 2021, doi: 10.3390/nano11051254.
- [143] R. KEK, S. L. YAP, S. F. KOH, C. H. NEE, T. Y. TOU, and S. S. YAP, “Effects of background gases and pressure in pulsed laser deposition of Al-doped ZnO,” *Thin Solid Films*, vol. 701, no. March, p. 137953, 2020, doi: 10.1016/j.tsf.2020.137953.
- [144] A. Görtler and C. Strowitzki, “Excimer Lasers – The powerful light source in the UV and VUV,” *Laser Tech. J.*, vol. 2, no. 2, pp. 46–50, 2005, doi: 10.1002/latj.200790037.
- [145] D. M. Gaudiosi *et al.*, “Multi-kilohertz repetition rate Ti:sapphire amplifier based on down-chirped pulse amplification,” *Opt. Express*, vol. 14, no. 20, p. 9277, 2006, doi: 10.1364/oe.14.009277.
- [146] G. A. Govindassamy, J. J. Prentice, J. G. Lunney, R. W. Eason, and J. I. Mackenzie, “Effect of laser repetition rate on the growth of Sc₂O₃ via pulsed laser deposition,” *Appl. Phys. A Mater. Sci. Process.*, vol. 128, no. 7, pp. 1–10, 2022, doi: 10.1007/s00339-022-05698-4.
- [147] L. Guan, D. M. Zhang, X. Li, and Z. H. Li, “Role of pulse repetition rate in film growth of pulsed laser deposition,” *Nucl. Instruments Methods Phys. Res. Sect. B Beam Interact. with Mater. Atoms*, vol. 266, no. 1, pp. 57–62, 2008, doi: 10.1016/j.nimb.2007.10.011.
- [148] D. B. Chrisey and G. K. Hubler, *Pulsed laser deposition of thin films*. New York: John Wiley & Sons, 1994. doi: LK - <https://worldcat.org/title/807873412>.
- [149] Š. Svirskas, D. Jablonskas, S. Rudys, S. Lapinskas, R. Grigalaitis, and J. Banys, “Broad-band measurements of dielectric permittivity in coaxial line using partially filled circular waveguide,” *Rev. Sci. Instrum.*, vol. 91, no. 3, 2020, doi:

10.1063/1.5136317.

- [150] J. Grigas, *Microwave dielectric spectroscopy of ferroelectrics and related materials*. London: CRC Press, 1996. doi: 10.1201/9780203747186.
- [151] I. Zamaraitė, S. Rudys, S. Lapinskas, R. Aleksiejunas, R. Grigalaitis, and J. Banys, “Computational electromagnetic analysis of partially-filled rectangular waveguide at X-band frequencies,” *Nonlinear Anal. Model. Control*, vol. 27, no. 6, pp. 1150–1167, 2022, doi: 10.15388/namc.2022.27.29533.
- [152] L. Song, S. Glinsek, and E. Defay, “Toward low-temperature processing of lead zirconate titanate thin films: Advances, strategies, and applications,” *Appl. Phys. Rev.*, vol. 8, no. 4, 2021, doi: 10.1063/5.0054004.
- [153] E. H. Kim, C. W. Moon, J. G. Lee, M. S. Lah, and S. M. Koo, “Synthesis and characterization of lead (IV) precursors and their conversion to PZT materials through a CVD process,” *Polyhedron*, vol. 177, p. 114270, 2020, doi: 10.1016/j.poly.2019.114270.
- [154] M. Veith, M. Bender, T. Lehnert, M. Zimmer, and A. Jakob, “Novel single-source precursors for the fabrication of PbTiO₃, PbZrO₃ and Pb(Zr_{1-x}Ti_x)O₃ thin-films by chemical vapor deposition,” *Dalt. Trans.*, vol. 40, no. 5, pp. 1175–1182, 2011, doi: 10.1039/c0dt00830c.
- [155] J. Le Scornec, R. Seveno, T. Dufay, and B. Guiffard, “Influence of the intermediate oxidation layer on the characteristics of lead zirconate titanate thin films with aluminium substrate,” *Thin Solid Films*, vol. 770, no. February, p. 139761, 2023, doi: 10.1016/j.tsf.2023.139761.
- [156] Y. Yamasaki, Y. Yokota, H. Shima, and H. Uchida, “One-axis-oriented growth of PZT thin films on transparent glass substrates using metal oxide nanosheets,” *Jpn. J. Appl. Phys.*, vol. 61, no. SN, 2022, doi: 10.35848/1347-4065/ac7e1a.
- [157] S. Barolin and M. G. Stachiotti, “Sol – gel synthesis and characterization of PZT thin films on FTO / aluminoborosilicate glass substrates,” vol. 1171, 2023, doi: 10.1007/s10854-023-

10596-3.

- [158] G. Tan, S. H. Kweon, and I. Kanno, “Piezoelectric properties of epitaxial Pb(Zr,Ti)O₃ thin films grown on Si substrates by the sol–gel method,” *Thin Solid Films*, vol. 764, no. December 2021, p. 139612, 2023, doi: 10.1016/j.tsf.2022.139612.
- [159] E. van der Veer, B. Noheda, and M. Acuatla, “Piezoelectric properties of PZT by an ethylene glycol-based chemical solution synthesis,” *J. Sol-Gel Sci. Technol.*, vol. 100, no. 3, pp. 517–525, 2021, doi: 10.1007/s10971-021-05651-6.
- [160] I. Vrejoiu, D. Hesse, and M. Alexe, “Single crystalline PZT films and the impact of extended structural defects on the ferroelectric properties,” *Handb. Adv. Dielectr. Piezoelectric Ferroelectr. Mater. Synth. Prop. Appl.*, pp. 695–723, Jan. 2008, doi: 10.1533/9781845694005.6.695.
- [161] F. Gellé, R. Chirita, D. Mertz, M. V. Rastei, A. Dinia, and S. Colis, “Guideline to atomically flat TiO₂-terminated SrTiO₃(001) surfaces,” *Surf. Sci.*, vol. 677, no. February, pp. 39–45, 2018, doi: 10.1016/j.susc.2018.06.001.
- [162] C. Borderon, A. E. Brunier, K. Nadaud, R. Renoud, M. Alexe, and H. W. Gundel, “Domain wall motion in Pb(Zr_{0.20}Ti_{0.80})O₃ epitaxial thin films,” *Sci. Rep.*, vol. 7, no. 1, pp. 1–7, 2017, doi: 10.1038/s41598-017-03757-y.
- [163] M. J. Haun, E. Furman, S. J. Jang, and L. E. Cross, “Thermodynamic theory of the lead zirconate-titanate solid solution system, part v: Theoretical calculations,” *Ferroelectrics*, vol. 99, no. 1, pp. 63–86, 1989, doi: 10.1080/00150198908221440.
- [164] S. Dussan, A. Kumar, J. F. Scott, and R. S. Katiyar, “Magnetic effects on dielectric and polarization behavior of multiferroic heterostructures,” *Appl. Phys. Lett.*, vol. 96, no. 7, 2010, doi: 10.1063/1.3327889.
- [165] V. Raicu, “Dielectric dispersion of biological matter: Model combining Debye-type and ‘universal’ responses,” *Phys. Rev. E - Stat. Physics, Plasmas, Fluids, Relat. Interdiscip. Top.*, vol. 60, no. 4, pp. 4677–4680, 1999, doi: 10.1103/PhysRevE.60.4677.

- [166] D. V. Kuzenko, "Temperature-activation mechanism of the temperature dependence of the dielectric constant of ferroelectric ceramics PZT," *J. Adv. Dielectr.*, vol. 12, no. 3, pp. 1–7, 2022, doi: 10.1142/S2010135X22500102.
- [167] N. D. Scarisoreanu, R. Birjega, A. Andrei, M. Dinescu, F. Craciun, and C. Galassi, "Phase Transitions, Dielectric and Ferroelectric Properties of Lead-free NBT-BT Thin Films," in *Advances in Ferroelectrics*, A. P. Barranco, Ed. Rijeka: IntechOpen, 2012. doi: 10.5772/52395.
- [168] S. Sasikumar, R. Saravanan, S. Saravanakumar, and K. Aravinth, "Charge correlation of ferroelectric and piezoelectric properties of $(1 - x)(\text{Na}_{0.5}\text{Bi}_{0.5})\text{TiO}_3\text{-xBaTiO}_3$ lead-free ceramic solid solution," *J. Mater. Sci. Mater. Electron.*, vol. 28, no. 13, pp. 9950–9963, 2017, doi: 10.1007/s10854-017-6753-5.
- [169] H. Lidjici, B. Lagoun, M. Berrahal, M. Rguitti, M. A. Hentatti, and H. Khemakhem, "XRD, Raman and electrical studies on the $(1-x)(\text{Na}_{0.5}\text{Bi}_{0.5})\text{TiO}_3\text{-xBaTiO}_3$ lead free ceramics," *J. Alloys Compd.*, vol. 618, pp. 643–648, 2015, doi: 10.1016/j.jallcom.2014.08.161.
- [170] A. R. West, *Solid State Chemistry and its Applications*. Wiley, 2014. [Online]. Available: <https://books.google.lt/books?id=Y4eTAAQBAJ>
- [171] T. Zheng and J. Wu, "Quenched bismuth ferrite-barium titanate lead-free piezoelectric ceramics," *J. Alloys Compd.*, vol. 676, pp. 505–512, 2016, doi: 10.1016/j.jallcom.2016.03.205.
- [172] Z. Yang *et al.*, "Re-entrant relaxor ferroelectric behaviour in Nb-doped $\text{BiFeO}_3\text{-BaTiO}_3$ ceramics," *J. Mater. Chem. C*, vol. 11, no. 6, pp. 2186–2195, 2023, doi: 10.1039/d2tc04702k.
- [173] K. H. Härdtl, "Electrical and mechanical losses in ferroelectric ceramics," *Ceram. Int.*, vol. 8, no. 4, pp. 121–127, 1982, doi: 10.1016/0272-8842(82)90001-3.
- [174] S. S. N. Bharadwaja, J. R. Kim, H. Ogihara, L. E. Cross, S. Trolier-McKinstry, and C. A. Randall, "Critical slowing down mechanism and reentrant dipole glass phenomena in $(1-x)\text{BaTiO}_3\text{-xBiScO}_3$ ($0.1 \leq x \leq 0.4$): The high energy density

- dielectrics,” *Phys. Rev. B*, vol. 83, no. 2, p. 024106, Jan. 2011, doi: 10.1103/PhysRevB.83.024106.
- [175] B. Pokharel, L. Shrestha, K. Ariga, and D. Pandey, “Demonstration of Reentrant Relaxor Ferroelectric Phase Transitions in Antiferroelectric-Based (Pb_{0.50}Ba_{0.50})ZrO₃ Ceramics,” *Energies*, vol. 11, no. 4, p. 850, Apr. 2018, doi: 10.3390/en11040850.
- [176] A. Surampalli, R. Egli, D. Prajapat, C. Meneghini, and V. R. Reddy, “Reentrant phenomenon in the diffuse ferroelectric BaSn_{0.15}Ti_{0.85}O₃: Local structural insights and first-order reversal curves study,” *Phys. Rev. B*, vol. 104, no. 18, p. 184114, Nov. 2021, doi: 10.1103/PhysRevB.104.184114.
- [177] A. Singh, C. Moriyoshi, Y. Kuroiwa, and D. Pandey, “Visualization of Bi³⁺ off-centering in the average cubic structure of (Ba_{0.70}Bi_{0.30})(Ti_{0.70}Fe_{0.30})O₃ at the electron density level,” *Appl. Phys. Lett.*, vol. 103, no. 12, pp. 0–4, 2013, doi: 10.1063/1.4822032.
- [178] A. Singh, C. Moriyoshi, Y. Kuroiwa, and D. Pandey, “Evidence for diffuse ferroelectric phase transition and cooperative tricritical freezing of random-site dipoles due to off-centered Bi³⁺ ions in the average cubic lattice of (Ba_{1-x}Bi_x)(Ti_{1-x}Fe_x)O₃,” *Phys. Rev. B - Condens. Matter Mater. Phys.*, vol. 85, no. 6, pp. 1–8, 2012, doi: 10.1103/PhysRevB.85.064116.
- [179] Y. Kuroiwa *et al.*, “Piezoelectricity in perovskite-type pseudocubic ferroelectrics by partial ordering of off-centered cations,” *Commun. Mater.*, vol. 1, no. 1, 2020, doi: 10.1038/s43246-020-00072-4.
- [180] Z. Yang, B. Wang, Y. Li, and D. A. Hall, “Enhancement of Nonlinear Dielectric Properties in BiFeO₃–BaTiO₃ Ceramics by Nb-Doping,” *Materials (Basel)*, vol. 15, no. 8, 2022, doi: 10.3390/ma15082872.
- [181] N. Masó and A. R. West, “Electrical properties of Ca-doped BiFeO₃ ceramics: From p-type semiconduction to oxide-ion conduction,” *Chem. Mater.*, vol. 24, no. 11, pp. 2127–2132, 2012, doi: 10.1021/cm300683e.

- [182] S. Srivastava *et al.*, “Synthesis of zinc oxide (ZnO) nanorods and its phenol sensing by dielectric investigation,” *J. Alloys Compd.*, vol. 644, pp. 597–601, 2015, doi: 10.1016/j.jallcom.2015.04.220.
- [183] T. Wang *et al.*, “Dielectric relaxation and Maxwell-Wagner interface polarization in Nb₂O₅ doped 0.65BiFeO₃-0.35BaTiO₃ ceramics,” *J. Appl. Phys.*, vol. 121, no. 8, pp. 0–9, 2017, doi: 10.1063/1.4977107.
- [184] K. L. Ngai, *Relaxation and Diffusion in Complex Systems*. New York, NY: Springer New York, 2011. doi: 10.1007/978-1-4419-7649-9.
- [185] D. Viehland, S. J. Jang, L. E. Cross, and M. Wuttig, “Freezing of the polarization fluctuations in lead magnesium niobate relaxors,” *J. Appl. Phys.*, vol. 68, no. 6, pp. 2916–2921, 1990, doi: 10.1063/1.346425.
- [186] R. Grigalaitis, J. Banys, A. Kania, and A. Slodczyk, “Distribution of relaxation times in PMN single crystal,” *J. Phys. IV*, vol. 128, pp. 127–131, Sep. 2005, doi: 10.1051/jp4:2005128020.
- [187] J. Macutkevic, J. Banys, R. Grigalaitis, and Y. Vysochanskii, “Asymmetric phase diagram of mixed CuInP₂(S_xSe_{1-x})₆ crystals,” *Phys. Rev. B*, vol. 78, no. 6, p. 064101, Aug. 2008, doi: 10.1103/PhysRevB.78.064101.
- [188] J. Banys, R. Grigalaitis, A. Mikonis, J. Macutkevic, and P. Keburis, “Distribution of relaxation times of relaxors: comparison with dipolar glasses,” *Phys. status solidi c*, vol. 6, no. 12, pp. 2725–2730, Dec. 2009, doi: 10.1002/pssc.200982529.
- [189] B. Li, T. Zheng, X. Wei, S. Zhong, Y. Li, and J. Wu, “Constructing Relaxor/Ferroelectric Pseudocomposite to Reveal the Domain Role in Electrostrain of Bismuth Ferrite-Barium Titanate Based Ceramics,” *ACS Appl. Mater. Interfaces*, vol. 14, no. 16, pp. 18713–18722, 2022, doi: 10.1021/acsami.2c03817.
- [190] X. Zhao, B. Li, D. Tai, T. Zheng, and J. Wu, “Destruction of conducting channels driven resistivity enhancement in bismuth ferrite-barium titanate based ceramics,” *J. Alloys Compd.*, vol. 1006, no. September, p. 176295, 2024, doi: 10.1016/j.jallcom.2024.176295.

- [191] M. A. Kniazeva *et al.*, “Ferroelectric to incommensurate fluctuations crossover in PbHfO₃-PbSnO₃,” *Phys. Rev. B*, vol. 105, no. 1, pp. 1–15, 2022, doi: 10.1103/PhysRevB.105.014101.
- [192] F. Kadlec, C. Kadlec, P. Kužel, and J. Petzelt, “Study of the ferroelectric phase transition in germanium telluride using time-domain terahertz spectroscopy,” *Phys. Rev. B*, vol. 84, no. 20, p. 205209, 2011, doi: 10.1103/PhysRevB.84.205209.
- [193] N. Blumenschein, C. Kadlec, O. Romanyuk, T. Paskova, J. F. Muth, and F. Kadlec, “Dielectric and conducting properties of unintentionally and Sn-doped β -Ga₂O₃ studied by terahertz spectroscopy,” *J. Appl. Phys.*, vol. 127, no. 16, 2020, doi: 10.1063/1.5143735.
- [194] I. Jankowska-Sumara, J. H. Ko, and A. Majchrowski, “The complexity of structural phase transitions in Pb(Hf_{0.92}Sn_{0.08})O₃ single crystals,” *J. Am. Ceram. Soc.*, vol. 104, no. 11, pp. 5990–6001, 2021, doi: 10.1111/jace.17967.
- [195] S. Kamba *et al.*, “Anomalous broad dielectric relaxation in Bi_{1.5}Zn_{1.0}Nb_{1.5}O₇ pyrochlore,” *Phys. Rev. B - Condens. Matter Mater. Phys.*, vol. 66, no. 5, pp. 541061–541068, 2002, doi: 10.1103/PhysRevB.66.054106.
- [196] A. A. Volkov *et al.*, “High-frequency dielectric spectra of AgTaO₃-AgNbO₃ mixed ceramics,” *J. Phys. Condens. Matter*, vol. 7, no. 4, pp. 785–793, 1995, doi: 10.1088/0953-8984/7/4/009.
- [197] P. Debye, *Polar Molecules*. Dover Publication, 1954.

6. SANTRAUKA LIETUVIŲ KALBA

Feroelektrinės medžiagos, ypač perovskitų oksidai, sulaukė dėmesio dėl įvairiapusio jų taikymo jutikliuose [1], aktuatoriuose [2], atminties įrenginiuose [3] ir energijos kaupikliuose [4]. Perovskitai, pirmą kartą aptikti 1839 m., pasižymi įvairiomis fizikinėmis savybėmis, priklausančiomis nuo jų sudėties ir katijonų išsidėstymo. Perovskitai pagaminti švino pagrindu, tokie kaip $\text{PbZr}_{0,2}\text{Ti}_{0,8}\text{O}_3$ ir $\text{PbHf}_{0,92}\text{Sn}_{0,08}\text{O}_3$, ilgą laiką dominavo dėl stiprių feroelektrinių savybių, kurias lemia švino jonai. Tačiau aplinkos ir sveikatos problemos, susijusios su švinu, paskatino tyrinėti alternatyvius švino neturinčius junginius, pavyzdžiui, natrio bismuto titanatą (NBT), bismuto feritą (BiFeO_3) ir jų kompozicijas, modifikuotas bario titanatu.

Impulsinis lazerinis nusodinimas (PLD) yra precizinis metodas ploniems perovskitų sluoksniams formuoti, leidžiantis pasiekti geresnes medžiagų savybes miniatiūrinėse elektronikos sistemose. Disertacijoje tiriami $\text{PbZr}_{0,2}\text{Ti}_{0,8}\text{O}_3$, $0,8(\text{Na}_{0,5}\text{Bi}_{0,5}\text{TiO}_3)-0,2(\text{BaTiO}_3)$ bei ZrSnSe_3 sluoksnių PLD parametrai ir dielektrinės savybės, taip pat $\text{PbZr}_{0,2}\text{Ti}_{0,8}\text{O}_3$, $\text{PbHf}_{0,92}\text{Sn}_{0,08}\text{O}_3$ ir $\text{BiFeO}_3\text{-BaTiO}_3$ (legiruoto ir nelegiruoto Nb) dielektrinės savybės temperatūros ir dažnio srityse. Darbe analizuojamas legiravimo poveikis šioms medžiagoms, terminis stabilumas ir nusodinimo sąlygų įtaka siekiant pagerinti tokias savybes kaip dielektrinė relaksacija ir faziniai virsmai.

Disertacijos tikslai ir uždaviniai

Šioje disertacijoje nagrinėjamas kompleksinių perovskitinių medžiagų, tokių kaip $\text{PbZr}_{0,2}\text{Ti}_{0,8}\text{O}_3$, $0,8(\text{Na}_{0,5}\text{Bi}_{0,5}\text{TiO}_3)-0,2(\text{BaTiO}_3)$ ir ZrSnSe_3 , plonų sluoksnių formavimas naudojant impulsinį lazerinį nusodinimą (PLD). Taip pat tiriamos dielektrinių $\text{PbHf}_{0,92}\text{Sn}_{0,08}\text{O}_3$ bei $\text{PbZr}_{0,2}\text{Ti}_{0,8}\text{O}_3$ sluoksnių savybių priklausomybė nuo temperatūros ir dažnio ir $\text{BiFeO}_3\text{-BaTiO}_3$ sluoksnių legiravimo Nb įtaka minėtiems efektams.

Disertacijos tikslams pasiekti buvo sprendžiami šie uždaviniai

1. Pagaminti $\text{PbZr}_{0,2}\text{Ti}_{0,8}\text{O}_3$ plonas plėveles impulsinio lazerinio nusodinimo būdu ir išmatuoti jų dielektrines bei feroelektrines savybes.
2. Pagaminti $0,8(\text{Na}_{0,5}\text{Bi}_{0,5}\text{TiO}_3)-0,2(\text{BaTiO}_3)$ plonas plėveles impulsinio lazerinio nusodinimo būdu ir išanalizuoti įvairių nusodinimo parametrų poveikį plėvelių kokybei ir stochiometrijai.
3. Pagaminti ZrSnSe_3 plonas plėveles impulsinio lazerinio nusodinimo būdu ir optimizuoti nusodinimo parametrus, siekiant gauti reikiamą kokybę fotovoltiniams taikymams.
4. Išmatuoti gryno ir Nb legiruoto $\text{BiFeO}_3\text{--BaTiO}_3$ sluoksnių dielektrines savybes bei ištirti Nb legiravimo įtaką $\text{BiFeO}_3\text{--BaTiO}_3$ dielektrinės relaksacijos dinamikai.
5. Ištirti $\text{PbHf}_{0,92}\text{Sn}_{0,08}\text{O}_3$ kristalų dielektrines savybes ir fazinių virsmų elgseną.

Disertacijos ginamieji teiginiai

1. Švino cirkonato titanato ($\text{PbZr}_{0,2}\text{Ti}_{0,8}\text{O}_3$) plonoji plėvelė, nusodinta ant SrTiO_3 padėklo, pasižymi žymiai padidėjusia liekamąja poliarizacija ($93 \mu\text{C}/\text{cm}^2$), kurią lemia deformaciniai efektai dėl substrato ir plėvelės kristalinių gardelių neatitikimo, išryškinantys unikalią plėvelės ir padėklo sąveikos įtaką feroelektrinėms savybėms.
2. $0,8(\text{Na}_{0,5}\text{Bi}_{0,5}\text{TiO}_3)-0,2(\text{BaTiO}_3)$ ir ZrSnSe_3 plonų plėvelių struktūros kokybei, stochiometrijai ir tolygumui didelę įtaką turi impulsinio lazerinio nusodinimo parametrai, tokie kaip buferinis sluoksnis, lazerio spinduliuotės srautas, padėklo temperatūra, aplinkos slėgis, atstumas tarp taikinio ir padėklo. Optimaliomis sąlygomis NBT-BT plėveliūngamybinaudojamas platinos buferinis sluoksnis, $1,5\text{--}2,1 \text{ J}/\text{cm}^2$ lazerio spinduliuotės srautas, $600 \text{ }^\circ\text{C}$ padėklo temperatūra, $0,3 \text{ mbar O}_2$ slėgis ir 55 mm atstumas tarp taikinio ir padėklo. Optimalūs ZrSnSe_3 parametrai yra $0,3 \text{ J}/\text{cm}^2$ lazerio srautas, argono dujų slėgis $0,01 \text{ mbar}$, substrato temperatūra $150 \text{ }^\circ\text{C}$, atstumas tarp taikinio ir substrato 95 mm ir minimalus lazerio dėmės dydis. Šie parametrai leidžia pagaminti aukštos kokybės kristalines plėveles su tikslia

stechiometrija ir kontroliuojama struktūra, išryškinant jų potencialą pažangioms technologijoms.

3. Bismuto ferito ir bario titanato (70 % BiFeO_3 ir 30 % BaTiO_3) kietojo tirpalo relaksorinė elgsena 270–400 K temperatūrų intervale pasižymi kompleksiškais termiškai indukuotais perėjimais tarp tvarkingų ir netvarkingų būsenų, nustatytais plačiajuoste dielektrine spektroskopija plačiame dažnių diapazone (20 Hz–30 GHz) ir temperatūrų intervale (200–500 K).

4. Švino hafnato, praturtinto alavu, ($\text{PbHf}_{0,92}\text{Sn}_{0,08}\text{O}_3$) kristalai pasižymi pastebimais dielektrinės dispersijos poslinkiais nuo 20 GHz iki 100 GHz ir slopinimo koeficiento pokyčiais 470–500 K temperatūrų ruože Curie temperatūros aplinkoje. Šie pokyčiai nustatyti plačiajuoste dielektrine spektroskopija ir paremti rezonansinės dispersijos modeliu.

Mokslinio darbo naujumas ir aktualumas

1. Siekiant ištirti impulsinio lazerinio nusodinimo būdu paruošto $\text{PbZr}_{0,2}\text{Ti}_{0,8}\text{O}_3$ sluoksnio dielektrines savybes, buvo sukurta nauja metalo–feroelektriko–metalų struktūra. Taileido sumažinti neigiamą gardelės defektų poveikį ir pasiekti $93 \mu\text{C}/\text{cm}^2$ liekamosios poliarizacijos vertę, viršijančią teorinę tūrinės medžiagos vertę ($70 \mu\text{C}/\text{cm}^2$).

2. Ištirta padėklo buferinio sluoksnio ir nusodinimo parametrų (buferinis sluoksnis, atstumas tarp taikinio ir pagrindo, padėklo temperatūra, aplinkos slėgis ir lazerio spinduliuotės srautas) įtaka impulsiniu lazeriniu nusodinimu paruoštų $0,8(\text{Na}_{0,5}\text{Bi}_{0,5}\text{TiO}_3)$ – $0,2(\text{BaTiO}_3)$ plonųjų sluoksnių struktūros kokybei ir stochiometrijai. Bandiniai buvo analizuoti rentgeno spindulių difrakcijos ir skenuojančios elektroninės mikroskopijos metodais ir nustatyti optimalūs parametrai geriausiai sluoksnių dielektrinei kokybei pasiekti.

3. Pirmą kartą, taikant optimizuotus parametrus, impulsinio lazerinio nusodinimo būdu iš nemodifikuotos bei modifikuotos sudėties ir dviejų dalinės sudėties taikinių (ZrSe_2 ir SnSe), sukurtos ZrSnSe_3 plonosios plėvelės, skirtos fotovoltiniams taikymams.

4. Pirmą kartą Nb legiruoto $\text{BiFeO}_3\text{--BaTiO}_3$ kietojo tirpalo relaksorinė elgsena ištirta plačiajuoste dielektrine spektroskopija plačiame dažnių (nuo 20 Hz iki 30 GHz) ir temperatūrų diapazone (nuo 200 iki 500 K). Rezultatai atskleidė termiškai indukuotus perėjimus tarp tvarkingų ir netvarkingų būsenų.

5. Plačiajuoste dielektrine spektroskopija (20 Hz – 200 GHz dažnių diapazone) ištirtos $\text{PbHf}_{0,92}\text{Sn}_{0,08}\text{O}_3$ kristalų dielektrinės savybės, ypatingą dėmesį skiriant dispersijai 10–100 GHz dažnių srityje. Temperatūriniai matavimai 300–500 K diapazone leido išanalizuoti dispersijos poslinkius nuo 20 Hz iki 100 GHz (470–500 K intervale) bei slopinimo koeficiento mažėjimą artėjant prie Curie temperatūros ($T_c = 494$ K), kas buvo patvirtinta eksperimentiniais matavimais, aproksimuotais modifikuotu Cole'o–Cole'o modeliu.

Autoriaus indėlis

0,8($\text{Na}_{0,5}\text{Bi}_{0,5}\text{TiO}_3$)-0,2(BaTiO_3) plonąsias plėveles impulsinio lazerinio nusodinimo būdu pagamino autorius, ZrSnSe_3 plėvelės buvo pagamintos bendradarbiaujant su Dr. Rokas Kondrotas, o $\text{PbZr}_{0,2}\text{Ti}_{0,8}\text{O}_3$ –Voriko universitete koordinuojant gamybą Dr. Marin Alexe. Autorius asmeniškai atliko daugumą technologinių paruošimo darbų, įskaitant padėklų paruošimą ir įrangos priežiūrą. Autorius taip pat paruošė visus bandinius dielektriniams tyrimams, atliko jų matavimus (išskyrus $\text{PbHf}_{0,92}\text{Sn}_{0,08}\text{O}_3$ kristalų tyrimus teraherciniame diapazone), analizavo gautus duomenis ir parašė publikacijas bendradarbiaujant su S. Svirsku, O. Suvorova, R. Grigalaičiu, J. Baniuir kitais bendraautoriais. Kai kuriuos disertacijos projekto aspektus padėjo įgyvendinti dirbtinio intelekto technologijos.

Disertacijos struktūra

Disertaciją sudaro penki skyriai santrauka ir cituotos literatūros sąrašas, kuriame yra 198 literatūros šaltiniai.

6.1 Apžvalga

Feroelektrinės medžiagos

Medžiagos vadinamos feroelektrinėmis, jei išorinis elektrinis laukas pakeičia jų savaiminę elektrinę poliarizaciją. Be to, kiekviena feroelektrinė medžiaga pasižymi kartu ir grįžtamąja elektrine poliarizacija, todėl yra pjezoelektrinė ir piroelektrinė. Feroelektriškumas yra susijęs su kristalinės gardelės struktūra; jos pakeitimai kartu su elektriniu lauku veikia savaiminę poliarizaciją. Esminė feroelektrinių medžiagų sąvoka yra dipolinis momentas, apibrėžtas lygtimi (1):

$$P = \sum_i e_i r_i, \quad (1)$$

čia e_i yra i -tosios dalelės krūvis, o r_i – šios dalelės vektorius.

Fazinių perėjimų feroelektrinėse medžiagose analizė

Remiantis dielektrinės skvarbos duomenų interpretacija, galima nustatyti ir klasifikuoti tiriamą feroelektrinę medžiagą. Įprastų feroelektrikų dielektrinė skvarba (ϵ^*) ties Kiuri temperatūra T_c pasižymi aiškiai išreikštu smailiu maksimumu. Ties šia temperatūra atomų padėtys kristalinėje gardelėje persitvarko taip, kad dipoliai išsidėsto viena kryptimi.

Relaksoriai feroelektrikai

Relaksoriai feroelektrikai yra feroelektrinės medžiagos, kurioms būdingas difuzinis fazinis perėjimas ir nuo dažnio priklausančios dielektrinės savybės. Skirtingai nei įprastiniuose feroelektrikuose, relaksoriuose feroelektrikuose fazinis perėjimas vyksta plačiame temperatūrų intervale, neturint aiškios ir staigios fazinio perėjimo ribos.

Manoma, kad tokią neįprastą elgseną sukelia polinės nano sritys (PNR), kuriose vietinė poliarizacija yra tvarkinga nanometrų mastu.

Antiferoelektrinės medžiagos

Pagrindinė antiferoelektrinių medžiagų makroskopinės savaiminės poliarizacijos priežastis yra priešingos (antiparalelinės) dipolių orientacijos. Be to, antiferoelektrinėms medžiagoms būdingi maži dielektriniai nuostoliai ir itin maža likutinė poliarizacija – mažesnė nei relaksoriniuose feroelektrikuose. Šios medžiagos yra svarbios įvairiems taikymams, nes elektrinio lauko veikiamos gali pereiti iš antiferoelektrinės į feroelektrinę fazę, pasižyminčią didele soties poliarizacija, ir vėl grįžti į pradinę būseną elektrinį lauką pašalinus. Šio grįžtamojo pokyčio priežastimi laikomas nedidelis krūvininkų laisvosios energijos skirtumas tarp lauko sukeltos feroelektrinės ir pradinės antiferoelektrinės fazės [5].

Dielektrinės relaksacijos modeliai feroelektrikuose

Keletas dielektrinės relaksacijos modelių aprašo, kaip poliarizacija reaguoja į išorinį elektrinį lauką:

1. Debye modelis: paprasčiausias modelis, darantis prielaidą, kad nesaveikaujantiems dipoliams būdingas vienas relaksacijos laikas.
2. Cole-Cole modelis: įveda relaksacijos laikų pasiskirstymą dielektrikuose.
3. Cole'o-Davidsono modelis: įvertina asimetrinį relaksacijos laikų pasiskirstymą.
4. Havriliako–Negami modelis: išplečia ankstesnius modelius ir aprašo sudėtingesnę dielektrinę elgseną.

Relaksacijos laiko kitimo modeliavimas nevienalytėse medžiagose

Dielektrinė relaksacija realiose medžiagose dažnai susijusi su relaksacijos laiko pasiskirstymu dėl sudėties ir struktūrinių

nehomogeniškumą. Šis modelis apima Arrenijaus lygtį, kuri tinka bandiniams, turintiems vieną aktyvacijos energiją:

$$\tau(T) = \tau_0 \exp\left(\frac{E_a}{k_B T}\right), \quad (2)$$

čia $\tau(T)$ – relaksacijos laikas esant temperatūrai T , τ_0 – priešeksponentinis koeficientas (charakteristinė laiko skalė), E_a – aktyvacijos energija, k_B – Bolcmano konstanta, T – absoliutinė temperatūra.

Medžiagoms, kurių relaksacijos dinamika nukrypsta nuo Arrenijaus elgsenos, relaksacijos laikų priklausomybė nuo temperatūros aprašoma Vogelio-Fulcherio-Tammano lygtimi. Šis modelis tinka peršaldytiems skysčiams ir stiklams, kuriuose relaksacijos trukmė žymiai ilgėja, artėjant prie stiklėjimo temperatūros:

$$\tau(T) = \tau_0 \exp\left(\frac{E_a}{k_B(T - T_f)}\right), \quad (3)$$

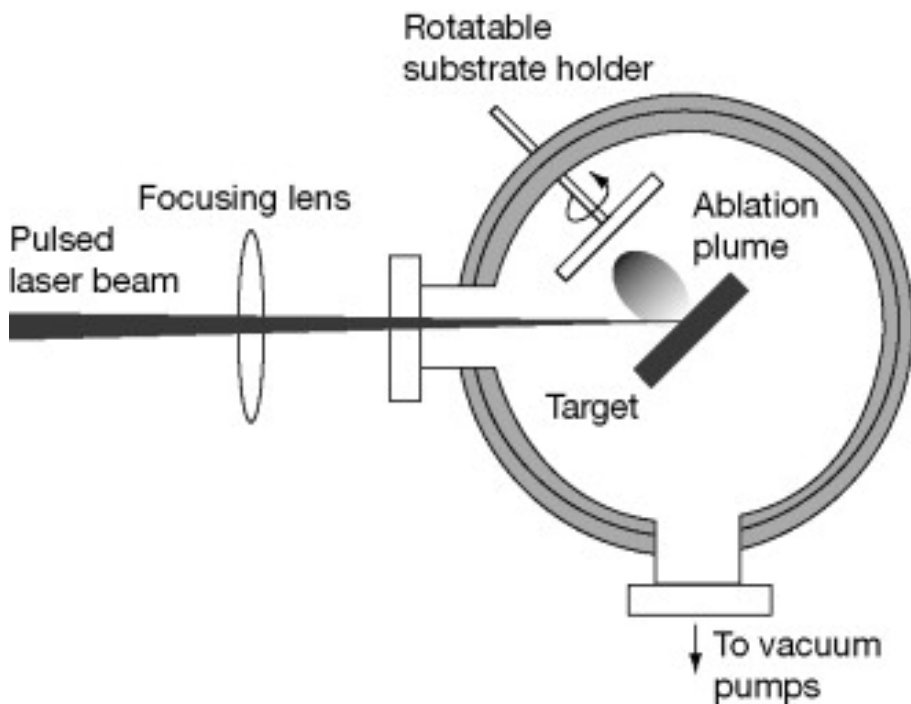
kur τ_0 , E_a , k_B ir T yra tokie patys kaip ir Arrenijaus lygtyje. T_f – temperatūra, kurioje relaksacijos procesas „užšąla“.

Impulsinio lazerinio nusodinimo (PLD) naudojimo motyvacija

PLD leidžia tiksliai kontroliuoti plonų sluoksnių stochiometriją, nusodinimo greitį ir kristališkumą, todėl yra tinkamas metodas aukštos kokybės feroelektrinėms plonomis plėvelėms gaminti. Šiuolaikinėmis technologijomis galima sukurti dirbtines heterostrukūras iki pat vienetinės gardelės tikslumu, sukelti dideles deformacijas dėl epitaksinių neatitikimų tarp sluoksnio ir substrato, bei tiksliai valdyti katijonų ir anijonų cheminę sudėtį ir defektų struktūras. Visa tai leidžia tirti naujas medžiagų būsenas ir neįprastus fizinius reiškinius.

Impulsinio lazerinio nusodinimo (PLD) pagrindai

Impulsinis lazerinis nusodinimas (PLD) yra fizikinis garų nusodinimo (PVD) metodas, naudojamas plonų sluoksnių gamybai medžiagų moksle ir inžinerijoje. Šio įrenginio schematinis vaizdas pateiktas 1 paveiksle. Tai metodas, skirtas įvairių medžiagų plonų sluoksnių nusodinimui ant substrato, kurio metu impulsiniu lazeriu vykdoma taikinio abliacija (medžiagos pašalinimas), po kurios abliatuota medžiaga nusėda ant substrato ir suformuoja ploną plėvelę [6]. Esminiai bandinių paruošimo šiuo metodu etapai apima taikinio paruošimą, tinkamo substrato parinkimą ir paruošimą, aplinkos slėgio nustatymą, lazerio energijos ir srauto reguliavimą, nusodinimo temperatūros ir slėgio nustatymą, kaitinimo bei aušinimo greičio kontrolę ir vėlesnį atkaitinimą.



1 pav. Impulsinio lazerinio nusodinimo įrenginio schema [7].

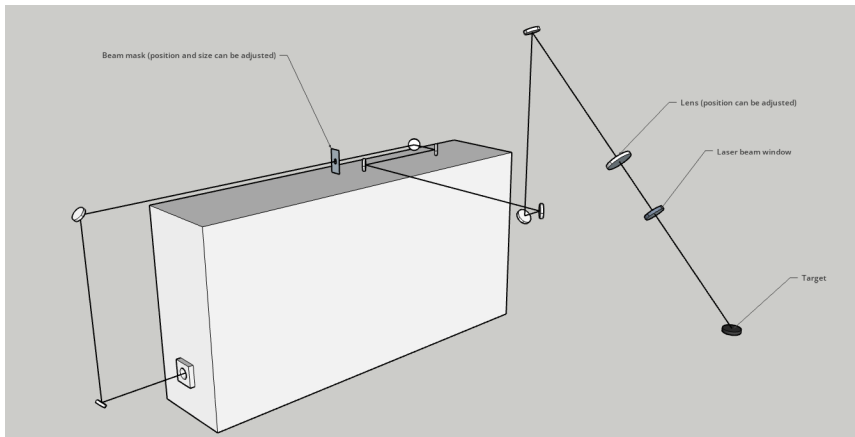
6.2. Eksperimentinė įranga ir metodai

Impulsinis lazerinis nusodinimas

Naudotos komercinės impulsinio lazerinio nusodinimo (PLD) sistemos, pagamintos TSST kompanijos (Nyderlandai), aprūpintos „Coherent COMPex Pro 205F KrF“ lazeriu ($\lambda = 248$ nm, impulso trukmė 20 ns (FWHM), didžiausias kartoavimo dažnis 50 Hz, didžiausia impulso energija 700 mJ, vidutinė galia 700 mJ).

PLD sistema turi dvi vakuumo kameras: pagrindinę ir įkrovimo kamerą. Pagrindinėje kameroje įrengtos Pfeiffer Vacuum MVP 015-2 ir HiPace 80 vakuuminės pompos, o įkrovimo kameroje – Pfeiffer Vacuum MVP 015-2 ir HiPace 80 pompos. Ši sistema leidžia pasiekti vakuumo lygį apie 10^{-7} mbar įkrovimo kameroje ir apie 10^{-9} mbar pagrindinėje kameroje. Substratai ir taikiniai įkeliami ir išimami per įkrovimo kamerą, taip sumažinant siurbimo laiką, palaikant itin aukštą vakuumą ir išvengiant medžiagų užteršimo.

Lazerio spindulys, nukreiptas per kintamąją spindulio kaukę, skirtą pašalinti nehomogeniškas spindulio dalis, pasižymi energijos pasiskirstymu, artimu „viršutinės kepurės“ profiliui išilgai horizontalios ašies ir beveik Gauso profiliui išilgai vertikalios ašies. Spinduliui nukreipti naudojami ultravioletinių spindulių lydyto silicio dioksido veidrodžiai, o spindulys fokusuojamas į taikinį per 75 mm skersmens planinį išgaubtą lęšį. Kiekvienas optinis elementas – veidrodis ar lęšis – sumažina spindulio energiją apie 10 %, todėl galutinė lazerio energija, pasiekianti taikinį, gali skirtis. Siekiant kontroliuoti lazerio energiją, priešingoje kameros pusėje įrengtas lazerio energijos matuoklis („Coherent EnergyMax“). Lazerio spindulio kelio schema pateikta 2 paveiksle. Ši schema gali skirtis priklausomai nuo naudojamo lazerio ir pageidaujamos lazerio fluencijos (paprastai lazerio kelias yra apie 5 metrus).



2 pav. Lazero spindulio kelio nuo lazerio iki taikinio schema.

Dielektrinės spektroskopijos matavimo įranga

Žemo dažnio sritis

Tilto metodas yra patikimas būdas nustatyti medžiagų dielektrines savybes žemo dažnio diapazone nuo 20 Hz iki 1 MHz. Matavimai buvo atlikti naudojant precizinį LCR matuoklį HP4284A („Hewlett-Packard“, JAV). Šis metodas remiasi nežinomos talpos dielektrinės medžiagos palyginimu su etaloniniais kondensatoriais tiltelio grandinėje.

Aukšto dažnio sritis

Aukšto dažnio dielektriniai matavimai diapazone nuo 1 MHz iki 1 GHz buvo atliekami naudojant koaksialinės linijos spektrometrą. Dėl kabelio induktyvumo įtakos matavimo rezultatai šiame diapazone atliekami naudojant bendraašę liniją ir spektrometrą su vektoriniu tinklo analizatoriumi (VNA). Bandinys talpinamas bendraašės perdavimo linijos gale, tarp vidinio laidininko ir trumpojo stūmoklio, tokiu būdu suformuojant kondensatorių [8].

Mikrobangų srities matavimai

Dėl matavimo apribojimų, kuriuose reikia matuoti dominuojantį TE₁₀ modą ir jo ribinį dažnį, buvo naudojami trys skirtingi bangolaidžiai: X juostos (8–12,5 GHz), Kα juostos (18–26,5 GHz). Bandiniai buvo tvirtinami sidabrine pasta prie bandinio laikiklio – metalinės plokštelės su anga, kurios dydis atitinka bangolaidžio skerspjuvį. Be to, matavimo įrangos kalibravimui ir sisteminių paklaidų sumažinimui naudotos dvi papildomos metalinės plokštelės – vientisa ir su anga.

Dažnio priklausomiems atspindžio (R*) ir perdavimo (T*) koeficientams matuoti naudoti generatoriai ГКЧ-60 (X juostai) ir vektorinis tinklo analizatorius (VNA) („ГКЧ-60“, X juostoje; „ГКЧ-60“ Kα juostoje). Bandiniai buvo pritvirtinti sidabro pasta prie metalinio laikiklio, kuriame buvo anga, atitinkanti bangolaidžio skerspjuvio dydį.

6.3. PbZr_{0,2}Ti_{0,8}O₃ plėvelės dielektrinių ir pjezoelektrinių savybių tyrimas

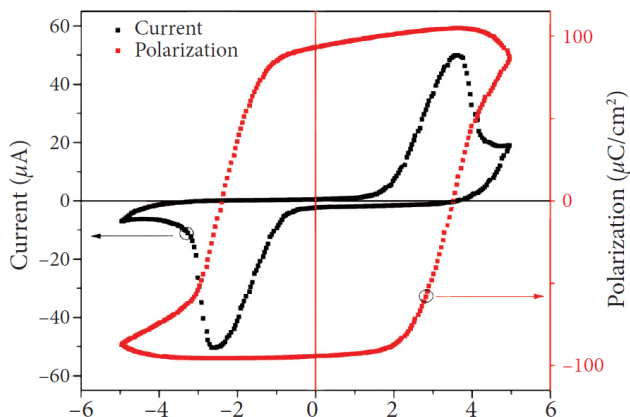
PbZr_{0,2}Ti_{0,8}O₃ (PZT) epitaksinės oksidų heterostruktūros buvo pagamintos impulsiniu lazeriniu nusodinimu ant SrTiO₃ (STO) monokristalinio substrato, orientuoto (100) kryptimi, 25 mm² plote.

Šiam darbui naudoti SrTiO₃ (001) substratai, kurių nupjovimo kampas buvo mažesnis nei 0,5°. Substratai buvo valomi ultragarsu acetone, siekiant pašalinti alyvas, tepalus ir organines liekanas, galimai susikaupusias ant substrato paviršiaus laikymo ar tvarkymo metu. Tada substratas buvo papildomai valomas izopropanoliu, kad būtų pašalinti acetono likučiai ir organiniai teršalai, taip užtikrinant švarų ir be likučių paviršių. Galiausiai substratas buvo chemiškai išdinamas 10:1 buferiniame vandenilio fluorida tirpale 20 sekundžių [9].

PZT plėvelė buvo nusodinta naudojant tikslius parametrus, siekiant optimizuoti jos augimą ir savybes. Nusodinimo parametrai: substrato temperatūra – 555 °C, aplinkos slėgis – 0,2 mbar, lazerio impulsų skaičius – 10 000, lazerio energijos srautas – pastovus, 1 J/cm². Po

nusodinimo bandiniai buvo atkaitinami in-situ deguonies atmosferoje, esant 200 mbar slėgiui. Atkaitinimo procesas buvo pradėtas atvėsus temperatūrai iki 250 °C ir truko 30 minučių. Atkaitinimas buvo atliktas siekiant sumažinti deguonies vakansijų skaičių bei minimizuoti plėvelės elektrinį nuotėkį. Bandiniai buvo aušinami 20 °C per minutę greičiu. Gautos plėvelės storis buvo apie 100 nm.

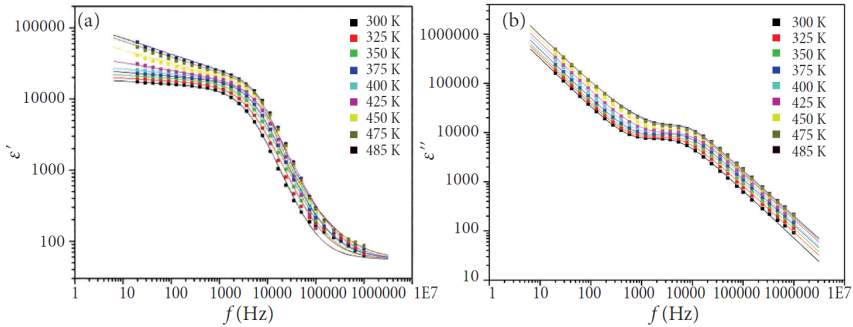
3 paveiksle pavaizduotos tipiškos bandinio poliarizacijos ir perjungimo srovės histerezės kilpos. Poliarizacijos kilpa rodo charakteringą feroelektrinę elgseną, pasižyminčią aiškia likutine poliarizacija ir prievartine įtampa. Be to, histerezės kilpos forma patvirtina įrenginio feroelektrines savybes. Aiškios teigiamos ir neigiamos perjungimo srovės matavimo viršūnės rodo poliarizacijos persijungimą.



3 pav. LSMO/PZT/Cu/Au sluoksnių feroelektrinio kondensatoriaus poliarizacijos ir srovės histerezės kilpos. Matavimai atlikti naudojant trikampio formos įtampos impulsą, kurio dažnis 1 kHz.

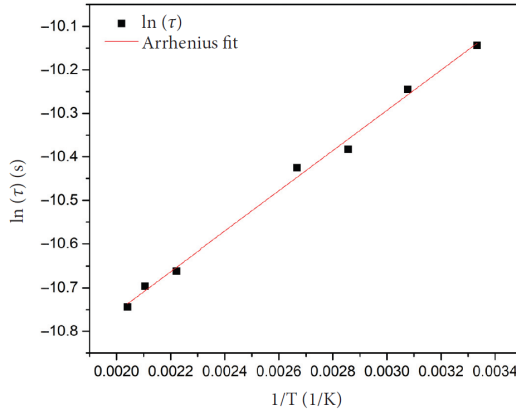
Dielektrinė skvarba buvo nustatyta iš talpos matavimų (žr. 4 pav.). Pastebėta, kad dielektriniai nuostoliai, kurie dažniausiai atsiranda dėl erdvinio krūvio ir domenų sienelių relaksacijos, mažėja didėjant išorinio lauko dažniui. Dielektrinių duomenų tinkinimas buvo atliktas naudojant formulę (4), apjungiančią Debye tipo ir „universalioją“ reakcijas bei įvertinančią laidumo indėlį, kuris eksperimentiškai stebimas žemų dažnių diapazone, pagal Raicu pasiūlymą [10].

$$\varepsilon(i\omega) = \varepsilon_{\infty} + \frac{\sigma}{i\omega} + \frac{\varepsilon_0 - \varepsilon_{\infty}}{[(i\omega\tau)^{\alpha} + (i\omega\tau)^{1-\beta}]^{\gamma}} \quad (4)$$



4 pav. PZT plėvelės dielektrinės skvarbos realiosios (a) ir menamosios (b) dalių priklausomybė nuo dažnio. Išsitiesinės linijos tiksliai atitinka duomenų taškus pagal Raicu sąryšį.

5 pav. pateikiama vidutinio relaksacijos laiko priklausomybė nuo atvirkštinės temperatūros vertės. Taškai atspindi vidutinius relaksacijos laikus konkrečiose temperatūrose, o linija gauta pritaikius Arenijaus lygtį (2) [11].



5 pav. Vidutinės relaksacijos trukmės priklausomybė nuo atvirkštinės temperatūros PZT keramikoje. Duomenų taškai rodo vidutinius relaksacijos laikus, o linija gauta pritaikius Arenijaus lygtį (2).

Ši priklausomybė atspindi ankstyvuosius domenų sienelių svyravimus vietiniame potencialo šulinyje [12].

6.4. 0,8(Na_{0,5}Bi_{0,5}TiO₃)-0,2(BaTiO₃) plonų plėvelių nusodinimo impulsiniu lazeriu parametrų optimizavimas

Taikinio ir substrato paruošimas

Pagal užsakymą pagamintas NBT-BT taikinyms buvo išanalizuotas rentgeno spindulių difrakcijos (XRD) metodu, patvirtinant fazės grynumą ir stochiometriją. Buvo naudojami substratai iš silicio su sidabro sluoksniu (nusodintu terminiu garinimu) ir silicio su platinos sluoksniu (nusodintu dulkinimo metodu). Rentgeno spindulių difrakcijos (XRD) matavimai patvirtino, kad plėvelės cheminė sudėtis atitinka taikinį ir leidžia pasiekti stochiometrinį augimą. Gauti XRD rezultatai daugiausia atitiko [96-210-3298] „Crystallography Open Database“ įrašą, skirtą natrio bismuto titanatui, tačiau pastebėti pokyčiai dėl bario titanato priemaišų (įrašas [96-901-4274]).

Plėvelės sudėties analizė

Plėvelės elementinė sudėtis buvo patvirtinta energinės dispersinės rentgeno spektroskopijos (EDX) ir rentgeno spindulių difrakcijos metodais.

Nusodinimo parametrų optimizavimas (pagrindinės išvados)

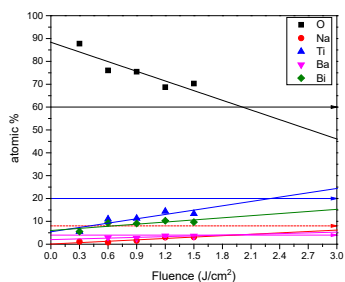
Lazerio fluencijos optimizavimas

Plėvelės stochiometrijai itin didelę įtaką darė lazerio fluencija. Siekiant išanalizuoti fluencijos poveikį plėvelės sudėčiai, visų bandinių EDX analizės duomenys buvo pateikti pagal nusodinimo fluenciją 1 lentelėje, įtraukiant tik tiriamos medžiagos sudėties elementus.

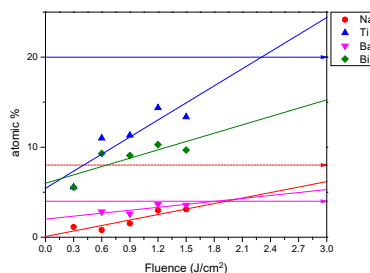
1 lentelė. Visų bandinių EDX analizė, kad būtų įtraukti tik mūsų medžiagos sudėties elementai.

Energijos tankis (J/cm ²)	Deguonis	Natrio	Titanas	Baris	Bismutas
0.3	87.78	1.14	5.57	-	5.54
0.6	76.06	0.8	11	2.83	9.3
0.9	75.49	1.53	11.32	2.59	9.08
1.2	68.71	2.98	14.38	3.65	10.28
1.5	70.3	3.1	13.36	3.57	9.68
Idealus	60	8	20	4	8

Kaip matyti, didinant energijos tankį galima pasiekti stochiometrinį augimą ir veiksmingiau padengti substrato paviršių. Kiekvieno komponento atveju pastebėta aiški tiesinė priklausomybė. Šios analizės rezultatai pateikti 6 paveiksle.



(a)



(b)

6 pav. a) Elementų atominės procentinės dalies priklausomybė nuo fluencijos nusodinimo metu, b) mažesnių elementų atominių procentinių dalių priartintas vaizdas.

Nustatyta, kad optimalus energijos tankis beveik stochiometriniam augimui yra maždaug 2,1 J/cm². Esant mažam srautui (pvz., 0,3 J/cm²), nusodinimas buvo nebaigtas ir medžiaga išsisklaidė.

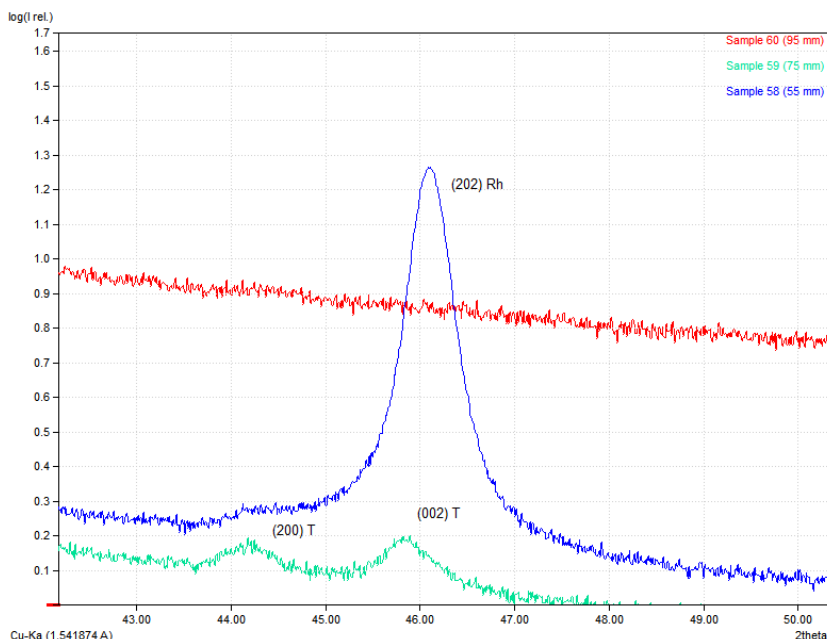
Padėklo temperatūros poveikis

SEM ir EDX analizės buvo atliktos esant skirtingoms substrato temperatūroms (550 °C, 600 °C ir 650 °C). Aukštesnė nusodinimo temperatūra (650 °C) reikšmingai pagerina grūdelių vystymąsi ir kristalines savybes, todėl ši temperatūra laikoma optimalia aiškiai suformuotoms, aukštos kokybės plonoms plėvelėms gauti.

Nustatyta, kad keičiant nusodinimo temperatūrą plėvelės cheminė sudėtis išlieka beveik nepakitusi. Tačiau aukštesnė temperatūra gali šiek tiek pakeisti natrio bismuto titanato ir bario titanato balansą medžiagoje, didindama pirmojo komponento dalį.

Atstumas tarp taikinio ir substrato (T-S atstumas)

Trys bandiniai (58, 59 ir 60) buvo nusodinti naudojant skirtingus atstumus tarp taikinio ir substrato: 55 mm, 75 mm ir 95 mm.



7 pav. Rentgeno spinduliuotės difrakcijos spektras (XRD) 58 (55 mm), 59 (75 mm) ir 60 (95 mm) bandiniams, pateikiantis rentgeno

spinduliuotės intensyvumo priklausomybę nuo 2θ kampo, su priartinta sritimi ties $46^\circ 2\theta$ kampu.

XRD rezultatai, pateikti 7 paveiksle, patvirtina perėjimą tarp rombinės ir tetragoninės fazių, kuris priklauso nuo nusodinimo sąlygų. Tai matyti iš (2 0 2) difrakcinės smailės skilimo į (0 0 2) ir (2 0 0) smailes, kaip buvo pastebėta (1-x)BNT-xBT keramikoje [13], [14].

Išvados ir būsimi darbai

Tyrimo metu buvo sėkmingai nustatytos optimalios impulsinio lazerinio nusodinimo (PLD) sąlygos NBT-BT plonomis plėvelėms, derinant stechiometriją, kristališkumą ir morfologinį vientisumą.

Tolesnės nusodinimo parametrų optimizacijos kryptys:

1. Temperatūra: rekomenduojama 600°C arba šiek tiek aukštesnė (iki 700°C , atsižvelgiant į galimas pasekmes).

2. Slėgis: siūloma ištirti tarpinius slėgius, pavyzdžiui, 0,15 mbar.

3. Atstumas: optimalus atstumas tarp taikinio ir substrato yra 55–75 mm, siekiant geriausiai subalansuoti kristališkumą ir paviršiaus kokybę.

4. Energijos tankis: siekiant optimalios cheminės sudėties, rekomenduojama fluenciją palaikyti apie $1,8\text{--}2,1\text{ J/cm}^2$.

6.5. ZrSnSe₃ plonų plėvelių nusodinimo impulsiniu lazeriu parametrų optimizavimas

Šiame skyriuje nagrinėjama ZrSnSe₃ plonų plėvelių gamyba ir optimizavimas naudojant impulsinį lazerinį nusodinimą (PLD). Buvo tiriamos plėvelių struktūrinės, morfologinės ir sudėties savybės, siekiant optimizuoti nusodinimo parametrus ir gauti aukštos kokybės plonas plėveles optoelektroniniams taikymams.

Pagrindinės išvados ir eksperimentinis metodas

Motyvacija ir $ZrSnSe_3$ plonų plėvelių svarba

$ZrSnSe_3$ yra perspektyvi medžiaga fotovoltiniams ir optoelektroniniams taikymams dėl siauro juostos tarpo ($\sim 0,65$ eV) ir stabilumo aplinkos sąlygomis. Plonos plėvelės pasižymi dideliu absorbcijos efektyvumu ir mažomis medžiagos sąnaudomis, todėl jos tinkamos plačiam taikymui.

Impulsinis lazerinis nusodinimas (PLD) ir taikinių gamyba

Pradžioje nusodinimui buvo naudojami 4 taikiniai: $ZrSe_2$, $SnSe$, $SnZrSe_3$ (šis taikiny s vėliau modifikuotas pridėdant 40 % $ZrSe_2$, tad galutinė sudėtis tapo 40 % $ZrSe_2$ + 60 % $SnZrSe_3$). $ZrSe_2$ ir $SnSe$ buvo įsigyti iš „Testbourne Ltd.“, o $SnZrSe_3$ pagamintas kietojo kūno reakcijos būdu (pradiniai elementai Sn, Zr, Se sumaišyti ampulėje ir kaitinti 700 °C temperatūroje 48 valandas). Kristalai sumalti į miltelius ir šaltai suspausti 100 MPa slėgiu į granules.

Naudoti du metodai norint gauti plonas plėveles:

1. Optimizuoti $ZrSe_2$ ir $SnSe$ taikinių nusodinimo parametrus, kad būtų suformuoti daugiasluoksniai sluoksniai, kuriuos vėliau atkaitinant būtų gauta vientisa plėvelė.

2. Naudoti pagal užsakymą pagamintą $SnZrSe_3$ taikinį vientisos plėvelės sukūrimui vieno nusodinimo metu.

Geros kokybės plėvelės kriterijai:

1. Švari paviršiaus morfologija, be lašelių ar kitų struktūrinių defektų.

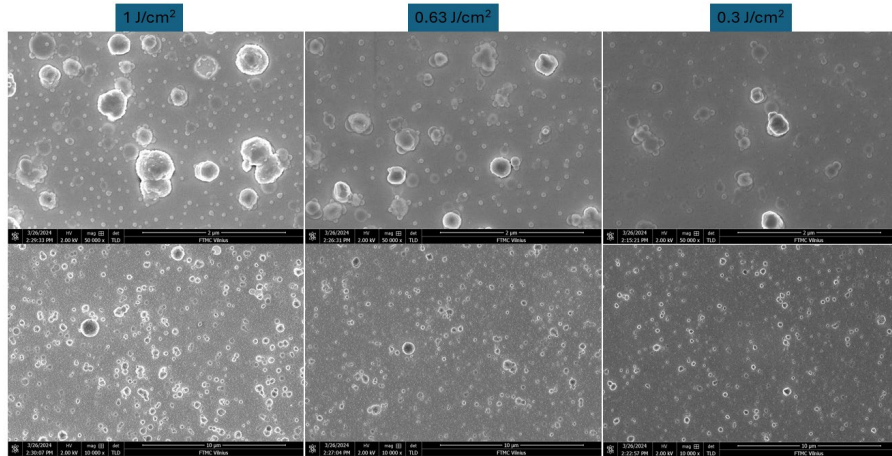
2. Tikslus Sn/Zr/Se elementų santykis (Se koncentraciją galima koreguoti vėlesniu atkaitinimu seleno prisotintoje aplinkoje).

3. Minimalus deguonies ar kitų priemaišų kiekis. Deguonies užterštumas kritiškai svarbus junginiams, turintiems Ti ar Zr, todėl būtina vengti oksidų susidarymo. Kadangi selenidai yra jautrūs oksidacijai, jie lengvai suyra, formuodami Zr-oksidas esant deguoniui.

Nusodinimo impulsiniu lazeriu parametru optimizavimas

Srauto poveikis

Optimalus lazerio srautas buvo nustatytas remiantis skenuojančios elektroninės mikroskopijos (SEM) vaizdais, gautais iš bandinių, nusodintų esant skirtingoms lazerio fluencijoms (pateikta 8 pav.).



8 pav. SEM vaizdai, gauti iš bandinių, nusodintų esant skirtingoms lazerio fluencijoms.

Pagrindinė problema, kuri pastebima šiose plėvelėse – „rieduliai“ (stambios dalelės), kurios trukdo tolygiam plėvelės augimui. Matyti, kad dalelių kiekis ant paviršiaus mažėja mažėjant lazerio fluencijai, todėl tolesniems eksperimentams buvo pasirinktas fluencijos intervalas tarp 0,3 ir 0,6 J/cm².

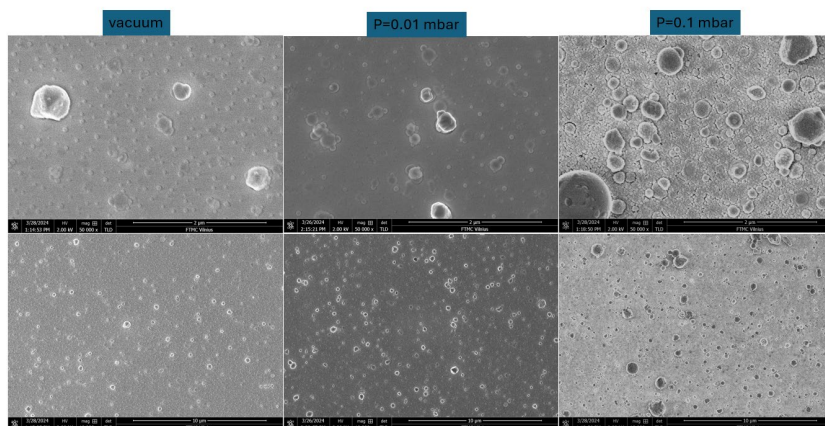
Se/Zr santykis nebuvo optimalus (pagal cheminę formulę idealus santykis turėtų būti 2:1). Deguonies koncentracija buvo įvertinta naudojant energinės dispersinės rentgeno spektroskopiją (EDX). Ši analizė neparodė deguonies pėdsakų, o tai būtina aukštos kokybės plėvelėms gauti (2 lentelė).

2 lentelė. Cheminė sudėtis ir elementų santykis ZrSnSe₃ plėvelėse, nustatyta pagal EDX analizės rezultatus.

Pavyzdys	Se/Zr santykis	Deguonis
ZR01, F: 1 J/cm ²	3,6	Jeį yra, minimalus
ZR02, F: 0,63 J/cm ²	4,0	Jeį yra, minimalus
ZR03, E: 0,3 J/cm ²	4,1	Jeį yra, minimalus

Aplinkos slėgio poveikis

Siekiant įvertinti aplinkos slėgio poveikį paviršiaus morfologijai, buvo pagaminti trys bandiniai, naudojant 0,3 J/cm² lazerio fluenciją, esant skirtingoms aplinkos slėgio sąlygoms: vakuume, 0,01 mbar ir 0,1 mbar. Gautų bandinių SEM vaizdai pateikti 9 paveiksle.

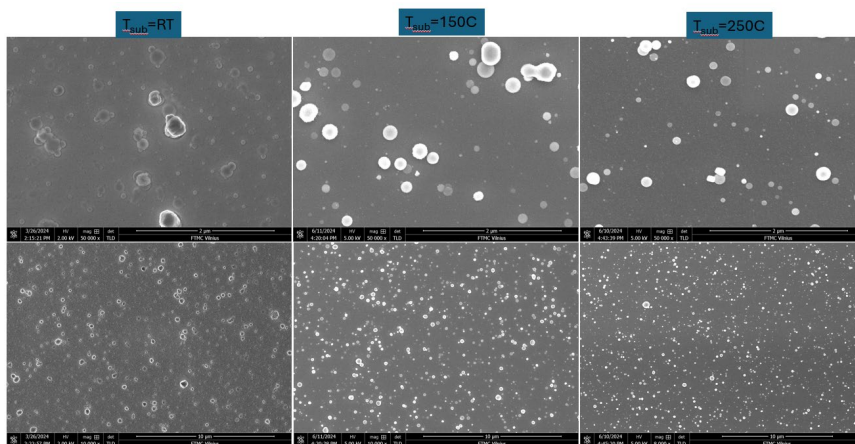


9 pav. SEM vaizdai ZrSe₂ bandinių, nusodintų esant skirtingam aplinkos slėgiui.

Kaip matyti, plėvelė, nusodinta vakuume, yra lygi, tačiau joje susidarė daug mažų dalelių (~50 nm skersmens). Nusodinant plėvelę esant 0,1 mbar argono slėgiui, pastebimos didesnės dalelės. Geriausi rezultatai gauti naudojant 0,01 mbar slėgį, kuomet mažų dalelių kiekis minimalus, o didelės dalelės praktiškai nesusidaro. Dalies dalelių netaisyklinga forma gali rodyti Stranskio–Kranštanovo (SK) augimo režimą.

Pagrindo temperatūros poveikis

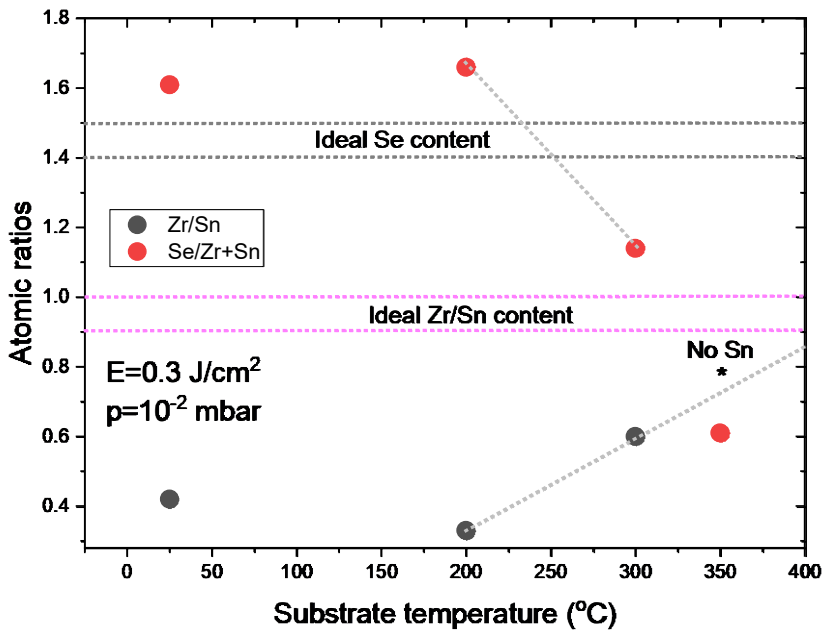
10 pav. pateiktas substrato temperatūros poveikis $ZrSe_2$ plėvelės morfologijai. Didėjant substrato temperatūrai, mažėja netaisyklingų dalelių kiekis ir dydis, o tai leidžia išvengti SK augimo režimo. Substrato temperatūros padidinimas iki $250\text{ }^\circ\text{C}$ taip pat padeda sumažinti dalelių kiekį ir jų dydį.



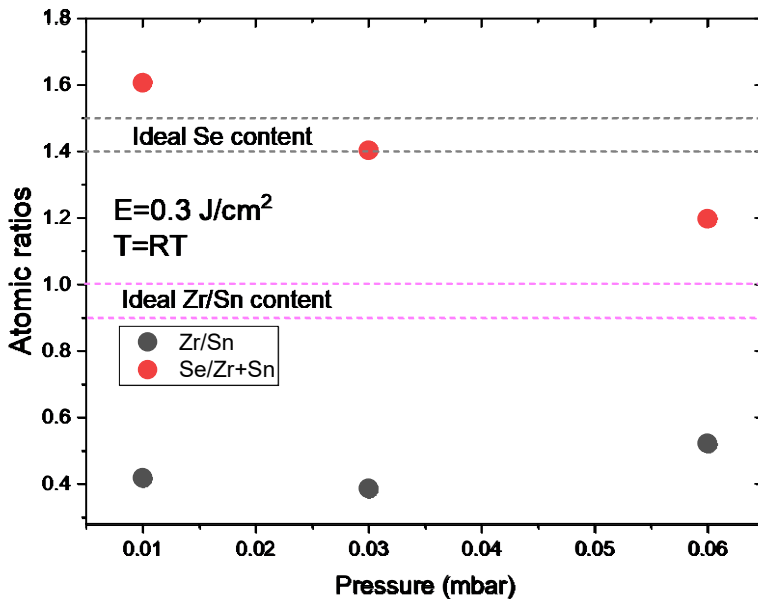
10 pav. $ZrSe_2$ bandinio, nusodinto esant skirtingoms substrato temperatūroms, SEM vaizdai.

Esant aukštesnei nei $300\text{ }^\circ\text{C}$ temperatūrai, pastebėtas medžiagos praradimas ir susiformavo nepageidaujamos $SnSe$ fazės.

Remiantis šiais matavimais, galima prognozuoti, kaip nusodinimo parametrai veikia plėvelės savybes ir kuriomis kryptimis vertėtų tęsti tyrimus.



11 pav. Atomų santykio priklausomybė ZrSnSe_3 bandiniuose nuo nusodinimo temperatūros.



12 pav. Atomų santykio priklausomybė ZrSnSe_3 bandiniuose nuo nusodinimo slėgio.

Iššūkliai ir ateities kryptys

Stechiometrinė kontrolė išlieka iššūkiu dėl skirtingų Zr ir Sn nusodinimo greičių. Tolesniuose tyrimuose rekomenduojama:

1. Sumažinti deguonies užterštumą, kad būtų išsaugotos optoelektroninės savybės;
2. Formuoti daugiasluoksnes $ZrSe_2$ ir $SnSe$ struktūras, siekiant pagerinti plėvelių homogeniškumą;
3. Ištirti atkaitinimo procedūras argono atmosferoje, siekiant padidinti plėvelių kokybę.

Išvados

Šiame skyriuje parodyta impulsinio lazerinio nusodinimo (PLD) metodo tinkamumas $ZrSnSe_3$ plonųjų plėvelių gamybai, aptarti pagrindiniai iššūkliai ir galimi jų sprendimo būdai. Tyrimas sudaro pagrindą tolesniam aukštos kokybės stochiometrinių $ZrSnSe_3$ plėvelių vystymui, siekiant jas panaudoti naujos kartos optoelektroniniuose prietaisuose.

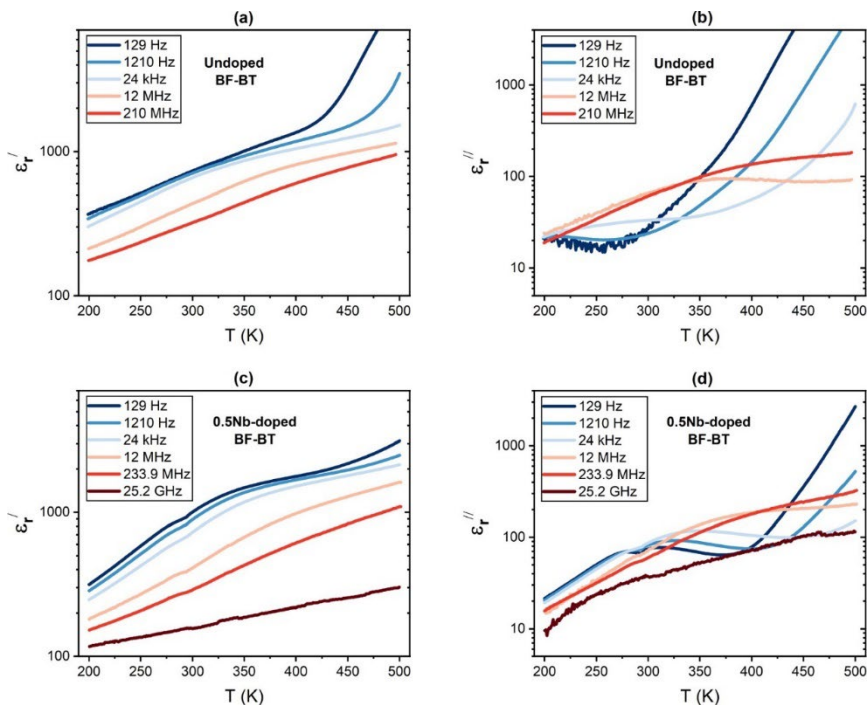
6.6. Nb legiruotos ir grynos $0,7(BiFeO_3)-0,3(BaTiO_3)$ keramikos dielektrinių savybių tyrimas

Sintezė ir apdorojimas

Gryna $(0,7BiFeO_3-0,3BaTiO_3)$ ir Nb legiruota $(0,7BiFe_{0,995}Nb_{0,005}O_3-0,3BaTiO_3)$ keramika buvo pagaminta kietojo kūno reakcijos metodu. Naudoti Bi_2O_3 (99 %), Fe_2O_3 (99 %), $BaCO_3$ (99 %), TiO_2 (99 %) ir Nb_2O_5 (99,99 %) milteliai (Sigma-Aldrich, Jungtinė Karalystė). Milteliai buvo kalcinuoti 800 °C temperatūroje 4 valandas, po to sukepinti 1010 °C temperatūroje 3 valandas. Gautų keramikos bandinių santykinis tankis siekė 95 %. Plokštuminės kondensatoriaus struktūros buvo suformuotos ant abiejų disko formos bandinio pusių uždedant sidabrinis kontaktus.

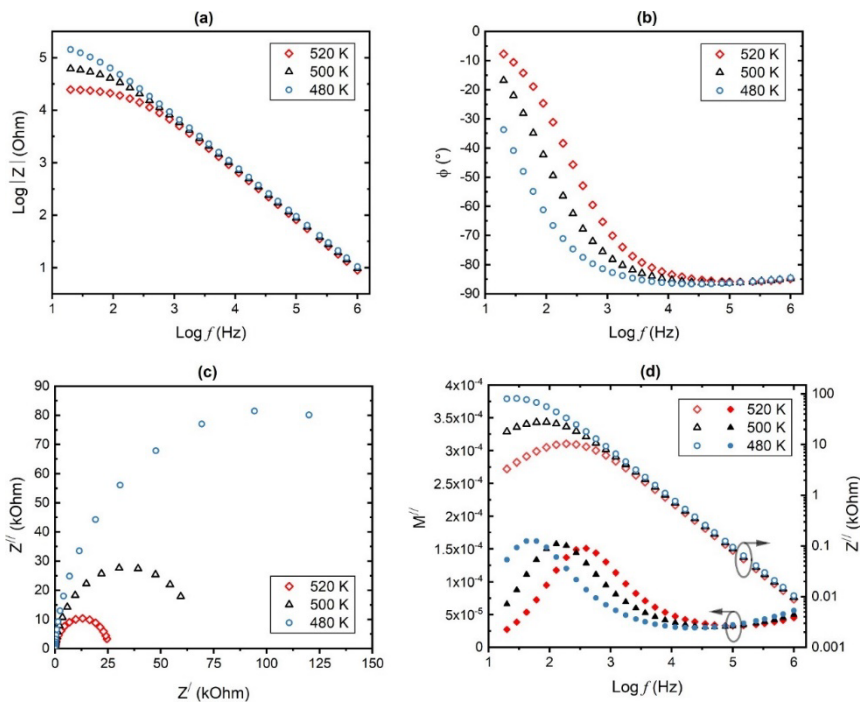
Dielektrinės savybės

13 pav. pateikta grynos (nedopuotos BF-BT) ir Nb legiruotos (0,5Nb-BF-BT) keramikos kompleksinės dielektrinės skvarbos realiosios ir menamosios dalių priklausomybė nuo temperatūros. Abiem atvejais realioji skvarbos dalis kinta priklausomai nuo dažnio ir stipriai išauga pradėdant nuo 200 K. Aiškų padidėjimą matomas ties 350 K, vėliau skvarba tolygiai didėja iki maksimumo, pasiekto ties Kiuri tašku (740 K) [15]. Nb legiruotos keramikos menamoji dielektrinės skvarbos dalis turi dažnio priklausomą maksimumą tarp 270 ir 400 K, kuris didėjant dažniui slenkasi į aukštesnės temperatūros pusę. Nedopuota BF-BT keramika taip pat pasižymi relaksaciniais efektais, tačiau silpnesniais.



13 pav. Nedopuotos (a)-(b) ir 0,5Nb legiruotos BiFeO₃-BaTiO₃ (BF-BT) keramikos (c)-(d) kompleksinės dielektrinės skvarbos realiosios (ϵ_r') ir menamosios (ϵ_r'') dalių priklausomybė nuo temperatūros, išmatuota plačiame dažnių diapazone [16].

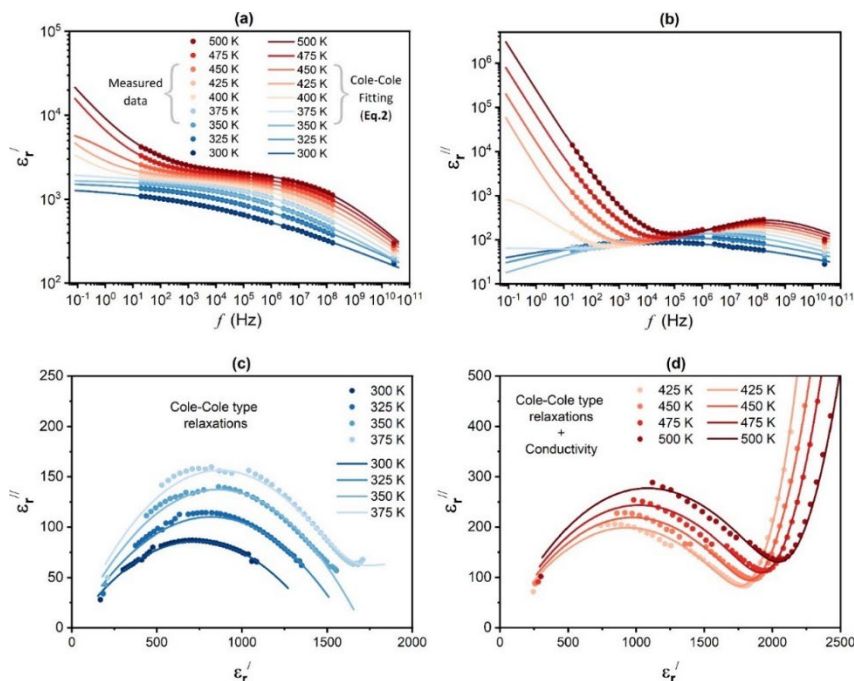
Terminiškai aktyvuota dielektrinė elgsena paprastai būdinga netvarkingiems kietiesiems kūnams, tokiems kaip dipoliniai stiklai ar relaksorinės feroelektrinės medžiagos. Šiose medžiagose pastebimas platus relaksacijos laiku diapazonas, kuris kyla dėl poliarinių nanosričių (PNR) arba frustruotų dipolių. Spartus dielektrinės skvarbos menamosios dalies (ϵ_r'') padidėjimas esant aukštesnei nei 400 K temperatūrai, kaip parodyta 14 pav. b ir d grafikuose, susijęs su išaugusiu medžiagos elektriniu laidumu (σ), kurio priklausomybė nuo dažnio šiame temperatūrų intervale yra aiškiai atvirkštinė [17].



14 pav. Nb legiruotos BF-BT keramikos impedanso spektroskopijos duomenys pateikti įvairiomis formomis, parodant elektrinio atsako pokytį iš talpinio (fazės kampas $< -45^\circ$) į varžinį (fazės kampas $> -45^\circ$) žemuose dažniuose ir aukštose temperatūrose. Diagramose pateikiami: (a) impedanso dydžio, (b) fazės kampo Bode grafikai, (c) kompleksinio impedanso grafikai ir (d) kompleksinio modulio bei impedanso menamųjų dalių Bode grafikai [16].

15 pav. pateikiami kompleksinės dielektrinės skvarbos duomenys, priklausantys nuo dažnio esant skirtingoms temperatūroms. Šie duomenys leidžia išsamiau analizuoti dielektrinės relaksacijos charakteristikas. Dielektriniai spektrai buvo analizuoti naudojant empirinę Cole-Cole lygtį (5), papildytą laidumo indėliu į nuostolius esant žemiems dažniams ir aukštoms temperatūroms. Šia lygtimi buvo modeliuojami eksperimentiniai kompleksinės dielektrinės skvarbos duomenys bei apskaičiuoti dielektriniai parametrai.

$$\varepsilon^* = \sum_{i=1}^n \left(\varepsilon_{\infty i} + \frac{\Delta \varepsilon_i}{1 + (i\omega\tau)^{1-\alpha_i}} \right) + \frac{\sigma}{2\pi i f k'} \quad (5)$$



15 pav. Parodyta 0,5Nb-BiFeO₃-BaTiO₃ keramikos dielektrinės skvarbos realiosios ir menamosios komponentės priklausomybė nuo dažnio esant įvairioms temperatūroms. Linijomis pažymėti optimalūs eksperimentinių duomenų taškų atitikimai pagal (5) lygtį. Kompleksinės dielektrinės skvarbos (Cole-Cole) grafikai atspindi

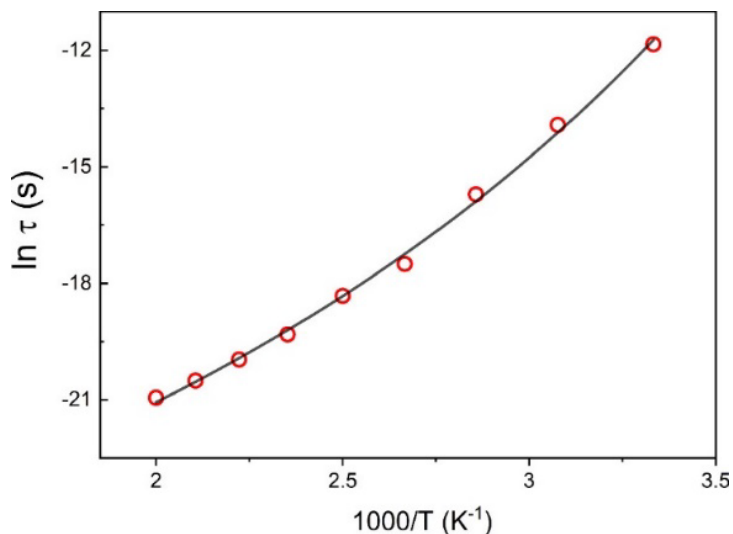
terminiškai aktyvuotus laidumo nuostolius žemos (c) ir aukštos (d) temperatūrose diapazonuose [16].

Dielektrinės savybės, išmatuotos tarp 300 ir 350 K, rodo vienalytę dispersiją visame tiriamajame dažnių diapazone, kaip parodyta 15 pav. (a) ir (b). Mažėjant temperatūrai, dispersija tampa ryškesnė žemesniuose dažniuose, tačiau išlieka simetriška ir buvo modeliuojama naudojant lygtį su vienu relaksacijos procesu ($n = 1$). Vienas dielektrinės relaksacijos mechanizmas taip pat aiškiai matomas pusapskritimio formos Cole-Cole grafike (15 pav. c).

Tarp 350 K ir 400 K dielektrinės dispersijos kreivės rodo papildomo žemo dažnio nuostolių proceso atsiradimą (15 pav. b ir d). Šis reiškinys susijęs su didėjančiu elektriniu laidumu. Esant temperatūrai virš 450 K, pastebimas nedidelis dielektrinės skvarbos padidėjimas kartu su augančiais dielektriniais nuostoliais. Tai galima paaiškinti lokalizuotų elektros krūvių kaupimusi grūdelių sąsajose ir jų judėjimu aukštoje temperatūroje, vadinamu Maksvelo-Vagnerio relaksacija [20].

Virš 400 K išlieka žemo ir aukšto dažnio dispersijos, kurių temperatūriniai pokyčiai vyksta pagal nuoseklų dėsnį. Jų dažninės priklausomybės buvo analizuotos tuo pačiu metodu. Kruopštesnė analizė atskleidė nedidelius neatitikimus 10^4 – 10^6 Hz dažnių diapazone (minimalūs dielektriniais nuostoliais). Tiksliausias suderinimas buvo pasiektas pritaikant antrinį Cole-Cole modelį. Tačiau dėl šios relaksacijos silpnumo ir persidengimo su aukšto dažnio relaksacija detalesnė analizė nėra įmanoma. Apskaičiuotos k reikšmės (1,001 esant 500 K, 1,006 esant 475 K, 1,012 esant 450 K ir 1,069 esant 425 K) išliko artimos 1, patvirtindamos, kad pagrindinį indėlį į ϵ_r'' lemia laidumo poveikis aukštesnėse temperatūrose.

Ryšys tarp vidutinės relaksacijos trukmės ir atvirkštinės temperatūros pateiktas 16 pav. Duomenys atitinka pritaikymo rezultatus, gautus aproksimuojant dielektrinės skvarbos dažninę priklausomybę pagal Cole-Cole formulę kartu su Vogel-Fulcher-Tamman dėsniu (3). Šie modeliai dažnai naudojami relaksorinių feroelektrikų relaksacinei dinamikai aprašyti [21].



16 pav. 0,5Nb-BiFeO₃-BaTiO₃ keramikos vidutinė relaksacijos trukmė yra atvirkščiai proporcinga temperatūrai.

Eksperimentiniams duomenims pritaikyta kreivė stipriai koreliuoja su šiais parametrais: $\tau_0=1,73 \times 10^{-12}$ s, $T_f=158 \pm 16$ K ir $E_a=0,194$ eV. Remiantis gautais duomenimis, akivaizdu, kad vidutinė relaksacijos trukmė didėja mažėjant temperatūrai ir gerokai skiriasi nuo Arrenijaus taisyklės esant nulinei temperatūrai ($T_f=0$). Todėl šis relaksacijos procesas yra panašus į dipoliniuose stikluose ar relaksoriniuose feroelektrikuose stebimus relaksacijos procesus, kuriems būdingas platus relaksacijos periodų diapazonas [23]-[25]. Aktyvacijos energija yra įprastame šioms sistemoms stebėtame intervale [24]. Palyginti su gryno BF-BT sudėtimi, BF-BT medžiagos papildymas Nb labai padidina medžiagos aktyvacijos energiją, o tai rodo, kad ilgo nuotolio sutvarkyta dipolinė konfigūracija sudėtingai vystosi veikiant elektriniam laukui dėl silpno kontakto tarp PNR [26], [27].

Išvada

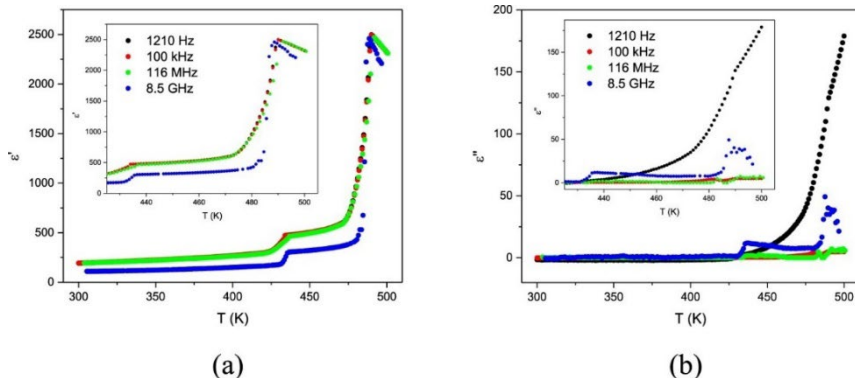
Nb legiruojant sėkmingai pagerinamos BF-BT keramikos dielektrinės, feroelektrinės ir elektrinės savybės. Empirinio Cole-Cole relaksacijos modelio panaudojimas rodo platų relaksacijos laikų diapazoną, kuriam būdingas pastebimas vidutinio relaksacijos laiko

nuokrypis. Šis mechanizmas panašus į feroelektrinių arba dipolinių stiklų relaksacijas ir vyksta temperatūrų intervale nuo 250 iki 500 K. Vogelio-Fulcherio-Tammano dėsnio laikymasis yra labai svarbus, nes jis pasižymi 158 K užšalimo temperatūra ir atitinkama 0,194 eV aktyvacijos energija. Šios vertės atitinka vertes, pastebėtas kitose relaksorinėse feroelektrinėse medžiagose. Ateityje reikėtų ištirti skirtingo Nb dopingo lygio įtaką fazinio perėjimo dinamikai ir dielektriko savybėms. Dielektrinės spektroskopijos derinimas su struktūrinio apibūdinimo metodais, tokiais kaip perdavimo elektronų mikroskopija (TEM), galėtų padėti geriau suprasti mikrostruktūrinės stebimo relaksorinio elgesio priežastis.

6.7. Dielektrinis $\text{PbHf}_{1-x}\text{Sn}_x\text{O}_3$ medžiagos tyrimas

$\text{PbHf}_{0.92}\text{Sn}_{0.08}\text{O}_3$ kristalai buvo išauginti savaiminės kristalizacijos metodu Taikosmosios fizikos institute MUT Varšuvoje (Lenkija). Kristalai buvo skaidrūs, jų forma - maži kubeliai ir strypeliai. Naudojant sidabro pastą, ant priešingų kristalų paviršių buvo pritvirtinti elektrodai, kuriais buvo atliekami dielektriniai matavimai tiltinėse ir bendraašėse sistemose.

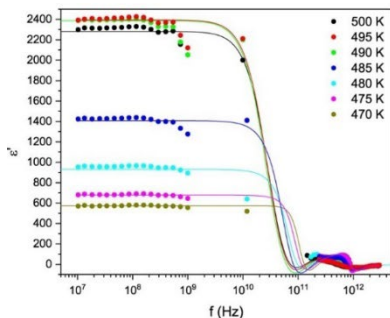
17 paveiksle pavaizduota temperatūros ir PHS kristalo kompleksinės skvarbos priklausomybė. Temperatūra T_1 , kuri šaldymo proceso metu yra 433 K, rodo tašką, kuriame įvyksta perėjimas tarp fazių A2 ir A1 [29]. Alavo (Sn) jonų pridėjimas į PbHfO_3 nesukelia tarpinės (IM) fazės susidarymo. Taip gali būti todėl, kad alavo koncentracija mūsų PHS ($\text{PbHf}_{1-x}\text{Sn}_x\text{O}_3$) junginiuose buvo mažesnė nei 6 %, t. y. mažiausia koncentracija, reikalinga tarpinei fazei susidaryti [29]. Perėjimas iš fazės A2 į fazę PE įvyksta esant kritinei temperatūrai T_c , apie 490 K. Įsivaizduojamosios skvarbos komponentės svyravimai esant kritinei temperatūrai (T_c) gali būti priskiriami kristalinės struktūros netobulumui, dėl kurio padidėja nuostoliai žemesniuose dažniuose.



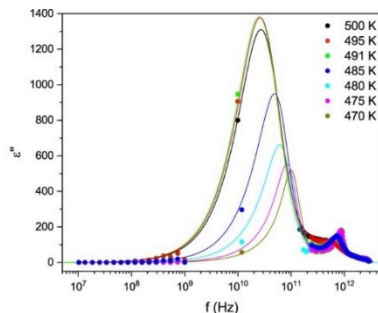
17 pav. PHS kristalų kompleksinės skvarbos tikrosios (a) ir įsivaizduojamos (b) dalies priklausomybė nuo temperatūros įvairiais dažniais.

Kompleksinės elektrinės skvarbos priklausomybė nuo dažnio (18 pav. (a ir b)) rodo tris atskirus reiškinius: Žemo dažnio dispersiją žemiau 10^2 Hz, didelį elektrinės skvarbos praradimą nuo 1 GHz ir nedidelę dispersiją terahercų (THz) diapazone. Pastarasis procesas vyksta esant aukštesnei nei 450 K temperatūroje. Artėjant Kiuri temperatūrai, grafike matoma didžiausia įsivaizduojamos komponentės vertė 8,5 GHz dažniu. Šio maksimumo aštrumas neleido jo tiksliai aprašyti klasikinėmis lygtimis, aiškinančiomis relaksacijos procesus. Norėdami išnagrinėti šią viršūnę, galime pasinaudoti rezonansinės dispersijos formule (6), sujungdami dvi pritaikytas viršūnes: vieną gigahercų (GHz) diapazone, o kitą - terahercų (THz) diapazone. Didėjant temperatūroje nuo 470 iki 500 K, smailės dažnis pasislenka nuo 20 iki 100 GHz, tačiau slopinimas mažėja, kai temperatūra artėja prie T_c .

$$\varepsilon^* = \varepsilon_\infty + \frac{\Delta\varepsilon\omega^2}{\omega - \omega_0 + i\omega_0\gamma}, \quad (6)$$



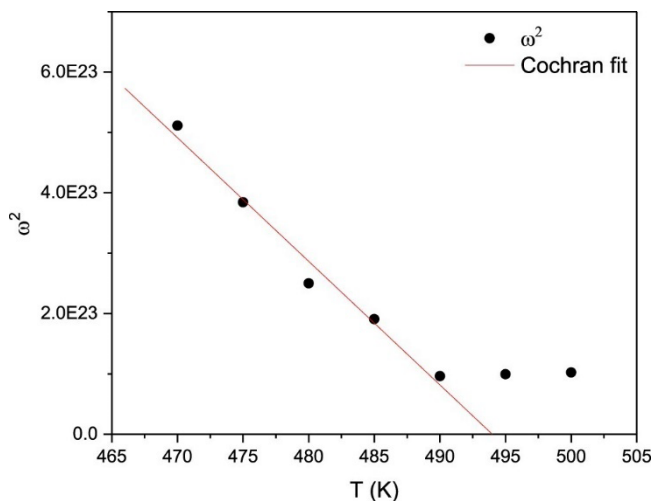
(a)



(b)

18 pav. Pavaizduota PHS keramikos leidžiamosios gebos duomenų realiosios (a) ir menamosios (b) dalių priklausomybė nuo dažnio esant aukštai temperatūrai. Linijomis pažymėtas optimalus eksperimentinių duomenų taškų išsidėstymas pagal (6) formulę.

19 paveiksle pavaizduota nubrėžta temperatūros ir osciliatoriaus dažnio priklausomybė, vaizduojanti rezonansinės dispersijos smailę apie fazinio perėjimo temperatūrą.



19 pav. Minkštojo režimo priklausomybė nuo dažnio.

Antiferoelektrinėse medžiagose minkštasis režimas pasižymi nuo temperatūros priklausomu minkštėjimu, kurį apibūdina Cochran dėsnis [30].

Išvados

$\text{PbHf}_{0.92}\text{Sn}_{0.08}\text{O}_3$ (PHS) kristalai pasižymėjo unikaliomis dielektrinėmis ir struktūrinėmis savybėmis, suteikiančiomis vertingų įžvalgų apie jų fazinio perėjimo dinamiką. Plačiajuostė dielektrinė spektroskopija atskleidė pirmosios eilės fazinį perėjimą netoli 494 K Curie temperatūros, kurį lydi reikšmingi histerezės efektai. Pastebėta rezonansinio tipo dispersija, kuri gali būti siejama su minkštojo režimo buvimu. Medžiaga išlaiko savo struktūrinį vientisumą ir kartu pasižymi geresnėmis dielektrinėmis savybėmis, kaip matyti iš tarpinių fazių nebuvimo esant mažai Sn koncentracijai (<6 %).

6.8. Apibendrinimas

Šioje disertacijoje aprašomas eksperimentinis impulsinio lazerinio nusodinimo taikymas šių medžiagų savybėms pagerinti ir plačiajuostis įvairių medžiagų (plėvelių ir biriųjų medžiagų) dielektrinių savybių tyrimas. Gautos šios išvados:

1. Švino cirkonato titanato ($\text{PbZr}_{0.2}\text{Ti}_{0.8}\text{O}_3$) plonosios plėvelės ant stroncio titanato (SrTiO_3) substratų pasižymi 32 % didesniu pjezoelektriniu poveikiu, palyginti su birių bandiniu, išryškinant unikalią nanomastelinių matmenų ir deformacijos poveikio įtaką.

2. Ištirtas nusodinimo parametrų $0,8(\text{Na}_{0.5}\text{Bi}_{0.5}\text{TiO}_3)$ - $0,2(\text{BaTiO}_3)$ poveikis ir įvairiais metodais patvirtinta optimali plėvelių kokybė bei parodytas geras plėvelės glotnumas, o stochiometrija artima mūsų tikslinei medžiagai.

3. Plonosios ZrSnSe_3 plėvelės buvo tiriamos taikant daigiatikslį ir vienatikslį metodus. Gautas ZrSnSe_3 , ZrSe_2 ir SnSe plonų plėvelių nusodinimo parametrų poveikis, kuris gali būti panaudotas daugiasluoksniams struktūroms ruošti, kad būtų pasiekta reikiama ZrSnSe_3 plėvelių kokybė.

4. Bismuto ferito ir bario titanato (70 % BiFeO_3 ir 30 % BaTiO_3) kietųjų tirpalų reentrantinio relaksoriaus elgsena rodo sudėtingus termiškai indukuotus perėjimus tarp tvarkingų ir netvarkingų būsenų, atskleistus plačiajuostės dielektrinės spektroskopijos būdu plačiame

dažnių diapazone nuo 20 Hz iki 20 GHz ir temperatūrų intervale nuo 270 K iki 400 K.

5. Švino hafnato alavo ($\text{PbHf}_{0,92}\text{Sn}_{0,08}\text{O}_3$) kristalai pasižymi žymiais dispersijos smailės poslinkiais ir slopinimo koeficiento pokyčiais netoli Curie temperatūros, kuri yra 494 K, kaip nustatyta plačiauoste dielektrine spektroskopija ir patvirtinta rezonansiniu dispersijos modeliu.

6.9. Nuorodos

- [1] D. Damjanovic, “Ferroelectric sensors,” *IEEE Sens. J.*, vol. 1, no. 3, pp. 191–206, 2001, doi: 10.1109/JSEN.2001.954832.
- [2] A. R. Balakrishna, J. E. Huber, and C. M. Landis, “Nano-actuator concepts based on ferroelectric switching,” *Smart Mater. Struct.*, vol. 23, no. 8, 2014, doi: 10.1088/0964-1726/23/8/085016.
- [3] R. S. Lous, “Ferroelectric Memory Devices, How to store the information of the future?,” no. July, p. 23 pp, 2011, [Online]. Available:
<https://www.rug.nl/research/zernike/education/topmasternanoscience/ns190lous.pdf>
- [4] K. Yao, S. Chen, S. C. Lai, and Y. M. Yousry, “Enabling Distributed Intelligence with Ferroelectric Multifunctionalities,” *Adv. Sci.*, vol. 9, no. 1, pp. 1–30, 2022, doi: 10.1002/advs.202103842.
- [5] M. H. Zhang *et al.*, “Electric-field-induced antiferroelectric to ferroelectric phase transition in polycrystalline NaNbO_3 ,” *Acta Mater.*, vol. 200, pp. 127–135, 2020, doi: 10.1016/j.actamat.2020.09.002.
- [6] R. Eason, S. Barrington, C. Grivas, T. May-Smith, and D. Shepherd, “Pulsed Laser Deposition of Thin Films: Applications-Led Growth of Functional Materials,” in *Pulsed Laser Deposition of Thin Films: Applications-Led Growth of Functional Materials*, 2006, pp. 383–420. doi: 10.1002/0470052120.
- [7] N. A. Shepelin, Z. P. Tehrani, N. Ohannessian, C. W. Schneider, D. Pergolesi, and T. Lippert, “A practical guide to pulsed laser

- deposition,” *Chem. Soc. Rev.*, vol. 52, no. 7, pp. 2294–2321, 2023, doi: 10.1039/d2cs00938b.
- [8] Š. Svirskas, D. Jablonskas, S. Rudys, S. Lapinskas, R. Grigalaitis, and J. Banys, “Broad-band measurements of dielectric permittivity in coaxial line using partially filled circular waveguide,” *Rev. Sci. Instrum.*, vol. 91, no. 3, 2020, doi: 10.1063/1.5136317.
- [9] F. Gellé, R. Chirita, D. Mertz, M. V. Rastei, A. Dinia, and S. Colis, “Guideline to atomically flat TiO₂-terminated SrTiO₃(001) surfaces,” *Surf. Sci.*, vol. 677, no. February, pp. 39–45, 2018, doi: 10.1016/j.susc.2018.06.001.
- [10] V. Raicu, “Dielectric dispersion of biological matter: Model combining Debye-type and ‘universal’ responses,” *Phys. Rev. E - Stat. Physics, Plasmas, Fluids, Relat. Interdiscip. Top.*, vol. 60, no. 4, pp. 4677–4680, 1999, doi: 10.1103/PhysRevE.60.4677.
- [11] J. D. S. Guerra, R. J. Portugal, A. C. Silva, R. Guo, and A. S. Bhalla, “Investigation of the conduction processes in PZT-based multiferroics: Analysis from Jonscher’s formalism,” *Phys. Status Solidi Basic Res.*, vol. 251, no. 5, pp. 1020–1027, 2014, doi: 10.1002/pssb.201350336.
- [12] D. V. Kuzenko, “Temperature-activation mechanism of the temperature dependence of the dielectric constant of ferroelectric ceramics PZT,” *J. Adv. Dielectr.*, vol. 12, no. 3, pp. 1–7, 2022, doi: 10.1142/S2010135X22500102.
- [13] S. Sasikumar, R. Saravanan, S. Saravanakumar, and K. Aravinth, “Charge correlation of ferroelectric and piezoelectric properties of (1 – x)(Na_{0.5}Bi_{0.5})TiO₃–xBaTiO₃ lead-free ceramic solid solution,” *J. Mater. Sci. Mater. Electron.*, vol. 28, no. 13, pp. 9950–9963, 2017, doi: 10.1007/s10854-017-6753-5.
- [14] H. Lidjici, B. Lagoun, M. Berrahal, M. Rguitti, M. A. Hentatti, and H. Khemakhem, “XRD, Raman and electrical studies on the (1-x)(Na_{0.5}Bi_{0.5})TiO₃-xBaTiO₃ lead free ceramics,” *J. Alloys Compd.*, vol. 618, pp. 643–648, 2015, doi: 10.1016/j.jallcom.2014.08.161.
- [15] Z. Yang *et al.*, “Re-entrant relaxor ferroelectric behaviour in Nb-

- doped BiFeO₃-BaTiO₃ ceramics,” *J. Mater. Chem. C*, vol. 11, no. 6, pp. 2186–2195, 2023, doi: 10.1039/d2tc04702k.
- [16] V. Haronin, Z. Yang, R. Grigalaitis, I. Calisir, J. Banys, and D. A. Hall, “Broadband dielectric spectroscopy of Nb-doped 0.7BiFeO₃-0.3BaTiO₃ ceramics,” *J. Phys. Commun.*, vol. 8, no. 6, pp. 0–8, 2024, doi: 10.1088/2399-6528/ad55a2.
- [17] K. H. Härdtl, “Electrical and mechanical losses in ferroelectric ceramics,” *Ceram. Int.*, vol. 8, no. 4, pp. 121–127, 1982, doi: 10.1016/0272-8842(82)90001-3.
- [18] K. S. Cole and R. H. Cole, “Dispersion and Absorption in Dielectrics I. Alternating Current Characteristics,” *J. Chem. Phys.*, vol. 9, no. 4, pp. 341–351, Apr. 1941, doi: 10.1063/1.1750906.
- [19] S. Srivastava *et al.*, “Synthesis of zinc oxide (ZnO) nanorods and its phenol sensing by dielectric investigation,” *J. Alloys Compd.*, vol. 644, pp. 597–601, 2015, doi: 10.1016/j.jallcom.2015.04.220.
- [20] T. Wang *et al.*, “Dielectric relaxation and Maxwell-Wagner interface polarization in Nb₂O₅ doped 0.65BiFeO₃-0.35BaTiO₃ ceramics,” *J. Appl. Phys.*, vol. 121, no. 8, pp. 0–9, 2017, doi: 10.1063/1.4977107.
- [21] K. L. Ngai, *Relaxation and Diffusion in Complex Systems*. New York, NY: Springer New York, 2011. doi: 10.1007/978-1-4419-7649-9.
- [22] D. Viehland, S. J. Jang, L. E. Cross, and M. Wuttig, “Freezing of the polarization fluctuations in lead magnesium niobate relaxors,” *J. Appl. Phys.*, vol. 68, no. 6, pp. 2916–2921, 1990, doi: 10.1063/1.346425.
- [23] R. Grigalaitis, J. Banys, A. Kania, and A. Slodczyk, “Distribution of relaxation times in PMN single crystal,” *J. Phys. IV*, vol. 128, pp. 127–131, Sep. 2005, doi: 10.1051/jp4:2005128020.
- [24] J. Macutkevic, J. Banys, R. Grigalaitis, and Y. Vysochanskii, “Asymmetric phase diagram of mixed CuInP₂(S_xSe_{1-x})₆ crystals,” *Phys. Rev. B*, vol. 78, no. 6, p. 064101, Aug. 2008, doi: 10.1103/PhysRevB.78.064101.
- [25] J. Banys, R. Grigalaitis, A. Mikonis, J. Macutkevic, and P. Keburis, “Distribution of relaxation times of relaxors: comparison

- with dipolar glasses,” *Phys. status solidi c*, vol. 6, no. 12, pp. 2725–2730, Dec. 2009, doi: 10.1002/pssc.200982529.
- [26] B. Li, T. Zheng, X. Wei, S. Zhong, Y. Li, and J. Wu, “Constructing Relaxor/Ferroelectric Pseudocomposite to Reveal the Domain Role in Electrostrain of Bismuth Ferrite-Barium Titanate Based Ceramics,” *ACS Appl. Mater. Interfaces*, vol. 14, no. 16, pp. 18713–18722, 2022, doi: 10.1021/acscami.2c03817.
- [27] X. Zhao, B. Li, D. Tai, T. Zheng, and J. Wu, “Destruction of conducting channels driven resistivity enhancement in bismuth ferrite-barium titanate based ceramics,” *J. Alloys Compd.*, vol. 1006, no. September, p. 176295, 2024, doi: 10.1016/j.jallcom.2024.176295.
- [28] M. A. Kniازهva *et al.*, “Ferroelectric to incommensurate fluctuations crossover in PbHfO₃-PbSnO₃,” *Phys. Rev. B*, vol. 105, no. 1, pp. 1–15, 2022, doi: 10.1103/PhysRevB.105.014101.
- [29] I. Jankowska-Sumara, J. H. Ko, and A. Majchrowski, “The complexity of structural phase transitions in Pb(Hf_{0.92}Sn_{0.08})O₃ single crystals,” *J. Am. Ceram. Soc.*, vol. 104, no. 11, pp. 5990–6001, 2021, doi: 10.1111/jace.17967.
- [30] P. Debye, *Polar Molecules*. Dover Publication, 1954.

6.10. Trumpa informacija apie disertacijos autorių

Vardas Pavardė: Vadzim Haronin

Išsilavinimas

2012-2017 m. studijavo Baltarusijos valstybė Informatikos universitetas ir radioelektronika ir įgijo elektronikos technikos inžinieriaus kvalifikaciją;

2017-2019 m. studijavo Baltarusijos valstybė Informatikos universitetas ir radioelektronika ir ir įgijo technikos mokslų magistro laipsnį;

2020-2024 m. studijavo Vilniaus universitete fizikos doktorantūroje.

Kontaktinis el. paštas: vadzim.haronin@ff.vu.lt.

PUBLIKACIJŲ SĄRAŠAS

1. V. Haronin, Z. Yang, R. Grigalaitis, I. Calisir, J. Banys, and D. A. Hall, “Broadband dielectric spectroscopy of Nb-doped 0.7BiFeO₃-0.3BaTiO₃ ceramics,” *J. Phys. Commun.*, vol. 8, no. 6, pp. 0–8, 2024, doi: 10.1088/2399-6528/ad55a2.

2. Haronin, V., Jankowska-Sumara, I., Kadlec, C., Majchrowski, A., Suvorova, O., Grigalaitis, R., & Banys, J. (2024). Broadband dielectric spectroscopy of a PbHf_{1-x}Sn_xO₃ material. *Phase Transitions*, 1–6. doi: 10.1080/01411594.2024.2369838.

3. V. Haronin, M. Alexe, R. Grigalaitis, J. Banys. Semiconductive lead zirconate titanate thin films grown by pulsed laser deposition, *Lithuanian Journal of Physics*, Vol. 64, No. 2, pp. 101–106 (2024). doi: 10.3952/physics.2024.64.2.3.

NOTES

NOTES

Vilniaus universiteto leidykla
Saulėtekio al. 9, III rūmai, LT-10222 Vilnius
El. p. info@leidykla.vu.lt, www.leidykla.vu.lt
bookshop.vu.lt, journals.vu.lt
Tiražas 15 egz.